

UC Irvine

UC Irvine Electronic Theses and Dissertations

Title

Femtosecond Holography of Sprays

Permalink

<https://escholarship.org/uc/item/9kv8v0qs>

Author

Minniti, Marco

Publication Date

2019

Copyright Information

This work is made available under the terms of a Creative Commons Attribution-NonCommercial-ShareAlike License, available at <https://creativecommons.org/licenses/by-nc-sa/4.0/>

Peer reviewed|Thesis/dissertation

UNIVERSITY OF CALIFORNIA,
IRVINE

Femtosecond Holography of Sprays

DISSERTATION

submitted in partial satisfaction of the requirements
for the degree of

DOCTOR OF PHILOSOPHY

in Mechanical and Aerospace Engineering

by

Marco Minniti

Dissertation Committee:
Professor Derek Dunn-Rankin, Chair
Professor Vasanth Venugopalan
Professor Mark Walter

2019

Portion of Chapter 6 © 2017 OSA Publishing
Portion of Chapter 6 © 2018 Begell House
Portion of Chapter 7 © 2019 Begell House
All other materials © 2019 Marco Minniti

DEDICATION

To my high school philosophy teacher, Ornella Costa, who introduced me to Galileo's "*Dialogue Concerning the Two Chief World Systems*," the reading that consolidated my budding interest in the sciences.

To my high school math teacher, who after realizing that I am a strong performer under deadline-induced stress, started questioning me at the blackboard every first day of school after the summer recess to "boost my motivation"... and start off my GPA with a 4/10 ("severely insufficient").

To my aerospace structures Professor at Politecnico di Milano, who during an oral exam told me: "You would make a fine chemical engineer, but not an aerospace one."

But most importantly, this is dedicated to my beloved parents, Carla and Silvio, who gifted me with self-reliance, confidence, curiosity, and the belief that through hard work I could attain whatever I wanted.

TABLE OF CONTENTS

LIST OF FIGURES	vii
LIST OF TABLES	xxii
ACKNOWLEDGMENTS	xxiii
CURRICULUM VITAE	xxvi
ABSTRACT OF THE DISSERTATION	xxx
1 Introduction	1
2 Fluid dynamics of spray atomization	7
2.1 Properties defining spray formation	14
2.2 Spray breakup regime.....	18
3 Review of imaging techniques for optically dense sprays	25
3.1 X-ray techniques.....	29
3.2 Time-gated ballistic imaging	33
3.3 Section summary	47
4 Monte Carlo simulation of photon transport in turbid media	50
4.1 Photon-transport theory (Beer-Lambert law)	51
4.2 Simulation results.....	55
4.2.1 Photon transport simulations in turbid media with OD=5	60
4.2.2 Simulation 1: 25 mm aperture at the lens plane	63
4.2.2.1 <i>No Time-Gate – soft spatial filter</i>	64
4.2.2.2 <i>Time-Gated – soft spatial filter</i>	65
4.2.2.3 <i>Ballistic photons – soft spatial filter</i>	66
4.2.2.4 <i>Simulation 1 - Observations</i>	67
4.2.3 Simulation 2: 3 mm aperture at the lens plane OD=5	67
4.2.3.1 <i>No gate – aggressive spatial filter</i>	68
4.2.3.2 <i>Time-gated – aggressive spatial filter</i>	69
4.2.3.3 <i>Ballistic photons – aggressive spatial filter</i>	70

4.2.3.4	<i>Simulation 2 - Observations</i>	70
4.2.4	Photon transport simulations in turbid media with OD=10	71
4.2.5	Simulation 3: 25 mm aperture at the lens plane, OD 10	72
4.2.5.1	<i>No gate – soft spatial filter</i>	74
4.2.5.2	<i>Time-gated – soft spatial filter</i>	75
4.2.5.3	<i>Ballistic photons - soft spatial filter</i>	76
4.2.6	Simulation 4: 3 mm aperture at the lens plane, OD 10	77
4.2.6.1	<i>No gate – aggressive spatial filter</i>	77
4.2.6.2	<i>Time-gated – aggressive spatial filter</i>	78
4.2.6.3	<i>Ballistic photons – aggressive spatial filter</i>	79
4.2.7	Simulations 3 and 4 – Observations	79
4.3	Comparison with experimental results	82
4.4	Section summary	83
5	Femtosecond off-axis digital holography	86
5.1	Interference	91
5.2	Coherence	96
5.2.1	Temporal Coherence	96
5.2.2	Spatial Coherence	99
5.3	Diffraction.....	101
5.4	Hologram recording and reconstruction	104
5.5	Numerical reconstruction of a digital hologram	108
5.5.1	Convolution Approach or Angular Spectrum Method (ASM)	113
5.6	Separation of virtual image, real image and dc term in off-axis holography....	115
5.6.1	Spatial frequency requirements	120
5.7	Recording intensity and dynamic range	121
5.8	Coherence filtering as an alternative to time-gating	122
6	Demonstrating coherence filtering on a polydisperse spray distribution with OD 12	129
6.1	Experimental setup.....	131
6.1.1	Spray setup	131
6.1.2	Optical setup	137
6.2	Measurements	142
6.2.1	Spray and scattering environment characterization	142
6.2.2	Holography results	158
6.2.2.1	<i>Effects of Nozzle Pressure (unobscured spray)</i>	158

6.2.2.2	<i>3-D focusing</i>	159
6.2.2.3	<i>Droplet microscopy in turbid media</i>	162
6.3	Section summary	173
7	Imaging of a realistic dodecane spray (ambient conditions)	175
7.1	Experimental Setup	177
7.1.1	Spray setup	177
7.1.2	Optical setup	182
7.2	Results	184
7.2.1	Imaging injection in the near nozzle region.	184
7.2.2	Holography of high-pressure dodecane spray in high OD environment. 190	
7.2.3	3D reconstructions of the gas to liquid interface in turbid media	195
7.3	Section summary	200
8	Challenges when imaging at high pressure and temperature	203
8.1	Experimental Setup Description.....	205
8.2	Results	208
8.2.1	Pulse broadening quantification and effects	208
8.2.2	Reconstructed images of USAF chart at high temperature and pressure 214	
8.3	CCD damage threshold	216
8.4	Section summary	217
9	Imaging of a realistic dodecane spray in engine-like conditions	219
9.1	Experimental setup description	221
9.1.1	Spray and pressure vessel	221
9.1.2	Optical Apparatus	221
9.2	Results	222
9.2.1	Ambient temperature and pressure	222
9.2.2	High-pressure, ambient temperature	231
9.2.3	Comparison to inline holography and lens less shadowgraph imaging	234
9.3	Issues	239
9.3.1	Window fouling	239
9.3.2	Synchronization challenges	240
9.3.3	Artifacts and noise	246
9.4	Section summary	252

10 Opportunities for improved performance	254
10.1 Reconstruction algorithm improvements.....	255
10.1.1 Batch reconstructions	255
10.1.2 Improved zero padding and reconstruction resolution	256
10.1.2.1 <i>USAF resolution chart – 100 px wide reconstruction area</i>	261
10.1.2.2 <i>USAF resolution chart – 400 px wide reconstruction area</i>	261
10.1.2.3 <i>Dodecane spray at early injection – 100 px wide reconstruction area</i>	262
10.1.2.4 <i>Dodecane spray at early injection – 400 px wide reconstruction area</i>	262
10.1.3 Addressing potential sources of aliasing from undersampling	264
10.1.3.1 <i>Pixel pitch and sampling frequency</i>	265
10.1.3.2 <i>Condition to record an off-axis digital hologram correctly</i>	267
10.1.3.3 <i>Validity of the angular spectrum method</i>	268
10.1.3.4 <i>Conclusions and corrective actions</i>	271
10.2 Optical improvements – lensed results.....	275
10.2.1 USAF reconstructions – lensed configuration f=180mm	276
10.2.2 Spray reconstructions – lensed configuration f=180mm	282
10.2.3 Comparison between lensed shadowgraph inline holography and off-axis holography	285
10.3 Section summary	289
11 Future recommendations	291
11.1 Beam Multiplexing	291
11.1.1 Multiple reference beams	292
11.1.2 Single reference and multiple object beams	293
11.2 Depth maps and 3D visualization	294
11.2.1 Stereo disparity method - recovering stereoscopic information from a single hologram	294
11.2.2 Stereoscopic viewing of digital holograms	296
12 Conclusions	297
13 Bibliography	303

LIST OF FIGURES

Figure 1.1 Envelopes associated with modern diesel, gas turbine, and gasoline direct-injection systems. The fuel surrogates used are respectively n-dodecane, n-decane, and iso-octane. The diagram assumes liquid fuel injection temperatures between 300 and 363 K [14].	6
Figure 2.1 Spray regions [17].	10
Figure 2.2 Microscope shadowgram showing flow inside a transparent nozzle tip [18].	11
Figure 2.3 Ballistic image at steady state of a diesel spray [3].	13
Figure 2.4 Ballistic image of a dodecane jet in the steady-state region. Chamber pressure of 30 bar and temperature of 445 K [10].	13
Figure 2.5 Ballistic image of a diesel jet taken 1.64 ms after injection start, between 1 and 4 mm from the nozzle exit (60 bar, 900 K) [10].	14
Figure 2.6 Flow regime at nozzle exit for an orifice plain nozzle [17].	15
Figure 2.7 Classification of breakup regimes as a function of Ohnesorge number versus Reynolds number on a log scale, the graph is populated with conditions found in relevant primary atomization models, as well as the experimental conditions applied in this dissertation.	19
Figure 2.8 Liquid volume fraction versus distance from the nozzle exit for a water spray for different pressure values [17].	23
Figure 3.1 Comparison between shadowgraph images (a and c) and X-ray PCI (b and d) of the same flow, the images are approximately 800 μm wide and 950 μm tall [56].	31
Figure 3.2 PCI simulation of a 150 μm core droplet behind arrays of multiple 30 μm droplets. Left side: 4 drops between the core drop and the scintillator. Right side: 8 drops between the core drop and the scintillator, the core drop cannot be detected. This condition corresponds to a visible light OD between 5 and 8 [18].	32
Figure 3.3 X-ray radiograph simulation by Linne. A larger 150 μm core droplet is imaged behind an array of μm droplets; the droplet concentration is increased from left to right, the shape of the core droplet cannot be resolved when attenuation is above 30%.	33
Figure 3.4 Time dependence of ballistic and multiple scattering photons with respect to the OKE gate transmission [8].	37

Figure 3.5 Typical single-shot time-gated ballistic imaging setup [18]	37
Figure 3.6 Ballistic images of a dodecane spray injected at 1450 atm, 700 μ s from the start of injection. The field of view covers 3 mm of spray length. [8].....	39
Figure 3.7 Full jet images (450 K and 3 MPa), for commercially available Diesel fuel: upper row contains ballistic images and lower row contains shadow images [1]	43
Figure 3.8 Comparison of fluid dynamic structures at the gas to liquid interface for ballistic imaging shadowgraph imaging. Commercial diesel fuel, T=450 K P= 3 MPa [1].	44
Figure 3.9 Comparison between shadowgraph imaging and ballistic imaging. Images showing the gas to liquid interface at 900 K and 6MPa, these are supercritical conditions for all these fuels in a nitrogen mixture. The ballistic images show cellular structures consistent with supercritical turbulent mixing layers that are more prominent in the butanol and dodecane case, the shadowgraph images shows Schieren style structures [1] 45	45
Figure 3.10 BI 0.8ms after injection start of a diesel jet at ECN Spray A conditions (T=900 K P= 60 bar), showing a region between 1 and 5 mm from the nozzle. The cellular transmissive structures at the spray edges suggest the presence of a supercritical mixing layer [10].....	45
Figure 3.11 Vapor-liquid equilibrium points for a mixture of dodecane fuel and nitrogen gas at different pressures [1].....	46
Figure 3.12 Graph showing atomization regimes for dodecane injected at 363 K into a chamber filled with gaseous nitrogen at different temperatures and pressures, the white region represents the classical spray regime, the gray region the diffusion dominated spray regime. Three lines represent the compression cycle for different diesel engines; the top line represents a turbo-charged compression cycle, the middle one a medium-load and the bottom one a light-load [14].....	46
Figure 4.1 Variation of irradiation energy dI for a collimated beam going through an elementary volume of a scattering medium.	52
Figure 4.2 Scattering orders for various optical depths of a collection of spherical fuel droplets (Long-Normal distribution of diameter 5 microns and σ =0.5 micron) [17]	55
Figure 4.3 Gated ballistic imaging setup simulated using the Monte Carlo code developed by the team at Lund University.	57

Figure 4.4 Spatially filtered shadowgraph setup simulated using the Monte Carlo code from the team at Lund University, notice the absence of an OKE gate.	57
Figure 4.5 Diagram showing the simplified simulated domain.	60
Figure 4.6 Temporal profile of the simulated imaging pulse and time-gate profile.	62
Figure 4.7 Mie Scattering phase function of the simulated turbid media.	62
Figure 4.8 Imaging pulse spectrum and particle size distribution of the simulated turbid media.	63
Figure 4.9 Intensity-based image and spatial profile of the photon count at the detector	64
Figure 4.10 Spatial and temporal intensity profile of the photon count at the detector – temporal profile of photon count at the detector.....	64
Figure 4.11 Intensity-based image and spatial profile of the photon count at the detector	65
Figure 4.12 Spatial and temporal intensity profile of the photon count at the detector – temporal profile of photon count at the detector.....	65
Figure 4.13 Intensity-based image and spatial profile of the photon count at the detector	66
Figure 4.14 Spatial and temporal intensity profile of the photon count at the detector – temporal profile of photon count at the detector.....	66
Figure 4.15 Intensity-based image and spatial profile of the photon count at the detector	68
Figure 4.16 Spatial and temporal intensity profile of the photon count at the detector – temporal profile of photon count at the detector.....	68
Figure 4.17 Intensity-based image and spatial profile of the photon count at the detector	69
Figure 4.18 Spatial and temporal intensity profile of the photon count at the detector – temporal profile of photon count at the detector.....	69
Figure 4.19 Intensity-based image and spatial profile of the photon count at the detector	70
Figure 4.20 Spatial and temporal intensity profile of the photon count at the detector – temporal profile of photon count at the detector.....	70

Figure 4.21 Temporal profile of the simulated imaging pulse and time-gate profile 72

Figure 4.22 Intensity-based image and spatial profile of the photon count at the detector 74

Figure 4.23 Spatial and temporal intensity profile of the photon count at the detector – temporal profile of photon count at the detector 74

Figure 4.24 Intensity-based image and spatial profile of the photon count at the detector 75

Figure 4.25 Spatial and temporal intensity profile of the photon count at the detector – temporal profile of photon count at the detector 75

Figure 4.26 Intensity-based image and spatial profile of the photon count at the detector 76

Figure 4.27 Spatial and temporal intensity profile of the photon count at the detector – temporal profile of photon count at the detector 76

Figure 4.28 Intensity-based image and spatial profile of the photon count at the detector 77

Figure 4.29 Spatial and temporal intensity profile of the photon count at the detector – temporal profile of photon count at the detector 77

Figure 4.30 Intensity-based image and spatial profile of the photon count at the detector 78

Figure 4.31 Spatial and temporal intensity profile of the photon count at the detector – temporal profile of photon count at the detector 78

Figure 4.32 Intensity-based image and spatial profile of the photon count at the detector 79

Figure 4.33 Spatial and temporal intensity profile of the photon count at the detector – temporal profile of photon count at the detector 79

Figure 4.34 Kerr effect ballistic imaging of group 4 USAF resolution target through 0.6-micron scattering particles media of various optical depths at 'open gate' and Kerr gated' modes. Notice how the 2nd row where only spatial filtering is applied provides substantial noise reduction, comparable to the one offered by time gating [11] 83

Figure 5.1 Recording a traditional hologram, the laser beam is split into a reference beam and an object beam. The object beam after being reflected from the object interferes with the reference beam and creates an interference pattern which is called hologram. [63] 90

Figure 5.2 Reconstruction of a traditional hologram: the photographic film over which the hologram was recorded is illuminated by the original reference beam. The reference beam is diffracted by the hologram reconstructing the original object beam. The observer can now see the object identical to the original one both in shape and position. [63] 90

Figure 5.3 Michelson interferometer..... 97

Figure 5.4 Young interferometer [63] 99

Figure 5.5 Huygens' principle [63].....101

Figure 5.6 Reference system [63].....103

Figure 5.7 Recording setup for off-axis holography [65].....104

Figure 5.8 Interference pattern of object and reference beam in space and frequency domain. In off-axis digital holography cross term and conjugate cross term are separated in the frequency domain (bottom right picture) this allows to easily pick the cross term for reconstruction thus obtaining a reconstructed image of superior quality with respect to inline Gabor holography [11].....108

Figure 5.9 Reconstruction setup for off-axis holography [65].....109

Figure 5.10 Coordinate system for numerical reconstruction of a hologram [63].....111

Figure 5.11 Digital holography (a) Recording (b) Reconstructing with reference wave E_R (c) Reconstructing with conjugate reference wave E_R^* [63].....111

Figure 5.12 Layout for the reconstruction of the virtual image [63].....112

Figure 5.13 Digital Gabor Inline Holography setup, hologram and reconstructed image of a 400 micron needle [11].....118

Figure 5.14 Example of reconstructed images at different distances from the sensor. Inline hologram [11].....118

Figure 5.15 Diagram showing how object and reference pulse interfere at an angle, creating an interference pattern that separates coherent and incoherent information in the Fourier domain, the cross-correlation term boxed in green can be reconstructed into an image of the object without including the multiple-scattering noise contained in the DC term.....118

Figure 5.16 Reconstructed images from digital picosecond holograms with varying gate times imaged through a small-particle-emulsion scattering cell. In the left image, the first 10 ps of the light pulse are transmitted, in the second image only the last 10 ps of the pulse are transmitted while in the last image the whole 30 ps pulse is transmitted [69]..125

Figure 5.17 A comparison between femtosecond OKE ballistic imaging with a picosecond time-gate and off-axis femtosecond digital holography. USAF resolution target placed behind a suspension with 0.6 microns particles. [11].....128

Figure 6.1 Schematic of the spray setup.131

Figure 6.2 Water injected at 80 PSI (left) and 100 PSI (right) at ambient pressure and temperature. This automotive fuel injector is used in the setup to represent the “liquid core” of a high-pressure diesel spray137

Figure 6.3 Diagram of the optical setup137

Figure 6.4 View of the experimental setup showing the 10 cm scattering cell.140

Figure 6.5 side view of the experimental setup showing the 5 cm scattering cell.....141

Figure 6.6 Side view of the experimental setup, the 10 cm scattering cell is filled with water mist generated by the ultrasonic atomizer, at the same time, the fuel injector placed at the center of the cell is fired. The 100 fs pulse enters the cell from the left, the camera sits on the right-hand side of the picture, outside of the field of view. Note the severe scattering environment which causes the violet glow shown in this image.....141

Figure 6.7 Laser diffraction particle sizing of the near nozzle region of the fuel injector. Water injected at approximately 80 PSI.143

Figure 6.8 Malvern laser diffraction particle size measurements for water injected at 45 PSI, near-nozzle region.....145

Figure 6.9 Near nozzle particle size distribution for water injected at 45 PSI. Note the two peaks between 600 and 700 microns. The bimodal distribution outliers suggest that in the near nozzle region there is a considerable amount non-atomized liquid making this injector an excellent candidate to provide a liquid column that will be imaged when surrounded by a veil of optically obscuring water mist.145

Figure 6.10 Malvern near nozzle region measurement parameters for water injected at 80 PSI.146

Figure 6.11 Near nozzle region particle size distribution for water injected at 80 PSI. These data show that only 10% of the spray volume is below 130 μm in size, making it a

candidate source of large droplets and liquid ligaments mimicking the liquid core of a high-pressure diesel spray.....	146
Figure 6.12 Malvern measurement parameters for water injected at 100 PSI, near-nozzle region.....	147
Figure 6.13 Particle size distribution for water injected at 100 PSI, near-nozzle region. .	147
Figure 6.14 Malvern measurement parameters for water injected at 120 PSI, near-nozzle region.....	148
Figure 6.15 Particle size distribution for water injected at 120 PSI, near-nozzle region. .	148
Figure 6.16 Malvern measurement parameters for diesel fuel injected at 85 PSI 0.5 inches away from the nozzle exit.	149
Figure 6.17 Particle size distribution for diesel fuel injected at 85 PSI 0.5 inches away from the nozzle exit.....	149
Figure 6.18 Water mist produced by an ultrasonic atomizer. The particle size distribution is measured by Malvern Spraytec laser diffraction particle sizer	153
Figure 6.19 Droplet size distribution at the ultrasonic atomizer nozzle exit.	153
Figure 6.20 Droplet sizes measured at the edges of a diesel spray in the near nozzle region at moderate pressure conditions [74].....	157
Figure 6.21 The 10 cm mist cell before (left side) and after (middle and right side) being filled with water mist. Scattering is so severe that no collimated portion of the original laser beam can be observed leaving the enclosure. Distance between the windows is 10 cm. A second chamber with a 5 cm distance between windows was used for lower OD values.	158
Figure 6.22. Reconstructed images of a water spray from a 0.1 mm single orifice injector with increasing injection pressure. Reconstruction depth is 142 mm from the sensor. Left image injection pressure is 10.3 Bar, middle image 11.7 Bar, right image 13.8 Bar.....	159
Figure 6.23. Reconstructed images of a spray from a 1996 automotive multi-orifice fuel injector for gasoline port injection; water injection pressure 6.9 bar.	161
Figure 6.24. Spray from an automotive fuel injector. Injection pressure 10.3 bar. OD 6. .	164
Figure 6.25. The left picture shows the region of interest highlighted in Figure 6.24 but reconstructed 112 mm from the sensor plane. The right picture shows the same ROI reconstructed 144 mm away from the sensor.	164

Figure 6.26. Spray from a 1996 automotive multi-orifice fuel injector for gasoline port injection. The bottom row of images is shot 2.5 mm downstream with respect to the top row and reconstructed at the same distance.....	165
Figure 6.27. Reconstructed images of the 0.1 mm single orifice nozzle – top row shows a water spray injected at 13.8 Bar ($We \cong 44.6$), the image on the right is shot 0.3 s after the one on the left. The bottom row shows a water spray injected at 3.45 Bar ($We \cong 8.5$), the image on the right is shot 0.1 s after the one on the left. Transmissivity of the whole spray field varies from 10^{-5} to 10^{-4} (OD $\cong 9-11$).	166
Figure 6.28. Reconstructed image with no surrounding mist (left) and with a mist of OD 12 (right). 0.1 mm single orifice nozzle, water injected at 2.06 bar.....	167
Figure 6.29. Reconstructed images from a 0.3 mm single orifice nozzle. Injection pressure 2 Bar. Depth of reconstruction 142 mm.....	168
Figure 6.30. Spray from a 0.3 mm single orifice nozzle injected at 2 Bar as it develops over time ($We \cong 11$). Images are reconstructed 142 mm from the camera sensor. The top row shows the spray with no mist; the bottom row shows the spray surrounded by a mist with transmissivity as low as $0.5 \cdot 10^{-5}$ (OD 12).....	169
Figure 6.31. Lens image of the spray, 2f imaging layout with $f=50$. Water is injected at 30 PSI through a 0.1 mm single orifice nozzle. The left image is acquired with no mist surrounding the spray; the middle image shows the effects of scattering noise at OD=11 (transmittance 10^{-5}). In the image on the right spatial filtering provided by a 4 mm aperture is used to match the holographic system’s numerical aperture and provide a fair comparison to the holographic reconstructions shown in Figure 6.30.	172
Figure 6.32 The image of a USAF resolution chart placed inside the vessel at the spray location is reconstructed. Element 2 of group 4 can be resolved, meaning that the object side resolution at this reconstruction distance (approx 10-15 cm) is approximately 27 μm	173
Figure 7.1 The Diesel Engine Simulator setup at UC Irvine.	177
Figure 7.2 Fuel injection setup. 1. Bosch LBZ injector, 2. Two custom single hole axial injector nozzles (160 and 320 microns), 3. Common Rail, 4. Pressure Transducer, 5. Air over fuel pressure accumulator,–6. High-pressure inline filter, 7. Direct Injector Driver Module, 8. Fuel tank.....	177
Figure 7.3 Vessel flow characterization performed at CSM to maintain the injection zone at a constant temperature.....	179

Figure 7.4 CSM diesel engine simulator fitted within the ultra-short pulse off-axis holography experiment at UC Irvine.	180
Figure 7.5 Fluent model used to validate the injector cooling jacket design.....	181
Figure 7.6 USPODH optical setup.....	182
Figure 7.7 Object and reference beam path.....	184
Figure 7.8 Dodecane spray imaged 575 μ s after the fuel spray is triggered. The left image is numerically refocused to highlight ligaments detaching from the spray core.....	185
Figure 7.9 Dodecane spray, P_{inj} = 1550 bar, 1 ms injection. Image reconstructed 311 mm from the camera sensor.	188
Figure 7.10 Comparison between holographic reconstruction and shadowgraph image captured using a Phantom camera. The Phantom image is superimposed on the reconstructed image, and its transparency is increased (from left to right 0%, 50 %, and 90% transparency).....	190
Figure 7.11 Phantom camera, shadowgraph image. 5th injection event.....	192
Figure 7.12 Phantom camera, shadowgraph image. 7th injection event.....	192
Figure 7.13 Hologram shot after the 7 th injection event, the object beam outline disappeared, and the interference pattern is almost invisible.	193
Figure 7.14 Fourier transform of the hologram shown above, acquired when the vessel is saturated by dodecane mist. The strong cross-correlation term suggests that enough information is present to reconstruct images of spray hidden behind the fuel mist successfully.....	193
Figure 7.15 Reconstructed image of a dodecane spray injected at 1550 bar, 320 mm from the camera sensor. At this moment in time, the vessel is filled with dodecane mist, and incoherent imaging conveys no information.....	195
Figure 7.16 Dodecane spray injected at 1800 bar, chamber at ambient temperature and pressure.	196
Figure 7.17 The region of interested shown in Figure 7.16 is reconstructed at different depths; voids and ligaments detaching from the spray core can be resolved. The in-depth resolution for a dense spray target has been estimated to be approximately 2 mm.....	199
Figure 7.18 The pressure vessel's window that is closer to the camera is approximately 14 cm from the camera sensor. If we numerically reconstruct the previous hologram 145 mm	

from the sensor, these droplets appear. These are fuel droplets residing on the window's surface.	200
Figure 8.1 USPODH setup showing the pressure cell containing a USAF resolution chart.	205
Figure 8.2 Small pressure cell with 1'' diameter windows.	207
Figure 8.3 USPODH setup including a small volume temperature-controlled pressure vessel to investigate the effects of strong refraction index and density gradients along the imaging path.	207
Figure 8.4 Optical delay stage adjustment required to maintain interference as pressure is increased at constant temperature (T=21.5 °C).	210
Figure 8.5 Optical delay stage adjustment required to maintain interference as pressure is increased at constant temperature (T=170 °C).	210
Figure 8.6 Interference fringe count at ambient temperature and pressure and at 18.34 bar - 443.15 K. Pulse broadening adds 100 more fringes at higher pressures.	213
Figure 8.7 The pulse elongation caused by the windows and pressurized media is noticeable when looking at reconstructed images since the increased number of fringes in the hologram (see Figure 8.6) creates a larger field of view in the reconstructed image.	213
Figure 8.8 Reconstructions from different shots at 170 C, ambient pressure. Group 4 and 5 can be seen coming in and out of focus (density fluctuations of the media cause minor defocusing in the reconstructed image).	214
Figure 8.9 The figures above show numerical reconstructions from a hologram of a 1951 USAF resolution chart imaged at 170 °C. Temperature gradients cause slight defocusing in the reconstructed images, but this can be compensated by: 1.Minor adjustment of the optical delay stage 2. Numerical refocusing.	215
Figure 8.10 Reconstructed image of a 1951 USAF resolution chart in a pressure vessel at 18.3 bar and 443.15 K. Element 1 of group 4 is resolved.	216
Figure 9.1 Optical apparatus	221
Figure 9.2 Intensity-based image reconstructed 290 mm from the camera sensor showing a dodecane spray injected at 1560 bar in a chamber at ambient pressure and temperature.	225

Figure 9.3 The ROI boxed in red in Figure 9.2 is reconstructed at 3 different distances from the camera sensor, 5 mm apart from each other. From measuring the spray core diameter we know what no spray is present in the 1st and 3rd image because they are located 10 spray diameters away from the nozzle, it is therefore important to develop algorithms to discern the focused spray image (middle one) from out of focus artifacts created by projecting the spray’s shadow.227

Figure 9.4 Intensity-based image reconstructed 290 mm from the camera sensor showing a dodecane spray injected at 1570 bar through a 160 μm nozzle in a chamber at ambient pressure and temperature.....229

Figure 9.5 Magnification of the ROI highlighted in Figure 9.4 showing primary breakup structures at the gas to liquid interface of the spray core.229

Figure 9.6 The same ROI is reconstructed 292 and 289 mm from the hologram plane. ..230

Figure 9.7 Intensity-based image reconstructed 290 mm from the camera sensor showing a dodecane spray injected at 1570 bar in a chamber filled with nitrogen at 6.41 bar and ambient temperature.....232

Figure 9.8 Intensity-based image reconstructed 290 mm from the camera sensor showing a dodecane spray injected at 1580 bar in a chamber filled with nitrogen at 11.03 bar233

Figure 9.9 Dodecane spray injected at 1560 bar into a nitrogen-filled vessel, P=17.4 bar T=294.15 K. The gas to liquid interface is magnified on the right-hand side of the image.234

Figure 9.10 Comparison between lens less shadowgraph (left), reconstruction from an inline hologram (center) and off-axis hologram reconstruction of a dodecane spray injected at 1560 bar into a vessel at 17.4 bar – 295 K.237

Figure 9.11 Reconstructed Inline Hologram, Z=302mm, 1000 px reconstruction area, P_{vessel}= 17.4 Bar T_{vessel}= 295 K. The inline hologram does not reject multiple scattering noise as effectively as the off-axis one, the spray appears wider, the gas to liquid interface has poor contrast and artifacts attached to the spray core are observed. The periodic distance between artifacts suggests that they are leftovers of the bow shocks observed in the shadowgraph image.....237

Figure 9.12 Reconstructed Off-axis Hologram, Z=302mm, 400 px reconstruction box, P_{vessel} =17.4 Bar – T_{vessel} =295 K. The off-axis hologram reconstruction resolves the gas to liquid interface with good contrast and rejecting artifacts generated by bow shocks. Higher

magnification and resolution would be desirable to identify turbulent fluid dynamic structures.....238

Figure 9.13 Dodecane condensation on the vessel window’s surface impedes interference between the object and reference pulse.....240

Figure 9.14 Latency between the SDG Elite laser synchronizer and the fuel injector actuation, 10 events.243

Figure 9.15 Latency between the SDG Elite laser synchronizer and the pulse generator, 10 events.243

Figure 9.16 Latency between the pulse generator and the fuel injector actuation, 10 events.244

Figure 9.17 Trigger signals timeline: the pre-trigger signal (in red) from the SDG elite laser synchronizer triggers a pulse generator, which in turn triggers the camera and the DIDS module (in blue) controlling the spray. The DIDS energizes the fuel injector (in green), and a pre-determined fuel injection sequence is initiated. The graph shows 10 different acquisitions of the described signal sequence.....244

Figure 9.18 Gas to liquid interface of the liquid core generated by a dodecane spray injected at 1560 bar at ambient temperature and pressure. Both images show the left-half of the spray liquid core at the interface with the surrounding gas. This region is located approximately 200 μm downstream from the nozzle orifice. Early results (above) are compared to the one produced by the current setup.247

Figure 9.19 Reconstructed images of a USAF resolution chart placed inside the CSM pressure vessel. The noise is mostly caused by fuel residue on the window's surface, notice how there is a trade-off between noise and resolution as the reconstruction region size is increased from 50 to 500 px.249

Figure 9.20 By restricting the are surrounding the cross-correlation term included in the reconstruction process (similar to applying a low pass filter) we can limit the number of artifacts observed in the reconstruction, at the expense of image resolution.250

Figure 9.21 Intensity-based images reconstructed 295, 290 and 285 mm from the camera sensor showing a dodecane spray injected at 1560 bar in a chamber at ambient pressure and temperature. From measuring the spray core diameter we know what no spray is present in the 1st and 3rd image because they are located 10 spray diameters away from the nozzle, it is therefore important to develop algorithms to discern the focused spray

image (middle one) from out of focus artifacts created by numerically propagating the spray's shadow in planes where no physical features exist.252

Figure 10.1 Diagram showing how the interference angle between object and reference beam is directly proportional to the interference pattern frequency, which in turn is proportional to the distance in the Fourier domain between the DC and Cross-correlation term.257

Figure 10.2 In off-axis holography, only a portion of the frequency domain space surrounding the cross-correlation term is numerically reconstructed into an intensity-based image of the target using an angular spectrum algorithm. This allows to tune in the amount of noise rejection at the expense of image resolution.259

Figure 10.3 The green rectangle represents the new, larger reconstruction area that is selected, zero-padded, and then processed for reconstruction.260

Figure 10.4 Left: USAF resolution chart image reconstructed 118 mm from the camera sensor using a 100px x 100px reconstruction area - Right: USAF resolution chart image reconstructed 118 mm from the camera sensor using a 100px x 1026px reconstruction area261

Figure 10.5 Left: USAF resolution chart image reconstructed 118 mm from the camera sensor using a 400px x 400px reconstruction area - Right: USAF resolution chart image reconstructed 118 mm from the camera sensor using a 400px x 1026px reconstruction area261

Figure 10.6 Left: Dodecane spray image reconstructed 290 mm from the camera sensor using a 100px x 100px reconstruction area - Right: Dodecane spray image reconstructed 118 mm from the camera sensor using a 100px x 990px reconstruction area.262

Figure 10.7 Left: Dodecane spray image reconstructed 290 mm from the camera sensor using a 400px x 400px reconstruction area - Right: Dodecane spray image reconstructed 118 mm from the camera sensor using a 400px x 990px reconstruction area.263

Figure 10.8 Fresnel zone plate (FZP) generated by the diffracting field from a point object source.266

Figure 10.9 Simulated intensity pattern of the diffracted field from a rectangular aperture propagated using the ASM, left propagation distance $z=0.05$ m, right propagation distance $z=0.2$ m (showing aliasing error) [65].268

Figure 10.10 Diagram showing the ranges of recording and reconstruction distance that allow alias-free recording and reconstruction of an off-axis hologram. The colored rhombus shapes show where the results presented in this dissertation belong to given their hologram properties and reconstruction distance.....272

Figure 10.11 Diagram showing the ranges of recording and reconstruction distance that allow alias-free recording and reconstruction of an off-axis hologram. The implementation of the FDM for reconstruction allows alias-free reconstruction of holograms at a working distance larger than 286 mm.....273

Figure 10.12 Diagram showing the ranges of recording and reconstruction distance that allow alias-free recording and reconstruction of an off-axis hologram. The addition of extra zero-padding allows extending the upper alias-free reconstruction limit of the ASM.....273

Figure 10.13 ASM (left) vs. FDM (right) reconstructed images of a resolution chart, 300 mm from the camera sensor, lensless off-axis holography.....274

Figure 10.14 ASM (left) vs FDM (right) reconstructed images of a resolution chart, $z=118\text{mm}$, lensed off-axis holography, $f=118\text{ mm}$274

Figure 10.15 Lensed USPODH setup276

Figure 10.16 Reconstructed off-axis hologram of a USAF resolution chart placed at the center of the pressure vessel at the fuel injector location, $z=118\text{mm}$, 400 px reconstruction mask, $d_o=39\text{ cm}$ $d_i=42\text{ cm}$ $f=180\text{mm}$278

Figure 10.17 Magnification of group 4 and 5, element 6 of group 4 can be resolved which corresponds to an object side resolution $17\text{ }\mu\text{m}$ 279

Figure 10.18 Reconstructed off-axis hologram of a USAF resolution chart placed at the center of the pressure vessel at the fuel injector location, $z=4\text{mm}$, $450\times 998\text{px}$ reconstruction mask, $d_o=35\text{ cm}$ $d_i=40\text{ M}=1.14$ $f=180\text{mm}$280

Figure 10.19.....280

Figure 10.20 Reconstructed off-axis hologram of a USAF resolution chart placed at the center of the pressure vessel at the fuel injector location, $z=135\text{mm}$, $400\times 1024\text{px}$ reconstruction mask, $d_o=35\text{ cm}$ $d_i=51\text{ M}=1.46$ $f=180\text{mm}$281

Figure 10.21 The higher magnification $M=1.46$ did not improve resolution we reached the resolution limit for the current combination of optics, target size, sensor size working distance, and numerical reconstruction method.....282

Figure 10.22 Reconstructed off-axis hologram - 988 x 400 rectangular mask - $z=-134.5$ - $d_o=35$ cm $d_i=51$ cm $M=1.46$ $f=180$ mm. The regions indicated by the red arrows are expanded in the next figure.283

Figure 10.23 Primary atomization fluid structures in the near nozzle region.....284

Figure 10.24 Focused shadowgraph (object beam only), brightness +80%, contrast +10%287

Figure 10.25 Reconstructed Inline hologram - 1000px reconstruction mask - $z=0$ mm - brightness +80%287

Figure 10.26 Reconstructed off-axis hologram, $z=0$ mm, 970x400px reconstruction mask, +40% brightness, +5% contrast288

Figure 10.27 Reconstructed off-axis hologram, $z=0$ mm, 970x400px reconstruction mask288

LIST OF TABLES

Table 2.1 Most relevant properties that influence spray atomization and geometrical aspects of sprays [17].....	18
Table 2.2 Classification of disintegration regimes [17].....	22
Table 4.1 Scattering regime as a function of OD.....	53
Table 4.2 Simulation parameters for imaging pulse and scattering media properties, OD 5 simulations.	61
Table 4.3 Simulation parameters for imaging pulse and scattering media properties, OD 10 simulations.	71
Table 6.1 Specifications of the fuel injector used in the experiment.....	136
Table 6.2 Particle size distribution metrics for the water mist produced by the ultrasonic atomizer measured by the Malvern Spraytec laser diffraction system.....	151
Table 7.1 Spray properties.	185
Table 8.1 Interference pattern visibility range and optical contrast setting measured at the object beam optical delay stage.	208
Table 9.1. Average spray properties.....	224
Table 9.2 Latency, standard deviation, and jitter for 10 acquisitions of the signal sequence actuating the fuel injector.	245
Table 10.1 Minimum recording distance (z) for an off-axis Fresnel hologram as a function of object size D	267
Table 10.2 ASM critical propagation distance (z) as a function of object size (M')	269

ACKNOWLEDGMENTS

Prof. Dunn-Rankin taught me a serendipitous approach to research and life, working with him I learnt to stop trying to control every little thing (even though I still try at times) and just trust that the repeated application of curiosity, integrity, and hard work with a little bit of luck will lead to the outcome you need (which sometimes is not the one you think you need). I hope he realizes what a fantastic mentor he has been, and how transformative his impact has been on my life.

I would not have been able to join UC Irvine if it wasn't for the opportunity granted me by my Master's thesis advisor at Politecnico di Milano, Professor Luigi de Luca, who had me join the Lasers Flames and Aerosols (LFA) Research Group to conduct my dissertation research work. My transition from Politecnico to UCI was pretty rocambolesque and required that many things happened at the right time with no possibility for second chances; I must thank Professor Michèle Lavagna for helping me make it happen.

I want to thank my dissertation readers and Ph.D. committee members, Professor Mark Walter for whom I had the pleasure to work as a teaching assistant, and is an outstanding example of professionalism and truly cares about his students; and Professor Vasanth Venugopalan, who granted me the opportunity to join the Short Course in Computational Biophotonics at the Beckman Laser Institute, an experience that helped me jumpstart my research in turbid media imaging.

Dr. Ali Ziaee started the holography research at LFA and showed me the ropes, he has been a friend and an excellent collaborator for the past years, and I look forward to continuing our work together.

I want to thank all our collaborators through the past years: Jim Trolinger and Andrei Dioumaev at Metrolaser, Professor Jason Porter and David Curran at Colorado School of Mines, Dr. Terry Parker at Florida Polytechnic University.

Professor Vince McDonnell was my valuable liaison to the spray research world and helped me by sharing the UCI Combustion Laboratory resources in multiple instances, and by letting me attend the Atomization and Sprays Short Course.

Professor Edouard Berrocal at Lund University granted me early access to his "Multi-Scattering©" photon transport code which provided priceless insight that is presented in this dissertation, he also allowed me to attend the "Laser Imaging of Spray Systems"

course at the Centre for Combustion Science and Technology at Lund University (CECOST) which was a precious learning and networking experience.

The LFA Research Group is a group of exceptional, talented researchers but most importantly great all-around humans. It is a wonderfully cooperative and supportive environment that made my Ph.D. experience even more enjoyable, I owe a great deal of gratitude to a lot of past and current members: Dr. Sunni Karnani, Dr. John Garman, Dr. Jesse Tinajero, Dr. Vinicius Sauer, Dr. David Escofet, Dr. Alice Yu Chien-Chien, Dr. Rosa Padilla, Andrea Biasioli, Michela Vicariotto, Joan Santacana, Claudia Camara López, Adriana Lladó Gambín, Navid Saeidi, Dorsa Shirazi, Brandon Esquivias Rodriguez and Dianalaura Cueto Duenas.

I was fortunate to mentor several talented undergrad researchers; a few of them made an impact on my research as well: Connor Watson, Baptiste Campenon, and Valentin Michaud.

Living 9733 km from home is not always easy, relationships suffer, and some connections are inevitably lost. I must thank my incredible friends, who made an effort to be there for me when I needed them: Marco Maggia, Enrico Cirací, Alessandro Bombelli, Julian and Spenser Scherle, Stephen Lukach, Peter and Emma John, Pietro and Laura Pierpaoli, Riccardo Morellini, and Evan Rouse. Out of all the Politecnico alumni that graduated the Space Engineering M.Sc., there are two that I still talk to at least every week for career advice, mutual support or fight over politics: Riccardo Carta and Ciro Farinelli, thank you for your friendship. Leaving my Corso Genova 21 family in Milan to attend UC Irvine was hard, I hope that Jacopo Luciola, Alberto Pavoncelli, Daniele Perotti and Matteo Guglielmi will be proud of this achievement, I will get a job after this guys, I promise.

Lastly, I thank my beloved, talented, intelligent, compassionate, colorful, fun girlfriend Ellen Spallino, she never ceases to inspire me, and she might not realize how her support was instrumental to my success, I love you.

Throughout the years, I had various sources of financial support, mainly through the privilege of teaching and mentoring students. I want to thank Professor Amhed Elwawil and Prof. Fadi Kurdahi for choosing me as a mentor for the Saudi Arabia International Program (SAIP), the California Alliance for Minority Participation (CAMP) program, and the California State Summer School for Math & Science (COSMOS) program. The work presented in this dissertation was also made possible by the following sources of funding. National Science Foundation (NSF); Grant Opportunities for Academic Liaison

with Industry (GOALI); CBET 1233728. NASA GRC SBIR project; Contract No. NNX16CACC90P; Dr. Yolanda Hicks, project officer. Army Research Office, Grant Number W911NF-17-1-0061; Dr. Ralph A. Anthenien, project manager. The views and conclusions contained in this document are those of the author and should not be interpreted as representing the official policies, either expressed or implied, of the Army Research Office or the U.S. Government. The U.S. Government is authorized to reproduce and distribute reprints for Government purposes notwithstanding any copyright notation herein.

CURRICULUM VITAE

Marco Minniti

EDUCATION

Ph.D., Mechanical and Aerospace Engineering 2014-2019
University of California, Irvine Irvine, California

M.Sc. Space Engineering 2009-2013
Polytechnic University of Milan Milan, Italy

B.Sc. Aerospace Engineering 2005-2009
Polytechnic University of Milan Milan, Italy

RESEARCH EXPERIENCE

Graduate Student Researcher 2014-2019
University of California, Irvine Irvine, California

Visiting Research Scholar 2012-2013
University of California, Irvine Irvine, California

Intern in Avionic Systems Design 2009
Logic SpA Cassina de' Pecchi, Italy

TEACHING EXPERIENCE

Teaching Assistant 2014-2019
University of California, Irvine Irvine, California

Instructor, MAE151 - "Mechanical Engineering Design" 2018
University of California, Irvine Irvine, California

MENTORING

Baptiste Campenon, Monte Carlo Simulation of Photon Transport through Turbid Media	2019
Connor Watson, Digital Image Processing Improvements to Off-Axis Hologram Reconstruction	2019
Valentin Michaud, E-Cigarettes particle size distribution and puff topography study using a novel laser scattering method.	2018
Jason Owusu, Design an automotive fuel injector testing bench using Arduino	2016
Marisela Miramontes, Design and manufacturing of a microfilm combustor turbine blade using rapid prototyping techniques.	2015
Muath Askar and Ahmed Alahrbi, Development of a solar cookstove for rural communities in India	2015
Saad Almuhanha, Minimize Particle Image Velocimetry (PIV) uncertainties when measuring a simple fluid flow	2015
Saud Alanazi, Efficient ocean water desalination using methane hydrates (Best in Symposium winner)	2014

PUBLICATIONS

Refereed Publications

Minniti, M., Ziaee, A., Curran, D., Porter, J., Parker, T., and Dunn-Rankin, D., Femtosecond Digital Holography in the Near-Nozzle Region of a Dodecane Spray, *Atomization and Sprays*, 2019. DOI: 10.1615/AtomizSpr.2019029444

Minniti, M., Ziaee, A., Trolinger, J., and Dunn-Rankin, D., ULTRASHORT PULSE OFF-AXIS DIGITAL HOLOGRAPHY FOR IMAGING THE CORE STRUCTURE OF

TRANSIENT SPRAYS, *Atomization and Sprays*, vol. 28, no. 6, pp. 565–578, 2018. DOI: 10.1615/AtomizSpr.2018024340

Ziaee, A., Dankwart, C., Minniti, M., Trolinger, J., and Dunn-Rankin, D., Ultra-short pulsed off-axis digital holography for imaging dynamic targets in highly scattering conditions, *Applied Optics*, vol. 56, no. 13, pp. 3736, 2017. DOI: 10.1364/AO.56.003736

Conference Papers with Presentation

Minniti, M., Ziaee, A., Curran, D., Porter, J., Parker, T., and Dunn-Rankin, D., Femtosecond Holography of a Dodecane Jet Spray at High-Pressure Conditions, *ILASS-Americas 30th Annual Conference on Liquid Atomization and Spray Systems*, (May), 2019. Tempe, AZ.

Minniti, M., Ziaee, A., Curran, D., Porter, J., Parker, T., and Dunn-Rankin, D., Ultra-short Pulse Off-axis Digital Holography Imaging under Realistic Diesel Spray Conditions, *ICLASS 2018, 14th International Conference on Liquid Atomization & Spray Systems*, 2018. Chicago.

Minniti, M., Ziaee, A., Trolinger, J. D., and Dunn-Rankin, D., Ultra-short Pulse Off-axis Digital Holography for Imaging the Core Structure of Transient Sprays, *ILASS Americas, 29th Annual Conference on Liquid Atomization and Spray Systems*, (May), 2017. Atlanta, GA.

Conference Papers

Ziaee, A., Minniti, M., and Dunn-Rankin, D., Ultra-short Pulsed Off-axis Digital Holography in the Formation Region of Atomizing Sprays, *PROCEEDINGS OF THE 19th INTERNATIONAL SYMPOSIUM ON APPLICATION OF LASER AND IMAGING TECHNIQUES TO FLUID MECHANICS*, 2018. Lisbon, Portugal.

Trolinger, J. D., Dioumaev, A. K., Ziaee, A., Minniti, M., and Dunn-Rankin, D., Spatially and temporally resolved diagnostics of dense sprays using gated, femtosecond, digital holography, In E. Novak & J. D. Trolinger (Eds.), *Applied Optical Metrology II* (Vol. 10373, p. 25), 2017. DOI: 10.1117/12.2274841

Padilla, R. E., Minniti, M., Jaimes, D., Garman, J., Dunn-Rankin, D., and Pham, T. K., Thin filament pyrometry for temperature measurements in fuel hydrate flames and non-premixed water-laden methane-air flames, *8th US National Combustion Meeting 2013, 1*, 2013.

Conference Posters

Holve, D., Hoornstra, J., Michaud, V., Minniti, M., and Dunn-Rankin, D., COMPARATIVE MEASUREMENTS OF PUFF AEROSOL SIZE AND CONCENTRATION OF COMBUSTION, HEATED TOBACCO, AND LIQUID E-CIGARETTES BY LIGHT SCATTERING METHOD, *TSRC, Tob. Sci. Res. Conf., 2018, 72, Abstr. 044*, 2018. DOI: 10.13140/RG.2.2.21960.98560

SHORT COURSES

Atomization and Sprays Short Course 2019
UCI Combustion Laboratory Irvine, California

Laser Imaging of Spray Systems 2017
CECOST at Lund University Lund, Sweden

Annual Short Course in Computational Biophotonics 2016
Beckman Laser Institute Irvine, California

Excellence in engineering communication 2016
University of California at Irvine Irvine, CA

OTHER PROFESSIONAL ACTIVITIES

Session Chair, “Experimental Methods & Instrumentation”, at ILASS-Americas 30th Annual Conference on Liquid Atomization and Spray Systems, (May), 2019. Tempe, AZ.

Session Chair, “Diagnostics III”, at *ICLASS 2018, 14th International Conference on Liquid Atomization & Spray Systems*, 2018. Chicago.

ABSTRACT OF THE DISSERTATION

Femtosecond Holography of Sprays

By

Marco Minniti

Doctor of Philosophy in Mechanical and Aerospace Engineering

University of California, Irvine, 2019

Professor Derek Dunn-Rankin, Chair

The study of liquid jet breakup near the nozzle exit under the complex conditions, where the liquid/gas density ratio is relatively low, where rapid shearing and droplet formation is intense, and where the optical scattering obscures the condensed phase structure, has been an important sub-field of spray and spray combustion research for decades. With combustion chamber pressures on the rise, and engine performance improvement demands unrelenting (reduced emissions, fuel tolerance, increased power density, and efficiency), gaining diagnostic access to this critical jet breakup domain is more important than ever. This research project contributes to the understanding of the near nozzle region of realistic fuel sprays by developing and quantitatively demonstrating ultra-short pulse off-axis holography (USPODH) as a coherence filtering tool for 3D evaluation, obscuration

avoidance, and transient imaging. USPODH is an interference-based single-shot technique that uses coherence filtering to allow single-shot imaging through media with optical density (OD) up to 12, conditions where other techniques resort to hardware time-gating solutions, multiple shot averaging or a synchrotron light source. The results show how USPODH can be successfully used in such environments. In particular, Monte Carlo photon transport simulations and experimental results show how coherence filtering can outperform picosecond time-gating for imaging in optically dense environments. Droplets as small as 25 μm , generated by a water spray hidden by a field of polydisperse droplets with OD up to 12 were successfully resolved. Performance in engine-relevant environments was demonstrated by imaging a USAF resolution chart at pressures up to 20 bar and temperatures up to 450 K. The effects on pulse broadening and image quality from pressure and temperature gradients and the presence of thick fused quartz windows were quantified. A gas-liquid interface in the near-nozzle region of a single-orifice dodecane spray injected at 1550 bar was imaged in a vessel at pressures up to 20 bar. Surface perturbations and ligaments detaching from the spray liquid core were observed with an object-side resolution of approximately 14 μm at a working distance of 35cm, and off-line numerical focusing allowed to focus on features of interest in depth planes tens of centimeters apart from each other. USPODH reconstructions were also compared to

lensed shadowgraph images and inline holograms reconstructions acquired in the same conditions, and the results show that USPODH is effectively rejecting the scattering light noise signature from the shroud of droplets surrounding the spray core in the nozzle proximity.

Chapter 1

1 Introduction

The work presented in this dissertation focuses on two main aspects: developing and improving a novel technique for optical imaging in highly scattering media, and using this technique to enhance the understanding of fluid dynamic phenomena for which limited and sometimes hard to interpret experimental data has been collected so far. The technique is called Ultra-Short Pulse Off-Axis Digital Holography (USPODH), as it is a variety of off-axis holography that relies on the use of short coherence length femtosecond laser pulses to select only ballistic and quasi-ballistic photons when imaging a target hidden in a turbid environment. This is achieved, similarly to what other techniques have achieved in the past, by rejecting multiply scattered photons that have encountered multiple light/matter interactions, and therefore have travelled a longer path on their way from the laser source to the camera sensor than photons that do not interact with the medium (i.e., ballistic photons). Differently from other techniques that adopt ultra-fast shutters to gate-out the delayed photons, USPODH relies on “coherence filtering” where a

reference pulse is routed around the target and is interfered with the object pulse that traveled through the scattering media. Only the ballistic photons of the object pulse will still be coherent with the reference and create an interference pattern on the camera sensor. This interference pattern is a hologram, and it can be numerically reconstructed into an image of the target field at a chosen distance from the pattern plane. This image will contain information pertaining primarily to ballistic and quasi-ballistic photons. Since these photons did not scatter off any particle while traversing the target field, they create a shadowgraph-like image of the target. Hence, a substantial part of this dissertation is dedicated to analyzing, predicting, quantifying and improving optical and numerical aspects of the technique, including resolution, scattering noise rejection performance in turbid media, and numerical methods used for image reconstruction.

The fluid science aspect of this dissertation focuses on imaging primary atomization fluid dynamic structures in the near-nozzle region of a high-pressure fuel injector and looking for evidence (or the lack thereof) for the presence of supercritical fluid at realistic injection conditions. The continuous design refinement driven by stricter environmental regulations and seeking higher efficiency and power output pushed the fuel injection conditions for modern direct injection engines to higher than ever chamber and injection pressures

(Figure 1.1), requiring a new narrative for describing the fluid dynamic phenomena that take place at these conditions. The mechanisms describing the early stages of diesel fuel injection into a high temperature and high-pressure environment have been the focus of extensive research [1]–[6], and the traditional understanding is that an intact stream of liquid fuel exists in the near-nozzle region; from this liquid core surface ligaments, bags and sheets form that eventually shed droplets via primary breakup. These primary atomization droplets create a shroud with highly optical scattering properties (i.e., high optical depth - OD) that surrounds the spray core. The size distribution of these droplets, bags, and ligaments have been predicted by models [4] and numerical simulations [2], [7] but partially because of the primary atomization shroud there is a lack of quantitative experimental data that are necessary for tuning, verification, and validation of those models [2], [5]. High-speed shadowgraph images have been shown to fail at accurately describing this gas-liquid interface because of the multiple scattering noise from the layer of smaller droplets surrounding the jet core [1], [2] obscuring the interface. The shortcomings of shadowgraphy led to the development of ballistic imaging which had better success in imaging ligaments and voids on the jet surface [1], [8]. Information can be inferred by observing the gas-fuel interface; for instance, ligaments may cease to exist when vessel conditions exceed the fuel’s critical point and would be replaced by a

turbulent diffusive mixing layer [1], [9], [10]. The very existence of a supercritical turbulent mixing interface at realistic injection conditions is still an object of debate by the community, as it has been observed for binary mixtures of pure fuel and nitrogen [10], but on the other hand it is not clear if it would exist in the case of a multi-component mixture of commercial diesel fuel and air. This dissertation will show how USPODH can potentially produce the kind of insight needed to resolve the debate by offering ballistic-imaging-like scattering noise rejection with the added convenience of enhanced depth of field (DOF) imaging, numerical off-line refocusing, and the potential for quantitative imaging offered by using the light phase information embedded in each hologram to measure refractive indexes in a transmissive configuration or to create topological maps of surfaces in a reflective configuration.

This combination of ultra-short pulse, transmission-based, off-axis holography has never been used for spray imaging before. Hence, to demonstrate its capability requires multiple demonstrations with increasing degrees of realism. The process starts with exploring the concept of femtosecond coherence filtering using resolution charts hidden behind scattering suspensions [11], [12], then moves to a water spray hidden within a dense water mist with a tailored OD and particle size [13] (chapter 6), then addressing the potentially

challenging effects of pressure and temperature gradients in a smaller pressure vessel (chapter 8), and finally examining a high pressure dodecane spray in a state of the art pressure vessel at ambient conditions (chapter 7) and then high pressure (chapter 9).

The fundamental goals that were achieved and described in this dissertation are:

- Identified the need in the spray science community for an imaging tool that can image fluid structures hidden in highly scattering clouds of droplets or identify supercritical mixing layers (chapters 2 and 3).
- Showed by means of simulations and experimental proof that coherence gating can be as effective as time gating at rejecting multiple scattering noise when imaging in optical conditions typical of a realistic fuel spray (chapter 4).
- Provided the necessary theoretical framework to allow tuning the experimental apparatus and numerical reconstruction methods for optimal scattering rejection and overall imaging performance in turbid media (chapter 5).
- Demonstrated scattering noise rejection performance when imaging through targets hidden by a polydisperse water mist with measured OD up to 12 (chapter 6).
- Proved the applicability of the technique in realistic engine-like environments to image supercritical mixing layers, which required demonstrating imaging

performance through thick windows, and when facing temperature and pressure gradients (chapter 8).

- Demonstrated imaging performance on a realistic fuel sprays, at both ambient and realistic chamber conditions (chapters 7 and 9).
- Investigated optical and numerical enhancements to address the technique's limitations and expand it beyond its current capabilities (chapter 10).

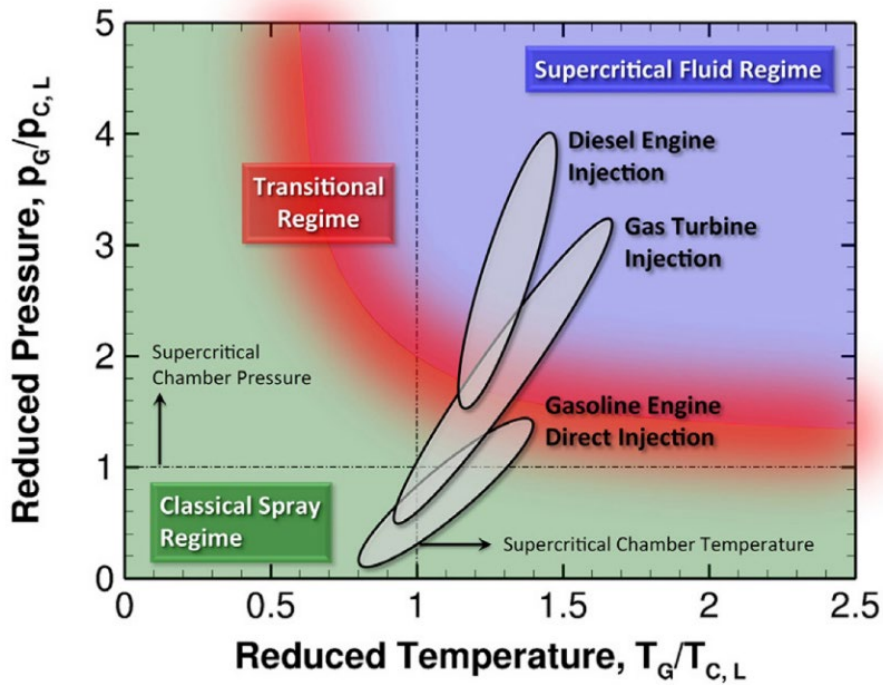


Figure 1.1 Envelopes associated with modern diesel, gas turbine, and gasoline direct-injection systems. The fuel surrogates used are respectively n-dodecane, n-decane, and iso-octane. The diagram assumes liquid fuel injection temperatures between 300 and 363 K [14].

Chapter 2

2 Fluid dynamics of spray atomization

Chapter 2 provides the necessary background on sprays, shows why diesel sprays are a challenging application for optical diagnostics techniques, and defines the non-dimensional numbers that help identify spray breakup regimes. Some essential references for these topics include the books by Lefebvre [15] and Sirignano [16].

The fluid dynamics of liquid atomization often have their genesis inside the spray nozzle [15]. High interior swirl, the level of turbulence, and tendency to cavitate are properties that can dominate the flow field that exits the nozzle. Just at the exit, intact liquid structures or a so-called “liquid core” extrude into the gas phase. But for highly atomizing sprays, evidence indicates that they break up very quickly (or immediately in some cases) via turbulence, cavitation, rapid development of surface wave structures, other forms of shear, or a combination of these mechanisms. The liquid core produces “primary droplets” as it disintegrates via “primary breakup” mechanics, and this defines the “spray formation

region” (also called the “dense spray” or “near field” region) (Figure 2.1). Once formed, primary droplets can undergo “secondary breakup” via shear mechanisms. Droplets can also collide and coalesce. In the “spray region,” the breaking, vaporizing, and slowing droplets grow smaller and more dispersed. Details of these processes are collected in the significant texts on sprays, namely the book by Lefebvre [15] for an extensive overview of spray mechanics, injector designs, and spray diagnostic techniques; and the book by Sirignano [16], for a rigorous analytical treatment of the fluid mechanic mechanisms driving droplet formation, breakup, evaporation, near-critical, trans-critical, and supercritical behavior.

The spray formation region contains a highly dynamic multiphase flow that most often exits the nozzle as a contiguous liquid structure and then disintegrates into primary drops as it flows away from the nozzle. Complex dynamics of breakup continues to occur as the fluid flows downstream, *but these dynamics can be obscured to ordinary observation by the optically dense drop cloud surrounding them.* The region farther downstream, where primary breakup is completed and the flow consists of drops in air, is clearly a spray according to standard definitions. This region can also be fairly dense near the spray

formation region, but as the spray breaks up further and vaporizes the optical density becomes relatively low allowing straightforward optical imaging.

The structure of a spray is influenced by a large number of parameters including the properties of the injected liquid (the dispersed phase), the properties of the surrounding gas (the continuous phase), and the physical characteristics of the injector itself. Depending on the operating conditions and on the design of the injector a wide variety of sprays can be produced but in general terms, a spray is composed of a series of adjacent fluid mechanical zones (Figure 2.1):

- The liquid core corresponding to the extension of the liquid body injected.
- The multi-phase mixing layers characterized by irregular elements and large drops and created by the atomization process.
- The dispersed flow in which small round drops are well-formed.
- The vaporization zone where the small droplets are evaporated.

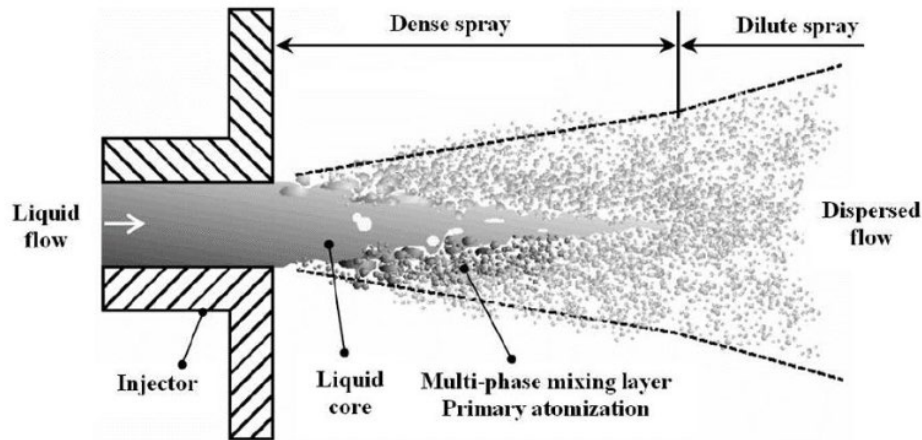


Figure 2.1 Spray regions [17].

Figure 2.2 depicts a transparent diesel fuel injector tip that was used to observe cavitation inside one hole of the tip, using microscopic shadowgraphy [18]. The first two zones described above can be observed. The spray does not spread immediately, which means that larger liquid structures visible inside the hole must still exist outside of the hole as intact liquid structures within the droplet cloud. These structures cannot be imaged by a camera because of the dense droplet cloud surrounding them. At optical wavelengths, the OD of the droplet cloud in the near field of a Diesel spray is on the order of OD 8-10. As a comparison, 1 mm of human tissue has an OD on the order of 11. OD 1-2 does not require special techniques for imaging. One can achieve excellent results using shadowgraphy with a white light source and camera with a sufficiently fast shutter to freeze motion. Low OD values usually occur well downstream in the spray region or at the periphery of the spray cone. OD 2-5 requires effort to image what happens inside the drop

cloud. The spray formation region for many flows has OD values in this range. Optical depths on the order of OD larger than 5 can be very challenging and they require advanced imaging methods. For OD larger than 10 the consensus is that it is not possible to image the interior flow without corruption due to scattering [18].

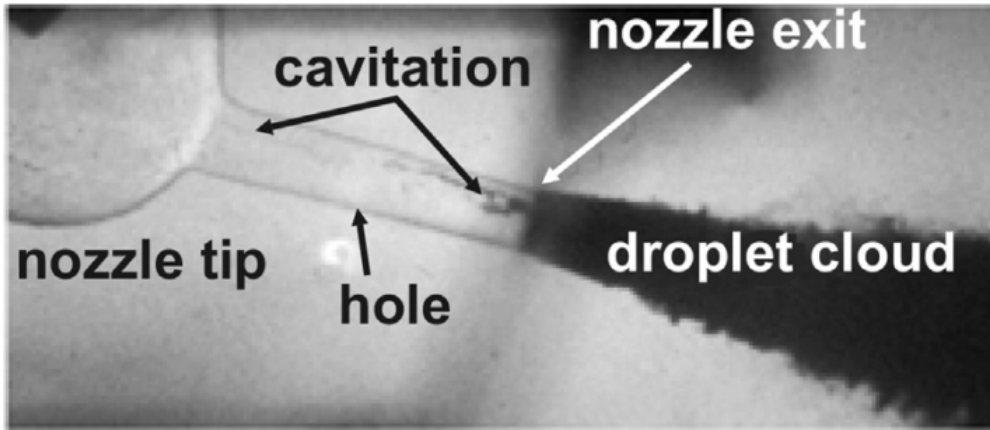


Figure 2.2 Microscope shadowgram showing flow inside a transparent nozzle tip [18].

The work presented in this dissertation will focus on developing a technique to image this primary atomization, optically dense region where a liquid core is hidden by the surrounding droplets. As mentioned earlier, and as will be repeated throughout this dissertation as its key focus, imaging the core jet is complicated due to the surrounding cloud of droplets which scatters almost every single photon penetrating it. Among the several techniques developed for the task “Ballistic Imaging” has historically been recognized as the most effective ([3], [8], [19]–[21]). An example of a ballistic image of a

diesel spray is shown in Figure 2.3-Figure 2.5. The technique is presented in detail in section 3.2.

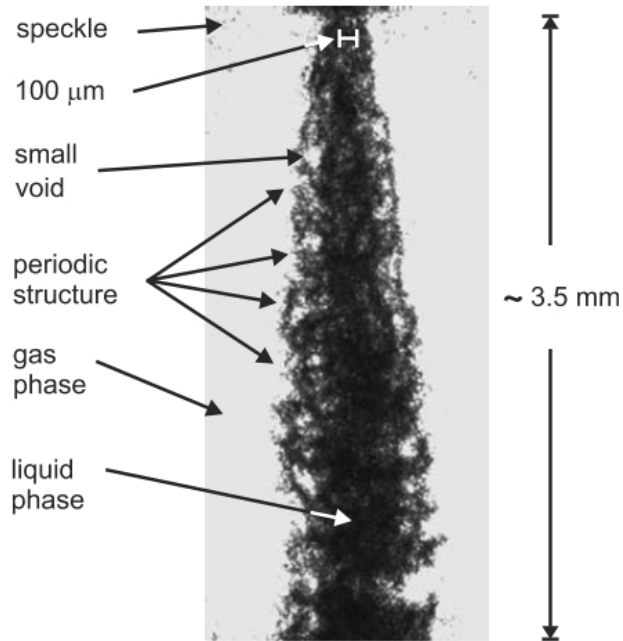


Figure 2.3 Ballistic image at steady state of a diesel spray [3]

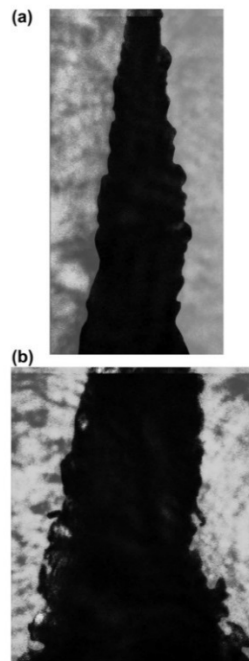


Figure 2.4 Ballistic image of a dodecane jet in the steady-state region. Chamber pressure of 30 bar and temperature of 445 K [10].

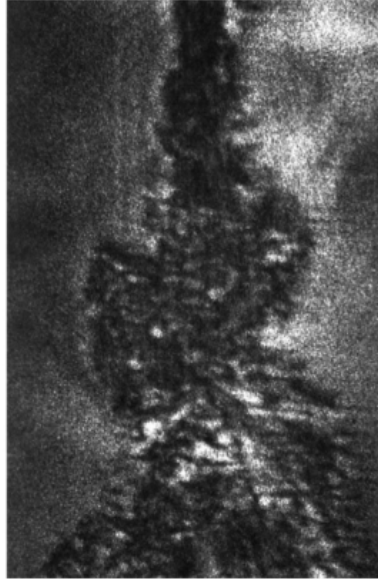


Figure 2.5 Ballistic image of a diesel jet taken 1.64 ms after injection start, between 1 and 4 mm from the nozzle exit (60 bar, 900 K) [10]

2.1 Properties defining spray formation

The fundamental parameters influencing liquid spray flow are the injection pressure, liquid velocity, and turbulence in the liquid stream. High-pressure injection and high liquid velocity increase the formation of instabilities and disturbances at the nozzle exit and increase the atomization efficiency. In order to classify different spray regimes, three dimensionless numbers: Reynolds, Weber, and Ohnesorge, are typically defined. These dimensionless numbers are well known and are described in the general spray references

already cited, but their definitions are repeated here to ensure that the physical values used are related to spray nozzles.

The Reynolds number relates the ratio of inertial to viscous forces:

$$Re = \frac{\rho_l LV}{\mu_l}$$

where ρ_l and μ_l are the density and viscosity of the liquid fuel, L is the characteristic length, and for fuel injection applications it is usually the injector orifice diameter, and V is the velocity of the liquid fuel. If Re is higher than a critical value, a flow originally turbulent will remain turbulent. If Re is smaller than the critical value, the flow will turn laminar in a straight tube. In the absence of a disturbance, a flow originally laminar would remain laminar even for high Reynolds number. However, its susceptibility to turning turbulent increases with Re .

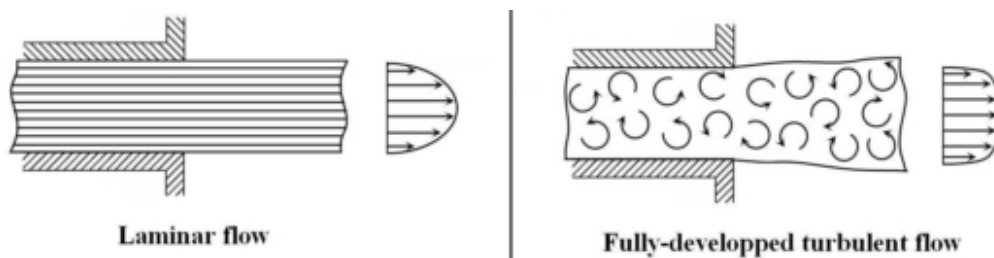


Figure 2.6 Flow regime at nozzle exit for an orifice plain nozzle [17]

The Weber number relates the ratio of momentum forces trying to break apart the liquid core to surface tension forces holding the liquid core together:

$$We_l = \frac{\rho_l LV^2}{\sigma}$$

where ρ_l is liquid fuel density, σ is the surface tension of the liquid fuel, V is the relative velocity between the liquid and gas phase, L is the characteristic length and is usually the injector orifice diameter in fuel injection applications. The Weber number is a parameter used to classify the disintegration regimes. The critical Weber number is identified as the value above which breakup occurs and below which droplets remain stable.

The Ohnesorge number is given by the ratio of the fourth root of the Weber number and the Reynolds number and it is an indicator of jet stability:

$$Oh = \frac{\sqrt[4]{We_l}}{Re} = \frac{\mu_l}{(\rho_l \sigma L)}$$

where ρ_l and μ_l are the density and viscosity of the liquid fuel, σ is the surface tension of the liquid fuel, V is the velocity of the liquid fuel, L is the characteristic length and is usually the injector orifice diameter. The Ohnesorge number can be seen as the ratio of viscous friction and surface tension. For a high Oh number (which is the case when liquid viscosity is high) an increase in inertial forces is required for breakup to occur.

The physical modeling of spray breakup is based on the use of Re , We and Oh , and for a given spray the liquid breakup length, the cone angle, the average droplet size, and

number density can be correlated to the values of Oh and We. Another relevant parameter is the ratio between the liquid density and the gas density ρ_l/ρ_g . Assuming that the gas surrounding the jet is air, for a given distance from the nozzle, higher air density creates smaller droplets and a more efficient liquid jet disintegration. The jet is forced to slow down faster by the higher air density which reduces the spray penetration distance L_p and the liquid core length L_c for higher gas pressures (see Figure 2.8).

Shape, size and flow regime of the liquid in the near nozzle region is mainly controlled by nozzle geometry. For the purpose of this research, we will focus on single orifice pressure atomizers. Pressure atomizers discharge the liquid through a small orifice under high pressure. The experiment will focus on these atomizers because they are of great interest to the spray research community that focuses on automotive and aerospace applications. Furthermore, there is a long-standing lack of experimental data describing the near nozzle region of single orifice jets in realistic conditions and the development of diagnostics that can deliver this data is highly sought after.

The most relevant properties impacting atomization and the most common spray geometric aspects that will be mentioned in this dissertation are described in Table 2.1.

Table 2.1 Most relevant properties that influence spray atomization and geometrical aspects of sprays [17]

Relevant properties for atomization		Geometrical aspects and characteristics of sprays	Illustration
Injected liquid:	<ul style="list-style-type: none"> - Surface tension - Viscosity - Density 	<ul style="list-style-type: none"> - Nozzle flow rate: U_I - Liquid jet or sheet thickness: d_0 - Radial and axial distances: r and x - Length of the liquid core: L_c - Distance of penetration: L_p - Mean drop size: \bar{D} - Drop size distribution: $P(d)$ - Drop number density: N - Radial patterning - Circumferential patterning - Spray angle: θ - Evaporation rate - Wavelength of disturbance: λ 	
Liquid flow:	<ul style="list-style-type: none"> - Injection pressure - Velocity - Turbulence in the liquid stream 		
Ambient gas:	<ul style="list-style-type: none"> - Gas density - Temperature 		
Gas flow:	<ul style="list-style-type: none"> - Absolute velocity - Relative gas-to-liquid velocity - Turbulence in the gas stream 		
Injector:	<ul style="list-style-type: none"> - Dimension of the orifice diameter - Internal structure and geometry of the nozzle 		

The dimensionless parameters described in this chapter are used to identify the breakup regime of interest to the research and verifies that the experimental setup offers a good representation of injection conditions in modern high-pressure diesel engines and other state of the art experiments.

2.2 Spray breakup regime

As seen in classical texts on sprays, the breakup of a jet may be classified into four regimes: (1) the Rayleigh breakup regime, in a very low jet speed, (2) the first and (3)

second wind-induced breakup regime where aerodynamic drag effects begin to dominate, and (4) the fully developed atomization regime at high speed where flow field instability makes a strong contribution to the breakup. Figure 2.7 shows different breakup regimes as a function of Ohnesorge versus Reynolds numbers. The graph is populated with the conditions related to relevant primary atomization models by Desjardins and Jarrabashi [22], [23] , compared to the experimental conditions corresponding to ECN’s “non evaporative spray A” [2] and the conditions recreated in the experiment presented in this dissertation.

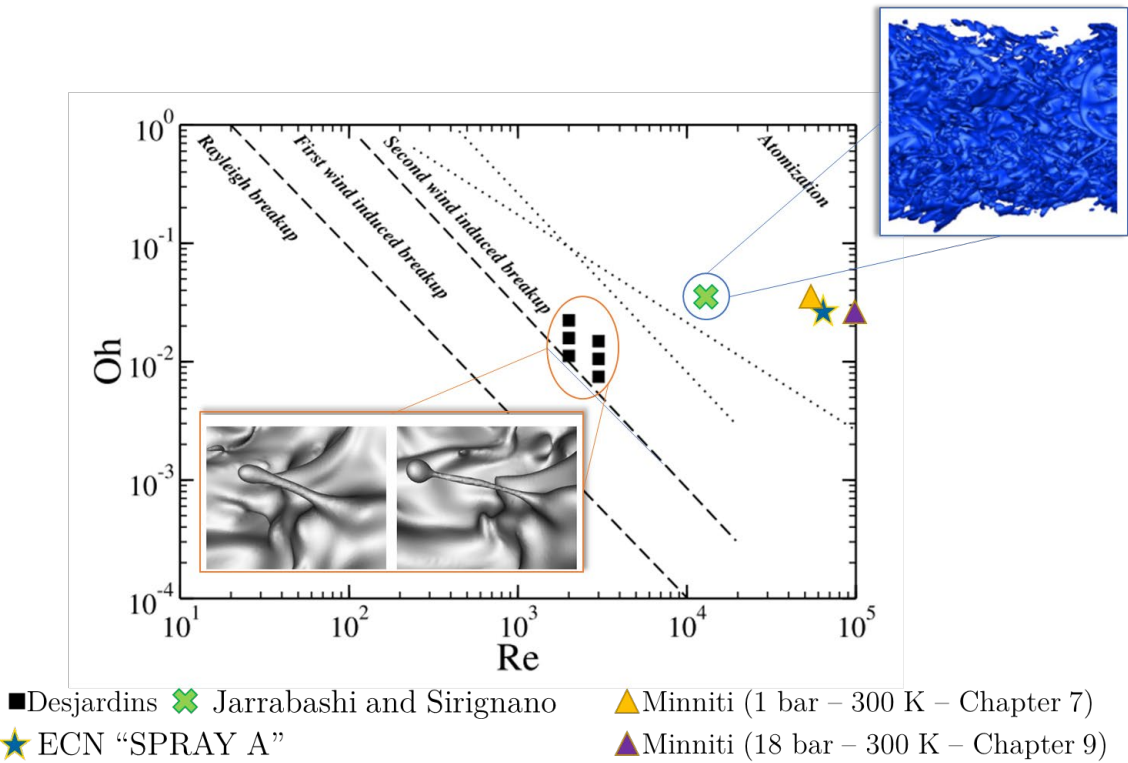


Figure 2.7 Classification of breakup regimes as a function of Ohnesorge number versus Reynolds number on a log scale, the graph is populated with


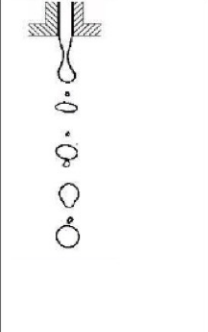
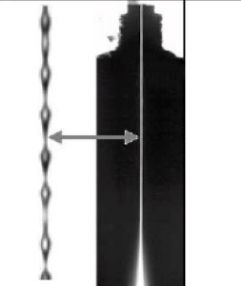
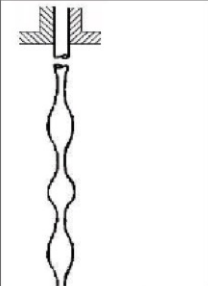
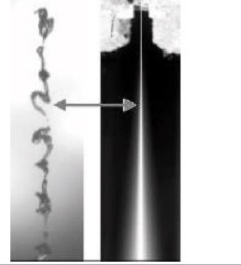
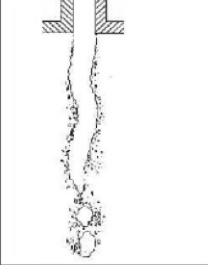
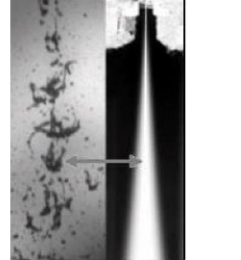
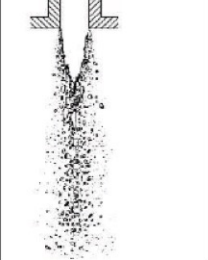
conditions found in relevant primary atomization models, as well as the experimental conditions applied in this dissertation.

The Rayleigh regime occurs at very low jet speed when the aerodynamic forces are negligible. At the exit of the liquid jet, axisymmetric surface waves are formed by the interaction of primary disturbances in the liquid and surface tension forces. The growth of disturbances eventually leads to the breakup of the jet. When the aerodynamic forces increase the axisymmetric surface waves formed under the Rayleigh regime, the disintegration regime becomes the first wind-induced breakup. In this case, the diameter of the drops is about the same as the jet diameter and the breakup process occurs several jet diameters downstream from the nozzle. If, however, the aerodynamic forces are responsible for sinuous (or axisymmetric) waves by increasing the relative air velocity, the disintegration regime is called second-wind breakup regime. In the second-wind induced breakup regime, the aerodynamic forces are responsible for the formation and growing of short wavelength disturbances (or harmonics) producing smaller droplets. As a result, the average droplet size is much smaller than the orifice diameter and a wide drop size distribution is generated. In this regime, breakup also occurs at several jet diameters downstream of the nozzle. The fourth disintegration regime is known as atomization; the liquid core is broken up directly at the nozzle exit. This process occurs at high relative liquid-gas velocities and produces a multitude of droplets much smaller than the original

jet diameter. Note that most fuel and industrial sprays operate in the atomization regime.

Each disintegration regime is described by their own characteristics in Table 2.2.

Table 2.2 Classification of disintegration regimes [17]

Breakup regime	Picture	Schematic	Dominant droplet generation mechanism	Weber number
Rayleigh			Surface tension force	$We > 0.4$
First wind			Surface tension Dynamic pressure of ambient air	
Second wind			Surface tension Dynamic pressure of ambient air opposed by surface tension initially	$We > 40.3$
Atomization			Aerodynamic and shear forces Turbulence Expansion Surface tension force initially	$We \rightarrow \infty$

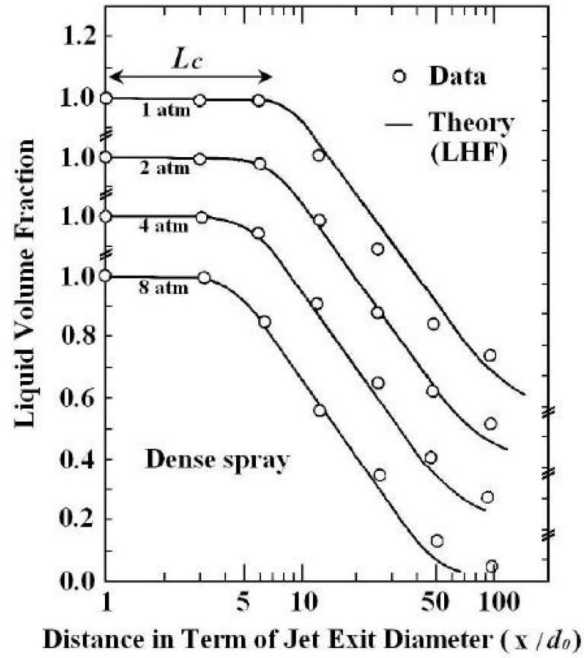


Figure 2.8 Liquid volume fraction versus distance from the nozzle exit for a water spray for different pressure values [17]

In a spray, the Liquid Volume Fraction (LVF) varies strongly with position. It is maximum in the near injector region, corresponding to the liquid core zone. It reduces rapidly with axial distance and the radial distance. At high LVF, droplet-droplet interactions such as collisions and coalescence occur, generating large droplets which are subsequently secondary atomized. Liquid core length, L_c , decreases when the ambient pressure is increased, implying faster mixing rates. So, the length of the liquid core is an indicator of the quality of the atomization, which is one of the reasons why the technique at the center of this dissertation focuses on imaging it. In general, small L_c is related to good atomization, and in some sprays, the amount of droplets surrounding the core is

such that the existence (or lack of) of a liquid core has not yet been proven [18]. The USPODH spray reconstructions presented in this dissertation will all be of sprays in the atomization regime (see Figure 2.7), in the dense spray region. We will mainly focus on the near-nozzle region with $x/d_o < 5$ where we will attempt to resolve the fluid dynamics structures responsible for generating primary atomization droplets, as well as quantify relevant spray metrics such as spray penetration depth, spray cone angle, surface wave curvature and more.

Chapter 3

3 Review of imaging techniques for optically dense sprays

This section will review a selection of techniques of interest for imaging dense sprays together with the relevant literature. The purpose is to show the need, opportunity, and rationale that led our research to focus on the development of off-axis femtosecond digital holography and its application to the high OD region of sprays.

As described above, to better understand the fluid flow mechanisms driving liquid fuel injection into the combustion chamber and the consequent droplet breakup, a variety of imaging and measurement techniques have been developed. Just to repeat, high-pressure injection creates a liquid column in the near field of the nozzle exit, shear between the liquid surface and the surrounding gas creates ligament structures that eventually break down into droplets. This atomization process happening in the near-nozzle region is primary atomization, as opposed to secondary atomization, which refers to the

disintegration-cascade process that generates smaller droplets from larger ones. Due to the turbid nature of this primary atomization region, significant efforts have been made to image the spray structure while rejecting scattered light.

Measurements in liquid fuel sprays are ideally non-intrusive and typically rely on laser interactions with the droplet field; therefore, measurements close to the injector tip must be able to monitor spray ligament and/or droplet sizes in spite of high number densities and high levels of attenuation [24]. Techniques such as Phase/Doppler measurements [25], [26] or imaging measurements that rely on separate images of droplets [27] are ineffective near the injector orifice due to multiple scattering in the overall system. Signal attenuation for ensemble light scattering techniques utilizing visible wavelengths makes these techniques of marginal use in dense spray [28], [29]. Diffraction based instruments [30] with obscuration levels greater than 50% require empirical or theoretical corrections [31], while polarization ratio measurements [29] can be insensitive to optical depth but have a limited dynamic range. X-ray imaging of fuel sprays has been applied to the near-orifice region of non-evaporating fuel sprays to measure fuel mass fraction [32], fuel velocity fields [33], the influence of gas density on penetration length, and the internal structure of the nozzle [34]. The x-ray approach is successful; however, challenges with this technique depending on the specific implementation include the need for tracer

seeding for adequate absorption of x-ray radiation, an insensitivity to droplets that limits visualization of some features during spray breakup, a limited potential for wider engine studies given the need for a synchrotron x-ray source.

Optical techniques are to this day the most versatile and widely used in fuel spray imaging, the recurring strategy in dense media optical imaging techniques is to detect a light signature that has not been corrupted by the multiple scattering interactions with liquid particles. Structured Laser Illumination Planar Imaging (SLIPI) illuminates the spray with a spatially structured laser sheet and relies on only detecting the light which has retained this spatial signature [35], [36]. Ballistic imaging relies on using short imaging laser pulses and retaining only transmitted (ballistic) light while adopting different time gating strategies to filter out multiple scattering photons. Ballistic imaging is especially helpful in the near-nozzle region where the size of the spray is comparable to the size of a laser sheet and SLIPI is ineffective. Kerr-effect time gating provides an opportunity to investigate the optically dense region of the spray by producing shadowgraph or schlieren-style images of structures that are embedded inside a turbid field [18]. Identifying embedded structures is especially relevant given conflicting predictions of both a negligible liquid core [31] and a core of up to 100 jet diameters in length [37]. Early published uses

of ballistic imaging were in the medical field for imaging tumors in breast tissue and this medical application typically used picosecond laser pulses [21], [38]–[43]. Paciaroni et al. applied ballistic imaging to fuel sprays nearly a decade ago [3], [44], [45]. Since that time several groups have used ballistic imaging in spray environments, including water sprays [46]–[51], oil sprays [52], and our work on high-injection-pressure diesel sprays injected into an elevated temperature and pressure environment [8]. The utility of the ballistic imaging technique for imaging dense sprays has been demonstrated previously [44], [45], but there remains the unfortunate circumstance that typical CS₂-based Kerr gates have gating times (2+ ps) that do not easily separate the important ballistic and snake photons from the multiply scattered light. Some gains are seen, however, in part due to a natural spatial filtering effect, so that diesel sprays injected into an ambient atmosphere indicate with their ps-ballistic images very significant mixing structures on the spray periphery (e.g., Figure 2) [3], [8]. More recent literature [51] suggests that in order to effectively time gate scattering photons in a realistic fuel spray environment a temporal detection with a 300 fs resolution is needed to discriminate scattered photons from ballistic ones. Therefore the use of faster second-harmonic generation (SHG) non-linear crystals must be used in place of Kerr Effect gates. This is confirmed by the Monte Carlo simulation results shown in Chapter 4, and it is one of the motivations for using coherence filtering in

lieu of time-gating, which delivers a 100-fs gate while doing away with the complexity of a Kerr or SHG time-gate.

For further information on non-holographic methods, the reader is referred to the excellent and comprehensive review of diagnostic techniques for the optically dense region of sprays by Linne [18]. For the comparative evaluation critical for this dissertation, we will mostly introduce the fundamentals of ballistic imaging, which is overwhelmingly regarded in the spray diagnostic technique as the benchmark optical diagnostic technique for dense sprays. The understanding of ballistic imaging will be valuable for the reader to appreciate the scattering rejection method and results obtained with USPODH.

3.1 X-ray techniques

X-ray techniques have been applied to sprays to image both internal nozzle flow and the dense, near-nozzle region. Most of this work used the Advanced Photon Source (APS) at Argonne National Laboratory (ANL). Their work focused on X-ray radiography and X-ray phase contrast imaging (PCI). PCI has been used at ANL to visualize the near-nozzle morphology of sprays and promote the understanding of primary breakup [53], [54]. The synchrotron source is operated in bunch mode and tuned to a photon energy that avoids

absorption, and the generated pulses illuminate the spray. The phase change experienced by the X-ray wavefront as it traverses the spray creates refraction patterns that can be sampled and imaged in several ways: interferometry, diffractometry, and in-line holography. The approach at ANL has been named “propagation-based imaging” where the beam is propagated for some distance after traversing the spray, the phase contrast image is converted into the visible spectrum by a scintillator which is imaged by a camera. This approach is simple (except for the complexity of the source) but suffers from a higher background signal. Phase contrast images are somewhat challenging to interpret because they contain signatures created by strong index gradients, which means that they represent just the edges of objects. The X-ray beam can traverse hundreds of droplets along its path, and since it does not scatter upon encountering them, as an optical pulse would, it retains the signature of all the edges that it encountered along its path (Figure 3.1). Therefore, when traversing even a relatively low number of drops, the x-ray beam acquires an intricate pattern that is difficult to interpret unambiguously. Linne by simulating PCI of larger drops hidden behind a range of concentration of smaller ones showed that 4 to 8 drop interactions are sufficient to obscure a liquid core. This corresponds to an OD in the visible spectrum between 5 and 8 [27].

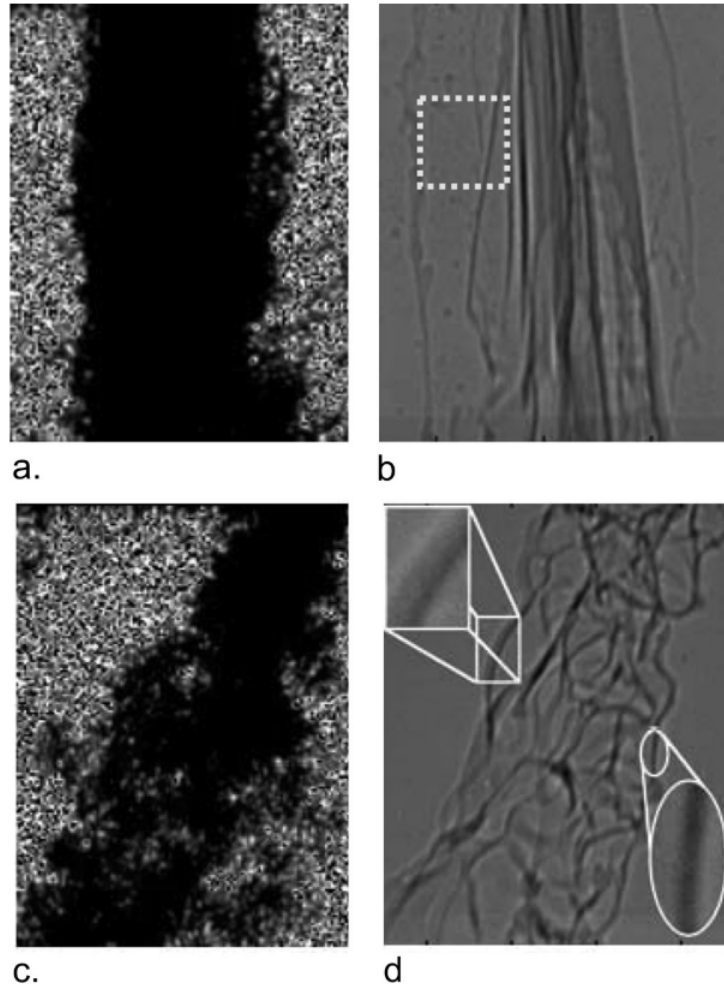


Figure 3.1 Comparison between shadowgraph images (a and c) and X-ray PCI (b and d) of the same flow, the images are approximately $800\ \mu\text{m}$ wide and $950\ \mu\text{m}$ tall [55]

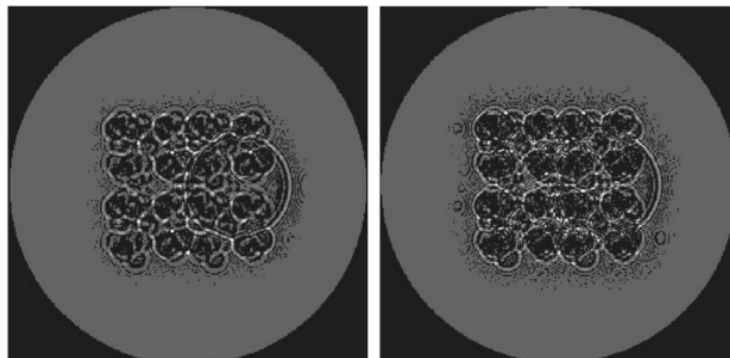


Figure 3.2 PCI simulation of a 150 μm core droplet behind arrays of multiple 30 μm droplets. Left side: 4 drops between the core drop and the scintillator. Right side: 8 drops between the core drop and the scintillator, the core drop cannot be detected. This condition corresponds to a visible light OD between 5 and 8 [18].

PCI spatial resolution has been found to be between 5 and 30 μm . The combination of spatial resolution and the detection of each edge from each droplet along the beam path could also cause the detection of separate droplets in a dense cloud as filaments, contiguous fluid structures typical of membranes. This should not be a concern for USPODH where the signature from smaller droplets below the imaging resolution is actively rejected. For all these reasons, images of structures inside droplet clouds will be corrupted in PCI. These issues can be surpassed when imaging at lower ODs, but at those regimes we can argue that several, more widely available, optical techniques can also be used. On the other hand, PCI's performance is unmatched in imaging internal nozzle flow.

X-ray radiography is a line of sight absorption imaging technique, and by measuring the beam attenuation, it provides a direct measurement of the quantity of liquid mass along the beam path at various locations. In its collimated version it provides a 2D absorption-based image, but higher resolution is achieved by focusing the beam and raster scanning the spray field, providing measurements that are spatially and temporally resolved but

averaged over many cycles. Kastengren et al. provide a spatial resolution value between 5 and 10 μm [56]. This absorption-based approach is challenging at higher pressures (above 20 bar) and temperatures, where absorption from the gas phase can become a considerable percentage of the liquid absorption. Simulations by Linne show how a larger 150 μm fluid drop hidden behind an array of 7 μm droplets can be distinguished only up to 30% attenuation [18].

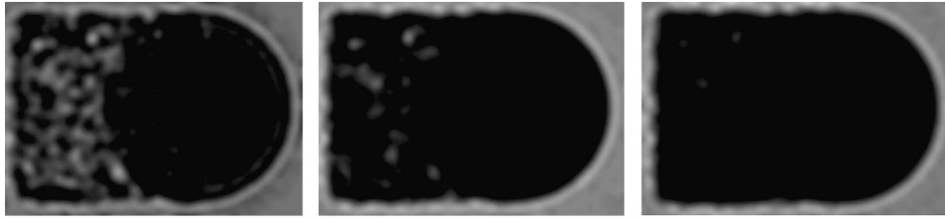


Figure 3.3 X-ray radiograph simulation by Linne. A larger 150 μm core droplet is imaged behind an array of μm droplets; the droplet concentration is increased from left to right, the shape of the core droplet cannot be resolved when attenuation is above 30%.

3.2 Time-gated ballistic imaging

Ballistic Imaging (BI) is the optical line of sight technique which relies on transmission of coherent light through the spray and the use of an ultrafast “shutter” to separate ballistic photons from scattered photons. It can create shadowgrams of fluid structures within clouds of droplets, and it does so by rejecting most of the light corrupted by multiple scattering. The combination of limited signal availability and the technique being single-

shot give shadowgrams that have a limited dynamic range. Ballistic imaging has been used in multiple instances to investigate primary atomization in a water spray [45] the near field of a diesel spray [3], [8], [57], the liquid core of a dodecane spray at pressures up to 1450 atm in evaporating conditions (600 °C) [8] as well as aerated sprays as the ones found in scramjet combustors [49] and of water sprays issuing into a gaseous crossflow [46].

Ballistic imaging relies on detecting and isolating a small population of photons that travels through the spray field without undergoing scattering or absorption events. If they were to be separated from the large population of photons that experience scattering events and adds noise onto the detector, these ballistic photons would provide a silhouette shadowgraph-like image of the spray field. BI uses time of arrival at the Optical Kerr Gate (OKE) as the criteria to filter photons in or out. Ballistic photons and single-scattering photons will reach the camera sensor before multiple scattering (corrupted light) photons because they traveled a shorter distance. This time dependence is depicted in Figure 3.4 and will be quantified by means of Monte Carlo photon transport simulations in the next chapter of this dissertation. For the time being the reader should know that no physical or electronic shutter is fast enough to let through the ballistic

photons while rejecting the multiple scattering ones. This is why an OKE gate is used together with crossed polarizers, and spatial filtering is used to filter the signal. This allows BI to select photons that meet the following criteria: they are nearly co-linear with the imaging beam (spatial-filtering), they have the same polarization of the imaging beam (polarization filtering), and they travel the shortest path (time-gating). We will see in the dedicated chapter how USPODH applies the same filtering criteria using a combination of numerical and optical means making the technique easier to deploy on any setup and more flexible than BI.

Figure 3.5 shows a typical BI setup for spray imaging. Most groups use femtosecond pulsed lasers as the light source for BI, with the exception of the group at Colorado School of Mines which uses a picosecond pulsed laser. The beam is split into an imaging and a switching beam, and the imaging beam goes through a delay stage that allows adjusting the temporal overlap of imaging and switching beam at the OKE gate, which in this depiction is a Carbon-disulfide (CS_2) cell. Soft spatial filtering is provided by carefully selecting physical apertures that do not excessively filter higher spatial frequencies, thus reducing resolution. The polarization of the imaging beam is assured by a series of polarizers. Time gating is applied by the OKE gate. With no switching pulse no photons

can reach the camera because the OKE gate has crossed polarizers, the first polarizer is oriented to pass the imaging beam, the second one is perpendicular to that. When the switching pulse arrives at the OKE gate, the pulse's electric field aligns the CS₂ dipoles along the polarization vector of the switching pulse (birefringence). This rotates the polarization of the imaging beam allowing approximately 70% of it to pass through the second polarizer. The birefringence time is dependent on the media used by the OKE, and for CS₂ is on the order of 1.5-1.8 ps. Fine-tuning of the temporal overlap between switching and imaging beam allows the detection of a photon population composed mainly of ballistic and single-scattering photons, providing a shadowgraph-like image of the target.

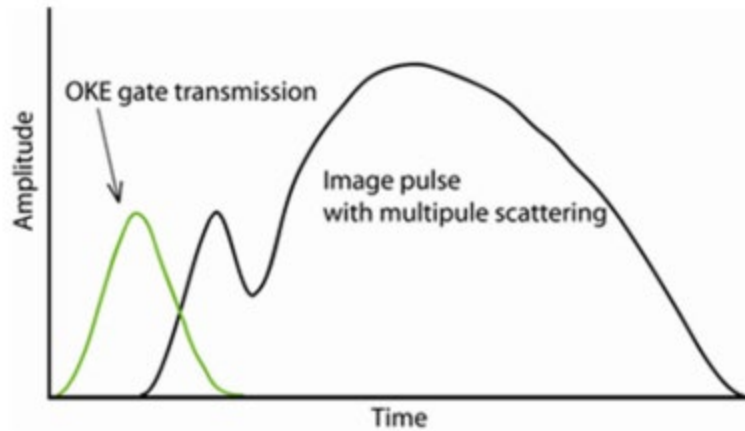


Figure 3.4 Time dependence of ballistic and multiple scattering photons with respect to the OKE gate transmission [8]

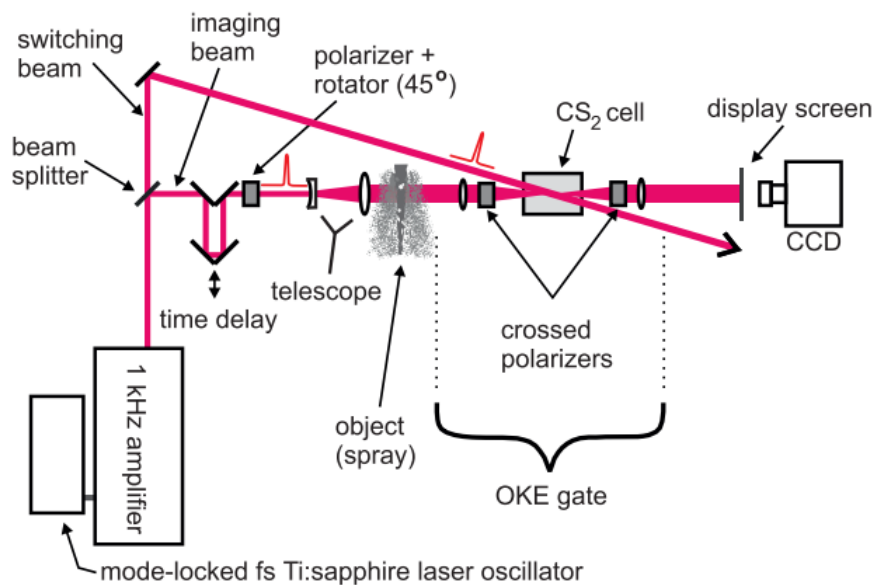


Figure 3.5 Typical single-shot time-gated ballistic imaging setup [18]

Figure 3.6 shows ballistic images in the near nozzle region of a dodecane spray injected at 1450 atm by Duran et al. [8]. The top row is shot in evaporating conditions, meaning that the chamber temperature is high enough to cause the fuel to evaporate, thus increasing

the harshness of the scattering environment. In ballistic images the fluid phase appears black. This is due to a combination of spatial filtering and the shortness of the time-gate, as light going through the liquid phase is delayed by a substantial amount of time (170 fs for every 100 μm of liquid fuel traversed), while the light passing around the spray and through drops might still be detected as quasi-ballistic. A quantitative study of pulse dispersion when traversing different scattering media is presented in the next chapter.

This combination of spatial filtering and time-gating creates an image which is likely to be saturated around the spray edges and below the noise floor in the liquid region. This represents a well-known dynamic range challenge for ballistic imaging that addressed and mitigated in USPODH. BI performs better in a moderate OD spray, with large drops and a smaller liquid core, while the worst scenario would be a spray of smaller drops with high OD and a large liquid core. This is because in such a scenario fewer photons would fall under the quasi-ballistic classification. This observation highlights how in the dense spray imaging community OD alone cannot be relied upon as the metric for the harshness of the imaging environment. More information should be provided to allow a fair comparison between different techniques, for instance, the SMD of the scattering media surrounding

the target. This concept will be expanded upon in the Monte Carlo photon transport simulation chapter of this dissertation.

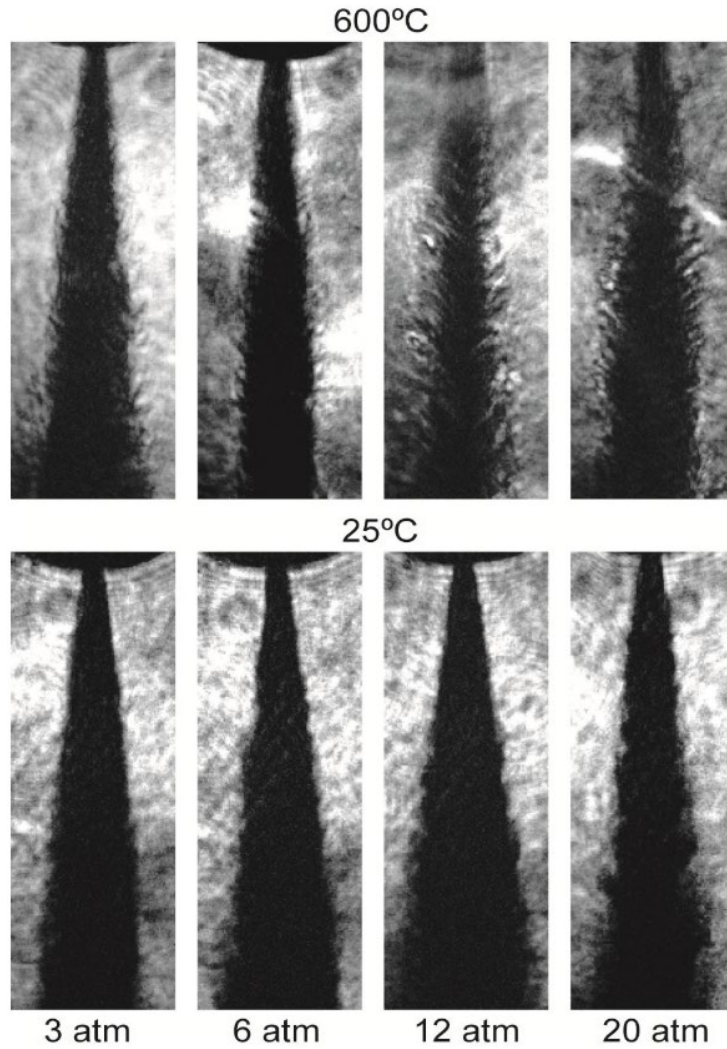


Figure 3.6 Ballistic images of a dodecane spray injected at 1450 atm, 700 μs from the start of injection. The field of view covers 3 mm of spray length. [8]

The OKE gate is adjusted to enhance the gas to liquid interface, and in general a faster switching time allows to better isolate quasi-ballistic photons from the rest at the expense of signal intensity. Several gating configurations can be found in the literature, but in

general OKE CS₂ gates cannot switch faster than 1.5 ps. The researchers at CORIA developed a time gate based on second harmonic generation that has a switching time of 270 fs [51] but with a much lower transmissivity than CS₂. Other possible solutions combine two OKE CS₂ gates for a switching time of 200 fs and good transmittance.

The presence of one or multiple OKE gates creates the risk of background patterns generated by the detection of the switching pulse, and the issue of carefully timing the switching pulse with the imaging pulse to obtain an effective gate of the desired temporal lengths are all BI challenges that USPODH addresses by adopting coherence filtering in lieu of time gating. These advantages will be demonstrated in the next chapters. BI can achieve a spatial resolution of 30-40 μm (FWHM PSF) in harsh scattering environments with OD 13-14 and 20-25 μm (FWHM PSF) in moderate scattering environments with OD 5-10.

The paper by Falgout et al. shows a comparison between shadowgraph imaging and BI when imaging the gas to liquid interface for a variety of fuels at realistic injection conditions. In this and other studies BI has been used to attempt to settle the ongoing debate in the spray science community that sprays under realistic diesel conditions can be

transitionally supercritical. Under subcritical conditions BI shows a defined gas to liquid interface, with surface waves, ligaments and voids, unobscured by the surrounding droplets (Figure 3.8). Under supercritical conditions, BI shows that the interface becomes a turbulent mixing layer with what is defined as a “cellular structure” that is typical of gas jets (Figure 3.9) [1], [10]. This current dissertation study will recreate similar experimental conditions to those found in the main BI studies of dodecane and diesel jets [1], [3], [8], [10], [45] in order to compare USPODH’s imaging performance to BI and shadowgraph imaging and provide evidence of primary atomization fluid structures hidden by clouds of droplets at the gas to liquid interface. An additional ideal future goal that has been only partially fulfilled in this study is to apply USPODH at conditions that will allow imaging transcritical or supercritical fluid regions. In order to completely fulfill this objective it will be necessary to source a pressure vessel capable of meeting the conditions dictated by the Engine Combustion Network (ECN) “Spray A” (6 MPa, 900 K). Figure 3.11 shows the vapor-liquid equilibrium points for a mixture of dodecane fuel and nitrogen gas at different pressures [1], the graph suggests that to ensure supercritical conditions, at least in some regions of the spray, the pressure vessel needs to reach a pressure of 6 MPa and exceed 650 K in temperature. These conditions would be at the edge of the transcritical region, as can be seen in Figure 3.12, raising the temperature further would ensure

the transition into the supercritical regime and allow the observation of the cellular structures typical of the diffusive boundary layer observed by BI at those conditions (Figure 3.9, Figure 3.10).

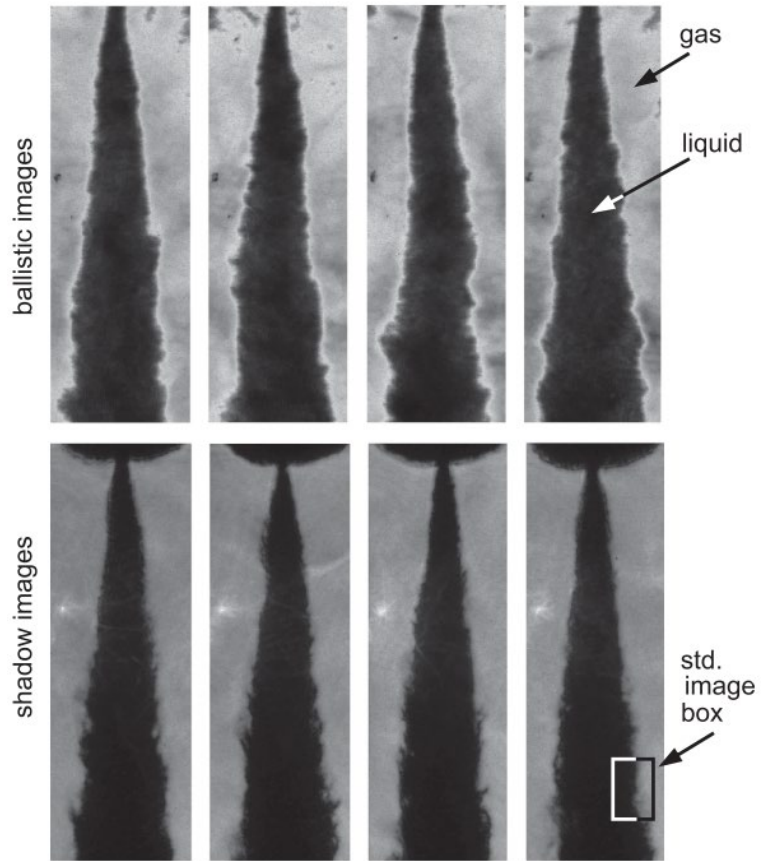


Figure 3.7 Full jet images (450 K and 3 MPa), for commercially available Diesel fuel: upper row contains ballistic images and lower row contains shadow images [1]

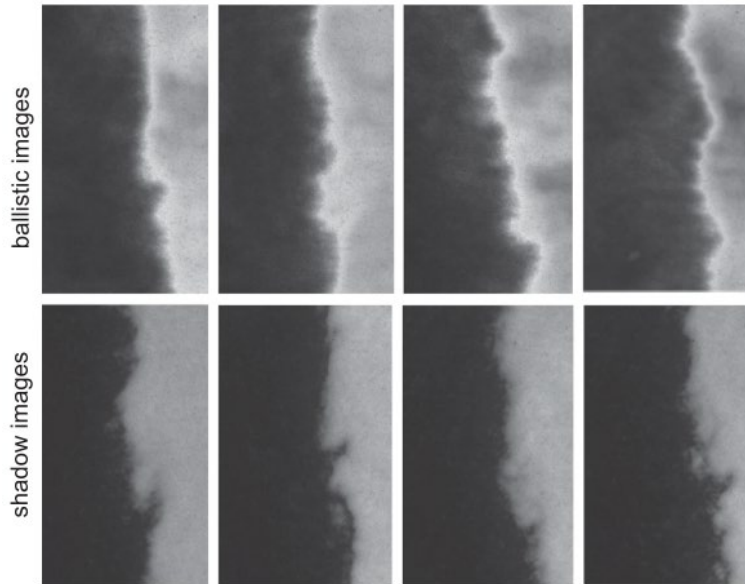


Figure 3.8 Comparison of fluid dynamic structures at the gas to liquid interface for ballistic imaging shadowgraph imaging. Commercial diesel fuel, $T=450\text{ K}$ $P= 3\text{ MPa}$ [1].

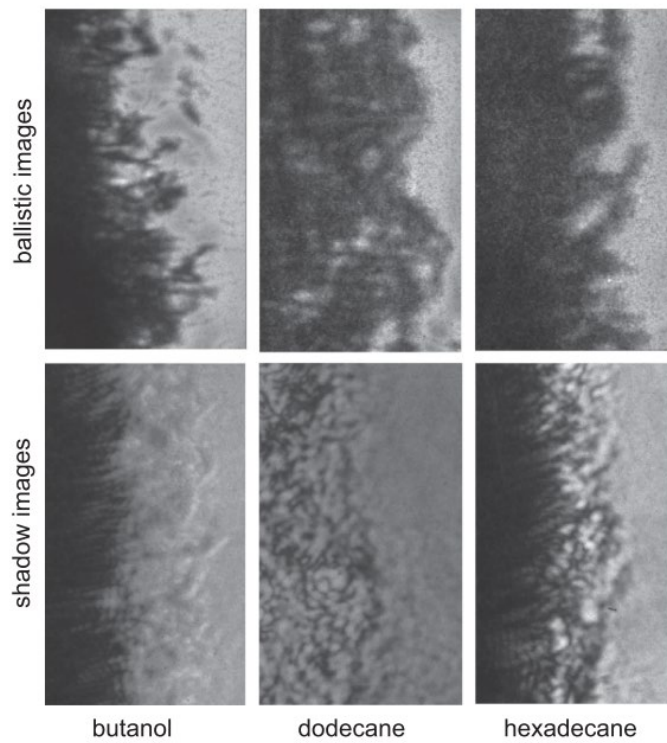


Figure 3.9 Comparison between shadowgraph imaging and ballistic imaging.

Images showing the gas to liquid interface at 900 K and 6MPa, these are supercritical conditions for all these fuels in a nitrogen mixture. The ballistic images show cellular structures consistent with supercritical turbulent mixing layers that are more prominent in the butanol and dodecane case, the shadowgraph images shows Schieren style structures [1]

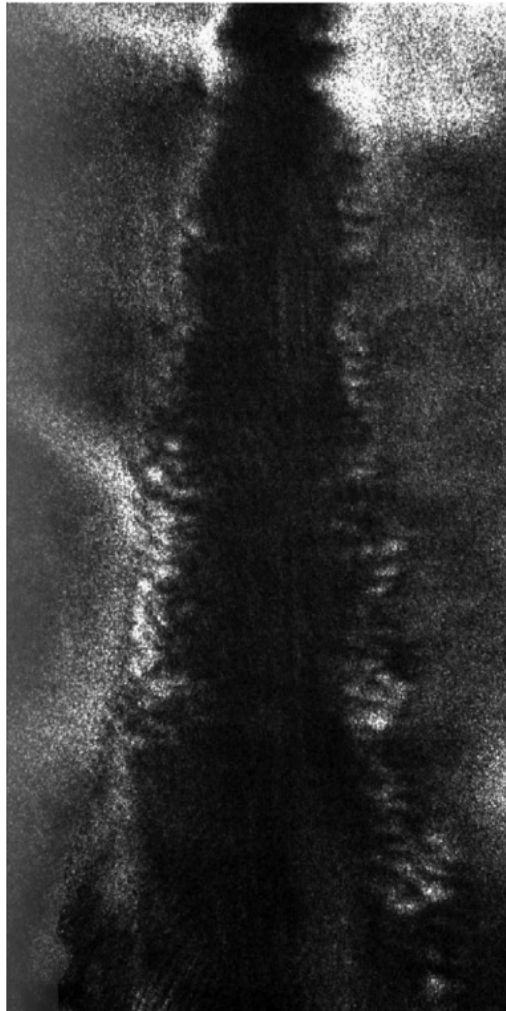


Figure 3.10 BI 0.8ms after injection start of a diesel jet at ECN Spray A conditions ($T=900$ K $P= 60$ bar), showing a region between 1 and 5 mm from the nozzle. The cellular transmissive structures at the spray edges suggest the presence of a supercritical mixing layer [10].

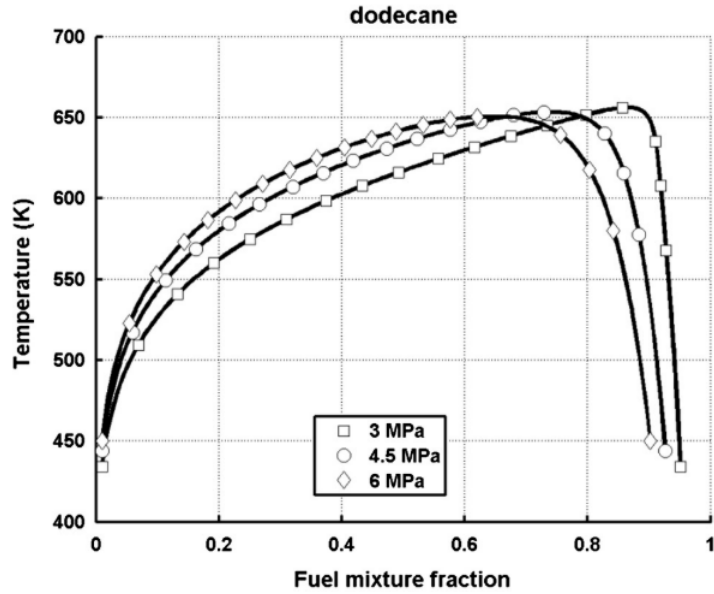


Figure 3.11 Vapor-liquid equilibrium points for a mixture of dodecane fuel and nitrogen gas at different pressures [1].

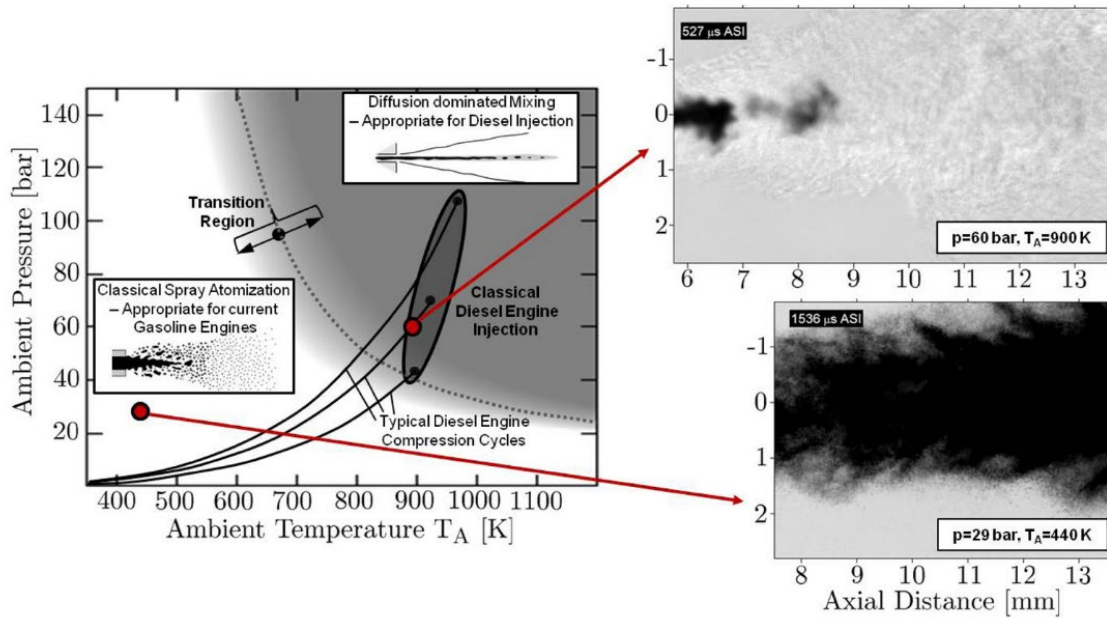


Figure 3.12 Graph showing atomization regimes for dodecane injected at 363 K into a chamber filled with gaseous nitrogen at different temperatures and pressures, the white region represents the classical spray regime, the gray

region the diffusion dominated spray regime. Three lines represent the compression cycle for different diesel engines; the top line represents a turbo-charged compression cycle, the middle one a medium-load and the bottom one a light-load [14].

3.3 Section summary

This chapter introduced a short review of techniques used to image the optically dense region of atomizing sprays. A selection of X-ray based techniques showed how they could fail at identifying liquid structures hidden behind a cloud of droplets at relatively moderate visible-equivalent OD values, or how they rely upon raster scanning and averaging of multiple shots. They also encounter limitations when used to image injections in environments at pressures above 20 bar. They are, however, the only techniques able to image internal nozzle flow and measure liquid mass over the spray field.

The chapter then focused on ballistic imaging, a line of sight optical technique used to probe the gas to liquid interface at the edge of the injected liquid column. This method allows identification of voids, ligaments, primary atomization droplets and surface waves at the spray edges, and in its time-gated version it allows this imaging at very high OD values, up to OD 15. BI has also been used at realistic “ECN Spray A” injection conditions to show evidence of the existence of supercritical mixing layers between the injected fuel and the surrounding gas. Nevertheless, BI is afflicted by limited dynamic

range. It provides information only regarding the edges of the spray; it has a strong background signal and is a 2D line of sight imaging technique. It is considered an elaborate apparatus to set up and operate, but so far it is the only one that has been proven capable of imaging large fluid structures inside high OD regions. Throughout this dissertation BI will be used as the benchmark to compare USPODH's imaging performance with. The main points over which we will be comparing USPODH to BI are:

- Polarization filtering strategy
- Spatial filtering (that can be varied numerically off-line in USPODH)
- USPODH superior sensitivity and dynamic range, which partially addresses BI's dynamic range limitations
- Coherence gating vs. time-gating, or how coherence gating provides a virtual gate switching time that always matches the imaging pulse duration optimizing noise scattering reduction performance

The next chapter will use Monte Carlo photon transport simulations to compare time-gating to coherence filtering, showing how the use of the latter in femtosecond off-axis digital holography can provide the same scattering noise rejection performance offered by ballistic imaging's most advanced gating configurations, in a more straightforward, more

comfortable to deploy and use experimental layout. The other topics mentioned above will be addressed in chapter 5.

Chapter 4

4 Monte Carlo simulation of photon transport in turbid media

In the previous chapter, we saw how ballistic imaging is a single-shot optical diagnostic technique capable of imaging the near nozzle region of dense sprays at ODs up to 14, thanks to time-gating's capability of filtering quasi-ballistic photons. This chapter introduces the reader to stochastic simulations of photon transport in turbid media, and essential concepts such as the Beer-Lambert law are presented. The goal is to formally validate the choice that led to the adoption of coherence filtering instead of time gating when imaging using femtosecond pulses by showing how matching imaging pulse length with the time-gate length provides the best image and contrast resolution, a condition always verified when using USPODH's coherence filtering. Monte Carlo models hinted at an improvement of spatial resolution by a factor of approximately two if the gate time could be matched to the image pulse width, but recent experiments at Chalmers

University, where the image pulse width was lengthened to 1.8 ps to match more closely the OKE gate time, did not produce the anticipated improvement [18].

A ballistic imaging setup where a target is imaged through a scattering media with OD up to 10 is simulated to provide insights into coherence and time gating as filtering approaches. Time-gating is compared to spatial filtering and shadowgraph imaging without a gate. The same is done experimentally, and the experimental results agree in showing how spatial filtering is more effective than time-gating in filtering higher scattering order photons in fs ballistic imaging experiment at high OD (section 4.3). These results were produced using the state-of-the-art Monte Carlo photon transport software “Multi-Scattering©” developed by Professor Berrocal’s research group at the University of Lund [17], [58], [59]. A comparison between time-gating and coherence filtering is presented in the next chapter in section 5.8.

4.1 Photon-transport theory (Beer-Lambert law)

The most important source of errors in all optical diagnostics of sprays is the multiple scattering of the incident laser radiation by the surrounding droplets. The understanding and adequate prediction of the radiative transfer in this scattering regime is a challenging

and non-trivial task. Light intensity from a collimated beam directed straight toward a detector through a homogeneous medium is exponentially reduced along a line of sight of length l :

$$I_f = I_i \cdot e^{-\mu_e \cdot l}$$

This is known as the Beer-Lambert law. I_f is the light intensity left after a beam of initial intensity I_i has traveled for a distance l through a scattering medium with an extinction coefficient μ_e .

The extinction coefficient μ_e is defined as the sum of scattering and absorption coefficient:

$$\mu_e = \mu_s + \mu_a$$

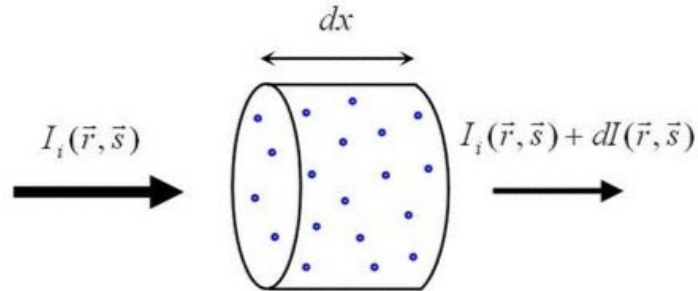


Figure 4.1 Variation of irradiation energy dI for a collimated beam going through an elementary volume of a scattering medium.

The mean free path between each photon interaction with a particle can result from either scattering or absorption and is given by:

$$\bar{l}_{fp} = \frac{1}{\mu_e}$$

This quantifies the *optical depth* of the scattering medium as the ratio between the length of the path through the scattering medium and the mean free path between each photon to particle interaction:

$$OD = \frac{l}{\bar{l}_{fp}} = l \cdot \mu_e$$

Optical depth approximates the mean number of scattering events occurring through a scattering medium of length l , and it is used to classify the light scattering regime in a spray (see Table 4.1).

Table 4.1 Scattering regime as a function of OD.

	Single scattering	Intermediate scattering	Multiple scattering
OD	≤ 1	2-9	≥ 10
	Single scattering approximation	The exact form of RTE cannot be calculated	Diffusion approximation

The following considerations assume anisotropic scattering, with dominant forward scattering, as stated by the Lorentz-Mie scattering theory. In the single scattering regime, ballistic photons are dominant, and the single scattering approximation is assumed. In the intermediate scattering regime, both single and high order scattering orders must be considered. Most laser diagnostics applications for sprays fall into this regime. In the multiple scattering regime, the relative amount of each scattering order tends to be equal, and the diffusion approximation is applied [17]. Figure 4.2 shows the relative photon

irradiance with respect to scattering order for different values of OD when imaging through a log-normal distribution of fuel droplets with a diameter of 5 μm . For low OD values, there is a substantial population of ballistic and quasi-ballistic photons, and as the OD number increases by either raising the number density of particles or the path length, the system enters the intermediate scattering regime for $\text{OD} \cong 6$. In this condition, single scattering photons are only 5% of the entire photon population making imaging under these conditions challenging. Moving to OD values that are of interest in near-nozzle spray research, $\text{OD} \cong 10$ and above, light can be treated as diffuse. In the multiple scattering regime approximately 1 photon of every 50000 makes it through the scattering media without encountering extinction, and at OD 13 this number drops to one every million photons. The tiny population of photons that are useful for imaging in such conditions makes it clear why scattering noise rejection strategies are essential to obtain a usable image of the target. The Monte Carlo photon transport simulations that follow answer the following fundamental questions:

- What is the ideal time gating duration for a given laser pulse when imaging through scattering media of OD representative of dense sprays?
- How many ballistic and quasi-ballistic photons are available when imaging through a dense spray like environment?

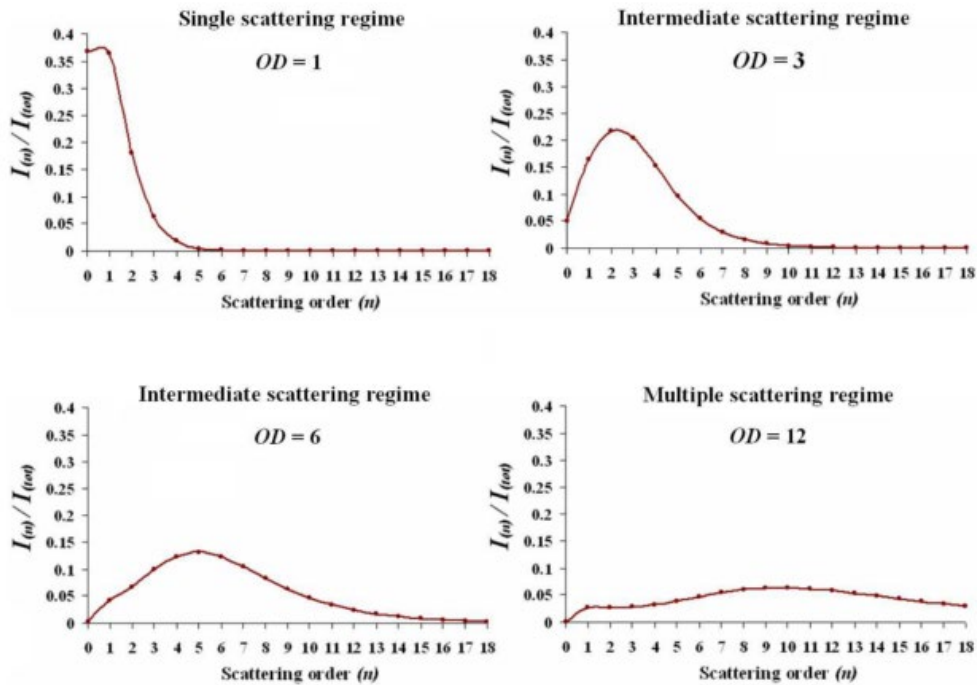


Figure 4.2 Scattering orders for various optical depths of a collection of spherical fuel droplets (Long-Normal distribution of diameter 5 microns and $\sigma = 0.5$ micron) [17]

4.2 Simulation results

This section presents a selection of the photon transport Monte Carlo simulations performed using the software Multi-Scattering© [58], [59]. The samples simulate and compare a shadowgraph image of a target to one obtained by applying time-gating in increasingly harsh scattering conditions. A third image, generated by only detecting ballistic photons, is also simulated to provide an idealized comparison to the other two;

the purely ballistic image is the one we would obtain by having an ideal gating technique. This image is also the ideal performance for what can be obtained via coherence filtering in USPODH, and we will corroborate this statement in the USPODH chapter. All cases are simulated with soft (25 mm aperture) and aggressive (3 mm aperture) spatial filtering (see the layout in Figure 4.4 for the location of the aperture).

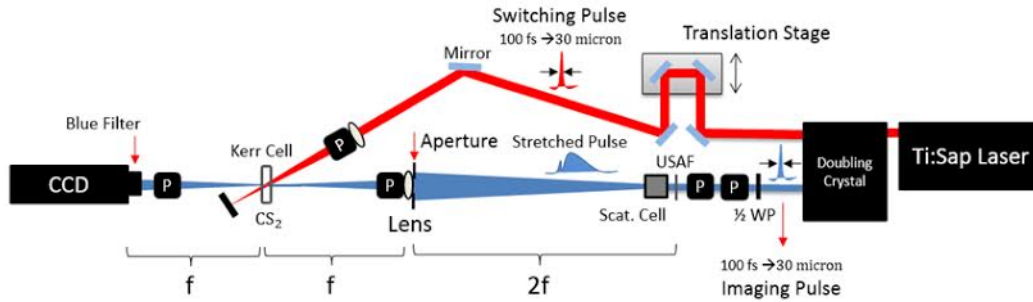


Figure 4.3 Gated ballistic imaging setup simulated using the Monte Carlo code developed by the team at Lund University.

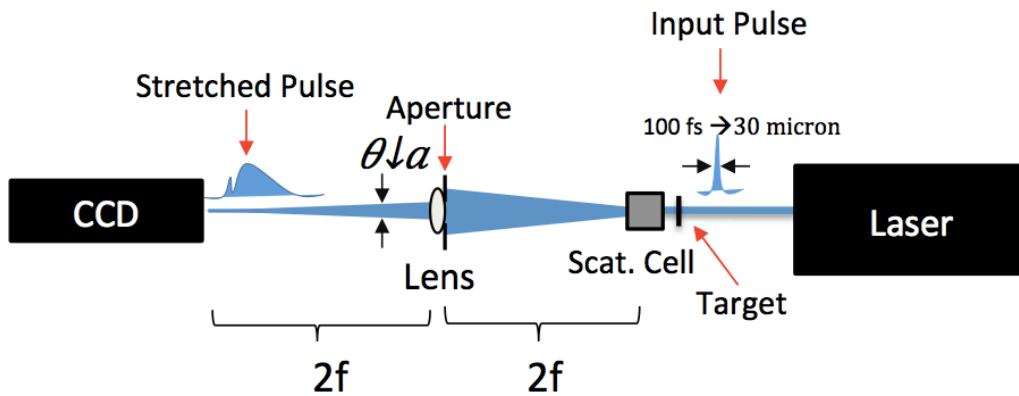


Figure 4.4 Spatially filtered shadowgraph setup simulated using the Monte Carlo code from the team at Lund University, notice the absence of an OKE gate.

The two imaging setups that have been simulated are shown in Figure 4.3 and Figure 4.4. The first is a ballistic imaging time-gated setup that was used by our group before the change to coherence filtering and UPSODH [11], and the second is a $2f$ lensed shadowgraph setup that uses spatial filtering to reject multiple scattering photons. Photons that encounter multiple scattering events are more likely to leave the scattering medium at a larger angle with respect to the ballistic ones; therefore, it is possible to filter

them just by applying spatial filtering. However, aggressive spatial filtering will eliminate the higher spatial frequencies in the imaging pulse, which also reduces the resolution.

The simulation parameters are:

- The imaging beam is collimated with a Gaussian profile of 2.3 mm FWHM. The USAF resolution chart target is simulated by blocking the beam with equidistant bars of 50 μm width with a center to center distance of 100 μm .
- The wavelength of the imaging beam is centered at 400 nm with a FWHM bandwidth of 10 nm.
- The pulse duration is measured at 100 fs and a Gaussian temporal profile is considered.
- The scattering media is made of polystyrene particles with an index of refraction of 1.57 suspended in water with an index of refraction of 1.33.
- Two different uniform distribution scattering media are simulated, one with number density of 14 million particles per cubic centimeter of 6-micron particles, the second with 840 million particles per cubic centimeter of 0.6-micron particles.
- The length of the scattering cell in both cases is 10 mm, representing a standard cuvette.

- A 2f imaging system with focal lengths of 100mm is used to form an image of the USAF resolution target on a CCD with a magnification of 1. A glass cuvette is placed after the USAF target (15 mm after the USAF) containing a suspension of polystyrene particles in water. A 3 mm or a 25 mm diameter aperture is placed right before the lens to reduce the numerical aperture of the imaging system, simulating the effects of spatial filtering.
- The Kerr cell is placed right before the focal point of the lens (about 95 mm from the lens). The transmission curve of the Kerr gate is close to a Gaussian curve with 40% transmission at peak and FWHM transmission window of 1.1 ps. The delay of the switching pulse is adjusted to transmit the imaging pulse at peak transmission when the scattering cuvette is just filled with water (no scattering cell).

The results compare the simulations in terms of both the temporal profile of the stretched pulse and the spatial intensity field recorded on the CCD when the gating is active (gated mode) and when the gate is not active and the whole pulse is transmitted to the CCD (open gate mode). These simulations should help assess:

- The ideal pulse length when imaging through dense sprays
- The ideal time gate temporal length for dense spray imaging
- The effects of spatial filtering vs. time-gating

- The number of ballistic photons available when imaging through a high OD medium, supporting the concept that selecting only ballistic photons using coherence filtering can provide an image of the target with sufficient resolution and contrast

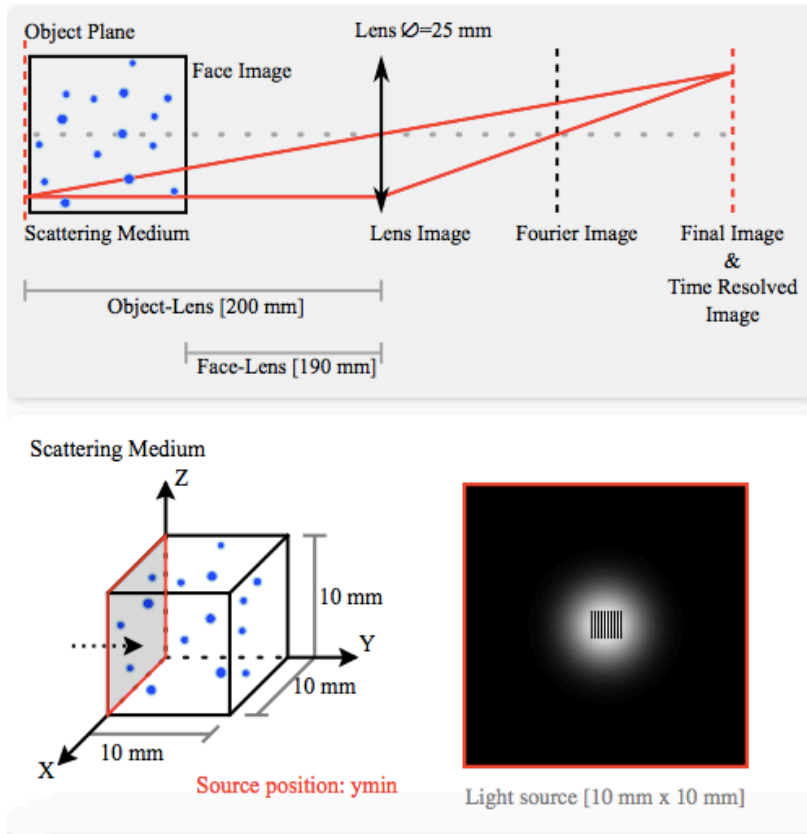


Figure 4.5 Diagram showing the simplified simulated domain.

4.2.1 Photon transport simulations in turbid media with OD=5

Simulations #1 and #2 compare different time gating and spatial filtering solutions when imaging a target through a 10 mm cuvette containing a water suspension of polystyrene

particles with a diameter of 0.6 μm and an OD of 5. These media represents moderately optically dense sprays in the secondary breakup region where smaller droplets are generated. All the figures presented in this chapter are generated by our simulations using the Multi-Scat Monte Carlo photon transport software [58], [59].

Table 4.2 Simulation parameters for imaging pulse and scattering media properties, OD 5 simulations.

Total number of photons simulated	P	99999.997952 *10 ⁶
Wavelength	λ	400 nm
Optical Depth	OD	5.096755
Averaged Scattering Event	S_{nb}	5.362731
Particle diameter	\varnothing_P	0.6 μm
Number density	N	8.4*10 ⁵ particle/mm ³
Lightpath length	L	10 mm
Extinction coefficient	μ_e	0.5096754 mm ⁻¹
Scattering Coefficient	μ_s	0.5096754 mm ⁻¹
Absorption Coefficient	μ_a	0 mm ⁻¹
Medium Absorption Coefficient	μ_{ma}	0 mm ⁻¹
Particle Refractive Index	n_p	1.57
Medium Refractive Index	n_m	1.33
Extinction Cross-Section	σ_e	6.067565 *10 ⁻⁷ mm ²
Scattering Cross-Section	Σ_s	6.067565 *10 ⁻⁷ mm ²
Absorption Cross-Section	σ_a	0 mm ²

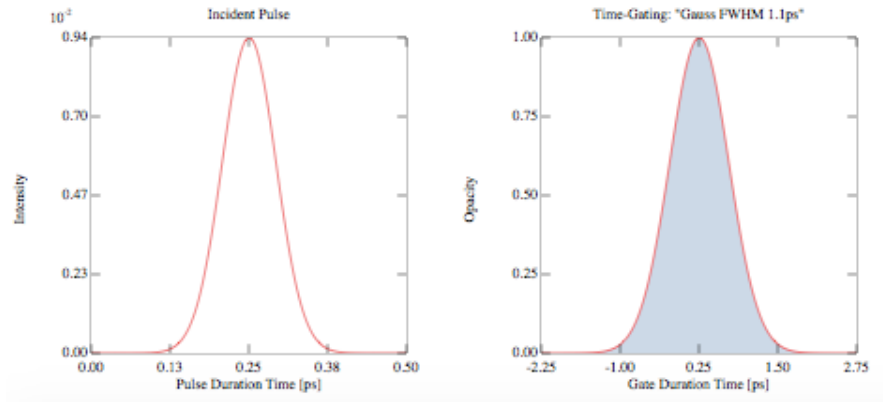


Figure 4.6 Temporal profile of the simulated imaging pulse and time-gate profile.

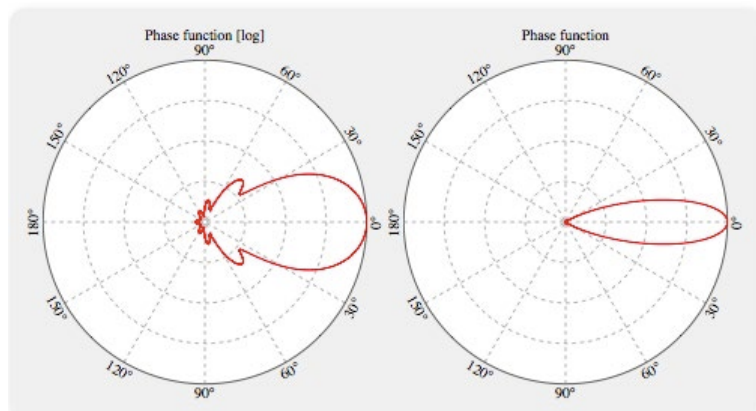


Figure 4.7 Mie Scattering phase function of the simulated turbid media.

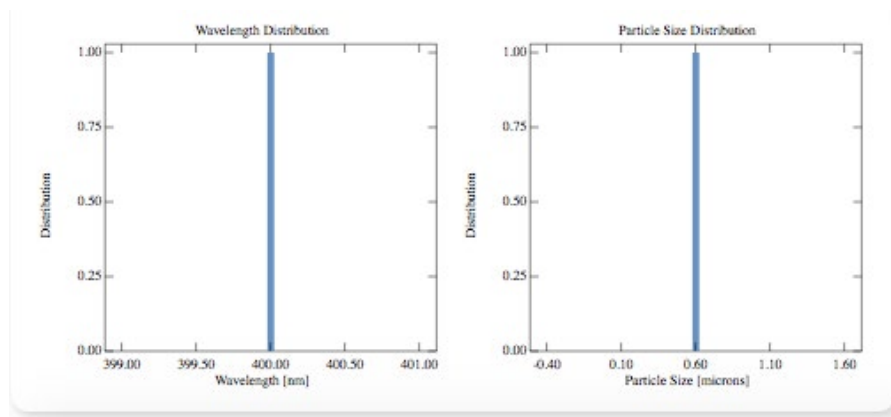


Figure 4.8 Imaging pulse spectrum and particle size distribution of the simulated turbid media.

4.2.2 Simulation 1: 25 mm aperture at the lens plane

Simulation 1 shows shadowgraph images acquired through a scattering media with moderate scattering harshness at $OD=5$ while applying soft spatial filtering by using a 25 mm aperture at the lens plane. For each simulation, the following results are presented: no time gate, time-gated, and ballistic photons. The ballistic photons results represent what would be the outcome when imaging with a perfect time gate that would allow the detection of ballistic photons only. This case is close to USPODH where only ballistic and quasi ballistic photons are detected.

4.2.2.1 No Time-Gate – soft spatial filter

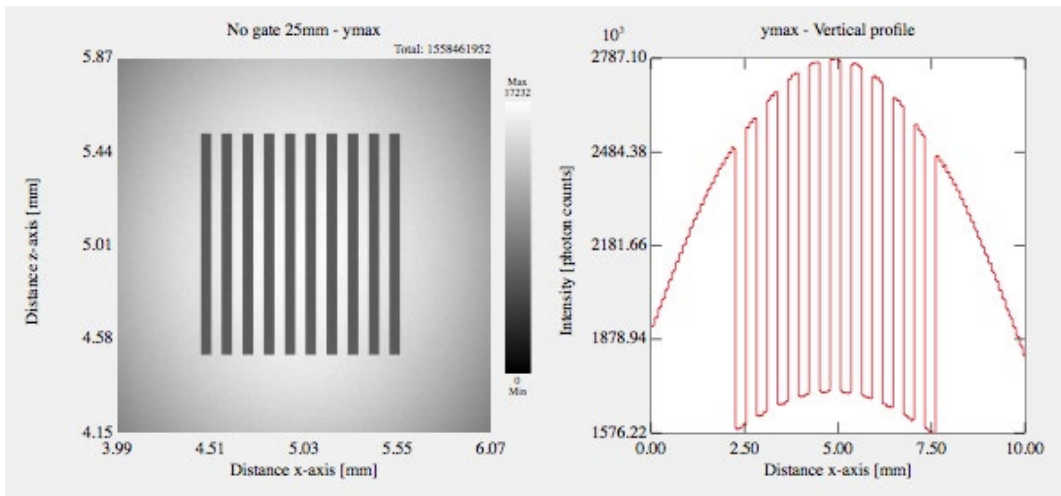


Figure 4.9 Intensity-based image and spatial profile of the photon count at the detector

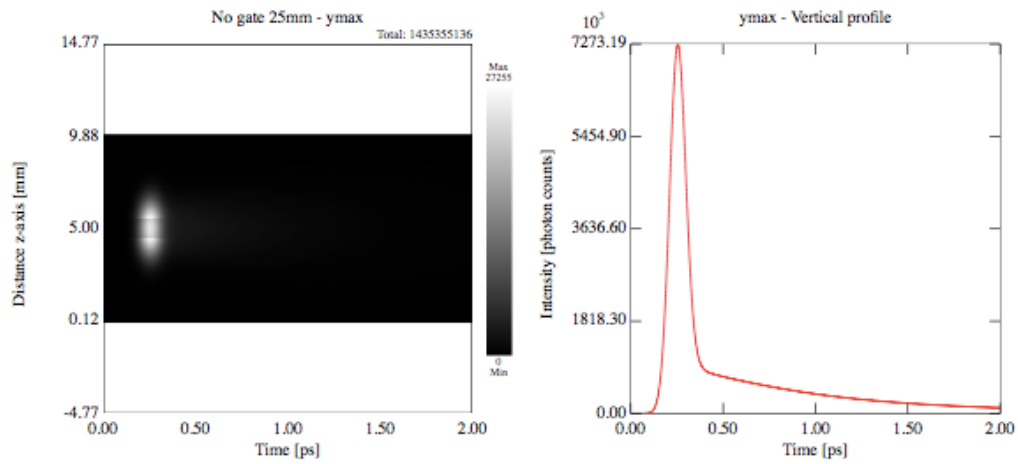


Figure 4.10 Spatial and temporal intensity profile of the photon count at the detector – temporal profile of photon count at the detector

4.2.2.2 Time-Gated – soft spatial filter

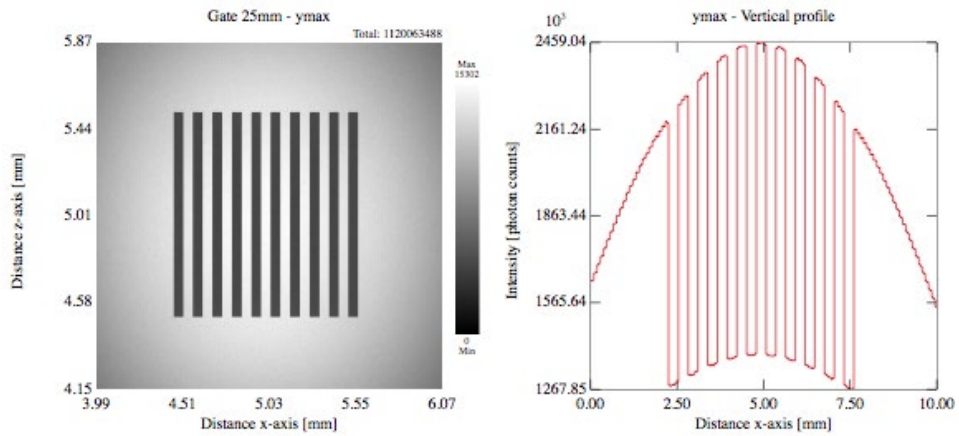


Figure 4.11 Intensity-based image and spatial profile of the photon count at the detector

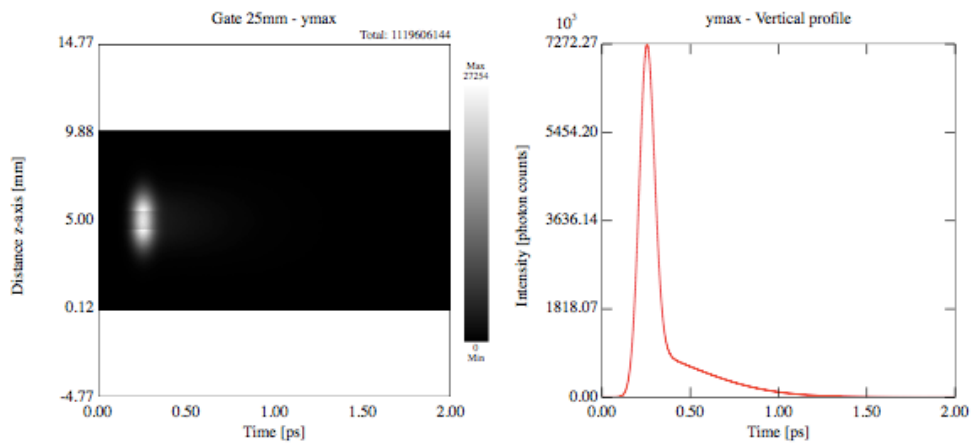


Figure 4.12 Spatial and temporal intensity profile of the photon count at the detector – temporal profile of photon count at the detector

4.2.2.3 Ballistic photons – soft spatial filter

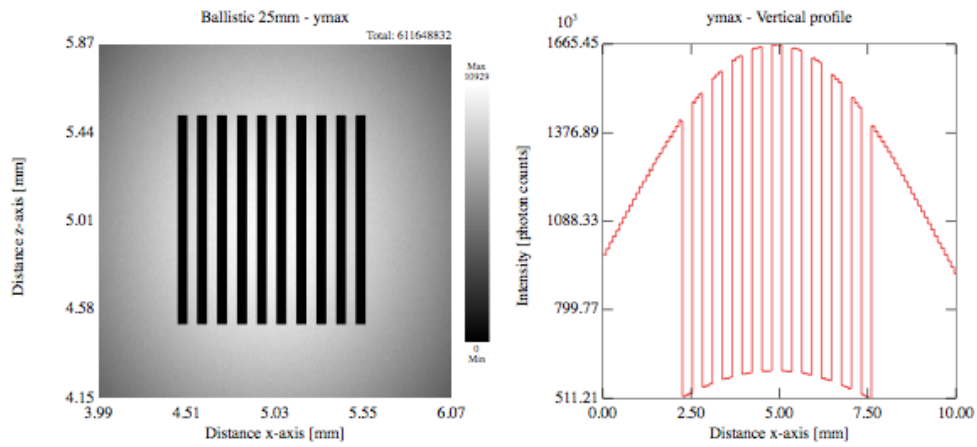


Figure 4.13 Intensity-based image and spatial profile of the photon count at the detector

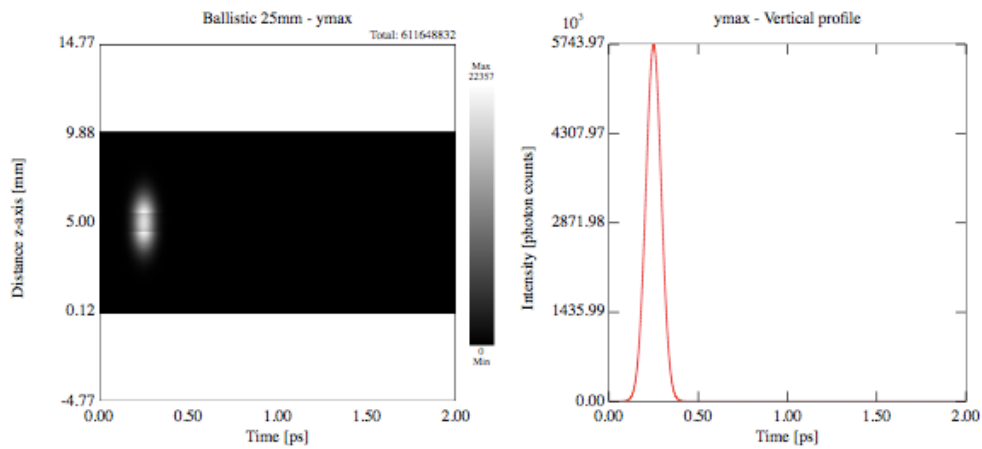


Figure 4.14 Spatial and temporal intensity profile of the photon count at the detector – temporal profile of photon count at the detector

4.2.2.4 Simulation 1 - Observations

- The temporal dispersion of the 100 fs pulse when traversing the scattering media is negligible.
- Spatial filtering using a 25 mm aperture does not seem aggressive enough to produce an image quality improvement at these conditions.
- The time-gated results are marginally better than the no gate spatially filtered ones, showing an image with slightly improved contrast.
- Having a shorter gate that matches the imaging pulse length would deliver the best image contrast and resolution (see ballistic photons results).

4.2.3 Simulation 2: 3 mm aperture at the lens plane OD=5

We now simulate a setup that uses a more aggressive spatial filtering strategy, by virtually placing a 3 mm aperture at the lens plane.

4.2.3.1 No gate – aggressive spatial filter

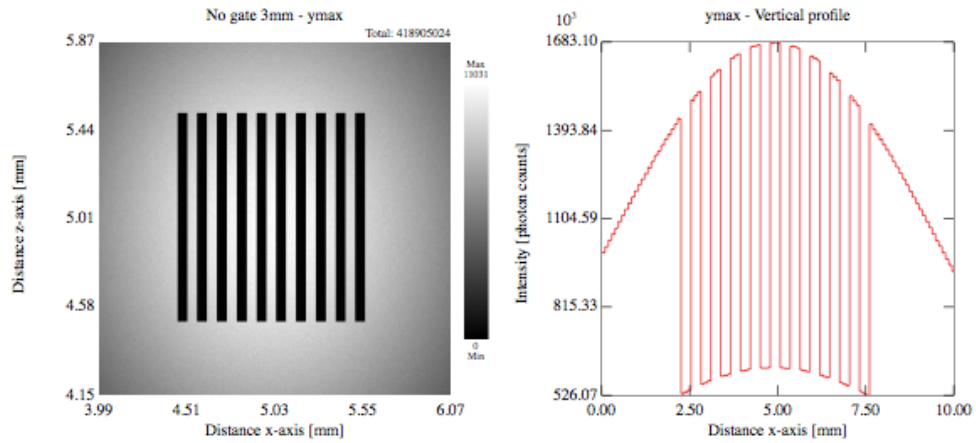


Figure 4.15 Intensity-based image and spatial profile of the photon count at the detector

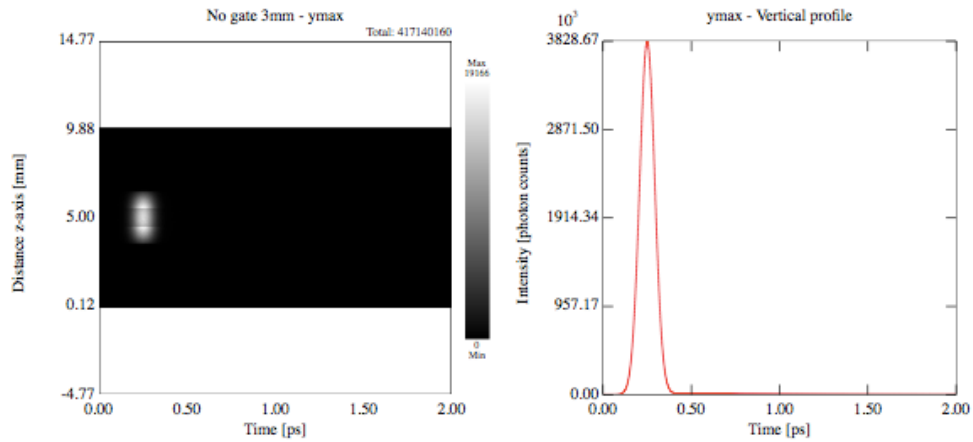


Figure 4.16 Spatial and temporal intensity profile of the photon count at the detector – temporal profile of photon count at the detector

4.2.3.2 Time-gated – aggressive spatial filter

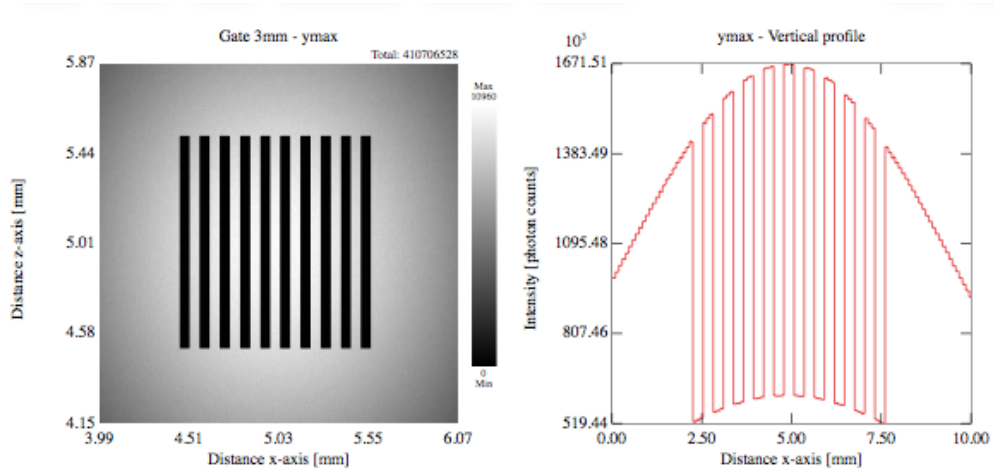


Figure 4.17 Intensity-based image and spatial profile of the photon count at the detector

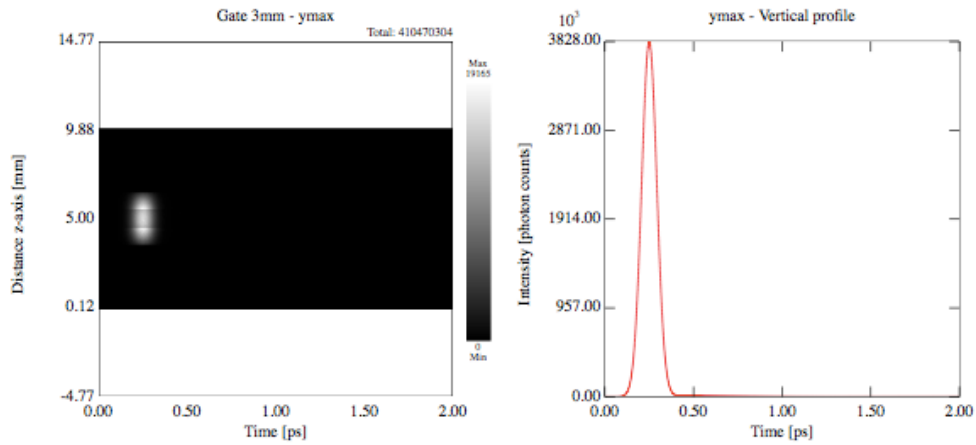


Figure 4.18 Spatial and temporal intensity profile of the photon count at the detector – temporal profile of photon count at the detector

4.2.3.3 Ballistic photons – aggressive spatial filter

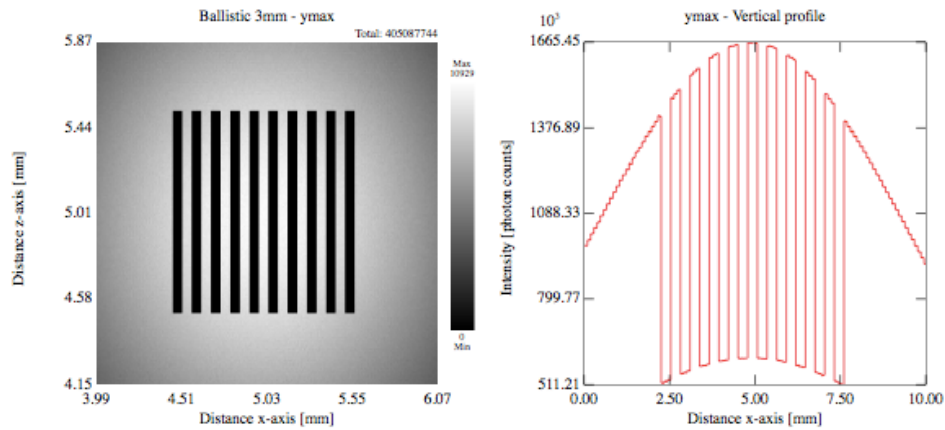


Figure 4.19 Intensity-based image and spatial profile of the photon count at the detector

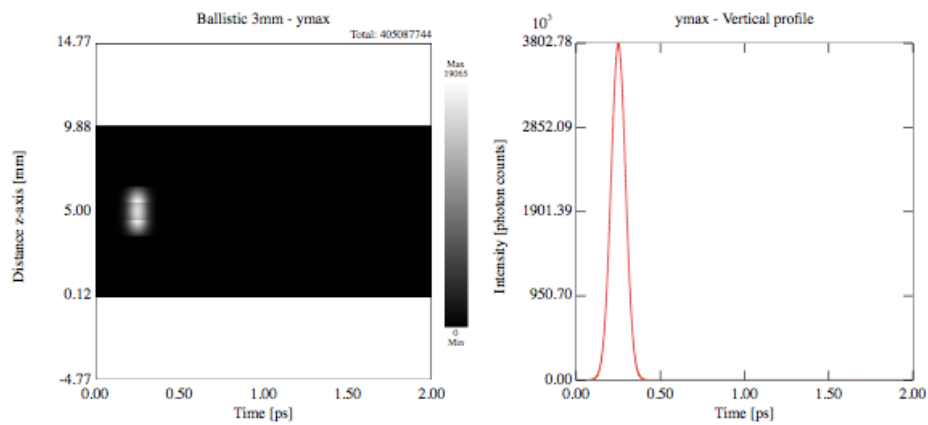


Figure 4.20 Spatial and temporal intensity profile of the photon count at the detector – temporal profile of photon count at the detector

4.2.3.4 Simulation 2 - Observations

The use of aggressive spatial filtering at OD 5 helped close the gap in image quality between the no gate and the time-gated images, and the difference in contrast and

resolution is marginal, suggesting that at these mild scattering conditions spatial filtering is an effective and easy to implement scattering noise reduction strategy that could be preferred to time gating because of its complexity and marginally improved results. It is crucial to notice that when trying to image higher spatial frequencies; however, aggressive spatial filtering might deliver results that are inferior to time gating. That is, since the spatial filtering acts as a low pass filter in the frequency domain, an aggressive spatial filter might end up reducing image resolution. This phenomenon has been investigated experimentally and is shown in section 4.3.

4.2.4 Photon transport simulations in turbid media with OD=10

Simulations #3 and #4 investigate the efficacy of spatial filtering and picosecond time gating when imaging through a turbid media with OD=10. This OD magnitude is considered by researchers to be comparable to the one produced by primary atomization droplets surrounding the liquid core in high-pressure fuel sprays [18].

Table 4.3 Simulation parameters for imaging pulse and scattering media properties, OD 10 simulations.

Total number of photons simulated	P	99999.997952 *10 ⁶
Wavelength	λ	400 nm
Optical Depth	OD	10
Averaged Scattering Event	S _{nb}	10.50867
Particle diameter	\varnothing_P	0.6 μ m

Number density	N	1.648108*10 ⁶ particle/mm ³
Lightpath length	L	10 mm
Extinction coefficient	μ_e	1 mm ⁻¹
Scattering Coefficient	μ_s	1 mm ⁻¹
Absorption Coefficient	μ_a	0 mm ⁻¹
Medium Absorption Coefficient	μ_{ma}	0 mm ⁻¹
Particle Refractive Index	n_p	1.57
Medium Refractive Index	n_m	1.33
Extinction Cross-Section	σ_e	6.067565 *10 ⁻⁷ mm ²
Scattering Cross-Section	Σ_s	6.067565 *10 ⁻⁷ mm ²
Absorption Cross-Section	σ_a	0 mm ²

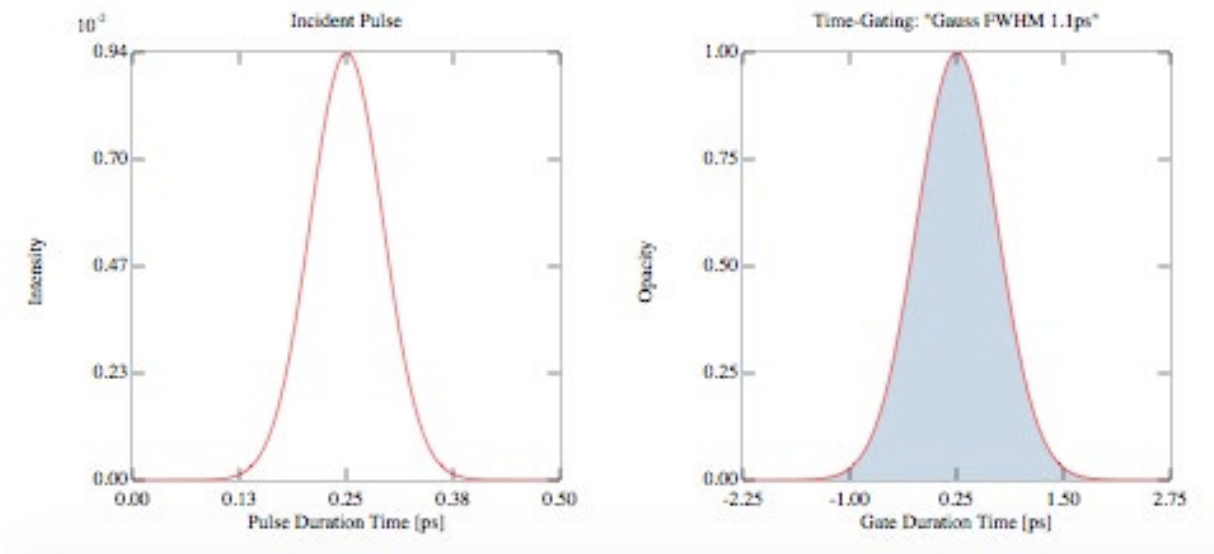


Figure 4.21 Temporal profile of the simulated imaging pulse and time-gate profile

4.2.5 Simulation 3: 25 mm aperture at the lens plane, OD 10

Simulation 3 shows shadowgraph images acquired through a scattering media with harsh scattering at OD=10 while applying soft spatial filtering by using a 25 mm aperture at

the lens plane. For each simulation, the following results are presented: no time gate, picosecond time-gated, and ballistic photons. The ballistic photons results represent what would be the outcome when imaging with a perfect time gate that would allow the detection of ballistic photons only. This case is close to USPODH, where only ballistic and quasi ballistic photons are detected.

4.2.5.1 No gate – soft spatial filter

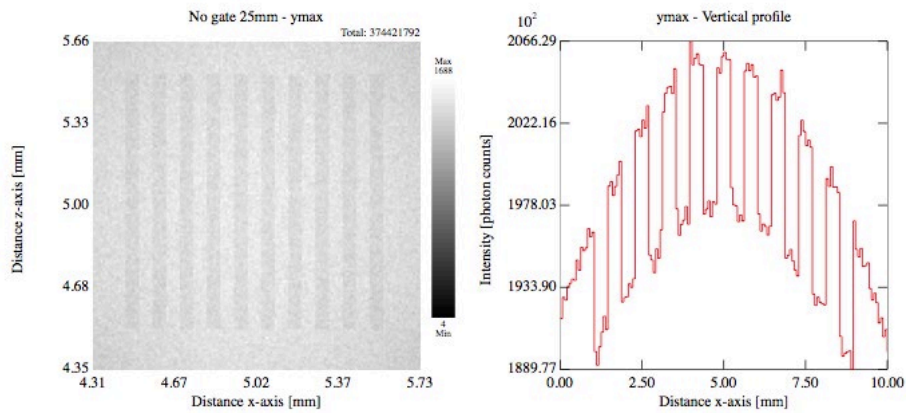


Figure 4.22 Intensity-based image and spatial profile of the photon count at the detector

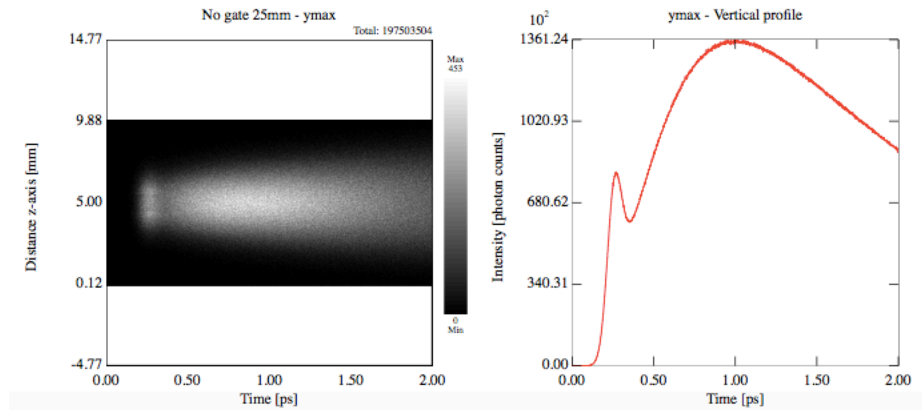


Figure 4.23 Spatial and temporal intensity profile of the photon count at the detector – temporal profile of photon count at the detector

4.2.5.2 Time-gated – soft spatial filter

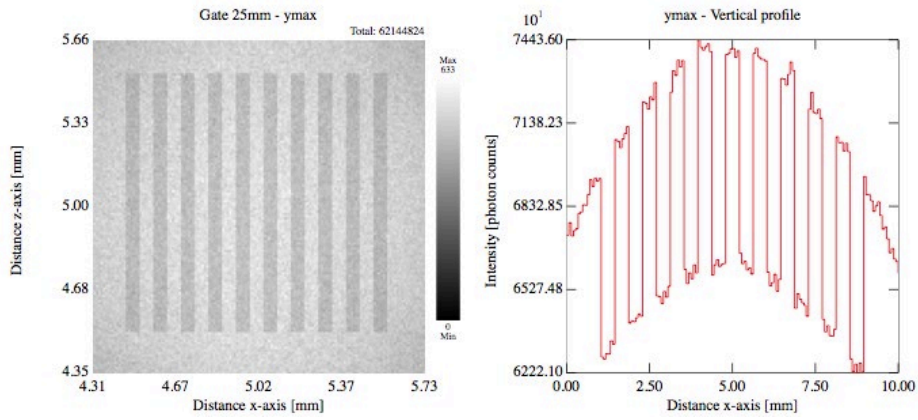


Figure 4.24 Intensity-based image and spatial profile of the photon count at the detector

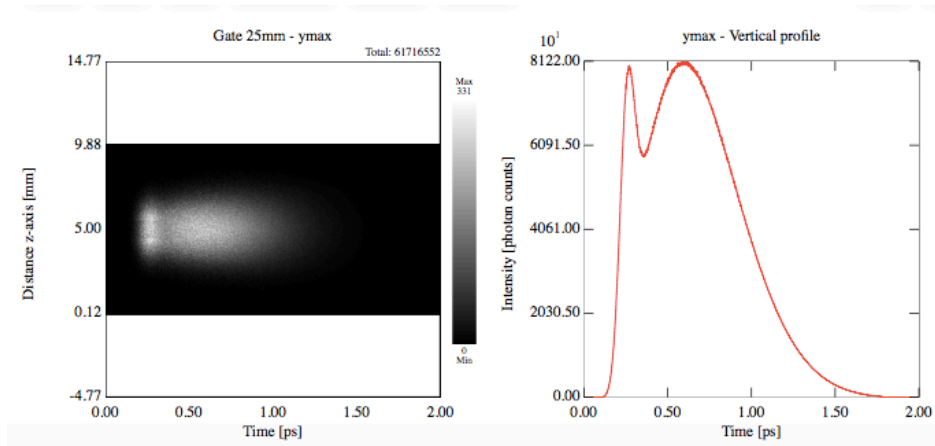


Figure 4.25 Spatial and temporal intensity profile of the photon count at the detector – temporal profile of photon count at the detector

4.2.5.3 Ballistic photons - soft spatial filter

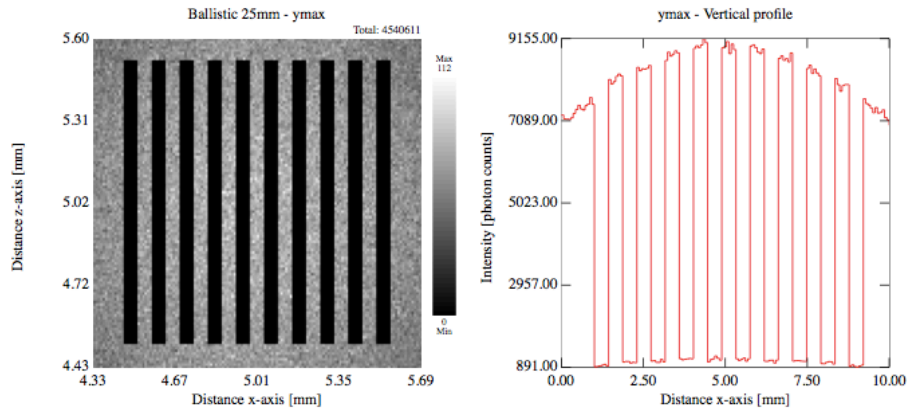


Figure 4.26 Intensity-based image and spatial profile of the photon count at the detector

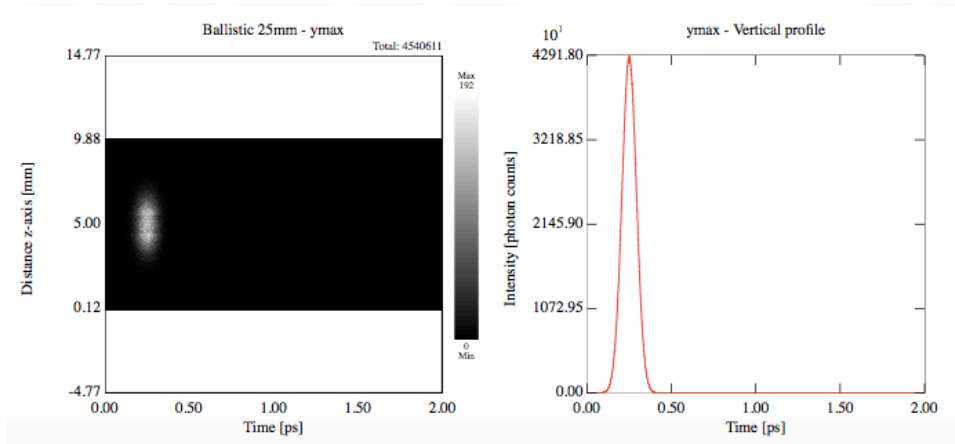


Figure 4.27 Spatial and temporal intensity profile of the photon count at the detector – temporal profile of photon count at the detector

4.2.6 Simulation 4: 3 mm aperture at the lens plane, OD 10

4.2.6.1 No gate – aggressive spatial filter

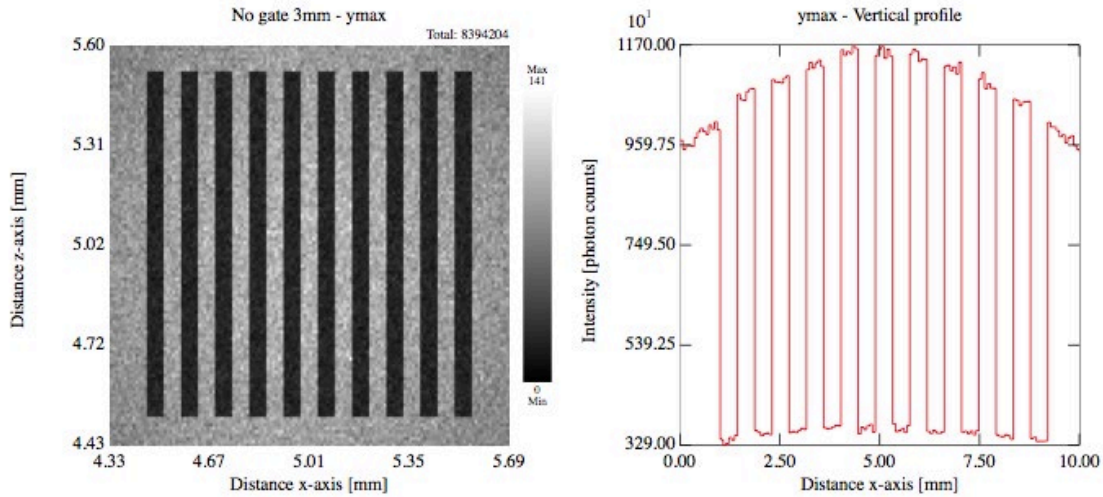


Figure 4.28 Intensity-based image and spatial profile of the photon count at the detector

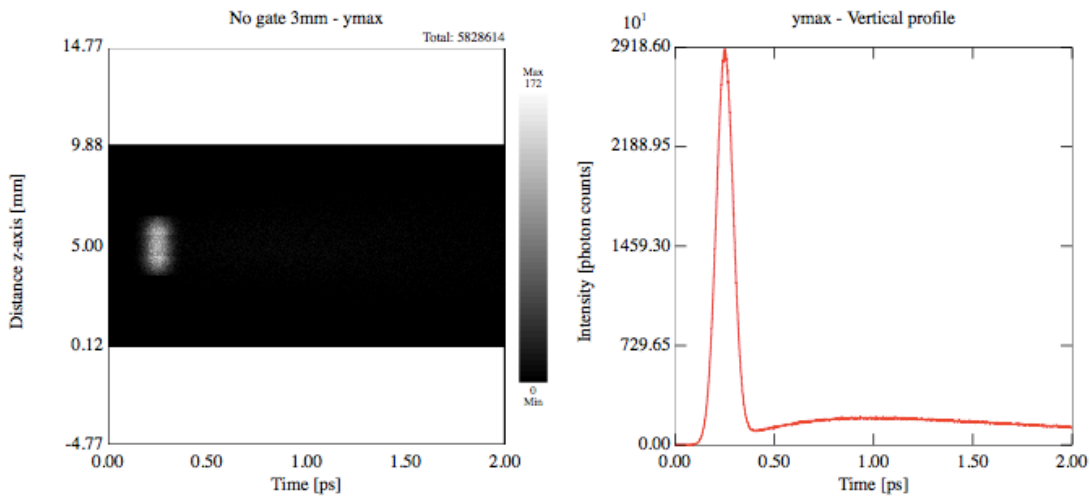


Figure 4.29 Spatial and temporal intensity profile of the photon count at the detector – temporal profile of photon count at the detector

4.2.6.2 Time-gated – aggressive spatial filter

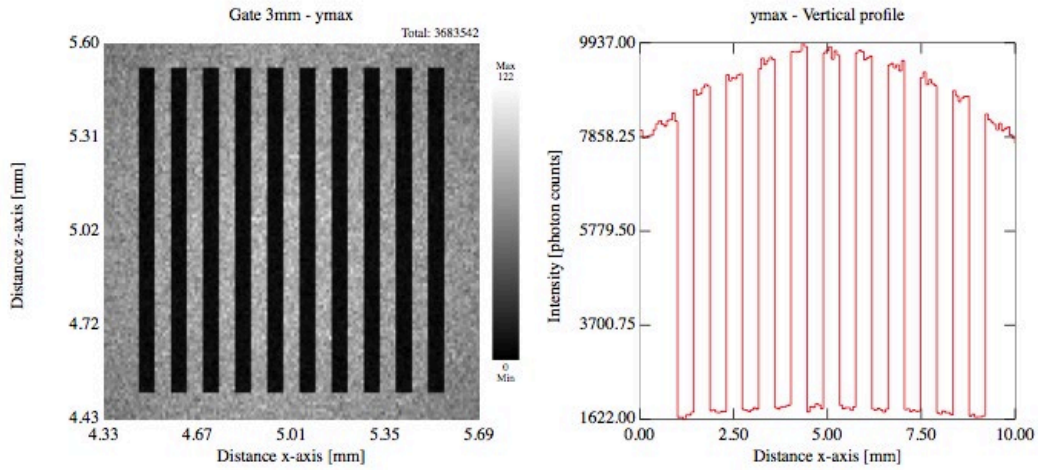


Figure 4.30 Intensity-based image and spatial profile of the photon count at the detector

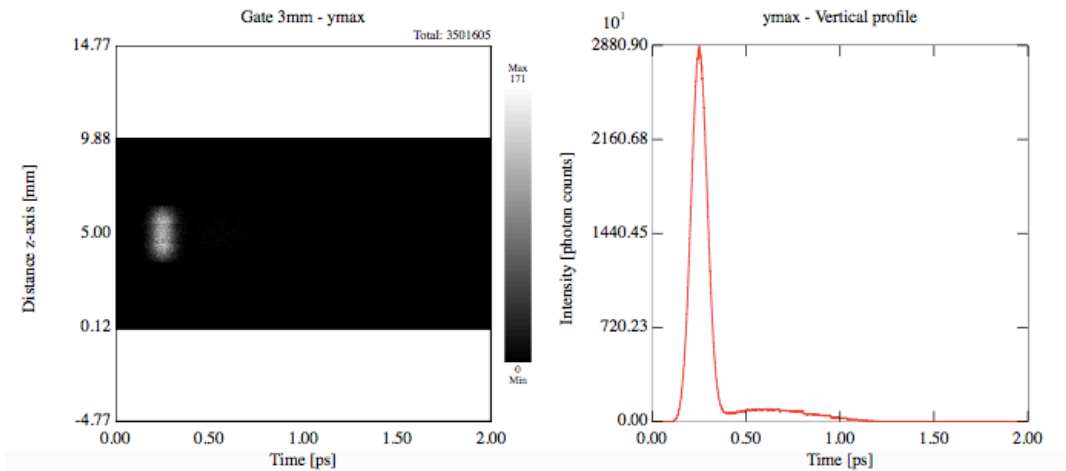


Figure 4.31 Spatial and temporal intensity profile of the photon count at the detector – temporal profile of photon count at the detector

4.2.6.3 Ballistic photons – aggressive spatial filter

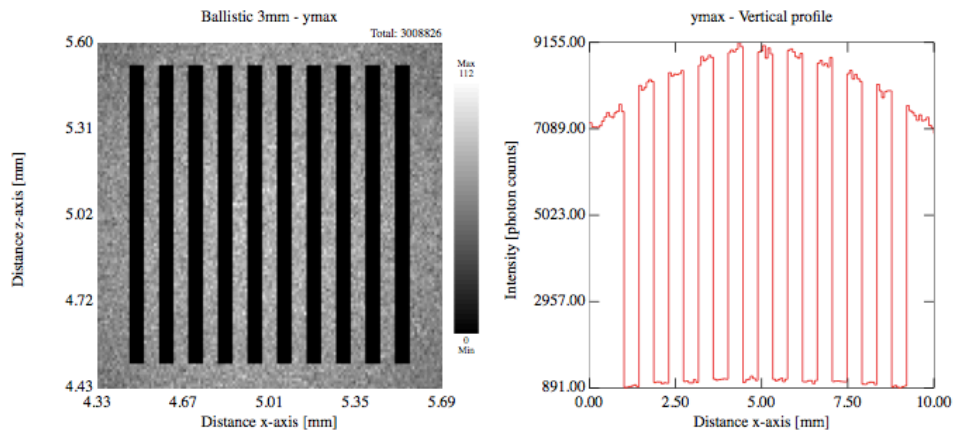


Figure 4.32 Intensity-based image and spatial profile of the photon count at the detector

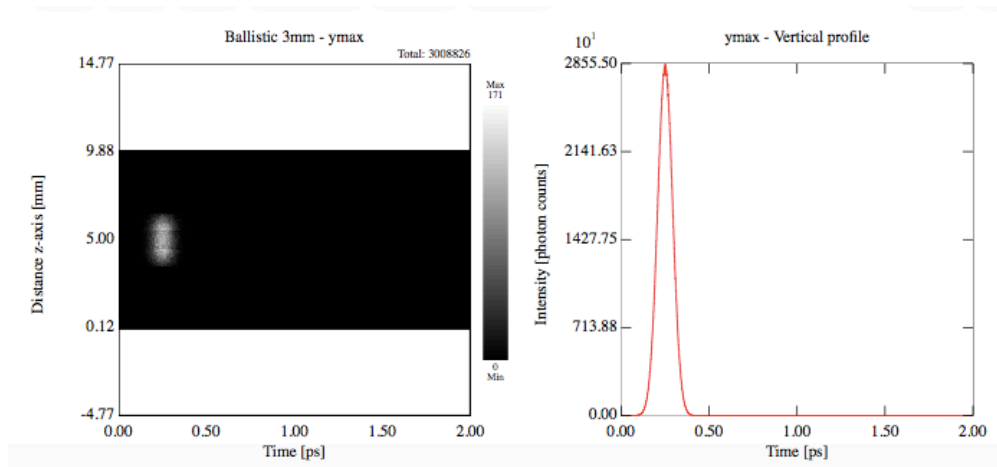


Figure 4.33 Spatial and temporal intensity profile of the photon count at the detector – temporal profile of photon count at the detector

4.2.7 Simulations 3 and 4 – Observations

The simulations at OD 10 show a severe temporal elongation of the imaging pulse, due to the dense scattering environment. The original 100 fs pulse stretches to more than 2 ps by the time it reaches the camera sensor, with the highest photon count at the 1 ps mark. In this harsher scattering environment, soft spatial filtering fails at rejecting the tail of delayed photons, with a total pulse elongation that well exceeds 2 ps as shown in Figure 4.23. The picosecond time gate, simulated to mimic an OKE CS₂ gate, rejects a substantial amount of this tail of photons effectively “cutting” the tail at the 1 ps mark, but it still delivers an image with poor contrast and strong noise as shown in Figure 4.25. The results suggest that in order to effectively time-gate most “snake” photons a time gate transmission window **faster or equal to 500 fs** would be appropriate. This result agrees with the findings of the BI diesel spray community that ultimately focused on using fs scale time gates that employ second harmonic generation or a combination of multiple Kerr gates [18], at the expense of transmissivity in the first case and layout complexity in the latter.

In the OD 10 results where an aggressive, 3 mm spatial filter is applied at the lens plane, we see that spatial filtering is contributing to a considerable improvement in image quality making time gating appear redundant. The pulse stretching is minimal since the

aggressive spatial filtering is excluding all those photons that are scattered multiple times, traveled a longer distance, and arrived at the detector with a trajectory that is incompatible with clearing the small 3 mm aperture. These results corroborate Ziaee's findings [11], where he experimentally observed that for ultra-short pulse off-axis digital holography coherence filtering and spatial filtering are overall more effective than time gating. This does not mean that aggressive spatial filtering will always be advantageous with respect to time gating when imaging at high OD values, as it could, as described earlier, cause a loss in resolution affecting the higher spatial frequencies. Nevertheless, these simulations suggest that spatial filtering should always be attempted before time-gating when imaging in harsh scattering conditions, and if time-gating is necessary, a gate that matches the duration of the imaging pulse is ideal. However, no shutter, OKE time-gate, second harmonic generation gate or combination of OKE time-gates can be as short as the 100 fs imaging pulse, and this is why we decided to explore holography's interferometric approach to time-gating, also called "coherence filtering." If the elongated pulse interferes with a reference pulse that did not travel through the scattering media, the only portion of the two pulses that can interfere coherently is composed by the ballistic photons of the imaging pulse and the whole reference pulse. An image can be numerically reconstructed from this interference pattern retaining only the information

conveyed by the ballistic photons. This approach eliminates the need for a physical time-gate device and provides a “virtual” coherence gate that always matches the original imaging pulse duration, and should deliver optimal noise reduction performance.

4.3 Comparison with experimental results

The simulations presented above directly match the experiments presented by Ziaee [11], where he compared the scattering rejection performance of picosecond time-gating, spatial and coherence filtering. A summary of his findings that are relevant to our simulations is shown in Figure 4.34.

As the medium OD increases, aggressive spatial filtering can still deliver a usable image at OD=10, while no target can be recognized in the ps time-gated results even averaging 500 exposures. This corroborates the main findings from the simulations presented in this chapter, i.e., that no time gate slower than 500 fs can effectively reject multiple-scattering photons at OD=10, and that aggressive spatial filtering performs better than ps time-gating at those conditions. A direct comparison between ps time-gating and coherence filtering is shown in Figure 5.17.

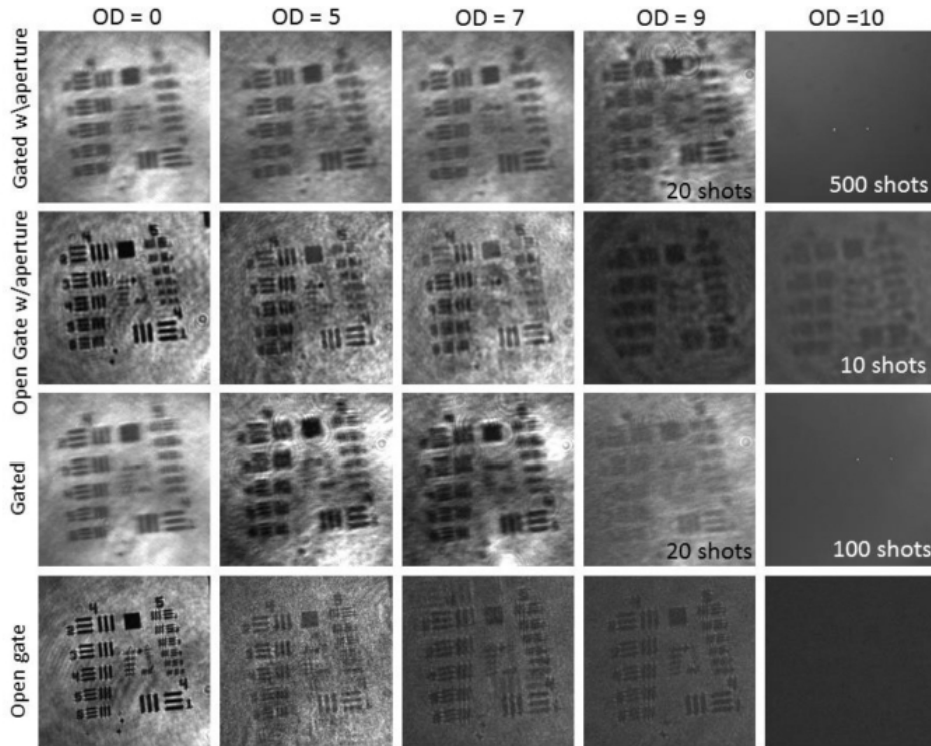


Figure 4.34 Kerr effect ballistic imaging of group 4 USAF resolution target through 0.6-micron scattering particles media of various optical depths at 'open gate' and Kerr gated' modes. Notice how the 2nd row where only spatial filtering is applied provides substantial noise reduction, comparable to the one offered by time gating [11]

4.4 Section summary

The photon transport simulations results presented in this chapter show that in order to efficiently separate ballistic photons from multiple scattering ones when imaging with short and ultra-short pulses at optical depth values representative of the primary atomization region of fuel sprays; higher image contrast is obtained when the duration of the incident pulse matches with the time-gate applied, or when the time gate has a

temporal resolution of at least 150 fs. These results confirm previous literature findings that described the necessity for a 300 fs time-gate in order to successfully image fluid structures in the near nozzle region of a fuel spray [18]. When using a CS₂ Kerr cell, with a time gate comprised between 1 and 2 picoseconds, we found that using an ultra-fast imaging source is therefore superfluous [60], furthermore the experimental results presented in this chapter show that at high OD values the benefit of ps Kerr-effect time gating with respect to simple spatial filtering is not clear. This further confirms the ineffectiveness of ps time gates paired up with a fs light source for dense spray imaging, as suggested by literature [18], our photon transport simulations (section 4.2), and our experimental results (4.3). Matching pulse length and time gate width generally delivers the best noise reduction outcome, together with using an ultra-fast source and time-gate. These conditions are always verified when using USPODH and coherence filtering because the time gate width is exactly the width of the original 100 fs imaging pulse. Creating fs scale time gates to be used in ballistic imaging requires using specialty SHG nonlinear crystals [51], while the holographic configuration dramatically reduces the system complexity by removing the time-gate component but requires an extra reference beam. Furthermore, holography can offer 3D imaging and has the potential of delivering

quantitative information about the target field thanks to its retention of light phase information, as will be shown in the next chapters.

Even though Berrocal et al. [60] conclude from their ballistic imaging simulations that a picosecond pulse might work just as well when paired with a picosecond gate in filtering out higher scattering order photons, this does not match our experimental experience in digital holography where pulse stretching (the duration of a pulse after leaving the scattering media) and the consequent broadening of the coherence length causes the reconstructed images to be of worse quality when using picosecond pulses in highly scattering media. This might be because when using a longer pulse that is further broadened in time by the scattering media, because of the longer coherence length we end up detecting a more considerable amount of higher scattering order photons that negatively affect SNR.

Chapter 5

5 Femtosecond off-axis digital holography

This chapter gives the reader the theoretical foundations of holography and digital holography. The reader is introduced first to the fundamentals of hologram formation and reconstruction and then shown both mathematically and experimentally why off-axis digital holography is preferable to inline holography when imaging in highly scattering environments, such as fuel sprays. Coherence filtering and its advantages are then introduced, and a comparison between ballistic imaging and digital holography reconstructed images at different OD values is made (section 5.8). A more detailed description of holographic theory can be found in the following selection of textbooks: “Digital Holography” by Schnars and Jueptner [59] for a clear overview of digital holography, “Introduction to Fourier Optics” by Goodman [60] for hologram formation and reconstruction theory, and “Introduction to Modern Digital Holography” by Poon [61] for implementing digital holography reconstruction algorithms using Matlab.

As was shown in the previous chapter the atomizing spray diagnostics research community agrees that (aside from synchrotron sourced x-rays) optical Kerr effect (OKE) time-gated ballistic imaging is the only optical technique suitable to image the primary atomization region of dense sprays (OD 5-15) [18]. Hence, the LFA Research group at UC Irvine first attempted picosecond ballistic imaging in dense media [61]. Pursuing the goal of optimal scattering noise rejection, this research evolved towards picosecond time-gated digital holography and then femtosecond off-axis digital holography without Kerr gating. USPODH can be seen as an example of ballistic imaging that takes advantage of coherence filtering in lieu of time gating while providing the possibility to reconstruct the target field in 3D. This chapter gives the details of the holographic imaging methodology, and the following ones will show the high potential of USPODH for microscopic imaging through highly scattering media. Resolution and image quality are comparable or superior to what the best OKE time-gated ballistic imaging setups have achieved.

Holograms are recorded interference patterns of electromagnetic waves. In digital holography a digital camera is used in place of a photographic film in order to record this interference pattern. The original hologram can be reconstructed by using a computer to back solve the electromagnetic wave transport equation. The peculiarity of holography is

that the reconstructed object beam is identical to the original object beam, thus allowing us to recover information belonging to different depth planes of the object. In digital holography numerical reconstruction and recovery of all the information contained in the original object beam is possible thanks to the reversibility of Maxwell's equations governing the propagation of light: phase and intensity information at any plane can be recovered, thus allowing images at different distances from the camera sensor.

Figure 5.1 shows a typical setup for recording a traditional hologram. Light with sufficient coherence length is split into two partial waves with a beam splitter (BS in the figure). The first wave, the object beam, illuminates the object. The object wave is then scattered at the object surface and reflected onto the recording medium (a photographic film in this case, but it could be a CCD or CMOS sensor as well). The other wave, referred to as the reference wave, simultaneously illuminates the recording medium directly. The interference pattern, or hologram, is thereby recorded.

In traditional holography, the original object wave is reconstructed by illuminating the hologram with the original reference wave, as shown in Figure 5.2. The observer then sees a virtual image which is indistinguishable from the original object since the light been

seen mimics precisely the light that had been scattered from the object. The image exhibits all the effects of perspective and depth of focus.

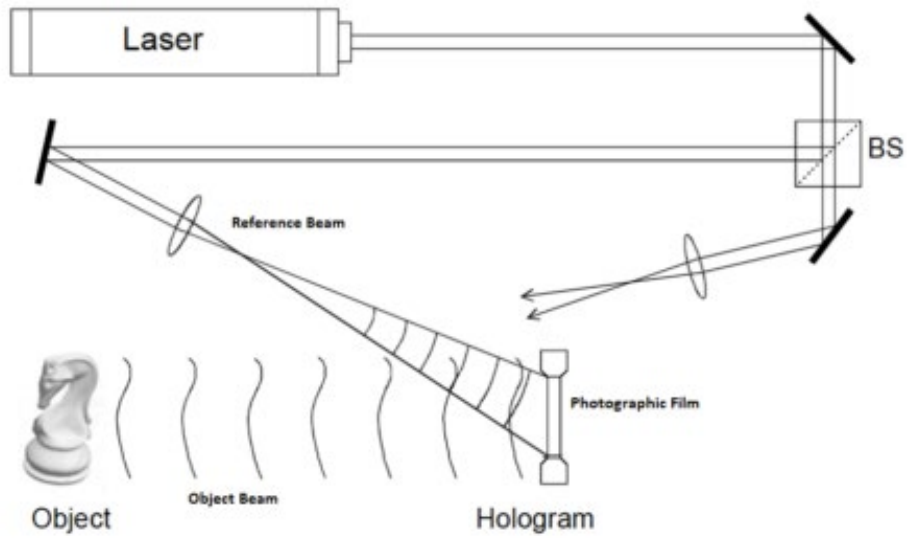


Figure 5.1 Recording a traditional hologram, the laser beam is split into a reference beam and an object beam. The object beam after being reflected from the object interferes with the reference beam and creates an interference pattern which is called hologram. [62]

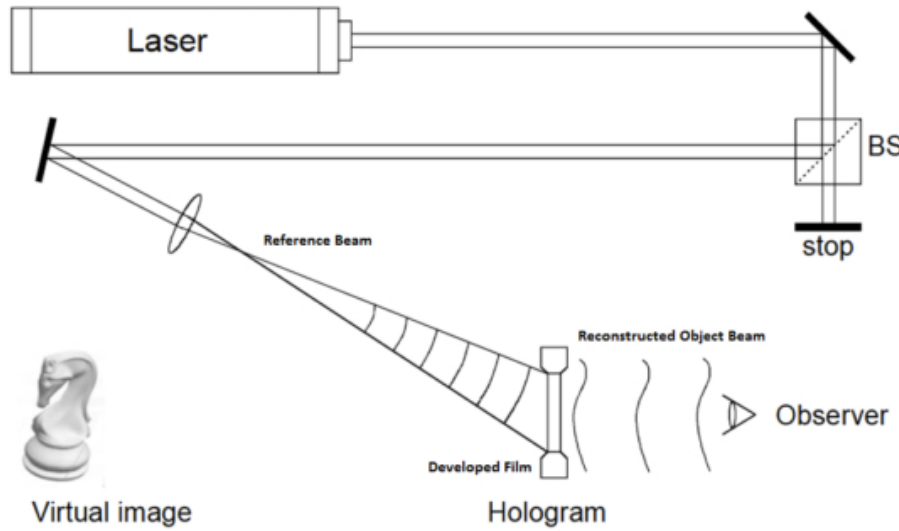


Figure 5.2 Reconstruction of a traditional hologram: the photographic film over which the hologram was recorded is illuminated by the original reference beam. The reference beam is diffracted by the hologram reconstructing the

original object beam. The observer can now see the object identical to the original one both in shape and position. [62]

5.1 Interference

Holography can be described by light diffraction and interference phenomena, which can only be explained when considering light as an electromagnetic wave. The appropriate theory is, therefore, the wave model of light, within the theory of classical electromagnetism. The electromagnetic wave equation in a vacuum, which is derived from Maxwell's equations is

$$\nabla^2 \vec{E} - \frac{1}{c^2} \frac{\partial^2 \vec{E}}{\partial t^2} = 0$$

Where \vec{E} is the electric field, t is time, c is the speed of light in vacuum and ∇^2 is the Laplace operator.

\vec{E} could vibrate in any direction perpendicular to light's propagation direction, in our case we will deal with polarized light sources, where the electric field vibrates in a single plane. Therefore, we can write the scalar wave equation, for a polarized light wave traveling in z -direction, as

$$\frac{\partial^2 E}{\partial z^2} - \frac{1}{c^2} \frac{\partial^2 E}{\partial t^2} = 0$$

A solution to the scalar wave equation can be described by a harmonic, linearly polarized plane wave as

$$E(x, y, z, t) = a \cos(\omega t - \vec{k}\vec{r} - \varphi_0)$$

Where $E(x,y,z,t)$ is the electric field vector modulus at point (x,y,z) and time t , a is the amplitude, ω is the angular frequency of the wave, and it relates to the light wave frequency f by a multiplying factor of 2π

$$\omega = 2\pi f$$

Light frequency is related wavelength by the well-known relation

$$c = \lambda f$$

\vec{k} is the wave vector indicating the wave's propagation direction

$$\vec{k} = k\vec{n}$$

Where \vec{n} is a unit vector in the wave's propagation direction. The modulus of \vec{k} is defined as the wavenumber and it is expressed as

$$|\vec{k}| \equiv k = \frac{2\pi}{\lambda}$$

The lightwave phase is the spatial varying term

$$\varphi = -\vec{k}\vec{r} - \varphi_0$$

where φ_0 is the initial wave phase. Points of equal phase are located on parallel planes, perpendicular to the propagation direction.

CCD sensors, similarly to the human eye, can only detect light intensity. Intensity (I) is a scalar quantity that represents the time average of the energy which passes in space through a unit area per unit time, proportional to the time average of the electric field

$$I = \varepsilon_0 c \langle E^2 \rangle_t = \varepsilon_0 c \lim_{T \rightarrow \infty} \frac{1}{2T} \int_{-T}^T E^2 dt$$

$\langle \rangle$ means time average over many light wave periods while ε_0 is the vacuum permittivity. Substituting E with its harmonic, linearly polarized plane wave description

$$I = \varepsilon_0 c a^2 \langle \cos^2(\omega t - \vec{k}\vec{r} - \varphi_0) \rangle_t = \frac{1}{2} \varepsilon_0 c a^2$$

So the light intensity is proportional to the square of the light wave amplitude. The scalar wave function can be written as a complex exponential

$$E(x, y, z, t) = a \exp(i(\omega t - \vec{k}\vec{r} - \varphi_0))$$

The spatial and temporal part can be factorized

$$E(x, y, z, t) = a \exp(i\varphi) \exp(i\omega t)$$

The spatial part of the electric field has complex amplitude

$$A(x, y, z) = a \exp(i\varphi)$$

Intensity can then be calculated by taking the square of the modulus of the complex amplitude

$$I = \frac{1}{2} \varepsilon_0 c |A|^2 = \frac{1}{2} \varepsilon_0 c A^* A = \frac{1}{2} \varepsilon_0 c a^2$$

Where $*$ is the conjugate complex. The intensity's absolute value is unimportant in many applications, and so the scaling factor $\frac{1}{2}\epsilon_0$ can be neglected. The intensity is then simply calculated as

$$I = |A|^2$$

Holograms are the recorded interference pattern of two different light waves: the object wave, that is modulated by the target (in our case the fuel spray), and the reference wave. If both waves from a coherent light source travel the same distance then an interference pattern is created at the camera sensor. Each wave i can be described by $\vec{E}_i(\vec{r}, t)$, which is a solution to the wave equation, and, since the wave equation is a linear differential equation, the superposition of multiple solutions is a solution as well

$$\vec{E}(\vec{r}, t) = \sum_i \vec{E}_i(\vec{r}, t) \text{ where } i=1,2, \dots$$

When recording a hologram, the object and reference wave are monochromatic, have the same wavelength and the same polarization direction. This allows us to describe the complex amplitudes of the waves as

$$A_1(x, y, z) = a_1 e^{i\varphi_1}$$

$$A_2(x, y, z) = a_2 e^{i\varphi_2}$$

The resulting amplitude of the interference pattern can be calculated by the sum of the two waves (object and reference)

$$A = A_1 + A_2$$

We can then write the intensity I as

$$\begin{aligned} I &= |A_1 + A_2|^2 = (A_1 + A_2)(A_1 + A_2)^* \\ &= a_1^2 + a_2^2 + 2a_1a_2 \cos(\varphi_1 - \varphi_2) \\ &= I_1 + I_2 + 2\sqrt{I_1I_2} \cos \Delta\varphi \end{aligned}$$

The intensity of the interference pattern is the sum of the intensity of the individual waves plus a term dependent on the phase difference between the two waves. Notice that the overall intensity will reach a maximum in all points where this difference makes the value of $\cos \Delta\varphi=1$, and it is in those points that we will have constructive interference.

Constructive interference occurs when

$$\Delta\varphi = 2n\pi \quad \text{for } n=0,1,2, \dots$$

The intensity will reach its minimum in all points where $\cos \Delta\varphi = -1$, which is destructive interference. This is verified when

$$\Delta\varphi = (2n + 1)\pi \quad \text{for } n=0,1,2, \dots$$

Therefore, the interference pattern consists of dark and bright fringes caused by the alternating constructive and destructive interference between the object and reference wave. If the two waves interfere at an angle θ , which is the case for off-axis holography, we obtain an interference pattern with constant spacing

$$d = \frac{\lambda}{2 \sin \frac{\theta}{2}}$$

The fringe spacing d is the distance between two successive dark (or light) fringes in the interference pattern of two planar wavefronts having an identical wavelength λ and an angle θ between their propagation directions. The distance d can be interpreted as a spatial frequency f

$$f = \frac{1}{d} = \frac{2}{\lambda} \sin \frac{\theta}{2}$$

5.2 Coherence

In order to generate an interference pattern, two waves must retain a specific correlation between their phases, and this is called coherence or the ability of light to interfere. Coherence can be separated into temporal and spatial coherence aspects. Temporal coherence describes the correlation of a wave with itself at different instants in time while spatial coherence describes the correlation of different parts of a wavefront.

5.2.1 Temporal Coherence

Temporal coherence can be demonstrated and quantified using a Michelson interferometer, where light emitted from a single laser source is split by a beam splitter (BS in Figure 5.3). The two resulting waves travel to two mirrors on the two separate arms of the interferometer, where they are reflected, recombined at the beam splitter, and

superimposed on a screen. They interfere on the screen at a small angle, creating a 2D interference pattern. If we define the pathlength from the beam splitter to the first mirror as l_1 and the path from the beam splitter to the other mirror as l_2 , the experiment shows that we will observe interference only when $l_1 - l_2$ does not exceed a specific length L . This is because the light source emits wave trains of finite length L , if the pathlength difference exceeds L the partial waves do not overlap with a constant phase relation and cannot interfere.

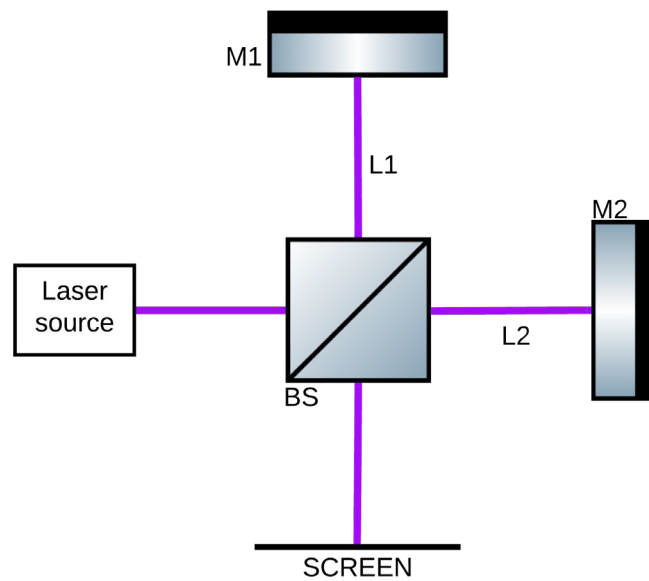


Figure 5.3 Michelson interferometer

The wave train length L is called *coherence length*, and it is related to the wave train emission time (coherence time) by

$$\tau = \frac{L}{c}$$

The Ti:Sapphire laser used for USPODH emits 100 fs wave trains. This means that the coherence length is

$$L = c * \tau = c * 100fs = 30 \mu m$$

Hence, any photon belonging to the object beam with a pathlength that is more than 30 μm different from that of the reference beam will not be able to interfere and contribute information to the hologram. This small coherence length property is fundamental for having successful coherence filtering, a topic that will be covered in section 5.8. In order to be able to record a hologram with optimal contrast, the object and reference beam need to be pathlength matched within a fraction of the coherence length, so USPODH requires very fine adjustment precision.-Ultrashort pulses from mode-locked lasers have a temporal profile that can be described by a Gaussian function, assuming that the pulse has no chirp (time dependence of its instantaneous frequency). Knowing the pulse duration τ_p at FWHM we can calculate the optical bandwidth of the imaging pulse

$$\Delta\nu \approx \frac{0.44}{\tau_p} = \frac{0.44}{100 fs} = 4.4 THz$$

Which is equivalent to a pulse optical spectrum of 2.35 nm. This is relevant information because the Fresnel-Kirchhoff diffraction approximation described next and used for the hologram recording and reconstruction process is valid for monochromatic light, which is a

reasonable assumption given the relatively narrow optical spectrum of our imaging pulse. It is also interesting to note that while the spectrum is sufficiently monochromatic for holography, the short pulse laser has a fairly broad spectrum in comparison to longer pulse and continuous wave lasers, so some of the spurious noise interference patterns seen with those lasers are reduced.

5.2.2 Spatial Coherence

Spatial coherence describes the relationship between different parts of the same wavefront.

Spatial coherence is measured and demonstrated by the Young interferometer.

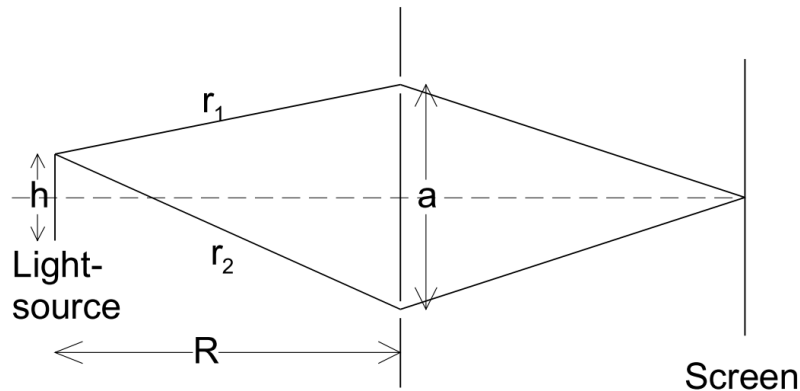


Figure 5.4 Young interferometer [62]

A single, extended, light source emits light from two different points (two slits in an aperture in the Young interferometer); light waves from each source travel to a screen where they can interfere and display fringes if the distance between the two sources is below the coherence distance a_k . The pathlength from each source point to the screen is

different for each point on the screen, and therefore each wave from different sources could either create an intensity maximum or minimum at any point on the screen depending on its pathlength. Usually, the contribution from each source compensates for each other, and no fringes can be observed. This compensation process does not happen when

$$r_2 - r_1 < \frac{\lambda}{2}$$

This condition is satisfied for all points of the light source if it is satisfied for the two points at the light source's ends

$$r_1^2 = R^2 + \left(\frac{a-h}{2}\right)^2 \quad r_2^2 = R^2 + \left(\frac{a+h}{2}\right)^2$$

Where h is the light source's width. It can be assumed that $a \ll R$ and $h \ll R$ so

$$r_2 - r_1 \approx \frac{ah}{2R}$$

We know that $r_2 - r_1 < \frac{\lambda}{2}$, therefore

$$\frac{ah}{2R} < \frac{\lambda}{2}$$

The critical limit for which this is satisfied or the coherence distance is

$$\frac{a_k h}{2R} = \frac{\lambda}{2}$$

The spatial coherence depends on both the light source properties and interferometer geometry.

5.3 Diffraction

Digital holographic reconstruction relies on the analysis of diffracted light. Consider a light wave hitting an opaque obstacle with transparent holes and a screen placed past the obstacle. If the diameter of the holes is comparable to the light wave wavelength, the shadow cast on the screen does not have sharp edges, but a pattern of dark and bright regions can be observed. This is caused by diffraction and can be interpreted through the Huygens' principle, which states that *every point of a wavefront can be considered as a source for secondary spherical waves called wavelets. The wavefront at any other location can be found as the coherent superposition of these wavelets.*

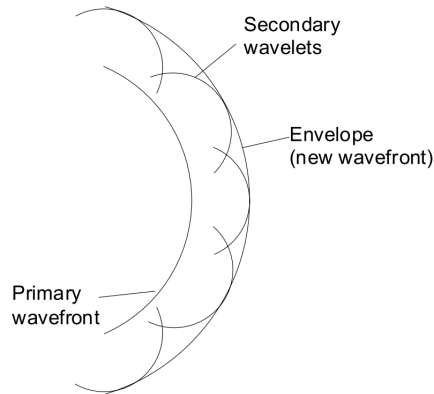


Figure 5.5 Huygens' principle [62]

This principle is described quantitatively by the Fresnel-Kirchhoff integral [63]

$$\Gamma(\varepsilon', \eta') = \frac{i}{\lambda} \iint_{-\infty}^{\infty} A(x, y) \frac{\exp\left(-i \frac{2\pi}{\lambda} \rho'\right)}{\rho'} Q dx dy$$

$$\rho' = \sqrt{(x - \varepsilon')^2 + (y - \eta')^2 + d^2}$$

$$Q = \frac{1}{2}(\cos \theta + \cos \theta')$$

Where $\Gamma(\varepsilon', \eta')$ is the wavefield in the observation screen plane, $A(x, y)$ is the complex amplitude in the plane of the aperture and ρ' is the distance between a point in the aperture plane and a point in the screen plane (refer to the reference system in Figure 5.6). The factor Q prevents the integral from describing nonphysical situations where light rays would travel backward from the aperture to the source; θ is the angle between the incident ray at the aperture and the vector normal to the aperture plane; and θ' is the angle between the normal vector and the diffracted light ray emerging from the aperture. Q approaches zero for $\theta \approx 0$ and $\theta' \approx \pi$.

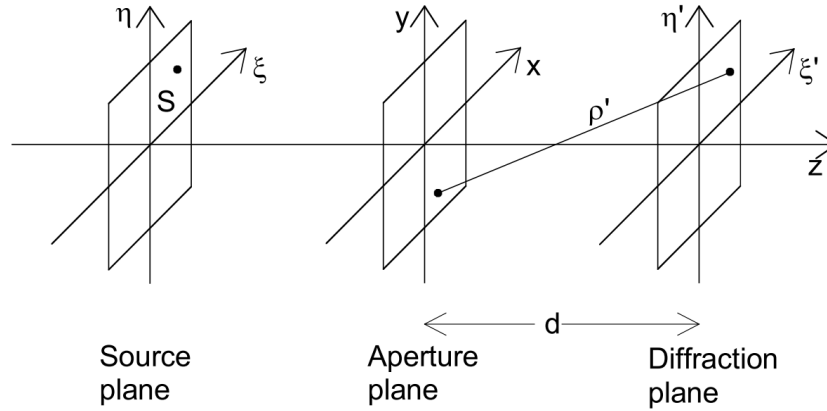


Figure 5.6 Reference system [62]

Referring to Figure 5.6, the spherical light waves emitted by the source S create a complex amplitude $A(x,y)$ in the aperture plane, where a hole is placed with coordinates (x,y) . This hole is the source of secondary wavelets that coherently superimpose at the diffraction plane. The Fresnel-Kirchhoff integral shows how the wavefield at the point (ξ',η') in the diffraction plane is proportional to the field at the source side of the aperture $A(x,y)$ and to the field created by the spherical wavelet from the source point (x,y) . If a more realistic aperture plane with multiple sources is considered, then the wavefield at the diffraction plane will be the integral over all-spherical wavelets emerging from the aperture plane. A hologram is a recording of a diffraction pattern in the diffraction plane, and through the reconstruction process we are able to reconstruct the intensity-based image of the object in the aperture plane that created the diffraction pattern.

5.4 Hologram recording and reconstruction

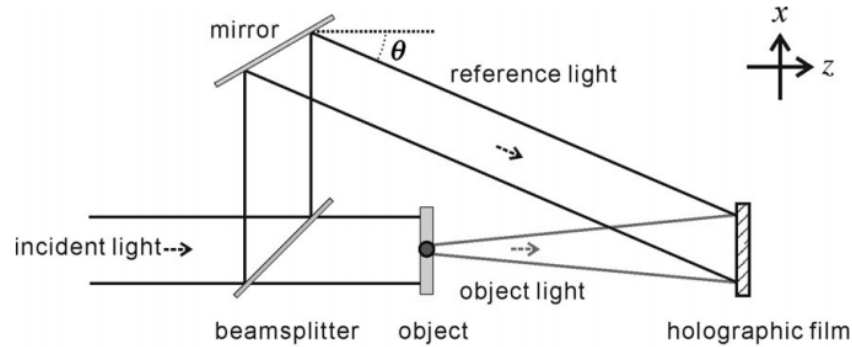


Figure 5.7 Recording setup for off-axis holography [64]

A typical setup for recording a hologram is shown in Figure 5.7. Light from a coherent light source is split using a beam splitter into an object and a reference wave. The object wave scatters and diffracts off the target and then reaches the recording medium, while the reference wave illuminates the recording medium directly. The interference pattern is recorded, and this recording is the hologram. If the hologram is illuminated by the reference wave, then an observer will be able to see the virtual image.

The following describes the formation and reconstruction process using the same formalism as the previous sections.

The complex amplitude of the object and reference wave are

$$E_o(x, y) = a_o(x, y)\exp(i\varphi_o(x, y))$$

$$E_R(x, y) = a_R(x, y) \exp(i\varphi_R(x, y))$$

Where E_O is the complex amplitude of the object wave and E_R is the complex amplitude of the reference wave, and a and φ are their respective real amplitude and phase. If the two waves interfere at the surface of the camera sensor or any other recording media, then the calculated intensity is

$$\begin{aligned} I(x, y) &= |E_O(x, y) + E_R(x, y)|^2 = (E_O(x, y) + E_R(x, y))(E_O(x, y) + E_R(x, y))^* \\ &= E_R(x, y)E_R^*(x, y) + E_O(x, y)E_O^*(x, y) + E_O(x, y)E_R^*(x, y) \\ &\quad + E_R(x, y)E_O^*(x, y) \end{aligned}$$

The hologram on a photographic plate that is used in traditional holography to record the hologram and later reconstruct the object beam wavefront is a transparent plate with a transmission function proportional to the intensity of the recorded interference pattern at each point

$$h(x, y) = h_0 + \beta\tau I(x, y)$$

where h is the transmission at point (x, y) of the developed film, h_0 is the transmission of the un-illuminated points of the film after development, β is a constant and τ is the exposure time. In digital holography h_0 can be neglected. As mentioned earlier, in traditional film holography, reconstructing the object beam wavefront is accomplished physically by illuminating the developed film with the reference beam. In digital holography, reconstruction is performed by numerically propagating the diffraction

pattern generated by illuminating the hologram interference pattern with the reference.

Mathematically this means we multiply the amplitude transmission function by the

complex amplitude of the reconstructing wave, which is the reference wave:

$$E_R(x, y)h(x, y) = (h_0 + \beta\tau(a_R^2 + a_O^2))E_R(x, y) + \beta\tau a_R^2 E_O(x, y) + \beta\tau E_R^2(x, y)E_O^*(x, y)$$

The expression of the reconstructed wavefront has three terms representing:

- DC term - the first term on the right-hand side (RHS) of the equation. It is the reference wave E_R multiplied by a factor; it represents the undiffracted wave passing the hologram (zero diffraction order).
- Cross-correlation term - the second term on the RHS is the reconstructed object wave which forms the virtual image. The real factor $\beta\tau a_R$ influences the brightness of the image, showing how in digital holography it is possible to obtain a bright, well-contrasted image even with an extremely low signal from the object beam thanks to this “amplification” that is proportional to the reference wave real amplitude a_R .
- Conjugate cross-correlation term - the third term on the RHS generates a pseudoscopic real image of the object. In Gabor holography this image overlaps with the virtual image of the object affecting the usefulness of the reconstruction,

in off-axis holography this is separated from the virtual image both spatially and in the frequency domain.

The three terms described above are shown in the frequency domain in Figure 5.8, in the case of an off-axis hologram. In off-axis holography the object beam and the reference beam propagate in different directions, so the virtual image, the real image, and the undiffracted wave are spatially separated and do not overlap each other in the frequency domain so long as the interference angle between object and reference wave is large enough; this separation gives a better quality reconstructed image without having to separate the waves using sophisticated image processing techniques. When the original reference wave is used for reconstruction, the virtual image appears at the position of the original object.

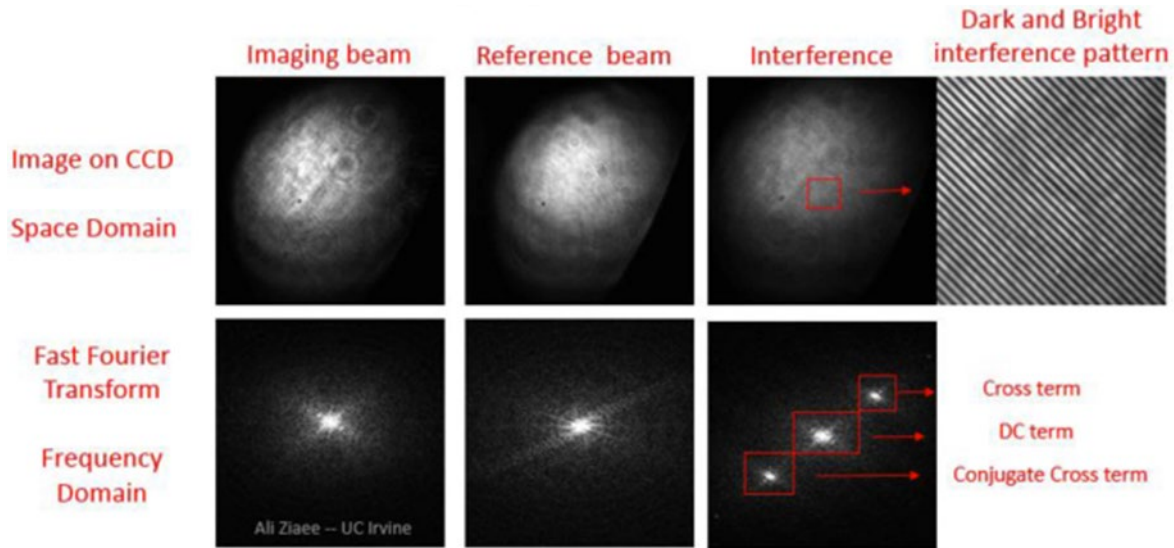


Figure 5.8 Interference pattern of object and reference beam in space and frequency domain. In off-axis digital holography cross term and conjugate cross term are separated in the frequency domain (bottom right picture) this allows to easily pick the cross term for reconstruction thus obtaining a reconstructed image of superior quality with respect to inline Gabor holography [11]

5.5 Numerical reconstruction of a digital hologram

When a hologram is optically reconstructed, a virtual image appears at the same position of the original object, at a distance d from the hologram plane. A real image is formed as well, at the same distance d from the hologram plane, but on the opposite side, as shown in Figure 5.9.

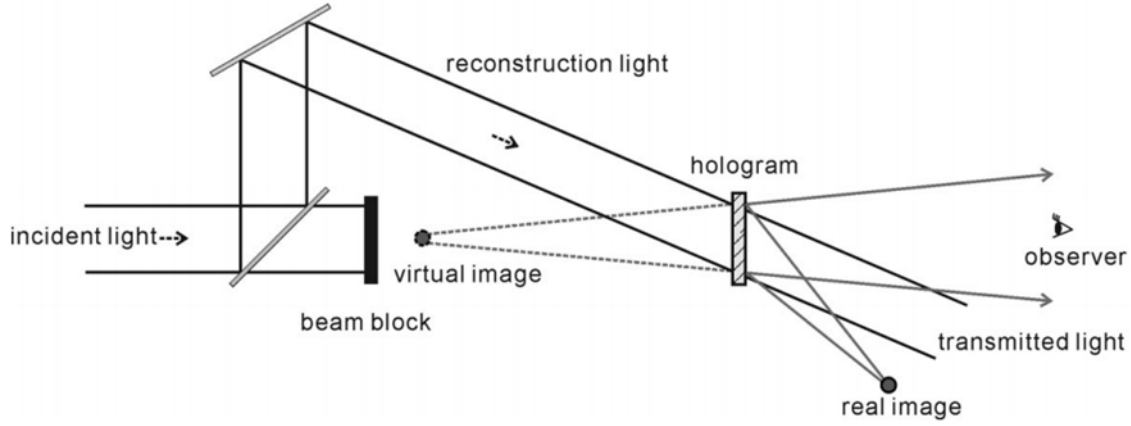


Figure 5.9 Reconstruction setup for off-axis holography [64]

The hologram acts as an aperture, and the diffraction of a light wave at an aperture that is perpendicular to the beam can be described by the Fresnel-Kirchhoff integral; therefore the reconstructed wave field expression is

$$\Gamma(\varepsilon', \eta') = \frac{i}{\lambda} \iint_{-\infty}^{\infty} h(x, y) E_R(x, y) \frac{\exp\left(-i \frac{2\pi}{\lambda} \rho'\right)}{\rho'} dx dy$$

$$\rho' = \sqrt{(x - \varepsilon')^2 + (y - \eta')^2 + d^2}$$

Where $h(x, y)$ is the hologram function and ρ' represents the distance between a point in the hologram plane and a point in the reconstruction plane (Figure 5.10). If the reference wave is a plane wave, then E_R is given by its real amplitude

$$E_R = a_R + i0 = a_R$$

The diffraction pattern is computed at a distance d from the hologram plane, and the complex amplitude of the object beam is numerically reconstructed in the real image

plane. The reconstructed wave field $\Gamma(\varepsilon', \eta')$ is a complex function, which means that even with only an intensity fringe pattern in the hologram, we can numerically reconstruct both intensity and phase. This capability, which is peculiar to digital holography and is not shared with its optical counterpart, allows valuable quantitative applications such as Digital Holographic Interferometry where the deformation of an object or the refraction index gradients through a gaseous media can be measured from the unwrapped phase information [65], [66]. As mentioned in section 5.4, the real image appears distorted (pseudoscopic). This can be avoided by reconstructing the hologram using the conjugate reference beam E_R^* (Figure 5.11)

$$\Gamma(\varepsilon', \eta') = \frac{i}{\lambda} \iint_{-\infty}^{\infty} h(x, y) E_R^*(x, y) \frac{\exp\left(-i \frac{2\pi}{\lambda} \rho\right)}{\rho} dx dy$$

$$\rho' = \sqrt{(x - \varepsilon)^2 + (y - \eta)^2 + d^2}$$

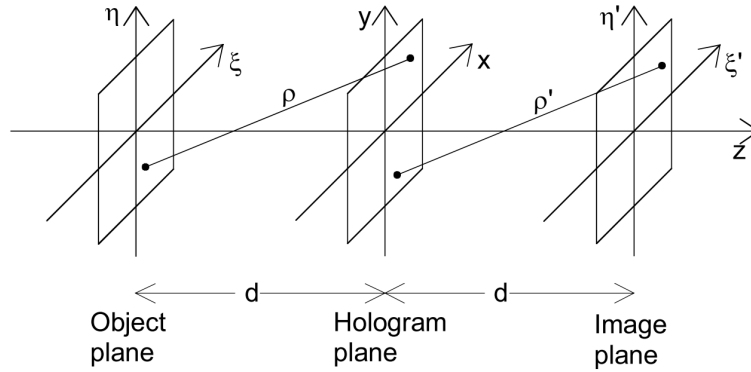


Figure 5.10 Coordinate system for numerical reconstruction of a hologram [62]

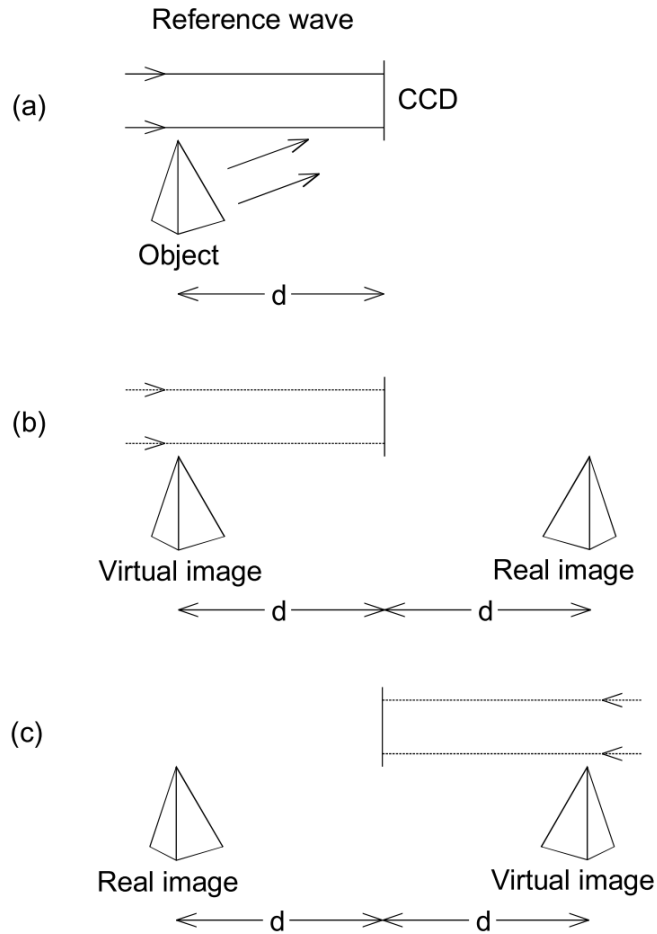


Figure 5.11 Digital holography (a) Recording (b) Reconstructing with reference wave E_R (c) Reconstructing with conjugate reference wave E_R^* [62]

The reconstruction of the virtual image can be performed by including the properties of a lens into the reconstruction algorithm. This lens corresponds to the eye lens of the observer looking through an optically reconstructed hologram and is located directly behind the hologram plane (Figure 5.12).

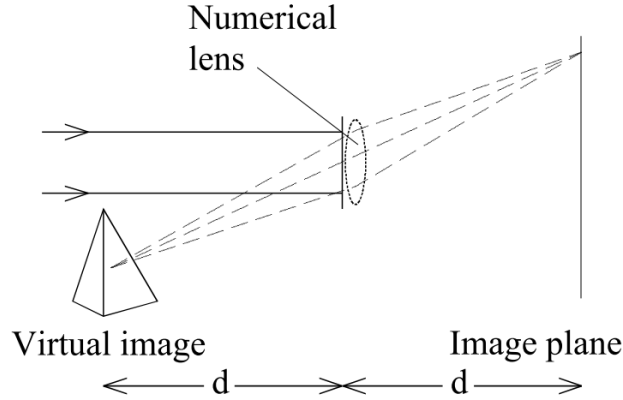


Figure 5.12 Layout for the reconstruction of the virtual image [62]

The imaging properties of a lens with focal length f can be described by a complex factor.

For a magnification of one we use a lens with $f=d/2$

$$L(x, y) = \exp \left[i \frac{\pi}{\lambda f} (x^2 + y^2) \right]$$

This lens will also cause phase aberration which must be corrected by multiplying the reconstructed wave field by a factor [62]

$$P(\varepsilon', \eta') = \exp \left[i \frac{\pi}{\lambda f} (\varepsilon'^2 + \eta'^2) \right]$$

So, the full equation describing the reconstructed wavefield for the reconstruction of the virtual image with a lens is

$$\Gamma(\varepsilon', \eta') = \frac{i}{\lambda} \iint_{-\infty}^{\infty} h(x, y) E_R^*(x, y) \frac{\exp\left(-i \frac{2\pi}{\lambda} \rho'\right)}{\rho'} dx dy$$

5.5.1 Convolution Approach or Angular Spectrum Method (ASM)

The numerical computation of the reconstructed wave field (Fresnel-Kirchhoff integral) without approximations is computationally costly. An equivalent formulation is known as the “convolution approach,” and also known as the “angular spectrum method,” is far more efficient. This formulation is implemented in the algorithm used for all holographic reconstructions presented in this dissertation and is part of the Holotool software that has been developed by Colin Dankwart and Ali Ziaee at the Laser Flames and Aerosols Research Group at UC Irvine [11]. As part of this dissertation, several improvements have been added to the Holotool software that will be discussed in chapter 10. We can interpret the wavefield reconstruction equation as a superposition integral

$$\Gamma(\varepsilon', \eta') = \frac{i}{\lambda} \iint_{-\infty}^{\infty} h(x, y) E_R^*(x, y) g(\varepsilon, \eta, x, y) dx dy$$

Where the impulse response $g(\varepsilon, \eta, x, y)$ is

$$g(\varepsilon, \eta, x, y) = \frac{i \exp \left[-i \frac{2\pi}{\lambda} \sqrt{d^2 + (x - \varepsilon)^2 + (y - \eta)^2} \right]}{\lambda \sqrt{d^2 + (x - \varepsilon)^2 + (y - \eta)^2}}$$

Where d is the reconstruction depth measured from the hologram plane. The linear system $g(\varepsilon, \eta, x, y) = g(\varepsilon - x, \eta - y)$ is space invariant, the superposition integral can be regarded as a convolution, and the convolution theorem applies. This means that the Fourier transform of the convolution of $h \cdot E_R^*$ with g is the product of their own transforms. Therefore to compute $\Gamma(\varepsilon', \eta')$ we take the inverse Fourier transform of the product between the transform of $h \cdot E_R^*$ and the transform of g , for a total of three Fourier transforms. The numerical impulse response function is

$$g(k, l) = \frac{i}{\lambda} \frac{\exp \left[-i \frac{2\pi}{\lambda} \sqrt{d^2 + \left(k - \frac{N}{2}\right)^2 \Delta x^2 + \left(l - \frac{N}{2}\right)^2 \Delta y^2} \right]}{\sqrt{d^2 + \left(k - \frac{N}{2}\right)^2 \Delta x^2 + \left(l - \frac{N}{2}\right)^2 \Delta y^2}}$$

Where $N \times N$ is the hologram size in pixels, Δx is the horizontal distance between adjacent pixels and Δy is the vertical distance between adjacent pixels. So, the wavefield reconstruction into the real image plane is

$$\Gamma(\varepsilon, \eta) = \mathfrak{F}^{-1}\{\mathfrak{F}(h \cdot E_R^*) \cdot \mathfrak{F}(g)\}$$

It is possible to skip one Fourier transform in the reconstruction process by calculating the analytical Fourier transform of $g(k, l) = G(n, m)$

$$G(n, m) = \exp \left\{ -i \frac{2\pi d}{\lambda} \sqrt{1 - \frac{\lambda^2 \left(n + \frac{N^2 \Delta x^2}{2d\lambda}\right)^2}{N^2 \Delta x^2} - \frac{\lambda^2 \left(m + \frac{N^2 \Delta y^2}{2d\lambda}\right)^2}{N^2 \Delta y^2}} \right\}$$

$$\Gamma(\varepsilon, \eta) = \mathfrak{F}^{-1}\{\mathfrak{F}(h \cdot E_R^*) \cdot G\}$$

When reconstructing the virtual image, as explained in the previous section, it is necessary to add a lens transmission factor $L(x, y)$ and a correction factor $P(\varepsilon', \eta')$

$$\Gamma(\varepsilon', \eta') = P(\varepsilon', \eta') \mathfrak{F}^{-1}\{\mathfrak{F}(h \cdot E_R \cdot L) \cdot G\}$$

When reconstructing using the convolution approach the pixel distance in the reconstructed images is the same as in the original hologram

$$\Delta\varepsilon = \Delta x \quad \Delta\eta = \Delta y$$

This represents a numerical resolution, while the physical image resolution is limited by diffraction

$$\Delta\varepsilon = \frac{\lambda d}{N\Delta x} \quad \Delta\eta = \frac{\lambda d}{N\Delta x}$$

5.6 Separation of virtual image, real image and dc term in off-axis holography

Gabor inline holography uses a single beam, as shown in Figure 5.13 and Figure 5.14. The part of the beam that is diffracted by the object acts as the object beam; the undiffracted part acts as the reference beam. This means that Gabor inline holography performs best when a considerable part of the beam is undiffracted, which is a condition that does not apply to turbid media where almost the entire beam is diffracted. Gabor holography assumes that the imaged object is highly transparent; if this assumption is not adopted an

additional wave component is generated and for a low transmittance target such as a dense spray, it can obliterate the weaker images. Therefore Gabor holography can create wavefront-reconstructed images of an object of opaque letters but not transparent letters on an opaque background, limiting its potential applications [63]. A more severe limitation of Gabor's holography applicability is the inseparability of the generated twin images, i.e. when the real image is brought into focus the same is true for the virtual image. Therefore the observer who focuses on the virtual image will also see a defocused image generated from the real image. This is especially true when the recording distance is short. Both these limitations have been addressed by using instead the Leith-Upatnieks configuration (developed in 1962 [67]), which is the off-axis hologram. By using a tilted reference beam (Figure 5.7) the real image is deflected off the object beam's optical axis by an angle approximately twice as large as the one between the reference and object wave. The tilted reference beam is described as

$$E_R = \exp\left(-i\frac{2\pi}{\lambda}x \sin \theta\right)$$

In off-axis holography, a separate reference wave is introduced in the recording process. By interfering object and reference waves at a small angle, a spatial frequency is applied to the signal in the form of an interference pattern. When taking the Fourier transform of an image containing any number of carrier frequencies these appear in the Fourier domain

as loci that are separated from the center of the image, where all the DC information is aggregated. This allows cropping of the cross-correlation term that is fed to the reconstruction algorithm to remove the multiple scattering noise that the conjugate cross-correlation and DC terms would convey to the image if they were to be included in the reconstruction [11].

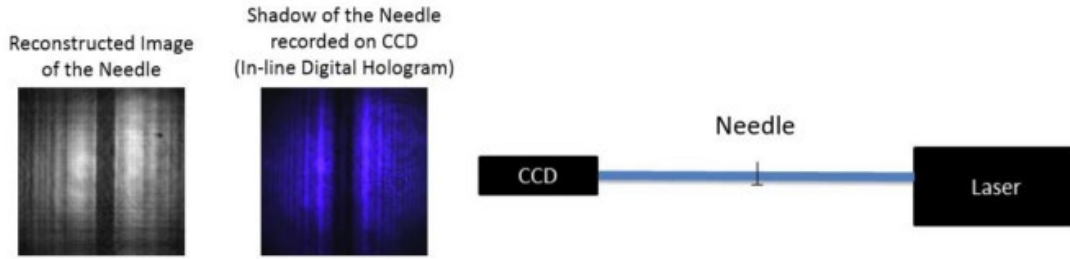


Figure 5.13 Digital Gabor Inline Holography setup, hologram and reconstructed image of a 400 micron needle [11].

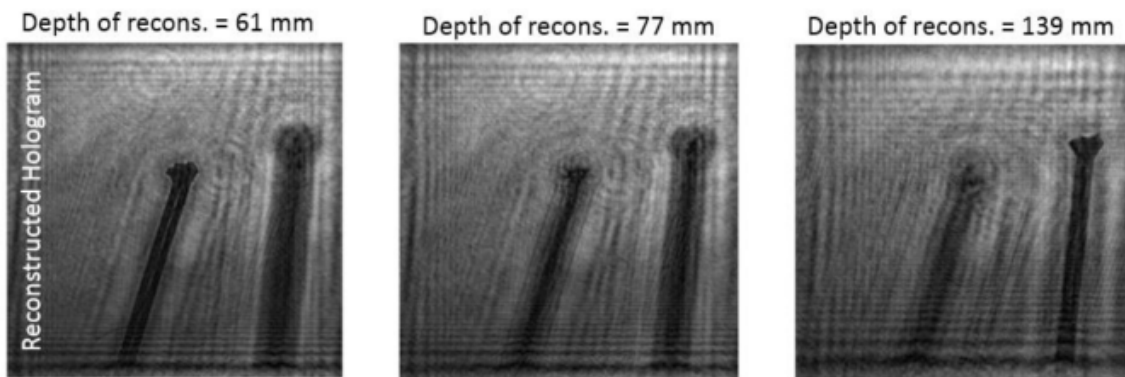


Figure 5.14 Example of reconstructed images at different distances from the sensor. Inline hologram [11].

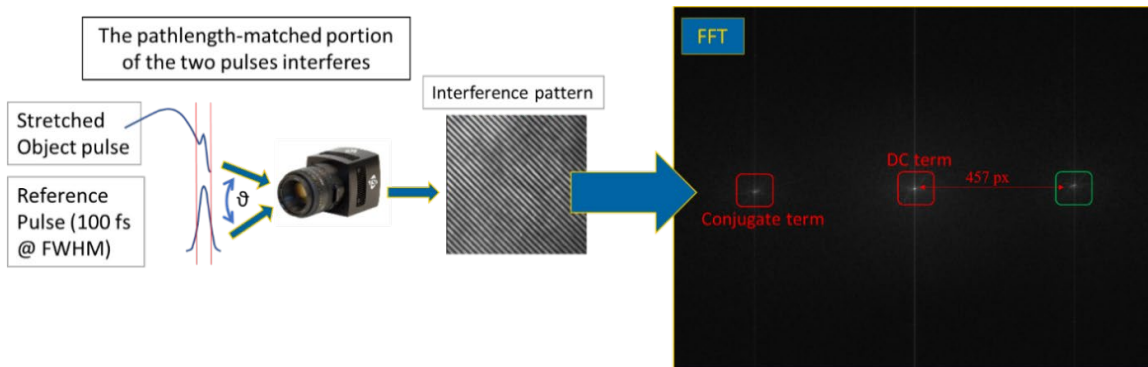


Figure 5.15 Diagram showing how object and reference pulse interfere at an angle, creating an interference pattern that separates coherent and incoherent information in the Fourier domain, the cross-correlation term boxed in green

can be reconstructed into an image of the object without including the multiple-scattering noise contained in the DC term.

Therefore off-axis holography is preferable to inline holography for spray imaging because it allows separation of the hologram's cross-correlation term from both the DC term and conjugate cross-correlation term in the Fourier domain (see Figure 5.15 above). Cropping the cross-correlation term in the Fourier domain and feeding it to the reconstruction algorithm allows reconstruction of the real image term that creates reconstructed images free from multiple scattering noise.

When reconstructing, the object field's modulation is calculated following the algorithms outlined in the previous sections, and the complex amplitude of the object wave is numerically computed in planes prior to the CCD sensor from which intensity is calculated to obtain a reconstructed image of the object at any plane. Off-axis holography presents the disadvantage of introducing much higher spatial frequencies on the CCD, and these frequencies are directly proportional to the reference beam tilt angle with respect to the object beam. Sensor pixel size limits the usable angle as we will see in the next paragraph.

5.6.1 Spatial frequency requirements

As described above, tilting the reference wave with respect to the object wave allows separating the virtual and the real image in off-axis holography. A larger interference angle creates a larger separation between the two (Figure 5.15), reducing crosstalk and leading to a better reconstructed image. Unfortunately increasing the interference angle also increases the spatial frequency of the interference pattern, and there is a limit to the highest spatial frequency that can be resolved by a CCD sensor. This limit is dictated by the CCD pixel size. The maximum spatial frequency to be resolved when interfering object and reference beam at an angle θ is

$$f_{max} = \frac{2}{\lambda} \sin \frac{\theta_{max}}{2}$$

Where θ_{max} is the maximum angle between the two waves. In our setup, the distance between pixels on the camera sensor is $\Delta x = 6.45 \mu\text{m}$, and the corresponding maximum resolvable spatial frequency is

$$f_{max} = \frac{1}{2\Delta x} \cong 77.5 \frac{lp}{mm}$$

Combining the previous two equations

$$\theta_{max} = 2 \sin^{-1} \left(\frac{\lambda}{4\Delta x} \right) \approx \frac{\lambda}{2\Delta x} \text{ (for small angles)}$$

Therefore, for our setup

$$\theta_{max} = 1.77^\circ$$

This is the maximum interference angle at which our sensor is still able to resolve the interference pattern but it is not the optimal interference angle since as we increase the interference angle the cross-correlation term used in the reconstruction process moves to the right in the frequency domain (as the carrier spatial frequency increases, Figure 5.15). At the maximum interference angle the cross-correlation term would be at the edge of the frequency space, and therefore we would need to use a very small reconstruction box around it in order to extract it, copy it at the center of a new hologram where the rest of the domain is zero-padded, and then feed it to the reconstruction algorithm. This small reconstruction domain would lead to a drastically reduced resolution and overall image quality (reduced hologram size N equals to lowered resolution, as shown in section 5.5). The optimal interference angle must, therefore, minimize crosstalk between DC and cross-correlation term while allowing to use the largest reconstruction mask possible.

5.7 Recording intensity and dynamic range

CCD cameras typically have a sensitivity of approximately 10^{-4} J/m² and a spectral response range between 400 nm and 1000 nm. These are both sufficient to successfully record holograms from a variety of laser sources. CCDs have the advantage of having high

linearity in their exposure curves, especially when compared to photographic film. This allows optimal contrast in the interference pattern, that is when the intensity ratio between object and reference beam is 1:1. Practically, this is assured by checking the brightness (by comparing the pixel values range) of the object beam versus the one of the hologram (reference and object beam together), the brightness of the hologram should be twice the brightness of the object wave alone. Most CCD sensors have a dynamic range of 8 bits (1:256), but dynamic ranges up to 14 bits (1:16384) are becoming more common. 8 bits is comparable to the dynamic range of photographic film. Holography has the further advantage with respect to incoherent, traditional imaging that objects exceeding the dynamic range of the recording medium can be still be reconstructed because the object information is coded as modulations in the interference pattern, not as intensity. This constitutes a dynamic range advantage with respect to ballistic imaging, which is known to struggle dealing with the juxtaposition of darkness from the spray core and extreme brightness from the laser light going around the liquid core and directly into the detector.

5.8 Coherence filtering as an alternative to time-gating

The fundamental concept behind time gating is to retain only the photons that are ballistic and quasi-ballistic. As shown earlier, these photons go through zero to one

scattering events and carry the information regarding the desired target image. At the same time, we want to filter out all the photons that go through multiple scattering events which add noise to the image. The technique is widely applied and considered to be the most important time filtering technique in ballistic imaging ([20], [21], [61], [68]–[70]). As we have seen in chapter 3.2, time-gating is achieved in practice by using a high-speed shutter, commonly an Optical Kerr Effect (OKE) cell. The Kerr effect is a change in the refractive index of a material in response to an applied electric field. To investigate picosecond time gating applied to ballistic imaging and digital holography, our research group utilized a CS₂ (carbon disulfide) adjustable time gate. The gate is excited by a laser beam, and it is timed to let only the first group of ballistic and quasi-ballistic photons reach the camera sensor. The effects of time gating, when applied to picosecond digital holography, was the focus of previous research from our group [69] and can be seen in Figure 5.16. The LFA group research effort moved from picosecond to femtosecond digital holography because it became clear that time gating using a CS₂ OKE cell was less beneficial when holography was already naturally coherence filtering the image, as suggested by Ziaee [11]. In fact, the switching response for the carbon disulfide gate in our setup was about 1.1 ps FWHM so that when dealing with femtosecond laser pulses that are shorter/faster than OKE CS₂ response time, gating becomes less effective in filtering

out the trail of multiply scattered photons that follow the ballistic photons. This has been corroborated by the photon transport Monte Carlo modeling presented in chapter 4, where the simulations show that a time-gate matching the imaging pulse is ideal, and a time gate with a switching response faster than 500 fs is essential when imaging dense fuel sprays.

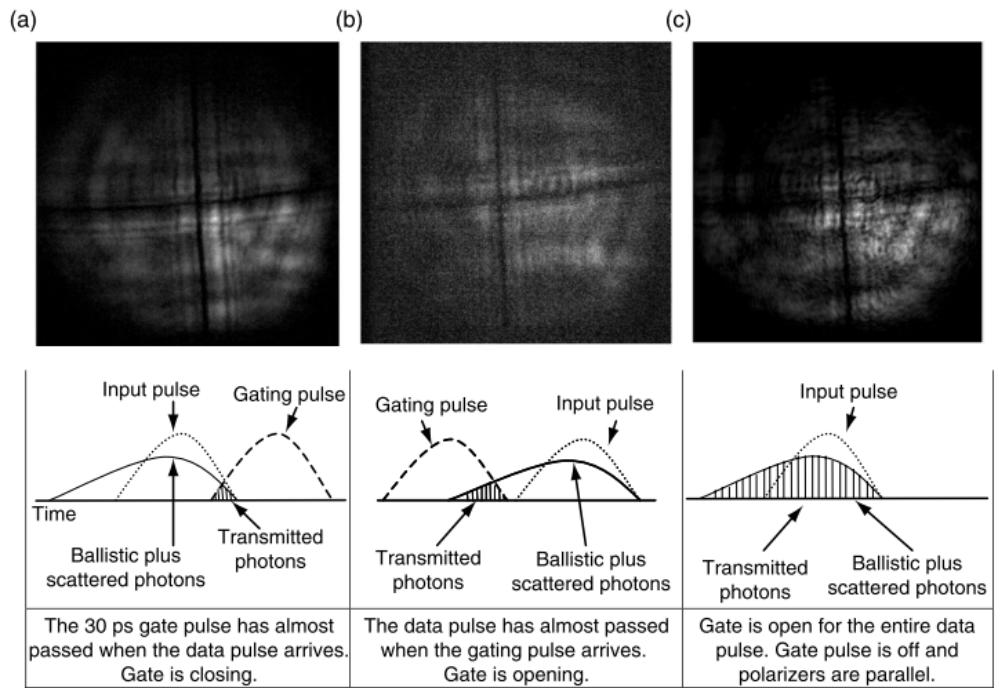


Figure 5.16 Reconstructed images from digital picosecond holograms with varying gate times imaged through a small-particle-emulsion scattering cell. In the left image, the first 10 ps of the light pulse are transmitted, in the second image only the last 10 ps of the pulse are transmitted while in the last image the whole 30 ps pulse is transmitted [68].

The following summarizes the requirements for light source pulse length and time gate switching response for dense fuel spray imaging that we can gather from the literature, from experimental data, and from Monte Carlo simulations:

1. Femtosecond pulsed lasers are the standard for dense fuel spray ballistic imaging because they allow to freeze the fast-evolving spray in time and to temporally separate ballistic and quasi ballistic photons from multiple scattering ones [18].
2. Experimental evidence from [1] shows that picosecond time gating is not effective when paired with a femtosecond laser pulse imaging through dense media with high OD; this has been corroborated by the photon transport simulations presented in chapter 4.
3. Photon transport simulations in dense media with OD up to 10 demonstrate that the ideal switching time for any hypothetical time gate should be below 500 fs to reject most multiple scattering photons, or ideally match the original imaging pulse length to only capture ballistic photons thus delivering the highest image quality. It is essential to recognize; however, that time gates respond to triggering laser

intensity which means that the shutter is not sharply instantaneous nor uniformly opaque.

4. Femtosecond-scale time gates do exist, but they either have lower transmissivities than OKE picosecond gates, or they are optically complex being composed by multiple OKE gates [18]. Tan et al. ([20], [71]) performed gated ballistic imaging using a tellurite glass optical Kerr effect gate, achieving a full width half maximum gate signal of 200 fs which would be of the same order of magnitude as our object beam (100 fs).

Coherence filtering relies on the short coherence length of the imaging femtosecond pulse to provide an “interferometric time gate” of ideal time length that always matches the imaging pulse length. When using a light source with short coherence length, only the portion of the object beam that is coherent with the reference is recorded in the hologram. This concept is described in Figure 5.15 where on the left-hand side of the image the elongated object pulse (above) is shown as it arrives at the camera sensor together with the 100 fs reference pulse (below). The portion of the object pulse that underwent multiple scattering events and traveled a longer path will not be coherent with the reference beam pulse. That is, multiple scattering photons will have a time delay that is much larger than the short coherence length of the pulse, and will also have different

polarization and phase (they will not be temporally and spatially coherent, as explained in section 5.2). Therefore, only the ballistic portion of the object pulse will be able to interfere with the reference pulse creating the hologram. In chapter 4 we computed the time delay that multiple scattering photons have with respect to ballistic photons when traveling through high OD media representative of fuel sprays and found that the first multiple scattering photons arrive at the sensor hundreds of fs later than the ballistic ones. The coherence length for the 100 fs pulse used in USPODH is 30 μm , therefore the only photons that can contribute to the hologram formation must be ballistic or quasi-ballistic. The multiple scattering photons are still detected by the camera sensor, but their contribution is congregated in the DC term. As described earlier in this chapter the off-axis layout adopted by USPODH applies a carrier spatial frequency to the hologram interference pattern that is proportional to the interference angle θ (see Figure 5.15). This allows reconstruction of an intensity-based image of the target from the cross-correlation term containing the ballistic photons' information, while almost wholly avoiding cross-talk with the DC term containing the incoherent noise from the multiple scattering photons, and altogether rejecting the contribution from the conjugate cross-correlation term that would deliver a pseudoscopic image of the target. The image results confirm that coherence filtering accomplished by the holographic approach is comparable to or superior

to that achievable with standard time gating approaches. In addition, the holographic method permits substantially higher dynamic range as compared to direct imaging, which helps overcome the limited intensity dynamic range of typical CCD camera sensors.

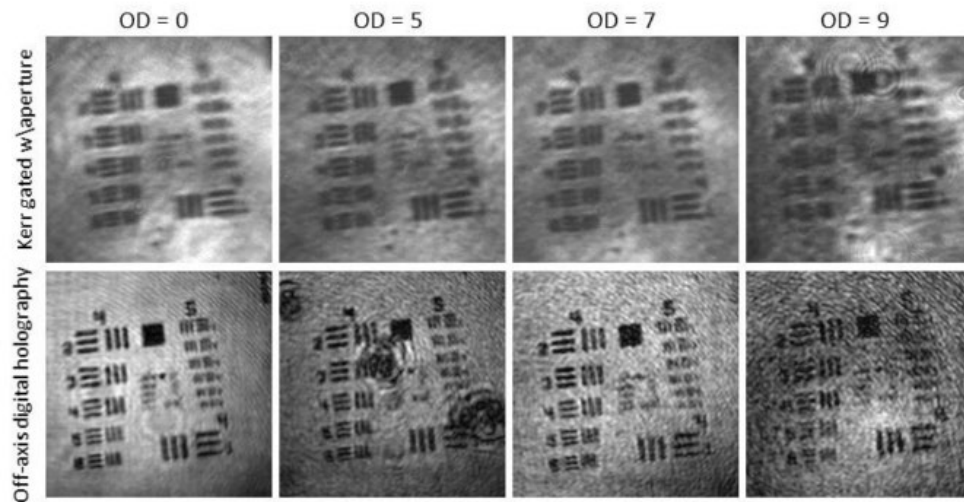


Figure 5.17 A comparison between femtosecond OKE ballistic imaging with a picosecond time-gate and off-axis femtosecond digital holography. USAF resolution target placed behind a suspension with 0.6 microns particles. [11]

Chapter 6

6 Demonstrating coherence filtering on a polydisperse spray distribution with OD 12

The Monte Carlo simulations results presented in chapter 4 show that a setup with a time gate with a switching time below 500 fs can successfully separate ballistic photons from multiple scattering ones when imaging through media with OD 10 using a 100 fs imaging pulse. We then introduced holography's coherence filtering, an "interferometric time-gate" that has a duration that always matches the imaging pulse one without the need for a combination of OKE gates. By avoiding physical Kerr gates, the disadvantages related to the complexity of such setups (low transmissivity, synchronization of multiple switching beams with the imaging beam, hazardous materials in the OKE gate) can be avoided. The recognition that short pulse holography naturally coherence filters the image further validated the idea of employing a femtosecond holographic imaging setup to observe optically dense fuel sprays, which the literature report as having ODs on the order of 9-12 [18]. Real sprays offer challenges that are difficult to completely re-create in simulations

such as: polydisperse size distribution of the scattering particles, non-spherical shape of scatterers, speed of target spray (up to 800 m/s) which might causes image-blur, temperature and pressure gradients in the media surrounding the spray, and optical windows ranging in thickness from sub-mm to several centimeters that can all cause chromatic dispersion, obscuration and scattering of the imaging pulse. In the experimental part of this dissertation, we address all these challenges and demonstrate USPODH applicability to fuel spray imaging in the near nozzle region.

This chapter aims at experimentally demonstrating the basic performance of coherence filtering when imaging a liquid spray core hidden in a highly scattering media. This first experiment is conducted at ambient temperature and pressure without windows to minimize the complications of these features while exploring the holographic imaging concept in optically dense environments. A bench spray representative of the optical conditions found in realistic optically dense fuel sprays was designed, built, and characterized. The target OD conditions were experimentally measured and validated using Monte Carlo photon transport simulations.

6.1 Experimental setup

6.1.1 Spray setup

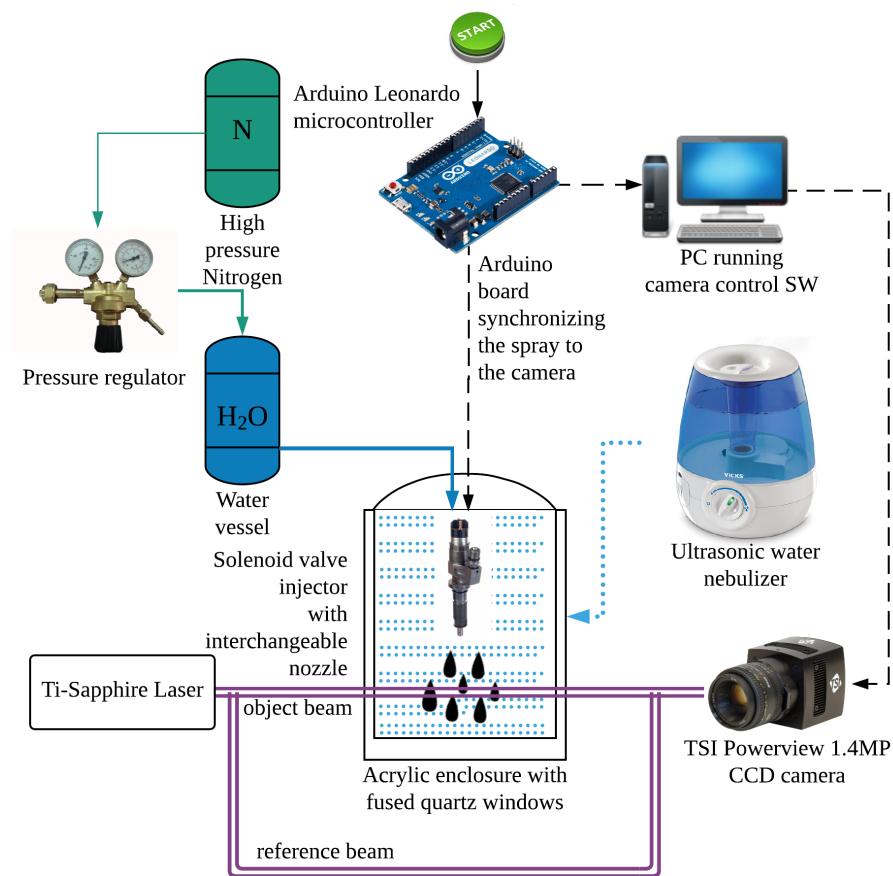


Figure 6.1 Schematic of the spray setup.

The experimental setup shown in Figure 6.1 recreates the optically dense conditions typical of the near nozzle region of diesel sprays, where an outer layer of primary

atomization droplets can potentially hide a core of larger droplets or liquid ligaments [45].

Approximating the realistic spray optical environment is achieved by surrounding the target spray with a mist produced using an ultrasonic atomizer.

The first task was to identify a benchmark spray to be replicated in the experimental setup, and from the literature study, it is clear that a high-pressure diesel spray would be the most challenging environment where to test USPODH's coherence filtering performance. Modern diesel engines present this challenging diagnostic environment because of their extreme injection pressure (100-150 MPa), high ambient pressure (5-10 MPa), turbulent clouds of potentially supercritical diesel fuel ([10],[6]), and controversy regarding the phase of the fluid in the primary atomization, near nozzle region ([72], [10], [57]). When there is not a clear phase boundary, optical methods that rely on surface refraction and diffraction can have difficulty distinguishing regions of smoothly varying density, as can happen at near-critical conditions.

The facilities and instrumentation initially available at the start of this research constrained the work to open (room temperature and atmospheric pressure) water sprays. Hence, this first set of experiments focused on creating a bench experiment that effectively

recreates the optical conditions of a realistic high-pressure fuel spray at ambient temperature and pressure. That is, the system should create a spray distribution that is similar optically to what is expected in a realistic diesel spray, but the mechanism for achieving that distribution need not be a real diesel injector. Matching the absolute breakup regime of a high-pressure diesel spray using a water spray in an unpressurized environment is not possible, as the non-dimensional numbers in Table 6.1 show. In addition, it is not practical even when considering fluids other than water. Therefore, for the first demonstration and implementation of USPODH for spray imaging, an optical environment representative of a realistic diesel spray is achieved rather than matching the breakup regime itself. This is a satisfactory demonstration of the optical challenge, which is the focus of this research. Furthermore, the optical challenge far exceeds the fluid dynamic one since even modern diesel sprays with injection pressures around 150 MPa and nozzle exit velocity around 700-800 m/s can be effectively frozen in time when imaged with a 100 fs ultra-short laser pulse. On the other hand, it is the multiple scattering environment of such sprays that have created the optical interference that challenges other imaging methods and may cause difficulty for the hologram.

A spray from an automotive fuel injector was placed behind a veil of smaller droplets generated by an ultrasonic water atomizer to recreate the primary-atomization region in a like optical environment. This method recreates an environment where an outer layer of highly atomized fluid is hiding a core of bigger droplets or liquid ligaments. Both the size of the core spray object and that of the outer sheath droplets match available experimental data for diesel sprays [73] and correlates well with the predicted droplet size distribution in the primary atomization region of “non-evaporative ECN Spray A” as simulated by Manin [2]. The optical depth for the whole target field was measured, and the measurement validated via Monte Carlo simulations. The results of this target characterization are presented in section 6.2. There is one crucial difference between a core spray surrounded by a secondary cloud of droplets and the diesel spray where the cloud is part of a continuum of droplet sizes coming from the core, and that is a clear bimodal distribution in the former case and a continuously varying size distribution in the latter. Nevertheless, the optical density challenge and the multiple scattering challenge can be evaluated effectively using the simulated diesel spray system.

Two enclosures were built, with a window-to-windows distance of 5 and 10 cm; so that by changing enclosure, different optical densities can be obtained.

As described earlier, optical density (OD) is defined as:

$$OD = -\ln\left(\frac{I_l}{I_o}\right)$$

Where I_o is the irradiance of the light before it enters the spray medium and I_l is the irradiance after the light has traveled through the highly scattering target enclosure. In the larger enclosure transmissivities as low as 6×10^{-6} were reached, which corresponds to OD 13. These are extremely harsh scattering conditions where techniques such as the state-of-the-art Ballistic Imaging (which also does not allow for 3-D reconstruction) achieved a spatial resolution of 30-40 μm [18], [44]. An automotive fuel injector from a V8 manifold injected gasoline engine is used to create the target jet spray. The fuel injector is controlled by an Arduino microcontroller, thus allowing the user to switch between continuous or pulsed spraying, the shortest pulse achievable with the setup is a 3 ms injection. This feature is helpful to better simulate automotive sprays which mostly operate in a transient state while modern diesel injectors are more rapid, firing about 1000 times per minute. In any case, the imaging laser pulse is so short that the holographic system experiences no difference in performance when switching from continuous to pulsed spraying. The enclosure is filled with water mist before the spray nozzle is activated, and the press of a pushbutton initiates the spraying sequence. The sequence entails: the Arduino microcontroller opening the spray's solenoid valve and simultaneously sending a

signal via USB to the PC controlling the camera; acquisition of a sequence of images is started, with each picture capturing a single 100 fs laser pulse (one image is acquired every 100 ms with an exposure time of 1 ms); after a user-defined amount of time the microcontroller stops the spray and camera acquisition.

Table 6.1 Specifications of the fuel injector used in the experiment

Spray type	Nominal injection pressure	Nozzle diameter	Nozzle exit velocity	Reynolds number	Weber number	Oh number
Water spray at ambient pressure	45-120 PSI	0.2 mm	40 m/s (@120 PSI)	9	4596	0.91
Diesel spray in engine like conditions	100-150 MPa	0.09 mm	500 m/s	$7 \cdot 10^4$	720000	$4 \cdot 10^{-4}$

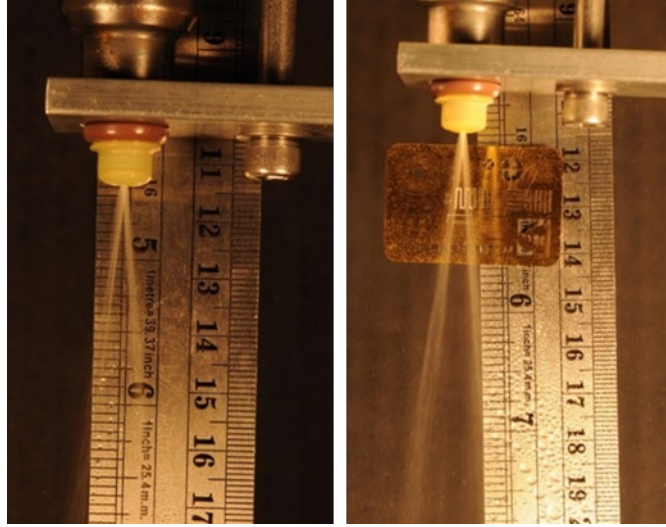


Figure 6.2 Water injected at 80 PSI (left) and 100 PSI (right) at ambient pressure and temperature. This automotive fuel injector is used in the setup to represent the “liquid core” of a high-pressure diesel spray

6.1.2 Optical setup

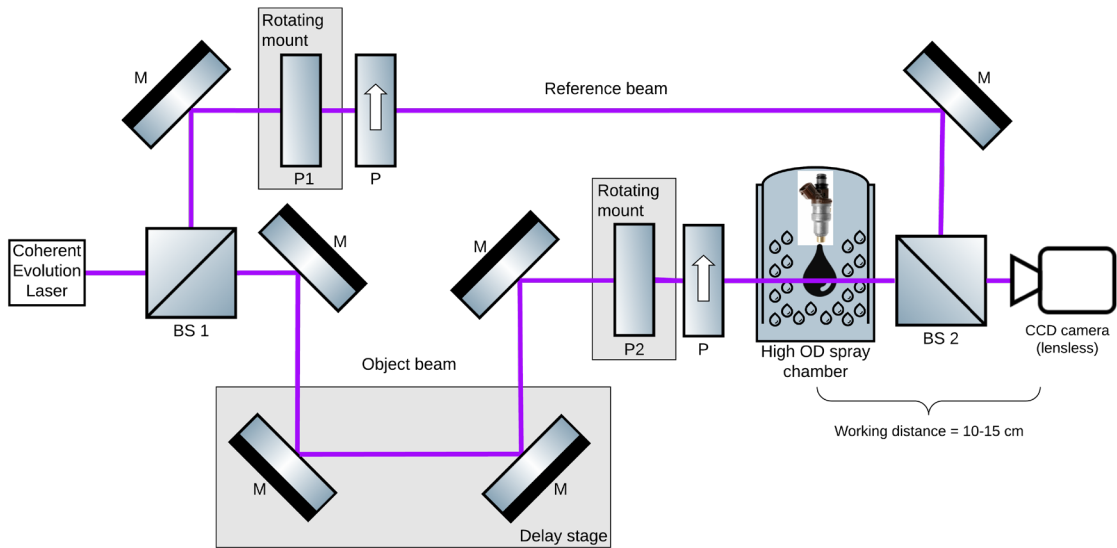


Figure 6.3 Diagram of the optical setup

Figure 6.3 shows the optical arrangement used for the results presented in this chapter. A Ti:Sapphire femtosecond laser generates 100 fs – 800 nm wavelength pulses at 1 kHz repetition rate. Each pulse is frequency-doubled to 400 nm using a doubling crystal; the pulse optical spectrum FWHM is less than 3 nm. The beam is split at the beamsplitter BS1 into object and reference beam, and the object beam travels through a delay stage that is adjusted manually to assure pathlength matching between the two beams. Both beams travel through a pair of polarizers that can be adjusted to match the beam intensities, thus generating an optimally contrasted hologram. The object beam travels through the spray chamber that is filled with water mist to mimic the high OD environment that is representative of the light scattering conditions found in the near nozzle region of realistic diesel fuel sprays. As mentioned earlier, two chambers of different sizes were built in order to simulate environments of different OD. The smaller chamber with a beam path of 5 cm has OD between 5 and 7 when filled with the water mist generated by the ultrasonic atomizer, and the larger chamber with a beam path of 10 cm reaches OD between 9 and 13. Both chambers have two, 1 mm thick fused silica windows. The object and reference beam are recombined at the beamsplitter BS2 and overlapped at the camera sensor while imposing a small angle between the two. When pathlength matched correctly the beams overlap to create a 2D interference pattern. The interference

angle θ is adjusted to optimize scattering noise rejection (avoiding crosstalk between DC and cross-correlation term, as noted in the analytical chapter earlier) and reconstruction resolution (by allowing for the largest hologram size in pixel while satisfying the previous condition). This condition translates into a fringe spacing of 3 pixels per fringe, which equates to approximately 13 μm between fringes on the sensor plane. In the Fourier domain this corresponds to approximately 440 pixels center to center between the DC and cross-correlation term, which allows to isolate a 400x400 pixels region of the hologram surrounding the cross-correlation term and process it for reconstruction while avoiding crosstalk.

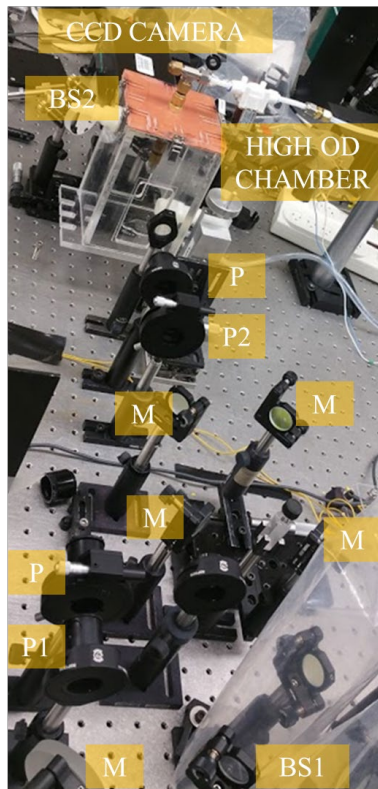


Figure 6.4 View of the experimental setup showing the 10 cm scattering cell.

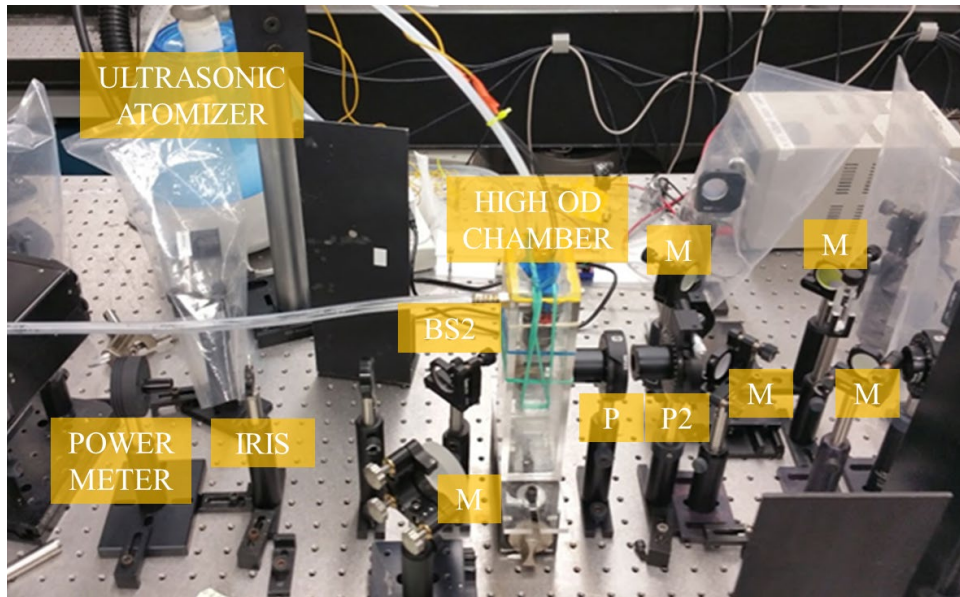


Figure 6.5 side view of the experimental setup showing the 5 cm scattering cell.

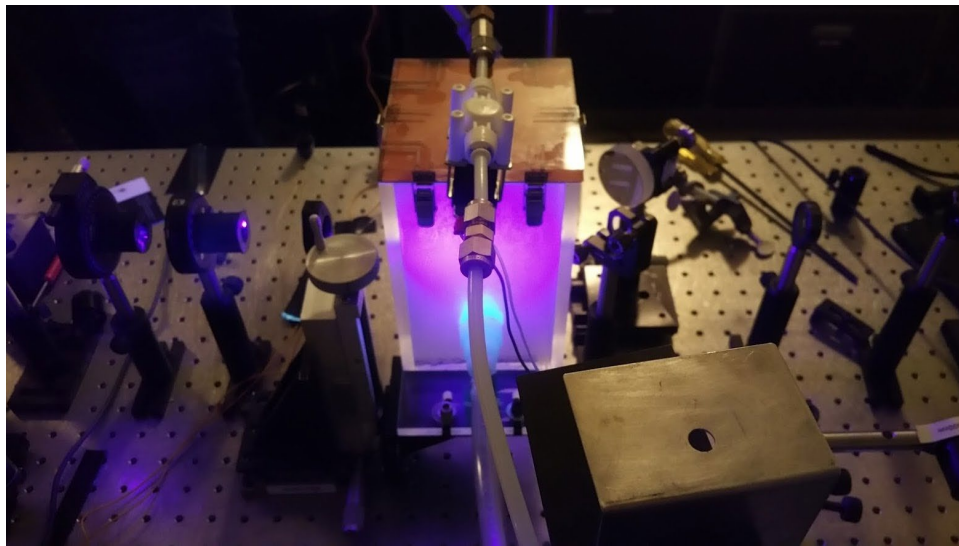


Figure 6.6 Side view of the experimental setup, the 10 cm scattering cell is filled with water mist generated by the ultrasonic atomizer, at the same time, the fuel injector placed at the center of the cell is fired. The 100 fs pulse enters the cell from the left, the camera sits on the right-hand side of the picture, outside of the field of view. Note the severe scattering environment which causes the violet glow shown in this image.

6.2 Measurements

6.2.1 Spray and scattering environment characterization

Droplet size distributions for both the spray and the water mist surrounding it were measured using a Malvern Spraytec laser diffraction particle sizer to assure that the particle size distribution of the target and its OD would match the desired one. The instrument was made available to us by the U.C. Irvine Combustion Laboratory. In order to obtain a characterization of the droplet size distribution produced by the injector, the droplet size is measured for different values of injection pressure. Water or diesel fuel pressurized with Nitrogen gas is injected into ambient pressure and temperature. Laser diffraction methods rely on Mie scattering theory to infer droplet size from an ensemble measurement of diffraction angle. These methods are not reliable in the near-nozzle region where a substantial amount of the spray appears as a continuous liquid stream and does not have the spherical shape required to satisfy Mie theory's assumptions. In addition, the Mie scattering methods rely on single scattering events, so any dense spray region with multiple scattering leads to inaccurate sizing results. The particle size measurements shown below are unreliable in the near-nozzle region, but they provide an accurate indicator for the substantial volume fraction of the spray. When the spray jet is not

completely atomized, very large droplet sizes are detected, and these sizes are outliers with respect to the typical Gaussian-shaped droplet size distribution (as in Figure 6.9). The size distribution is most reliable when such outliers are not present.



Figure 6.7 Laser diffraction particle sizing of the near nozzle region of the fuel injector. Water injected at approximately 80 PSI.

The following figures show a summary of the measurements performed using laser diffraction particle sizing to characterize our fuel injector at different injection pressure. It is clearly shown that moving from 45 PSI injection pressure (Figure 6.9) up to 80 PSI (Figure 6.11) and eventually 100 PSI (Figure 6.13) the droplet size decreases as a result of the overall increment of inertial forces that promote breakup. Even though atomization is

promoted when going to higher injection pressure, the average particle size is always well above 100 microns, even when using diesel fuel instead of water (Figure 6.17 and Figure 6.18). The relatively poor atomization performance of this fuel injector fortuitously makes it a good candidate for a “liquid core” target. Since our goal is to image hidden liquid ligaments at the core of highly atomized dense diesel sprays this fuel injector provides a reliable source of large liquid ligaments and droplets to represent the liquid core of the primary atomization region of a diesel spray.

Measurement Parameters			Aug 9 2016 11:58:40
Valid Data Record			
No Tag Defined			
Standard Values:			
Transmission = 69.64%	Dv(10) = 177.69 (µm)	Span = 0.97	
Cv = 2796.4 (PPM)	Dv(50) = 566.74 (µm)	D[3][2] = 280.06 (µm)	
SSA = 0.021 (m ² /cc)	Dv(90) = 729.17 (µm)	D[4][3] = 471.50 (µm)	
Measurement Values and Settings			
Path Length = 11.99 (mm)	Particulate Density = 1.00 (gm/cc)		
Qe (Avg) = 2.01	Laser Wavelength = 670.0 (nm)		
Pscat (Avg) = 0.49 (0.00)	Mesh Factor = 1.00		
Calibration : (ST45AIAC.CAL, STAESFSE.IMG, STD0501.RSP)			
Lens = 450			
Media Refractive Index = 1.00 + 0.00i			
Particulate Refractive Index = 1.50 + 0.50i			

Figure 6.8 Malvern laser diffraction particle size measurements for water injected at 45 PSI, near-nozzle region.

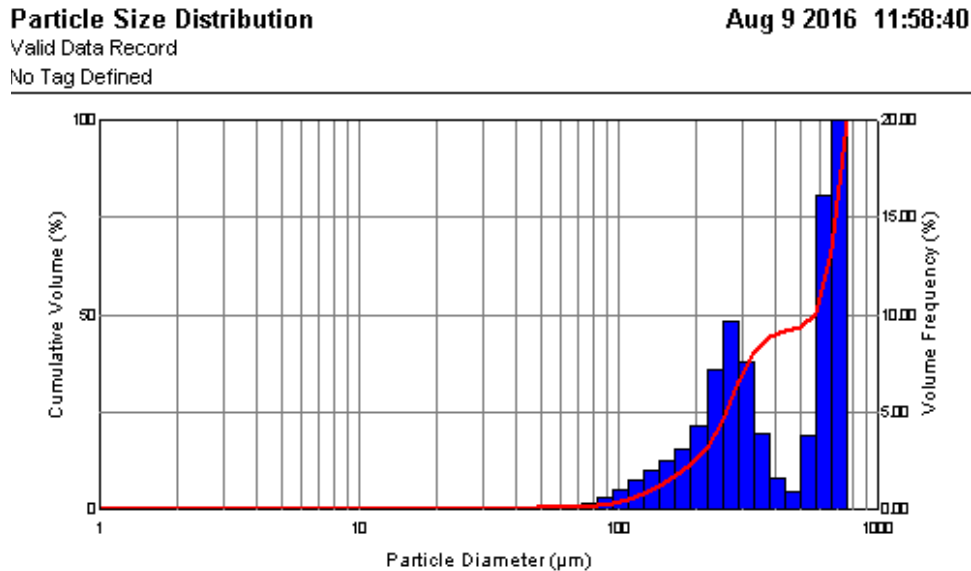


Figure 6.9 Near nozzle particle size distribution for water injected at 45 PSI. Note the two peaks between 600 and 700 microns. The bimodal distribution outliers suggest that in the near nozzle region there is a considerable amount non-atomized liquid making this injector an excellent candidate to provide a liquid column that will be imaged when surrounded by a veil of optically obscuring water mist.

Measurement Parameters

Aug 9 2016 12:04:10

Valid Data Record

No Tag Defined

Standard Values:

Transmission = 61.01%	Dv(10) = 129.14 (μm)	Span = 1.43
Cv = 2173.7 (PPM)	Dv(50) = 325.00 (μm)	D[3][2] = 159.73 (μm)
SSA = 0.038 (m ² /cc)	Dv(90) = 594.10 (μm)	D[4][3] = 342.73 (μm)

Measurement Values and Settings

Path Length = 11.99 (mm)	Particulate Density = 1.00 (gm/cc)
Qe (Avg) = 2.02	Laser Wavelength = 670.0 (nm)
Pscat (Avg) = 0.48 (0.00)	Mesh Factor = 1.00

Calibration : (ST45AIAC.CAL, STAESFSE.IMG, STD0501.RSP)

Lens = 450

Media Refractive Index = 1.00 + 0.00i

Particulate Refractive Index = 1.50 + 0.50i

Figure 6.10 Malvern near nozzle region measurement parameters for water injected at 80 PSI.

Particle Size Distribution

Aug 9 2016 12:04:10

Valid Data Record

No Tag Defined

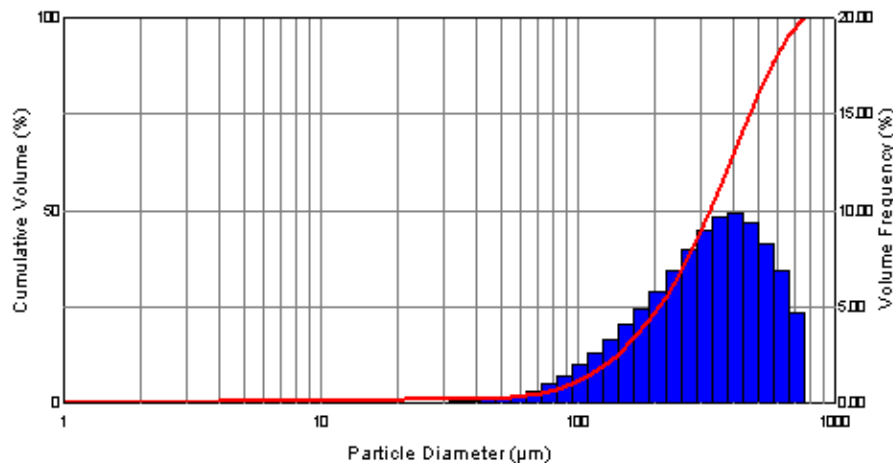


Figure 6.11 Near nozzle region particle size distribution for water injected at 80 PSI. These data show that only 10% of the spray volume is below 130 μm in size, making it a candidate source of large droplets and liquid ligaments mimicking the liquid core of a high-pressure diesel spray.

Measurement Parameters

Aug 9 2016 52 (R)

Valid Data Record

No Tag Defined

Standard Values:

Transmission = 58.71%	Dv(10) = 123.68 (µm)	Span = 1.46
Cv = 2162.0 (PPM)	Dv(50) = 334.49 (µm)	D[3][2] = 147.46 (µm)
SSA = 0.041 (m ² /cc)	Dv(90) = 608.78 (µm)	D[4][3] = 349.25 (µm)

Measurement Values and Settings

Path Length = 11.99 (mm)	Particulate Density = 1.00 (gm/cc)
Qe (Avg) = 2.02	Laser Wavelength = 670.0 (nm)
Pscat (Avg) = 0.47 (0.00)	Mesh Factor = 1.00

Calibration : (ST45AIAC.CAL, STAESFSE.IMG, STD0501.RSP)

Lens = 450

Media Refractive Index = 1.00 + 0.00i

Particulate Refractive Index = 1.50 + 0.50i

Figure 6.12 Malvern measurement parameters for water injected at 100 PSI, near-nozzle region.

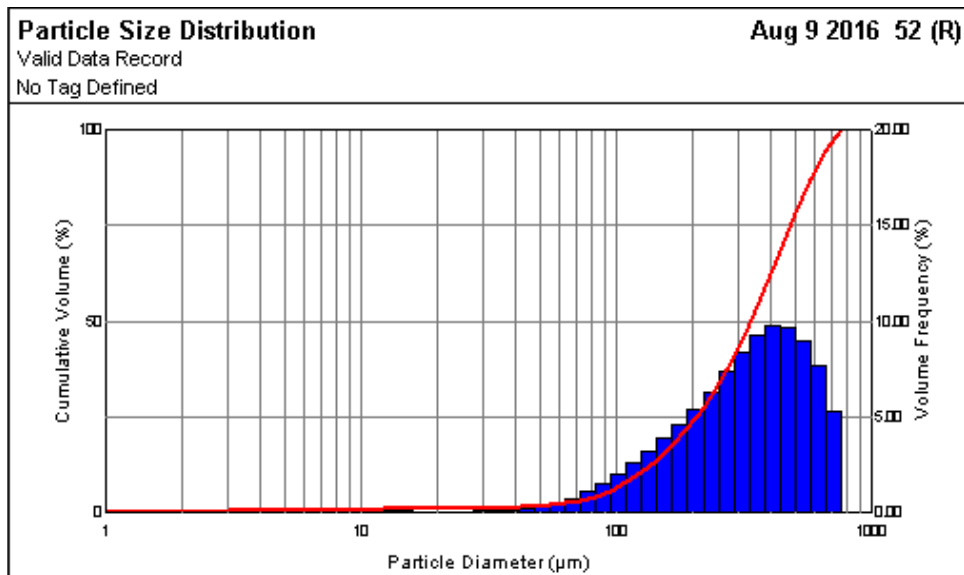


Figure 6.13 Particle size distribution for water injected at 100 PSI, near-nozzle region.

Measurement Parameters			Aug 9 2016 12:43:36
Valid Data Record			
No Tag Defined			
Standard Values:			
Transmission = 52.43%	Dv(10) = 125.07 (µm)	Span = 1.35	
Cv = 2430.8 (PPM)	Dv(50) = 376.81 (µm)	D[3][2] = 136.71 (µm)	
SSA = 0.044 (m ² /cc)	Dv(90) = 632.48 (µm)	D[4][3] = 376.59 (µm)	
Measurement Values and Settings			
Path Length = 11.99 (mm)	Particulate Density = 1.00 (gm/cc)		
Qe (Avg) = 2.02	Laser Wavelength = 670.0 (nm)		
Pscat (Avg) = 0.47 (0.00)	Mesh Factor = 1.00		
Calibration : (ST45AIAC.CAL, STAESFSE.IMG, STD0501.RSP)			
Lens = 450			
Media Refractive Index = 1.00 + 0.00i			
Particulate Refractive Index = 1.50 + 0.50i			

Figure 6.14 Malvern measurement parameters for water injected at 120 PSI, near-nozzle region.

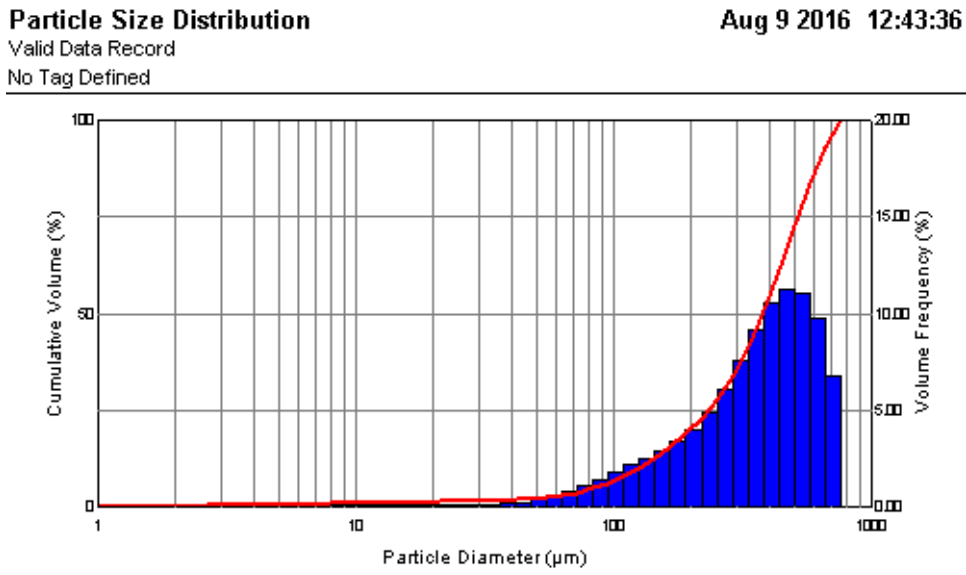


Figure 6.15 Particle size distribution for water injected at 120 PSI, near-nozzle region.

Measurement Parameters			Aug 9 2016 14:57:37
Valid Data Record			
No Tag Defined			
Standard Values:			
Transmission = 66.00%	Dv(10) = 82.39 (µm)	Span = 2.18	
Cv = 1735.7 (PPM)	Dv(50) = 227.92 (µm)	D[3][2] = 151.93 (µm)	
SSA = 0.039 (m ² /cc)	Dv(90) = 580.04 (µm)	D[4][3] = 282.42 (µm)	
Measurement Values and Settings			
Path Length = 11.99 (mm)	Particulate Density = 1.00 (gm/cc)		
Qe (Avg) = 2.02	Laser Wavelength = 670.0 (nm)		
Pscat (Avg) = 0.51 (0.00)	Mesh Factor = 1.00		
Calibration : (ST45AIAC.CAL, STAESFSE.IMG, STD0501.RSP)			
Lens = 450			
Media Refractive Index = 1.00 + 0.00i			
Particulate Refractive Index = 1.50 + 0.50i			

Figure 6.16 Malvern measurement parameters for diesel fuel injected at 85 PSI 0.5 inches away from the nozzle exit.

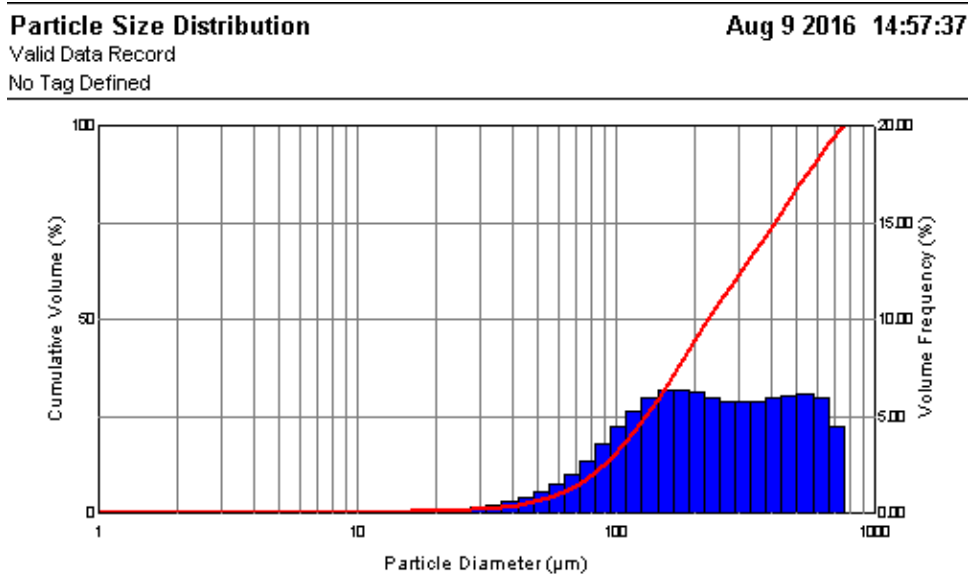


Figure 6.17 Particle size distribution for diesel fuel injected at 85 PSI 0.5 inches away from the nozzle exit.

The laser diffraction particle sizing data above show that for water injection pressures ranging from 80 to 120 PSI only 10% of the spray volume in the near-nozzle region is composed of droplets less than 125 µm in diameter, suggesting that this fuel injector

condition could be a good candidate to create the “liquid ligament core” or the larger droplets that the USPODH system intends to image when hidden behind a scattering medium. The injector measurements show that this nozzle can produce the target spray objects of the appropriate size but not the surrounding mist that would obscure them optically. A second atomization method (ultrasonic) was employed to create that mist.

There is little experimental data available to confirm the particle size distribution created by primary breakup mechanisms in the near-nozzle region of high-pressure fuel sprays. The mechanism describing the early stages of diesel fuel injection into a high temperature and high-pressure environment has been the focus of extensive research [1]–[5], and the traditional understanding is that an intact stream of liquid fuel exists in the near-nozzle region. From this liquid core, surface ligaments, bags, and sheets form that eventually shed droplets via primary breakup. The size distribution of these droplets, bags, and ligaments have been predicted by models [4] and numerical simulations [2], [7] but there is a lack of quantitative experimental data necessary for verification and validation of those models. High-speed shadowgraph images do not accurately describe this gas-liquid interface because of multiple scattering noise from a layer of smaller droplets surrounding the jet core [1], [2]. The most recent DNS simulations and the limited experimental data

available suggest that in order to recreate the optical conditions typical of the primary atomization region it would be ideal to surround the larger liquid core with a droplet population between 3-10 μm and an OD up to 12. Ultrasonic atomizers produce a large number of small droplets in this size range, and that is what is used in the current experiment. In this device, a piezoelectric transducer resonating at ultrasonic frequencies creates capillary waves on the liquid surface; when these waves become too tall to support themselves small droplets fall off the tip of each wave resulting in atomization of the fluid. The mist for our ultrasonic atomizer has been sized using the Malvern Spraytec droplet size measurement system. The Sauter Mean Diameter (SMD or D_{32}) of the mist produced is 4.3 microns, the D_{v50} is 7.8 μm and the D_{v90} is 23.3 μm , meaning that 50% of the total spray volume is made by droplets with a diameter smaller or equal than 7.8 μm and 90% of the spray liquid volume is made up of droplets with a diameter which is less than or equal to 23.3 μm . Sizing data are reported in Table 6.2 below.

Table 6.2 Particle size distribution metrics for the water mist produced by the ultrasonic atomizer measured by the Malvern Spraytec laser diffraction system.

Metric	Value (μm)
D_{32}	4.28
$D_v(50)$	7.8
$D_v(90)$	23.3
D_{43}	11.33
$D_v(10)$	1.74

These sizes compare well with the limited droplet size experimental data available in the literature for the outer layer of diesel sprays [73] and the primary breakup droplet size distribution predicted by the most up to date numerical simulations [74]. This particle size distribution is approximately equivalent to one produced by the primary breakup mechanism of an injector where diesel fuel is injected at 139 bar producing a spray with $We \cong 2 \cdot 10^3$.

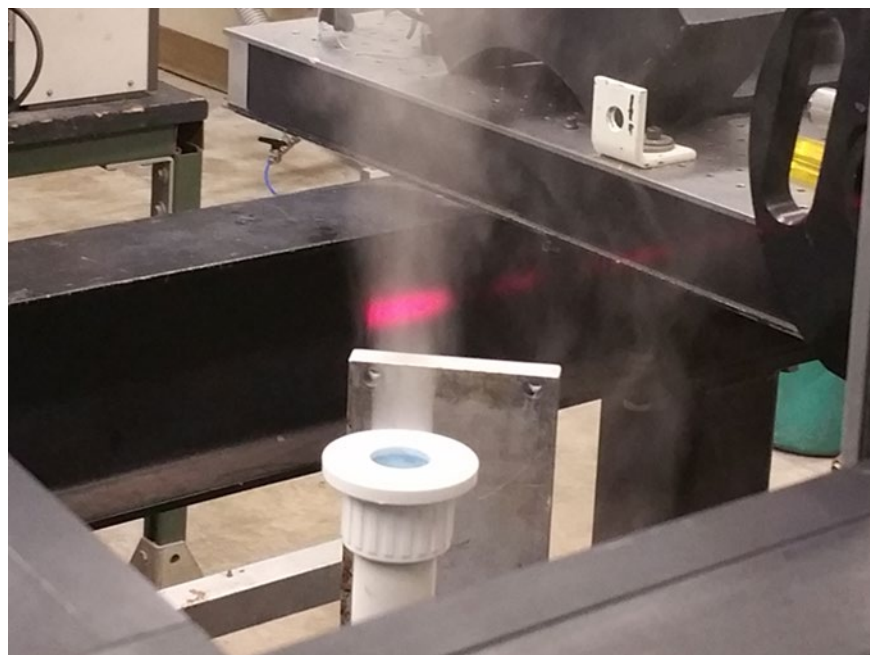


Figure 6.18 Water mist produced by an ultrasonic atomizer. The particle size distribution is measured by Malvern Spraytec laser diffraction particle sizer

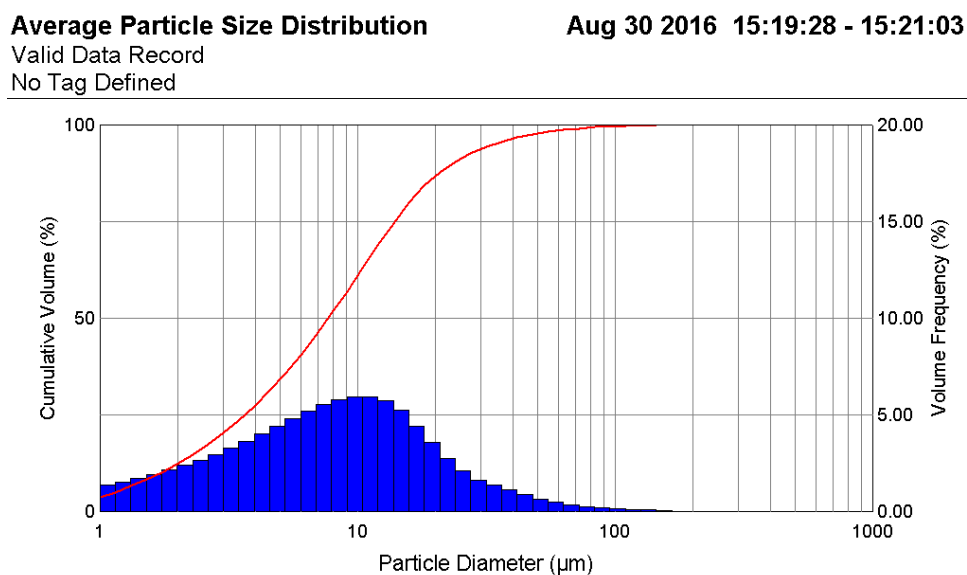


Figure 6.19 Droplet size distribution at the ultrasonic atomizer nozzle exit.

As mentioned before, the breakup events observed in this setup are different from the ones likely to occur in engine-relevant spray conditions, where both Weber and Reynolds numbers will be orders of magnitude larger. However, this stage of the research aims at mimicking the optical and scattering conditions of a realistic spray's fine mist of droplets surrounding a core liquid, as multiple scattering noise suppression in such sprays has been a significant visualization challenge. When moving to realistic high-pressure sprays, some differences are likely (due to size distribution effects), but there is no physical issue expected as the 100 fs exposure time is short enough to capture any fast breakup event without motion blur. For instance, if we consider a common rail diesel fuel injector where dodecane is injected at 1400 Bar into a vessel at 1 Bar, we can expect Weber numbers of magnitude of $2 \cdot 10^4$ and nozzle exhaust velocities of approximately 600 m/s; which means that a droplet in the near nozzle region will only travel $6 \cdot 10^{-11}$ m while illuminated by the 100 fs imaging pulse.

The gasoline injector/ultrasonic mist system uses a fast solenoid valve to control the core spray. Two different nozzle sizes are used (orifice diameter of 0.1 and 0.3 mm). Water is pressurized to the desired value by a high-pressure nitrogen tank and a pressure regulator. It is then injected into the acrylic enclosure with 1 mm thick fused quartz windows. The

OD in the enclosure was measured after filling it with water mist. As described earlier, the smaller enclosure measured at OD 5-7 while the larger one measured at OD 9-13. This OD range is ideal for testing a dense spray diagnostic technique as the literature agrees that ODs above 9-10 are common in the near-nozzle region of diesel sprays, where only ballistic imaging proved to be effective [18], [45]. OD is measured by placing a power meter where the laser beam exits the target enclosure. The pulse power is measured with no scattering media in the beam path, then water mist is introduced in the enclosure while the spray is fired, and the light collected on the far side of the enclosure is measured again. The ratio between the two measurements (beam attenuation) is used to calculate a practical OD. An iris with an aperture slightly smaller than the beam waist at the focal plane is placed between the enclosure and the power meter and provides spatial filtering by blocking most of the scattered light. Measuring only ballistic and forward scattered photons assures us that the calculated OD value can only be an underestimation of the actual OD, since OD by definition should be calculated measuring only non-scattered light. The measurements were validated by simulating the same target field using the “Multi-Scat” photon transport software; the simulations confirmed the magnitude of the OD values that were observed experimentally.

Although OD is commonly used in the dense spray visualization literature, as a single parameter it is not an ideal metric in gauging the harshness of the scattering environment. For example, two spray fields with the same OD but different scatterer distribution could produce different optical or hologram outcomes. For example, fewer but larger scatterers can cause more obscuration and compromise image quality. Another variable affecting phase coherence between object and reference beam would be the size of the scattering media region (photon pathlength within the media) and the proximity between scatterers. Our setup approximates the optical condition found in a real spray since the particle size distribution is close to the experimental data available for diesel sprays of $We \cong 2 \cdot 10^3$, and the target field has an OD comparable to that of high-pressure sprays. Our system achieves OD 12 over a pathlength of 10 cm while a high-pressure spray has the same attenuation factor (though achieved over smaller distances ~ 1 cm), and both systems satisfy the independent scattering approximation.

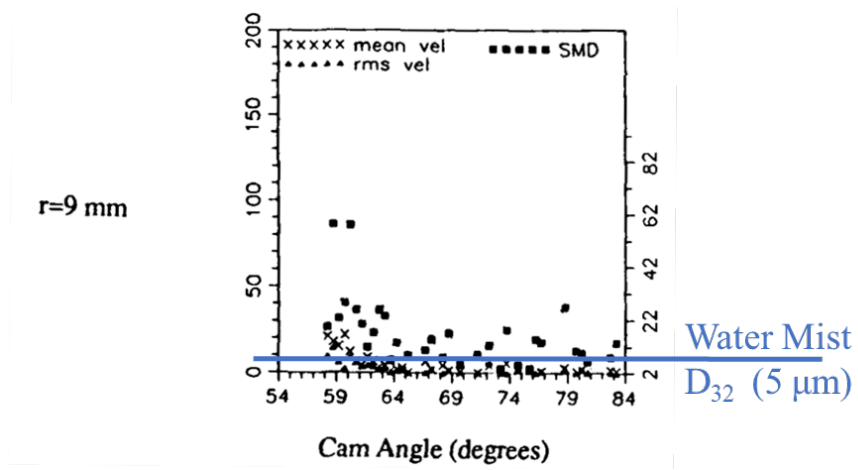


Figure 6.20 Droplet sizes measured at the edges of a diesel spray in the near nozzle region at moderate pressure conditions [73]

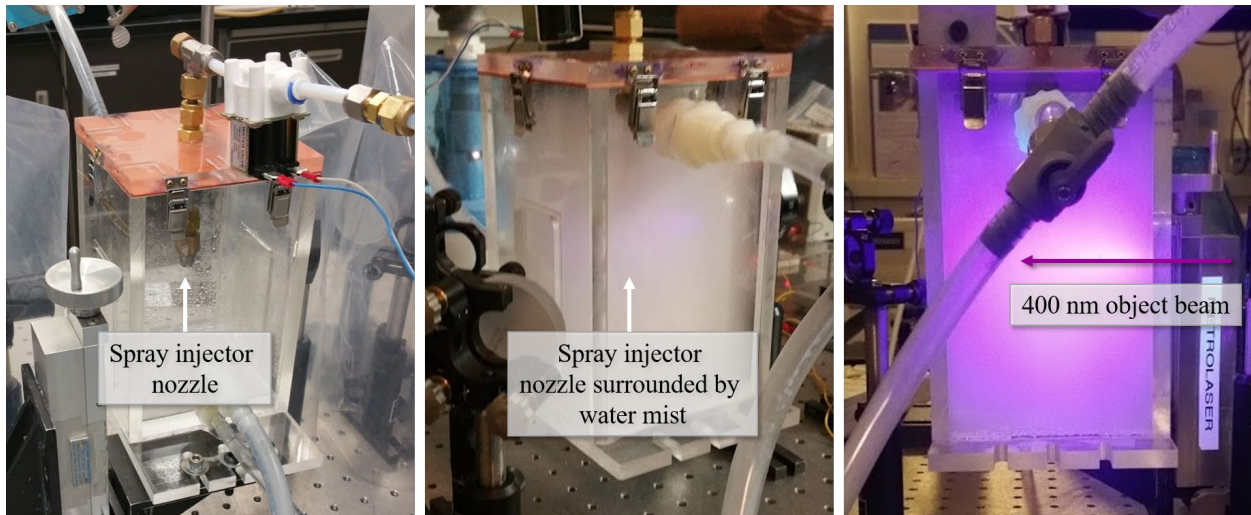


Figure 6.21 The 10 cm mist cell before (left side) and after (middle and right side) being filled with water mist. Scattering is so severe that no collimated portion of the original laser beam can be observed leaving the enclosure.

Distance between the windows is 10 cm. A second chamber with a 5 cm distance between windows was used for lower OD values.

6.2.2 Holography results

This section showcases USPODH's spray image reconstruction performance. The liquid used with all the injectors presented in this chapter is water. All sprays are injected into a chamber at ambient pressure and temperature.

6.2.2.1 *Effects of Nozzle Pressure (unobscured spray)*

Figure 6.22 shows reconstructed images in the near nozzle region of the spray generated by a 0.1 mm single orifice injector. These holograms were acquired with no mist surrounding the core spray in order to provide a comparison for the spray images in highly scattering conditions that will be presented next. At 10.3 bar injection pressure, the fluid looks like a cylindrical column; then, downstream from the nozzle, ligaments start to form, and the ligaments eventually break down into droplets. As the water injection pressure is raised to 11.7 and 13.8 bar we observe a transition into a new breakup mechanism, where the fluid appears to form sheets that downstream separate

into ligaments and droplets. As pressure increases the spray cone angle increases while the penetration depth decreases.

The image quality is excellent and comparable to a state-of-the-art shadowgraph image, with no significant noise being observed and high contrast between the background and the spray liquid interface.

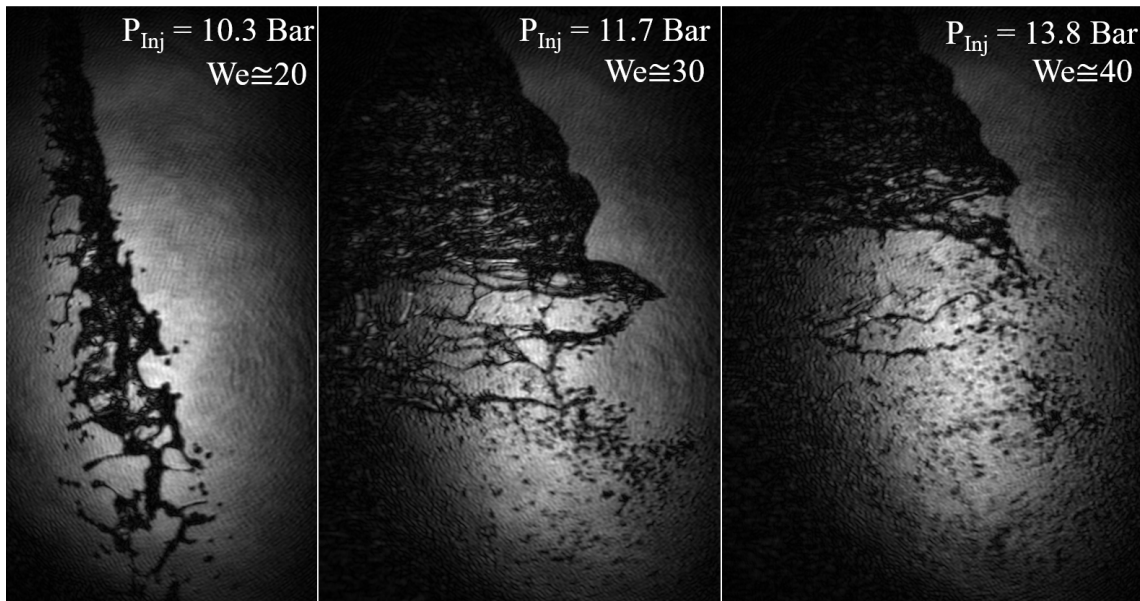


Figure 6.22. Reconstructed images of a water spray from a 0.1 mm single orifice injector with increasing injection pressure. Reconstruction depth is 142 mm from the sensor. Left image injection pressure is 10.3 Bar, middle image 11.7 Bar, right image 13.8 Bar.

6.2.2.2 3-D focusing

As was demonstrated in section 5.5, holography can instantaneously capture the volumetric information of measurement fields so that the particle reconstruction plane can

be freely chosen *a posteriori*, thus freeing the user from having to know in which focal plane does the feature of interest reside in order to focus correctly. The setup we use, in contrast to other spray holography studies [69], [75], [76], takes advantage of an off-axis configuration and an ultrashort pulse laser for maximum coherence filtering and multiple scattering noise mitigation.

The short coherence length of the laser pulse does not limit the depth of reconstruction achieved by the system because holograms are created by interfering forward scattered photons from the object beam with photons from the reference beam. These path-matched photons can interfere over a considerable distance that is not limited by coherence length. This can be easily demonstrated experimentally by reconstructing images from a single hologram where we can focus on droplets within the spray field that are several millimeters away from each other but also on drops residing on windows that are centimeters away from the spray. Focusing is currently accomplished manually because there are few better sensors than the human eye for evaluating the overall quality of the image. The user numerically reconstructs images at different depths while monitoring the edges of a feature of interest. The ideal depth of reconstruction is assumed to be the one where the feature shows the sharpest edges. Manual evaluation is often

superior as it includes a wide range of quality judgments that are difficult to quantify. Nevertheless, for consistency in the future this task can later be automated using an algorithm that monitors the Fourier transform of the reconstructed images at various depths and picks the image with the largest amplitude of the higher spatial frequencies as the “best focused” image, or by employing the correlation coefficient method [77].

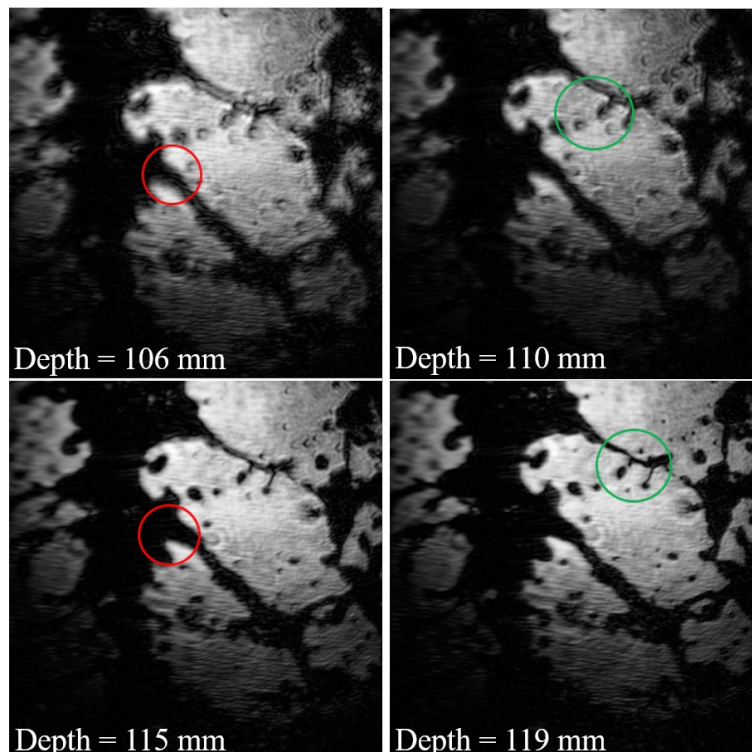


Figure 6.23. Reconstructed images of a spray from a 1996 automotive multi-orifice fuel injector for gasoline port injection; water injection pressure 6.9 bar.

Figure 6.23 shows images reconstructed at different depths within the spray field produced by the automotive fuel injector. The numerical reconstructions span over a

distance of 13 mm. The colored circles show how it is possible to resolve and focus on different features residing at different depths within the spray. The fluid ligament that is out of focus in the top left reconstruction 106 mm away from the camera can be seen coming into focus in the bottom left reconstruction, at 115 mm. The ligaments and droplet that can be seen out of focus in the top right reconstruction, 110 mm from the sensor plane, can be seen coming in focus in the bottom right image, at 119 mm. There is no theoretical limit to the propagation distance from the hologram plane at which we can reconstruct the object wave field, but, as shown in section 5.5, resolution degrades as the reconstruction distance increases.

6.2.2.3 Droplet microscopy in turbid media

This section demonstrates the system performance when imaging a spray in optically dense environments. Recall that the scattering media surrounding the spray is a water droplet mist with SMD of 4.28 microns, and this droplet size is an excellent approximation to the expected droplet size surrounding the core of a typical diesel spray [2], [23], [73]. Figure 6.24 shows a detail from the spray produced by the automotive fuel injector when the spray is buried in the ultrasonic atomizer mist. The target field has an OD of 6, which corresponds to a transmissivity of $2 \cdot 10^{-3}$. Water is injected at 10.3 bar, and the image is reconstructed 120 mm from the camera sensor. Distinct droplets can be

seen within the region of interest (ROI) surrounded by the red rectangle. This ROI is reconstructed in two different depth planes in Figure 6.25. As we move 8 mm closer to the sensor (left picture) the same particles that were visible in the 120 mm depth plane are still visible, but more appear on the right. When looking at the reconstruction on the right, which is 32 mm away from the one on the left, all those particles disappear, and a different droplet appears in focus at the center of the ROI.

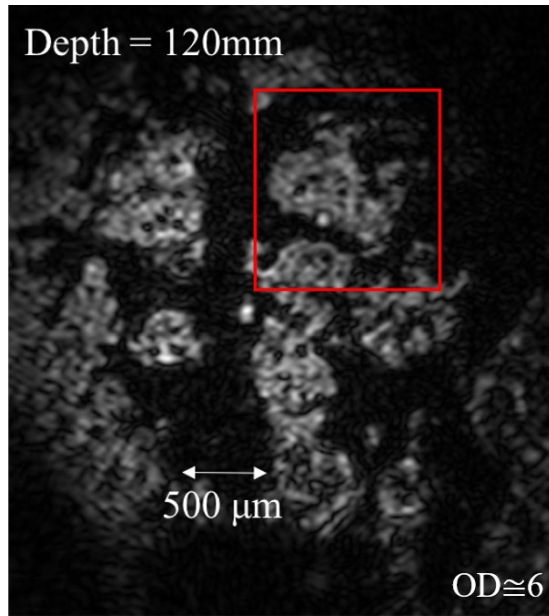


Figure 6.24. Spray from an automotive fuel injector. Injection pressure 10.3 bar. OD 6.

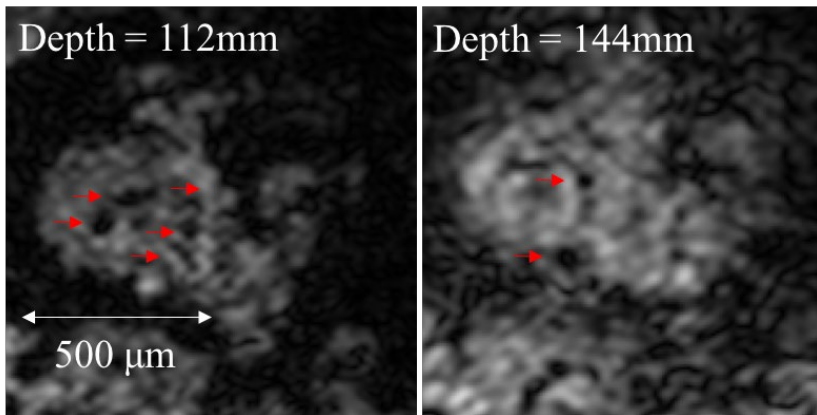


Figure 6.25. The left picture shows the region of interest highlighted in Figure 6.24 but reconstructed 112 mm from the sensor plane. The right picture shows the same ROI reconstructed 144 mm away from the sensor.

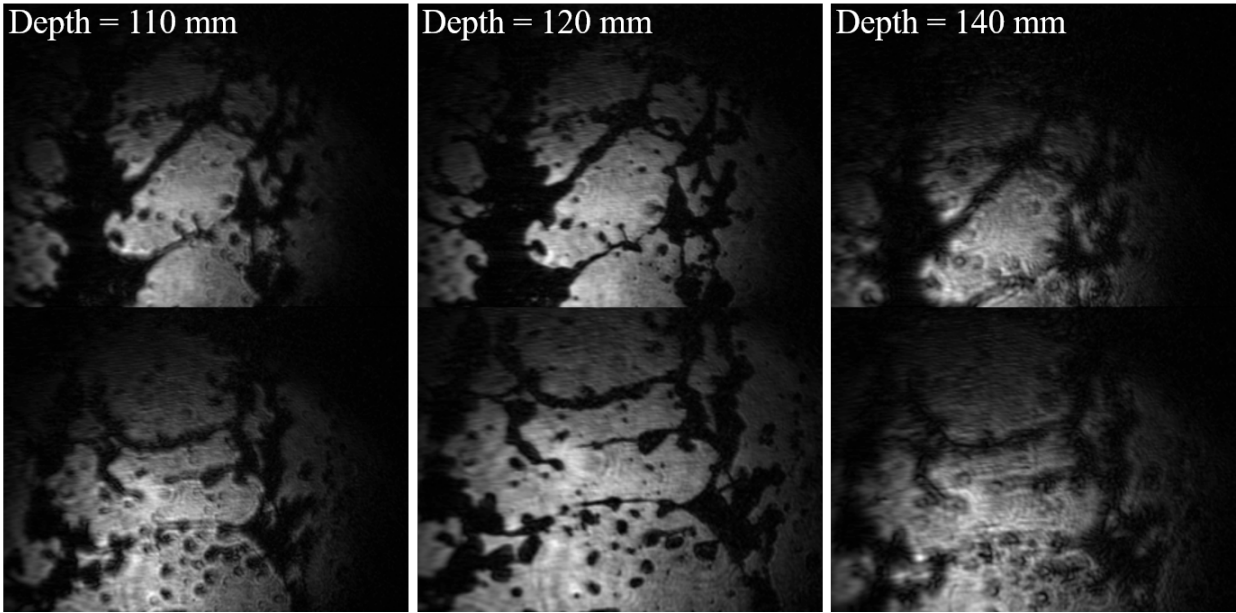


Figure 6.26. Spray from a 1996 automotive multi-orifice fuel injector for gasoline port injection. The bottom row of images is shot 2.5 mm downstream with respect to the top row and reconstructed at the same distance.

Figure 6.26 shows images from the automotive fuel injector where water is injected at 6.9 bar and immersed in an even denser mist. The measured transmissivity of the whole target field is 1×10^{-3} , which corresponds to almost OD 7. As we reconstruct images at different depths, ligaments and droplets come into focus, and the breakup mechanisms are observable in 3-D. The bottom row of images is taken 2.5 mm downstream from the location of the first row. The area imaged is approximately 9 mm^2 , and it is cropped from the whole hologram that in this configuration covers an area of 64 mm^2 .

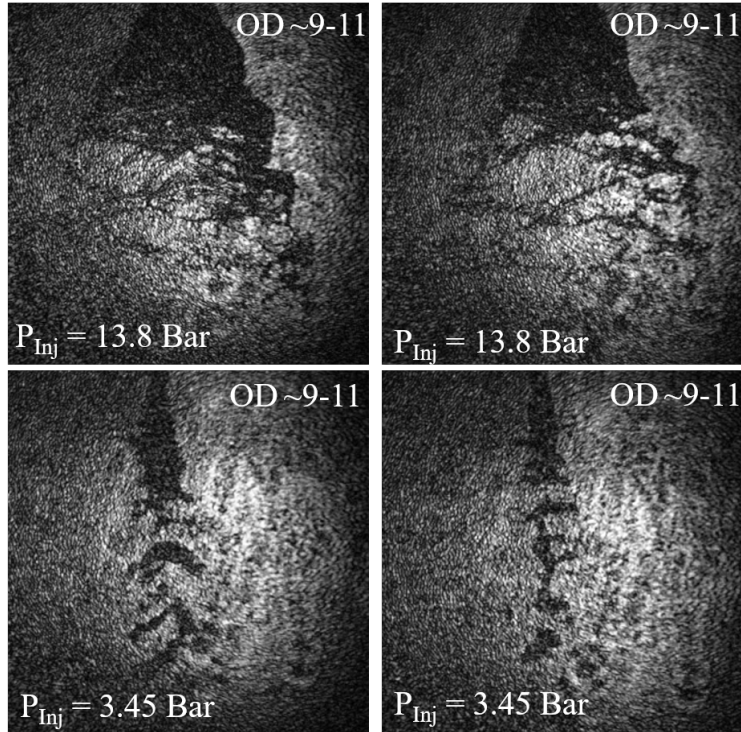


Figure 6.27. Reconstructed images of the 0.1 mm single orifice nozzle – top row shows a water spray injected at 13.8 Bar ($We \cong 44.6$), the image on the right is shot 0.3 s after the one on the left. The bottom row shows a water spray injected at 3.45 Bar ($We \cong 8.5$), the image on the right is shot 0.1 s after the one on the left. Transmissivity of the whole spray field varies from 10^{-5} to 10^{-4} (OD $\cong 9-11$).

Figure 6.27 shows the spray from a 0.1 mm single orifice nozzle where water is injected at 13.8 bar (top row) and 3.45 bar (bottom row). The overall target transmissivity is 2×10^{-5} , or OD 11. In this extreme scattering condition, the breakup process is still visible even though the image quality has deteriorated substantially.

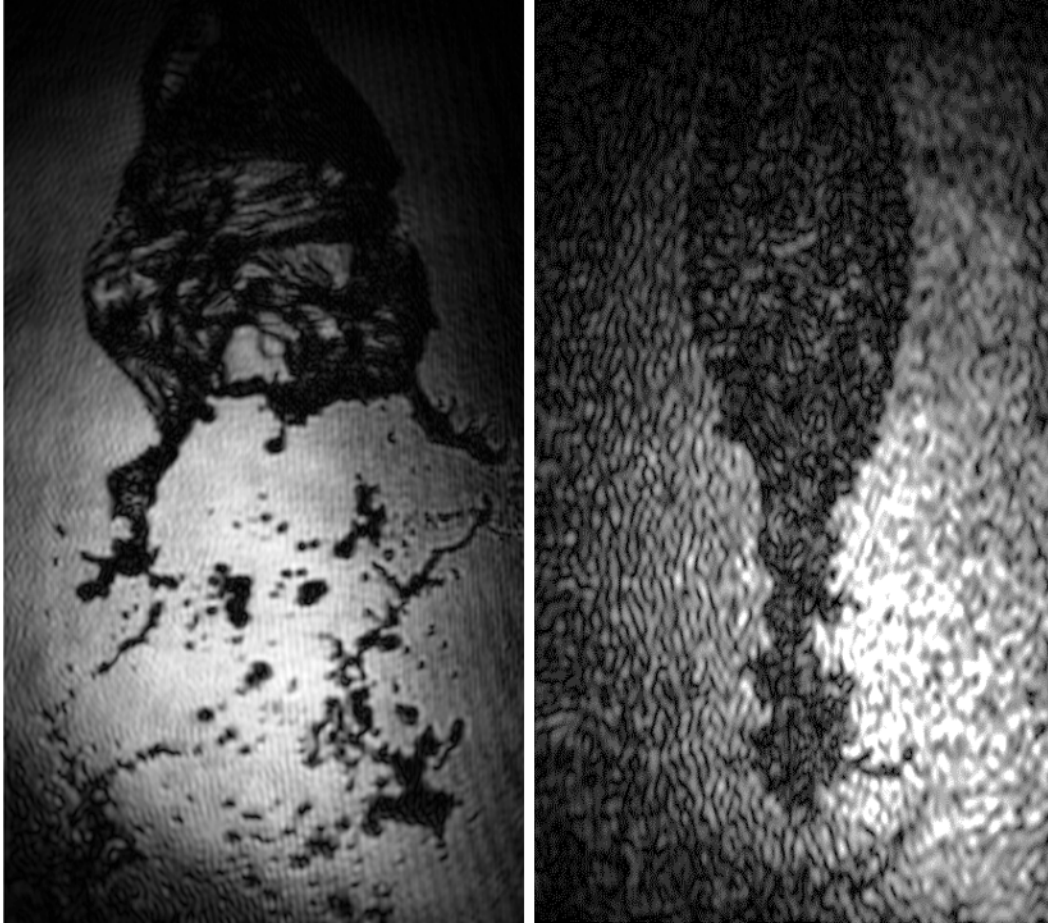


Figure 6.28. Reconstructed image with no surrounding mist (left) and with a mist of OD 12 (right). 0.1 mm single orifice nozzle, water injected at 2.06 bar.

Figure 6.28 shows a side by side comparison where the same spray is imaged with and without a surrounding mist. The environment OD is approximately 12, meaning that only 2 photons out of a million traverse the target field without encountering a scattering event. The target field is essentially optically opaque in the visible range. These images are compelling evidence of the efficacy of femtosecond coherence filtering in reducing multiple scattering noise for the conditions of these experiments.

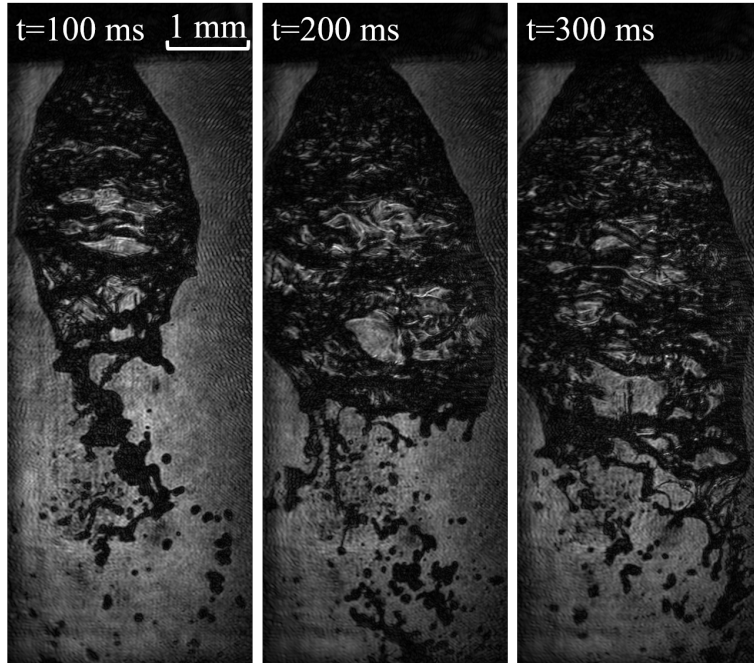


Figure 6.29. Reconstructed images from a 0.3 mm single orifice nozzle. Injection pressure 2 Bar. Depth of reconstruction 142 mm.

Figure 6.29 Shows numerical reconstructions of the spray created by a 0.3 mm single orifice nozzle as it develops over time. Images are taken 100 ms apart; no mist is present. A higher frame rate would be desirable to image the spray dynamics, but the current system is limited by the 1 kHz repetition rate of the Ti-Sapphire laser and the limited camera burst acquisition rate.

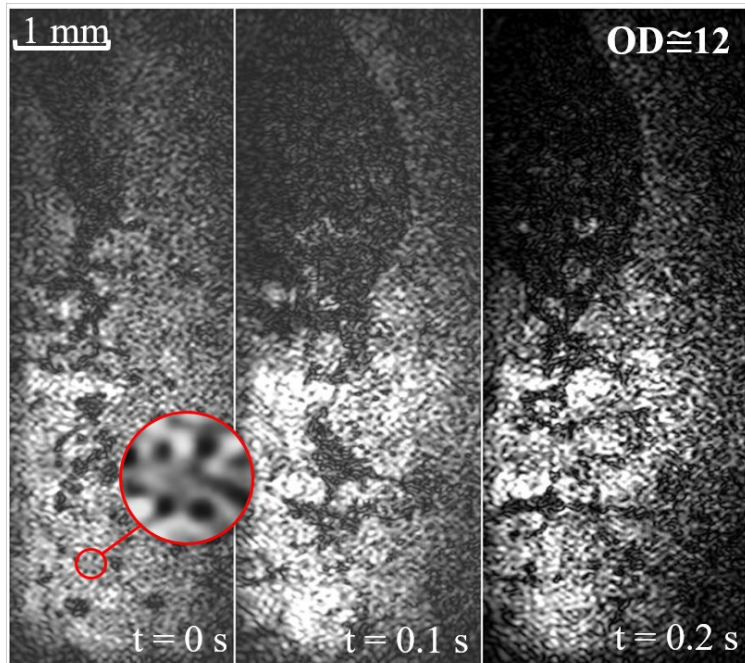
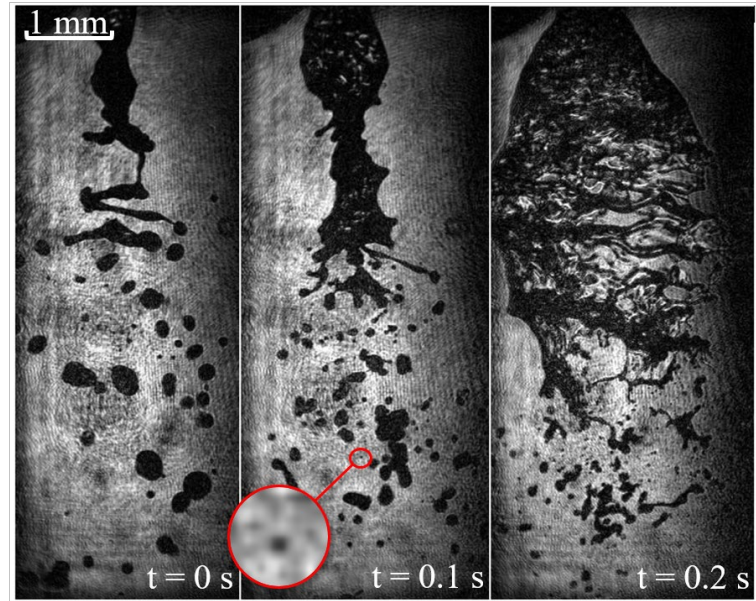


Figure 6.30. Spray from a 0.3 mm single orifice nozzle injected at 2 Bar as it develops over time ($We \approx 11$). Images are reconstructed 142 mm from the camera sensor. The top row shows the spray with no mist; the bottom row

shows the spray surrounded by a mist with transmissivity as low as $0.5 \cdot 10^{-5}$ (OD 12).

Figure 6.30 shows the spray generated by a 0.3 mm single orifice injector, with and without mist surrounding it. Water is injected at 2 bar. The top row is imaged without any mist, and each image is shot 100 ms after the one to its left; the jet starts as a liquid column, and it then develops instabilities that form ligaments and droplets. Eventually, liquid sheets form and break up into ligaments and then droplets. The smallest droplets we can resolve (highlighted by the red circle) have an apparent diameter of approximately 25 micrometers. Although this is not a very fine resolution, droplets of this size can be resolved even when they reside in planes several centimeters away from each other, a remarkable depth of field feature of holographic imaging that is not shared by other imaging methods.

Reconstructions in the bottom row show the same spray imaged in OD 12 conditions. Once again, every image is shot 100 ms after the one to its left. Even though the mist clearly degrades the image quality, it is still possible to resolve droplets with a diameter of approximately 25 μm , circled in red. To appreciate the multiple scattering noise rejection capability of UPODH, Figure 6.31 shows a regular lens image where spatial filtering rejects some of the multiple scattering noise; this image was acquired in OD 11 conditions.

The spray outline is barely recognizable, and no droplets can be resolved. This lens image was captured using a $2f$ arrangement, with $f=50\text{mm}$. The optical lens is placed in the hologram plane replacing the CCD so that the CCD and the spray are on opposite sides of the lens both at a distance equal to $2f$. This configuration forms a real image of the spray on the CCD with a magnification of one. An iris is placed before the lens so that the numerical aperture of the $2f$ system matches the digital holography system's aperture. This means that any improvement in image quality and scattering noise reduction achieved by the holographic system is due to the technique's coherence filtering and is independent of the numerical aperture. This comparison favorably shows coherence filtering's efficacy in suppressing multiple scattering noise, especially considering how the Monte Carlo simulations presented in chapter 4 show that spatial filtering is a theoretically adequate means of scattering noise rejection for ODs up to 10, but fails to deliver an image under realistic experimental conditions with OD 11.

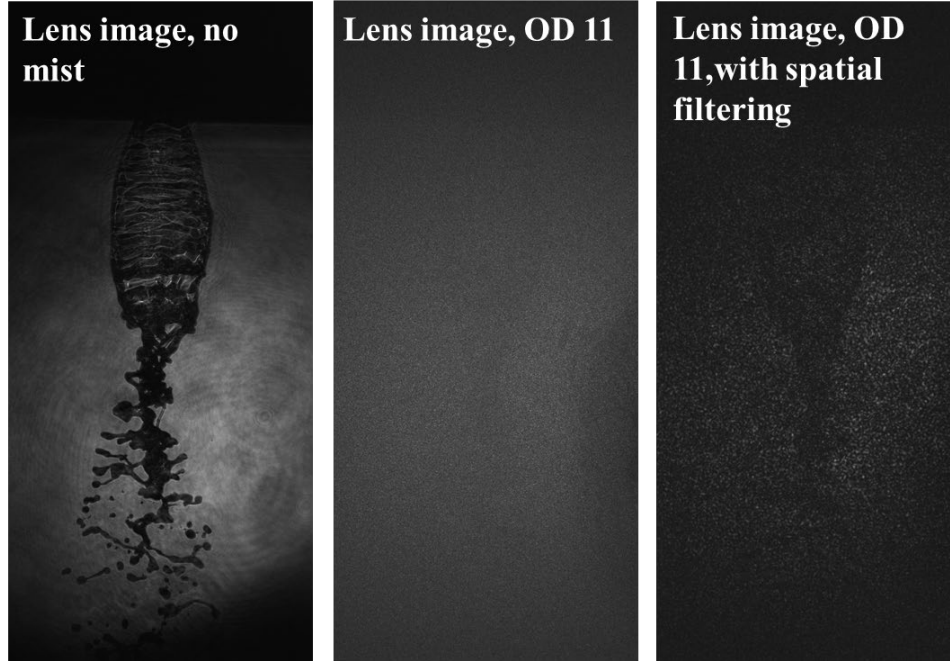


Figure 6.31. Lens image of the spray, $2f$ imaging layout with $f=50$. Water is injected at 30 PSI through a 0.1 mm single orifice nozzle. The left image is acquired with no mist surrounding the spray; the middle image shows the effects of scattering noise at $OD=11$ (transmittance 10^{-5}). In the image on the right spatial filtering provided by a 4 mm aperture is used to match the holographic system's numerical aperture and provide a fair comparison to the holographic reconstructions shown in Figure 6.30.

The theoretical object-side lateral resolution achievable by the system is:

$$\Delta x = \sqrt{\frac{3\lambda^2 z}{L_c}}$$

Where λ is the laser central wavelength, 400 nm, z is the depth of reconstruction which in our setup is in the order of 100 mm, and L_c is the laser pulse coherence length which is 30 microns. These values give us a theoretical lateral resolution of 40 microns; which compares well with what is observed experimentally.

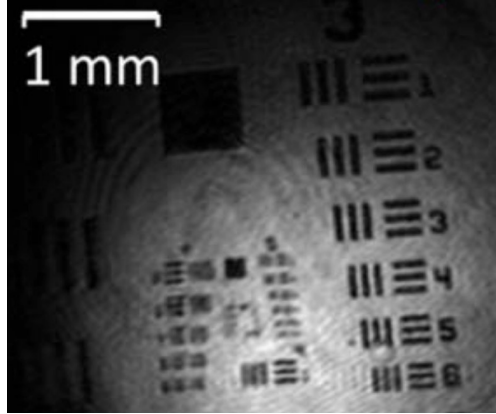


Figure 6.32 The image of a USAF resolution chart placed inside the vessel at the spray location is reconstructed. Element 2 of group 4 can be resolved, meaning that the object side resolution at this reconstruction distance (approx 10-15 cm) is approximately 27 μm .

6.3 Section summary

This chapter described the results obtained using an ultrashort-pulse off-axis digital holography system to image small particles within highly scattering turbid media. We found that using high-energy ultra-short pulses in digital holography maximizes the efficacy of coherence gating in suppressing multiple scattering noise in these conditions. Furthermore, the technique can be beneficial when imaging fast transient phenomena, such as atomizing sprays.

A target spray designed to recreate the optically dense conditions of a high-pressure diesel spray was used to prove the efficacy of coherence filtering as a means of multiple

scattering noise reduction in extreme scattering spray environments typical of a diesel spray. Droplets as small as 25 microns were positively identified in optically dense conditions with OD up to 12. In these conditions, the target field is substantially opaque. A comparison to spatially filtered shadowgraph images that simulations and previous experiments showed to be a reliable scattering noise suppression solution at ODs up to 9-10 was provided, showing how spatial filtering alone fails to deliver a recognizable spray image under these experimental conditions. The 3-D, depth scanning capability of the technique was also demonstrated by reconstructing and resolving fluid ligaments and droplets residing in depth planes centimeters away from each other. The resolution achieved when imaging in highly scattering conditions matches or surpasses that achieved by the current state-of-the-art time-gated ballistic imaging systems.

The following chapters address the remaining factors that still need to be investigated in order to validate the efficacy of USPODH as a dense spray imaging technique, proving how the technique is unaffected by the pulse dispersion that is inevitable when imaging in realistic fuel injection environments with intense pressure and temperature gradients and thick optical windows.

Chapter 7

7 Imaging of a realistic dodecane spray (ambient conditions)

This chapter will demonstrate USPODH's first application imaging a realistic high-pressure fuel spray, the two main goals are to fine-tune the technique so that it can be effectively deployed in realistic high-pressure spray laboratory environments in the future and to produce new data of the gas to liquid interface in the primary atomization region of a diesel-like spray.

This research was conducted in collaboration with researchers at the Colorado School of Mines (CSM), with their role being to provide the use of a state-of-the-art pressure vessel and fuel injection system called the "Diesel Engine Simulator" (Figure 7.1). Using this new spray facility required building a new USPODH setup that would address not only the changes in geometric demands of this engine simulator but also the challenges that naturally occur when working with targets in high-pressure, high-temperature

environments, such as: long working distance, imaging through thick pressure rated windows that cause pulse dispersion, synchronization of the laser-spray-camera system to reliably acquire images of early injection events, and automating the experiment so that it can be operated from a safe location when pressurized. These topics and more will be discussed in the next chapters. The experimental work described was a collaboration as mentioned above, with the ultimate goal being the comparison of holographic imaging methods with ballistic imaging approaches used by the CSM team. All of the work presented here, however, is the author's, including operating the simulator, and all optical measurements. Follow-on work is expected to continue with the CSM group.

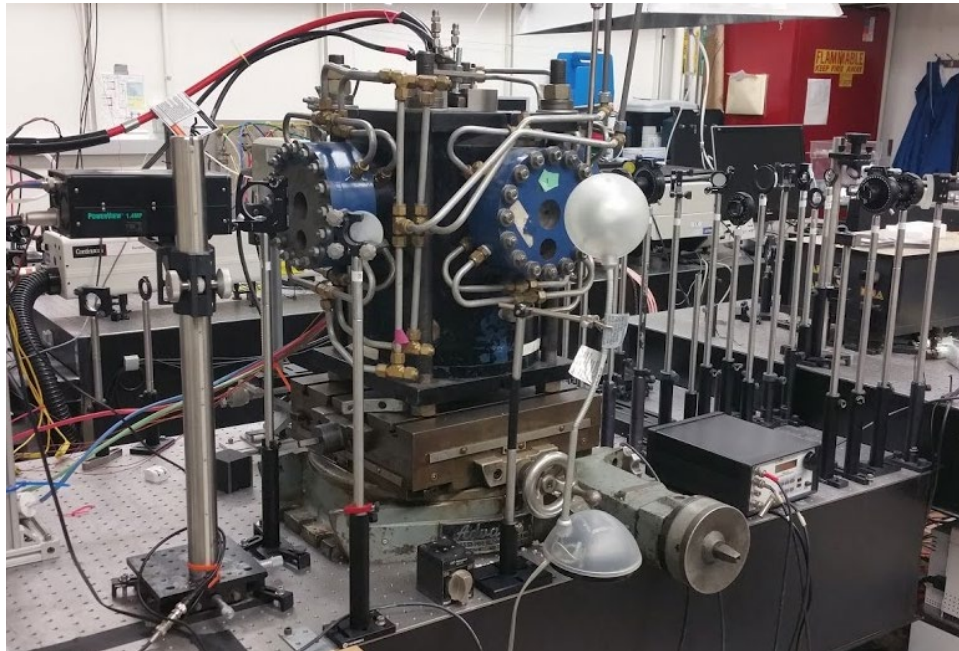


Figure 7.1 The Diesel Engine Simulator setup at UC Irvine.

7.1 Experimental Setup

7.1.1 Spray setup

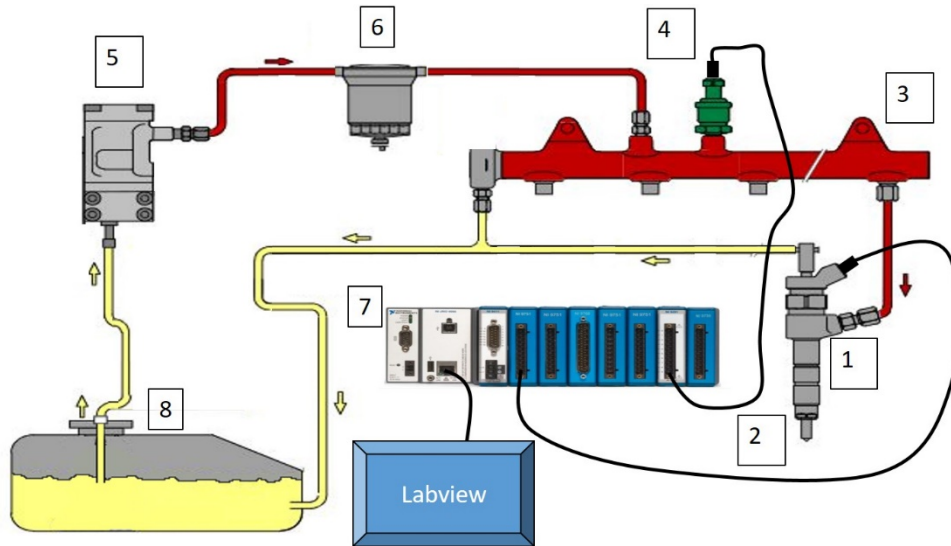


Figure 7.2 Fuel injection setup. 1. Bosch LBZ injector, 2. Two custom single hole axial injector nozzles (160 and 320 microns), 3. Common Rail, 4. Pressure Transducer, 5. Air over fuel pressure accumulator, -6. High-pressure inline filter, 7. Direct Injector Driver Module, 8. Fuel tank.

The “Diesel Engine Simulator” from the Colorado School of Mines is composed of a heated pressure vessel, a flow control panel to control nitrogen pressure and flow rate in and out of the vessel and a common rail diesel injection system controlled by a National Instruments DIDS interface that allows full control of the injection events timing. Figure 7.2 shows the layout of the common rail fuel injection setup. The fuel injector is a Bosch

LBZ that has been customized to have a single orifice nozzle with a diameter of 160 μm , a second injector with a 320 μm nozzle diameter is also available. The common rail pressure is set between 1500 and 1700 bar by a nitrogen driven booster pump, connected through a flow control panel to a 6-bottle rack of nitrogen bottles. Injection pressure, duration, and the number of events are controlled via a National Instruments Direct Injector Driver System DIDS-2023. A TTL signal from the TI-Sapphire laser synchronizer triggers the PCO Camera, the fuel injector and the Phantom camera. The user can set the time at which the hologram is to be acquired from the beginning of the injection sequence so that transient, early injection events can be imaged. The fuel injector is fit inside a pressure vessel [57], which is heated and rated for pressures up to 40 bar with temperatures up to 650 $^{\circ}\text{C}$. A cooling jacket where chilled water is recirculated provides cooling to the fuel injector body. The pressure vessel has three heating zones to maintain the injection region at a constant, controllable temperature. One zone heats the walls surrounding the injection area, while the other two heat a packed bed of steel spheres which heats a flow of nitrogen to supply a constant gas temperature. Using a fine wire thermocouple that reads gas temperatures in the center of the injection region provided the required flow rate through the packed bed to overcome natural convective cells within the vessel as the pressure increases. The chart below shows flow rate through the packed bed (SLPM) vs.

pressure of the vessel (PSIG) necessary to maintain a constant gas temperature of 600° C with all heating zones set to 630° C. A logarithmic line fit of the data indicates a flow rate of ~50 SLPM through the packed bed at 40 bar pressure is needed to overcome natural convective flow cells.

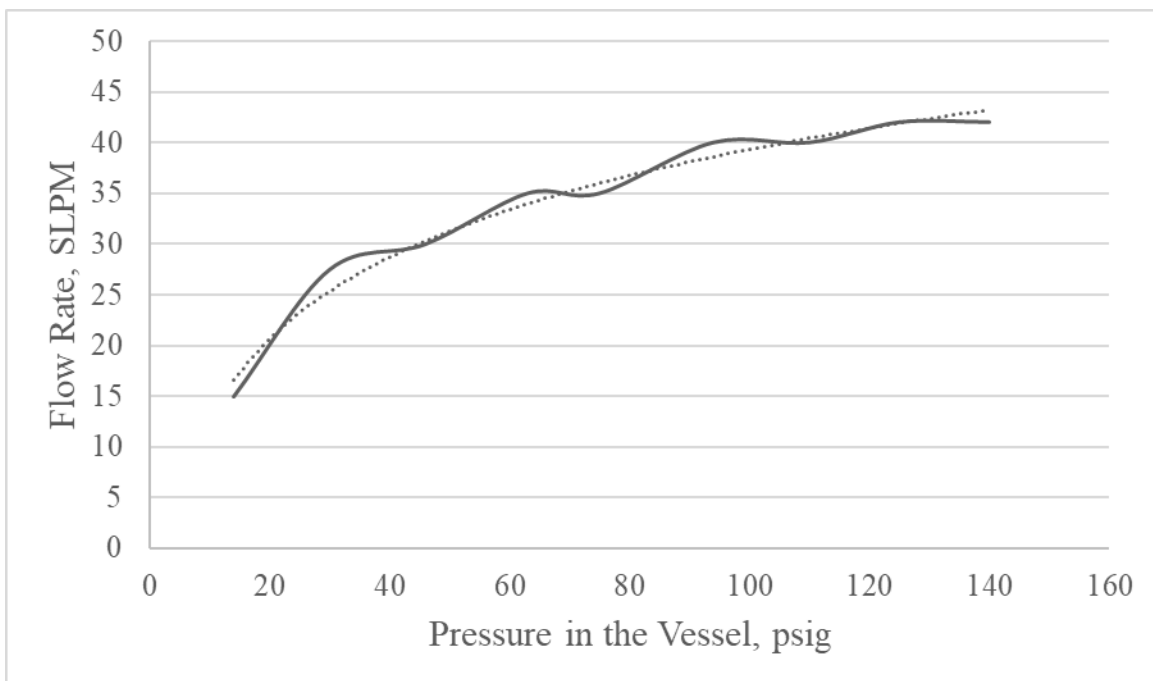


Figure 7.3 Vessel flow characterization performed at CSM to maintain the injection zone at a constant temperature.

The vessel has 4 fused silica windows along 2 orthogonal optical access axes; the windows are 1.5 cm thick with a 3 cm diameter. Two windows are used by the holographic system while the other windows can be used for traditional high-speed imaging, in this case, the standard imaging is performed using a Phantom V4 high-speed video camera which

provides shadowgraph movies of the spray that can be compared to the holographic reconstructions (Figure 7.4).

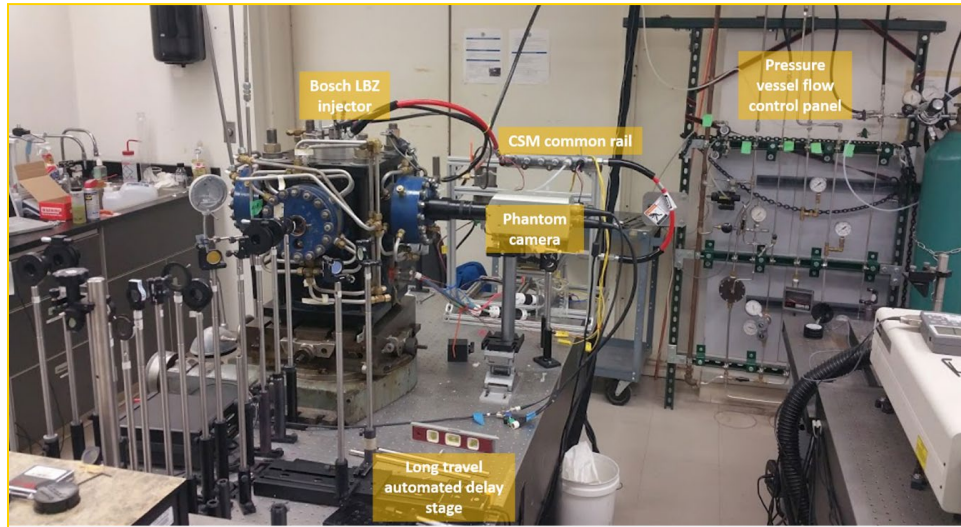


Figure 7.4 CSM diesel engine simulator fitted within the ultra-short pulse off-axis holography experiment at UC Irvine.

In addition to evaluating the natural convective flow in the vessel, the CSM group also designed and fabricated a new injector housing to accommodate the Bosch LBZ injectors. The injector core temperature must be kept below 200 °C to prevent coking of the diesel fuel (n-dodecane). Using ANSYS FLUENT software, the CSM group was able to design an injector housing with a water-cooled jacket for the injector that cools the injector to below the critical decomposition temperature of n-dodecane while simultaneously allowing the injector tip to be in the simulated engine environment. The figures below show the FLUENT model for the cooling jacket.

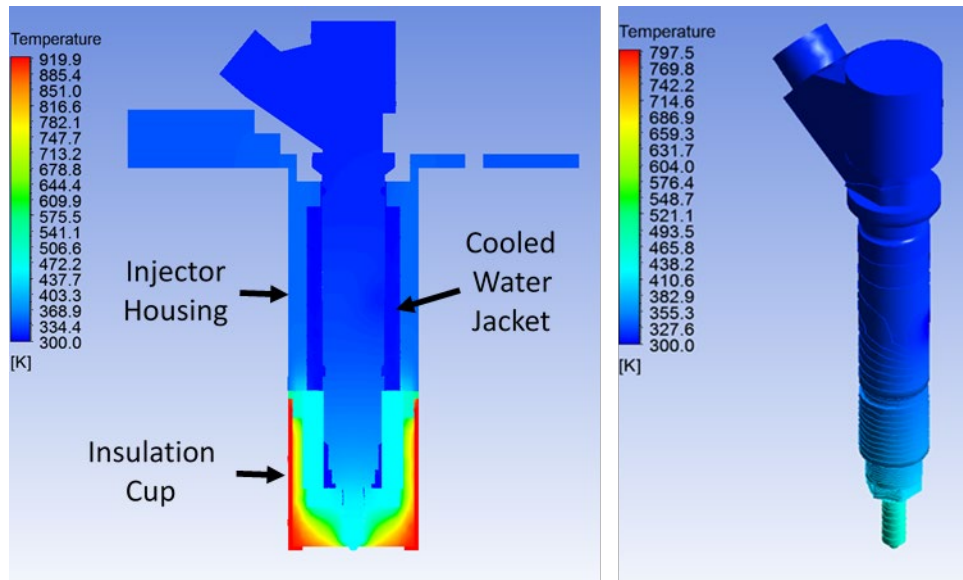


Figure 7.5 Fluent model used to validate the injector cooling jacket design.

The boundary conditions for the FLUENT model are as follows:

- Constant temperature at the insulation cup, $T = 923$ K (ignition chamber condition).
- Constant temperature at the outer housing wall, $T = 350$ K (vessel body temperature).
- Convection $h = 5$ W/m²K, $T = 300$ K (surfaces not in contact with vessel).
- Room temperature ($T = 300$ K) water cycled through injector housing at $\dot{Q} = 0.01$ kg/min.

7.1.2 Optical setup

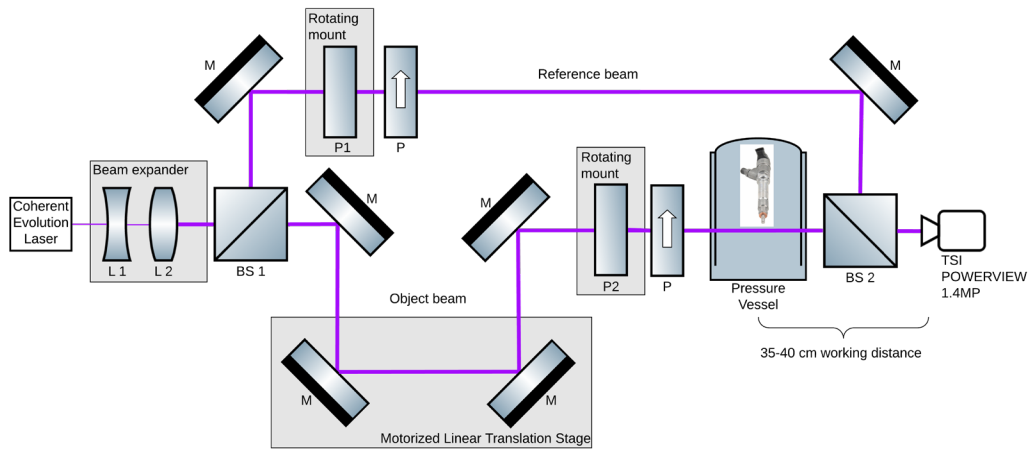


Figure 7.6 USPODH optical setup

The optical layout is similar to a Mach-Zender interferometer with an adjustable delay stage and a pressure vessel along the “test path” (object beam from now on), and a reference path that goes around the pressure vessel. The two paths are pathlength matched to achieve interference at the camera sensor plane. Figure 7.6 shows the optical layout of the system, while Figure 7.7 shows the actual setup from above. Looking at the figure from the left-hand side, a doubling crystal converts the pulse wavelength from 800 to 400 nm; then a Galilean telescope is used to expand the beam and collimate it. The expanded beam diameter is 9 mm. Beam expansion enlarges the field of view so that a larger portion of the spray can be reconstructed, while at the same time offering a larger area that is homogeneously illuminated. This has been partially successful, but the beam

illumination is still inhomogeneous. In future efforts, further expansion of the beam coupled with larger diameter optics will be employed. After the expansion, a beam splitter (BS1) separates the object and reference beam. The object beam goes through a delay arrangement mounted on a motorized translation stage that is used to pathlength match the two beams so that they interfere on the camera sensor. The stage has a travel range of 300 mm, a minimum step size of 0.1 μm , and an on-axis accuracy of 5 μm ; these specifications allow reliable pathlength matching for the two beams over any pressure and temperature condition that the vessel can achieve. The object beam enters the vessel through a 1.5 cm thick, fused quartz window. It then passes just underneath the spray nozzle and exits the vessel from another window of the same size and material. The reference beam is routed around the vessel. The two beams meet at a beam splitter that is placed just in front of the camera; this beam splitter is angled so that the two beams interfere at a small angle of $\vartheta = 0.03$ radian. As was extensively discussed in previous chapters this angle is of great importance in off-axis holography because if it is too small, then the DC and cross-correlation terms would be overlapping in the frequency domain, thus hindering the reconstruction of the cross-correlation term free from the noise induced by the DC term. If the angle is too large, the interference pattern of the two beams covers only a narrow band of the CCD sensor, thus reducing the size of the hologram which in

turn reduces the resolution of the reconstructed images. The optimization process necessary to find the appropriate value for ϑ is presented in section 5.6 and [12]. The pathlength matched reference and object pulse interfere on the camera sensor, and the interference pattern is recorded. The camera is a TSI Powerview 1.4MP; it has a cooled, monochromatic, CCD sensor with a $6.45 \mu\text{m}$ pixel size.

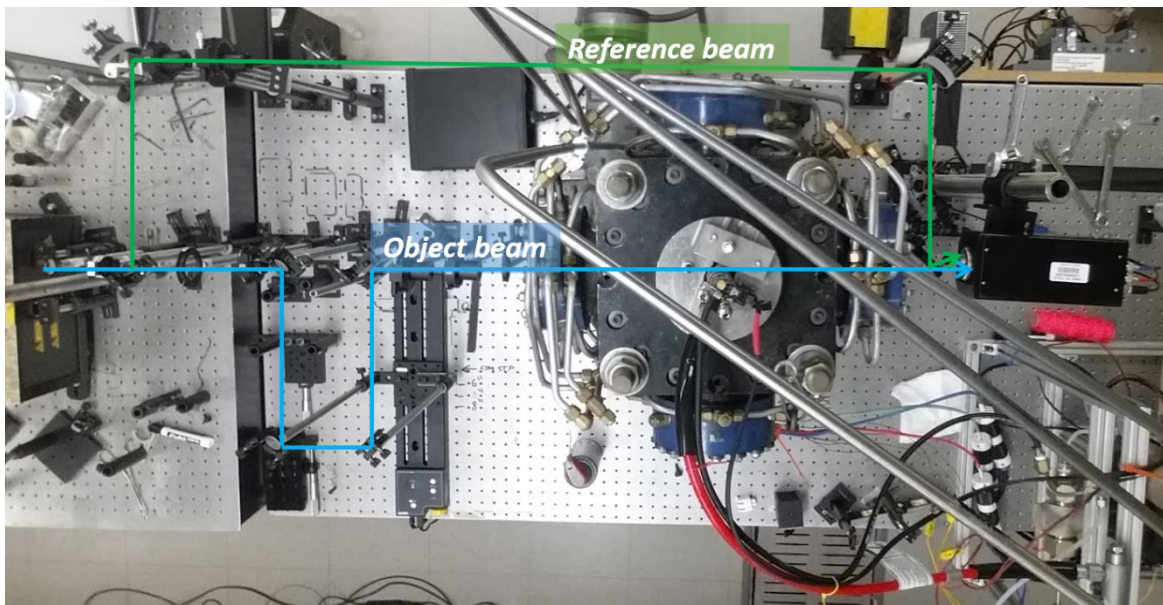


Figure 7.7 Object and reference beam path.

7.2 Results

7.2.1 Imaging injection in the near nozzle region.

This section shows the performance achieved by the technique when imaging early injection events in the near nozzle region. The fuel used in all these results is dodecane,

injected at pressures between 1500 and 1700 bar. The vessel is at ambient pressure and temperature. The average spray properties are reported in the following table.

Table 7.1 Spray properties.

Temperature (K)	295
Dynamic viscosity (Pa*s)	0.00134
Surface tension (mN/m)	25.35
Density (Kg/m ³)	750
Exit fluid velocity (m/s)	643
Re	57555
We	1.95*10 ⁶
Oh	0.00065
Density ratio (ρ_L/ρ_G)	596.5

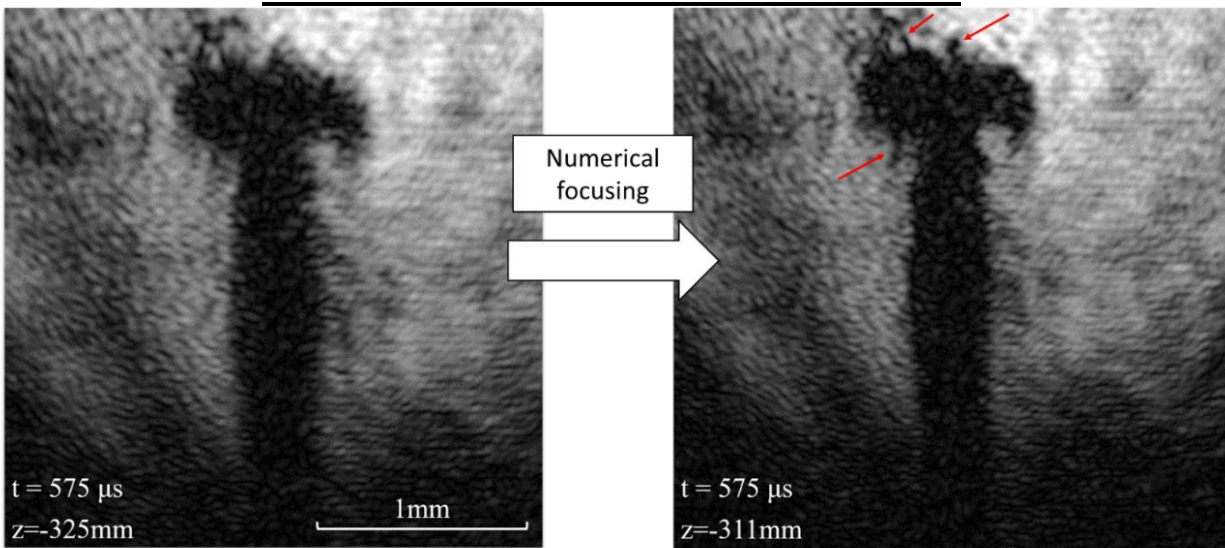


Figure 7.8 Dodecane spray imaged 575 μ s after the fuel spray is triggered. The left image is numerically refocused to highlight ligaments detaching from the spray core.

Figure 7.8 shows the spray produced by dodecane fuel injected at 150-180 MPa. This frame is shot 575 μ s after triggering the injector. The nozzle is at the bottom of this image

and is not illuminated. The figure on the left shows a numerical reconstruction in a plane 325 mm from the camera sensor, which is a position past the fuel injector nozzle. The image is out of focus since it is reconstructed past the plane where the spray resides. As the reconstruction plane is gradually moved towards the actual location of the spray nozzle, features start coming in focus. The figure on the right is reconstructed 311 mm from the sensor and shows ligaments detaching from the top of the spray core (highlighted by arrows). Numerical focusing allows the user to map the location in space of features such as droplets and ligaments without having to optically focus beforehand. Hence, one advantage offered by digital holography with respect to traditional incoherent imaging techniques is that the user can take advantage of the extended depth of field recorded in a single hologram to numerically focus on any feature of interest.

Looking at the highlighted ligaments in Figure 7.9, the ligament in the top left region (labeled as “1”) is approximately 30 μm wide and 86 μm long, ligament 2 extends 163 μm from the spray core and is 38 μm wide, ligament 3 is 127 μm long and 40 μm wide. These measurements are consistent with the measured object-side resolution that at this reconstruction depth is approximately 35 μm . The whole spray core is 2.2 mm long and has a constant width of 0.4 mm, while the “mushroom” shape at the top of the jet is twice

as wide measuring 0.86 mm in width. The core's constant width suggests that it is still intact at this distance from the nozzle with no significant mass shedding. It is still liquid, and no breakup has happened yet. The object-side resolution at this reconstruction depth is approximately 35 μm . This early injection mushroom-like structure at ambient temperature and pressure has been reported before by other researchers, including the existence of the microscopic ligaments that we observed ahead of the jet. Crua et al. attributed it to residual fuel trapped inside the nozzle orifice between injections and showed that it could also happen at engine-like conditions [78].

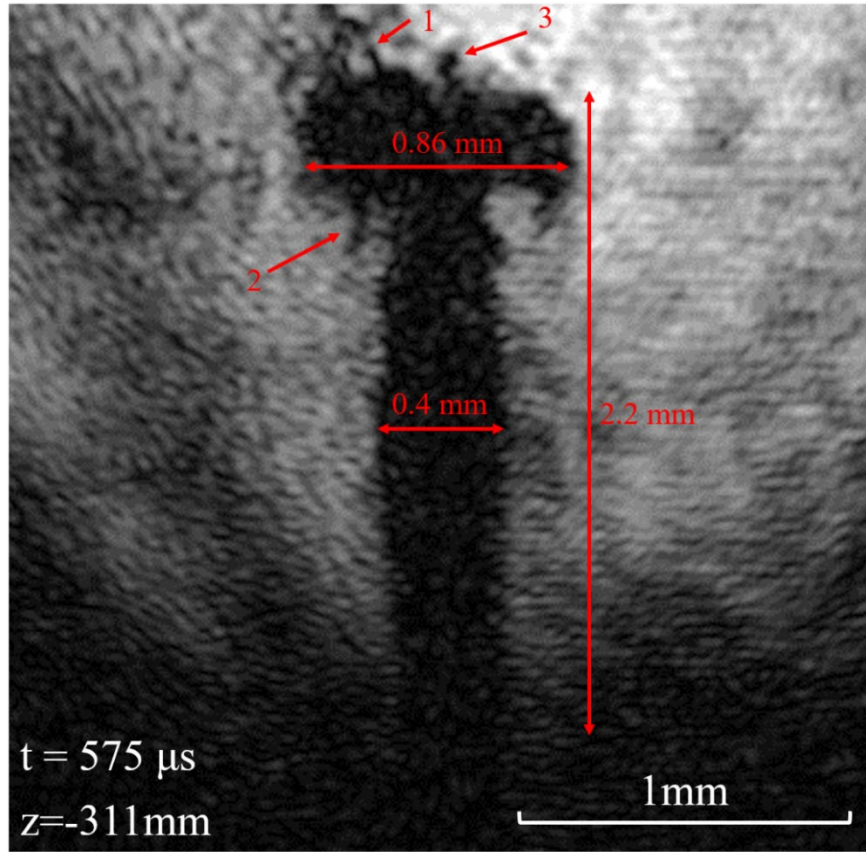


Figure 7.9 Dodecane spray, P_{inj} = 1550 bar, 1 ms injection. Image reconstructed 311 mm from the camera sensor.

Figure 7.10 shows a comparison between a shadowgraph image shot by a Phantom camera and a numerical reconstruction from a single shot hologram. The two images are shot at the same instant, and the Phantom's shadowgraph is superimposed on the reconstructed image. Looking from left to right the transparency of the shadowgraph is increased to highlight the differences between the two. The shadowgraph image appears blurry and less detailed due to the relatively low Phantom camera resolution and due to the poor optical sectioning provided by incoherent imaging. That is, when using

incoherent imaging the user can either choose a high F-number lens, thus increasing depth of field to bring features residing in different planes all in focus or pick a low F-number lens with a shallow depth of field and focus only on the layer of interest (thus having to know at which depth focus should be carefully set). The holographic numerical reconstruction instead allows *a posteriori* focusing and provides a sharper image thanks to its superior optical sectioning. On the other hand, coherent imaging suffers from stronger speckle noise which conveys a granular appearance to the image; future iterations of this technique will adopt speckle noise suppression strategies.

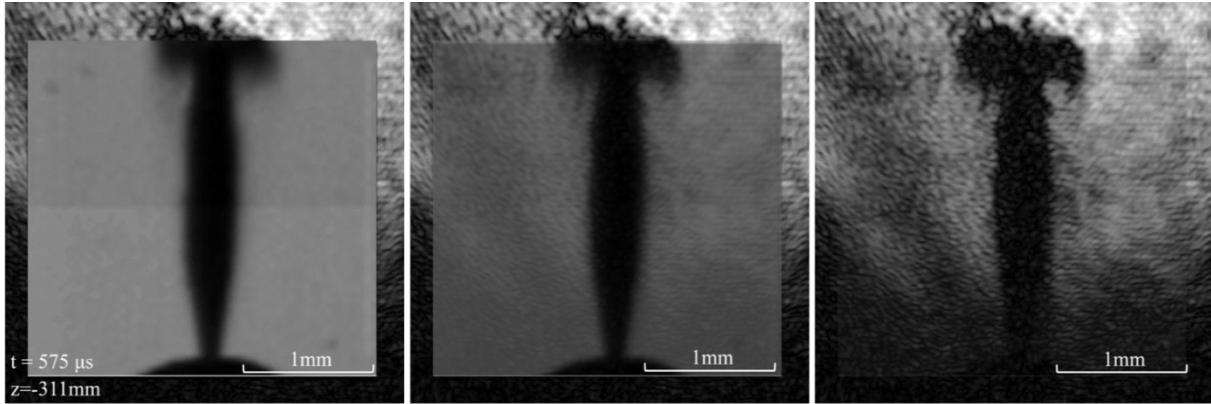


Figure 7.10 Comparison between holographic reconstruction and shadowgraph image captured using a Phantom camera. The Phantom image is superimposed on the reconstructed image, and its transparency is increased (from left to right 0%, 50 %, and 90% transparency).

7.2.2 Holography of high-pressure dodecane spray in high OD environment.

Another advantage of coherent imaging is its ability to image targets hidden by a turbid media. In this configuration, where the source light is transmitted through the spray field, the light scattered from each point of the object spreads out and covers a large area of the camera sensor, so there is not a one-to-one correspondence between a portion of the hologram and a region of the object. This means that the information about any object point is recorded over the whole hologram and only a small portion of the hologram is required to reconstruct an image of the entire object [79]. This is especially convenient when imaging through regions with harsh scattering conditions or even when imaging

using a damaged sensor. Only relatively few ballistic photons are needed to successfully reach the sensor and interfere with the reference pulse in order to reconstruct an image of the target. When in the same conditions incoherent image would provide no helpful information [12], [80], [81]. To show this ability to image through turbid media, the fuel injection rig was programmed to perform consecutive 5 ms long injection events with a 10 ms period between them; the pressure vessel had no flow flushing the chamber from the dodecane mist accumulating after each event. The shadowgraph images acquired by the Phantom camera show that around the 5th injection event (Figure 7.11) the outline of the spray cone is barely visible, and by the 7th injection the chamber volume is flooded with dodecane mist, and incoherent imaging becomes ineffective (Figure 7.12).

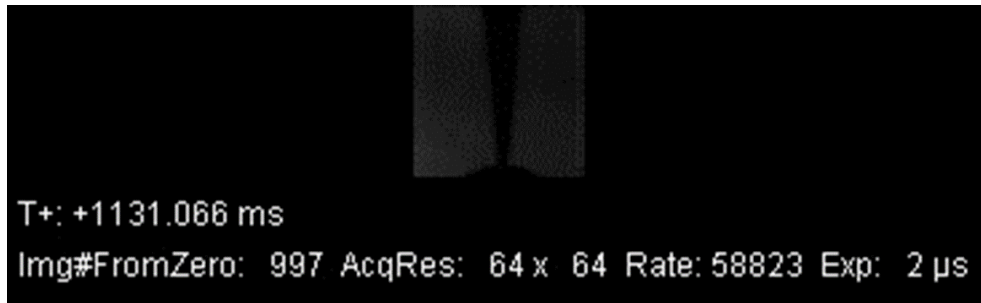


Figure 7.11 Phantom camera, shadowgraph image. 5th injection event.



Figure 7.12 Phantom camera, shadowgraph image. 7th injection event.

When looking at the raw hologram recorded under the same conditions (after the 7th injection event when dodecane mist entirely obscures the vessel) it appears that no object-beam information is left, and the interference pattern is almost invisible (Figure 7.13). But even though there is no visible image of the object beam, the Fourier transform of the hologram (Figure 7.14) shows a strong cross-correlation term from which an image of the target can be reconstructed. This shows digital holography's resilience to signal corruption caused by multiple scattering, one of its advantages with respect to conventional incoherent imaging. This is due to the amplitude of the reference beam multiplying the complex amplitude of the object beam in the expression of the

interference pattern intensity: the reference beam is modulating and amplifying the information conveyed by the object beam.

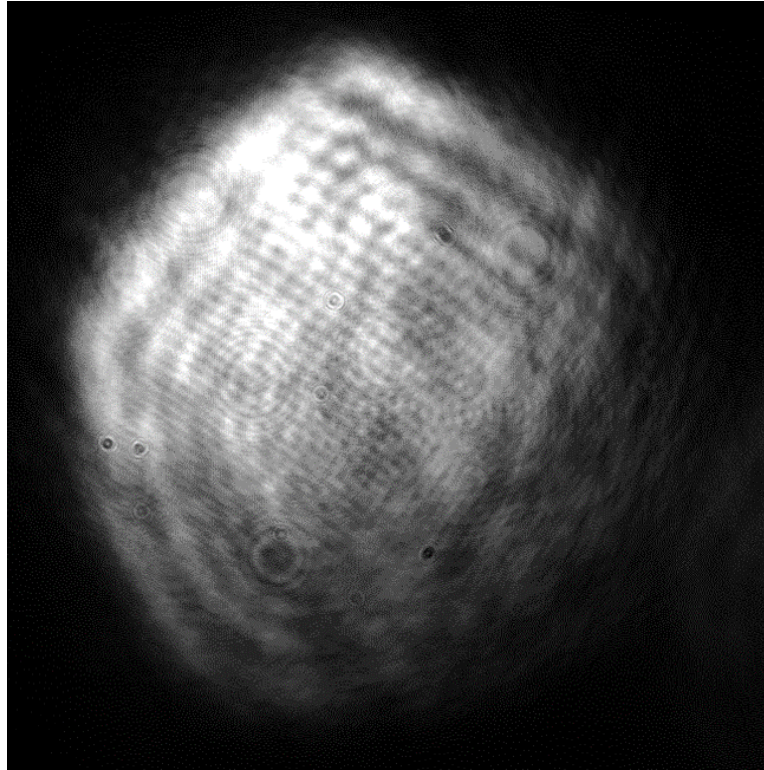


Figure 7.13 Hologram shot after the 7th injection event, the object beam outline disappeared, and the interference pattern is almost invisible.

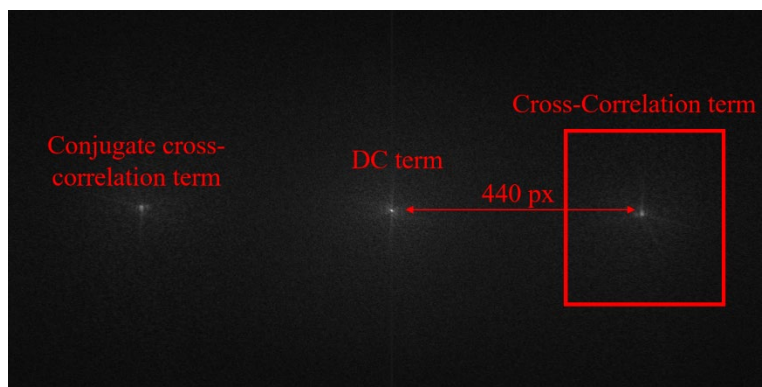


Figure 7.14 Fourier transform of the hologram shown above, acquired when the vessel is saturated by dodecane mist. The strong cross-correlation term

suggests that enough information is present to reconstruct images of spray hidden behind the fuel mist successfully.

Figure 7.15 shows a numerical reconstruction from the obscured vessel hologram. The reconstruction plane is 320 mm from the camera sensor, and the spray core is clearly visible. The reference beam modulating and amplifying the information delivered by the surviving ballistic photons of the object beam allows holography to provide reconstructed images of the target even in these challenging conditions where traditional incoherent imaging fails to show the spray.

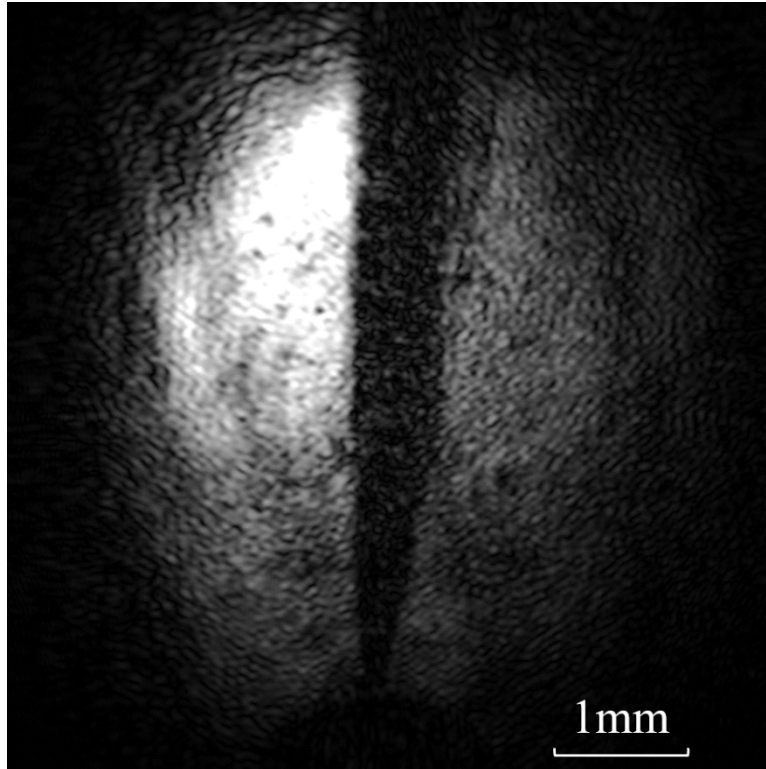


Figure 7.15 Reconstructed image of a dodecane spray injected at 1550 bar, 320 mm from the camera sensor. At this moment in time, the vessel is filled with dodecane mist, and incoherent imaging conveys no information.

7.2.3 3D reconstructions of the gas to liquid interface in turbid media

In this section, a region of interest around the spray core edges is numerically reconstructed at different depths. This hologram is acquired in the same optically dense conditions presented in the previous section (pressure vessel filled with dodecane mist produced by multiple injection events). The goal is to demonstrate that the technique can potentially identify ligaments that are expected to lead to droplet breakup in space.

Identifying these ligaments is a feature that is highly desirable in the spray imaging community.



Figure 7.16 Dodecane spray injected at 1800 bar, chamber at ambient temperature and pressure.

Below, a series of reconstructions are shown, starting 330 mm away from the camera and approaching the plane where the spray resides approximately 270 mm from the camera sensor. As we numerically move closer to the spray location, features appear at the spray edges (highlighted by arrows). Ligaments and voids are visible and can be located in space. Speckle noise is noticeable, and in future work this noise will be addressed using a speckle reduction algorithm. The speckle removal is not critical for the current goal of

demonstrating the technique's ability to resolve voids and ligaments in an optically dense environment.

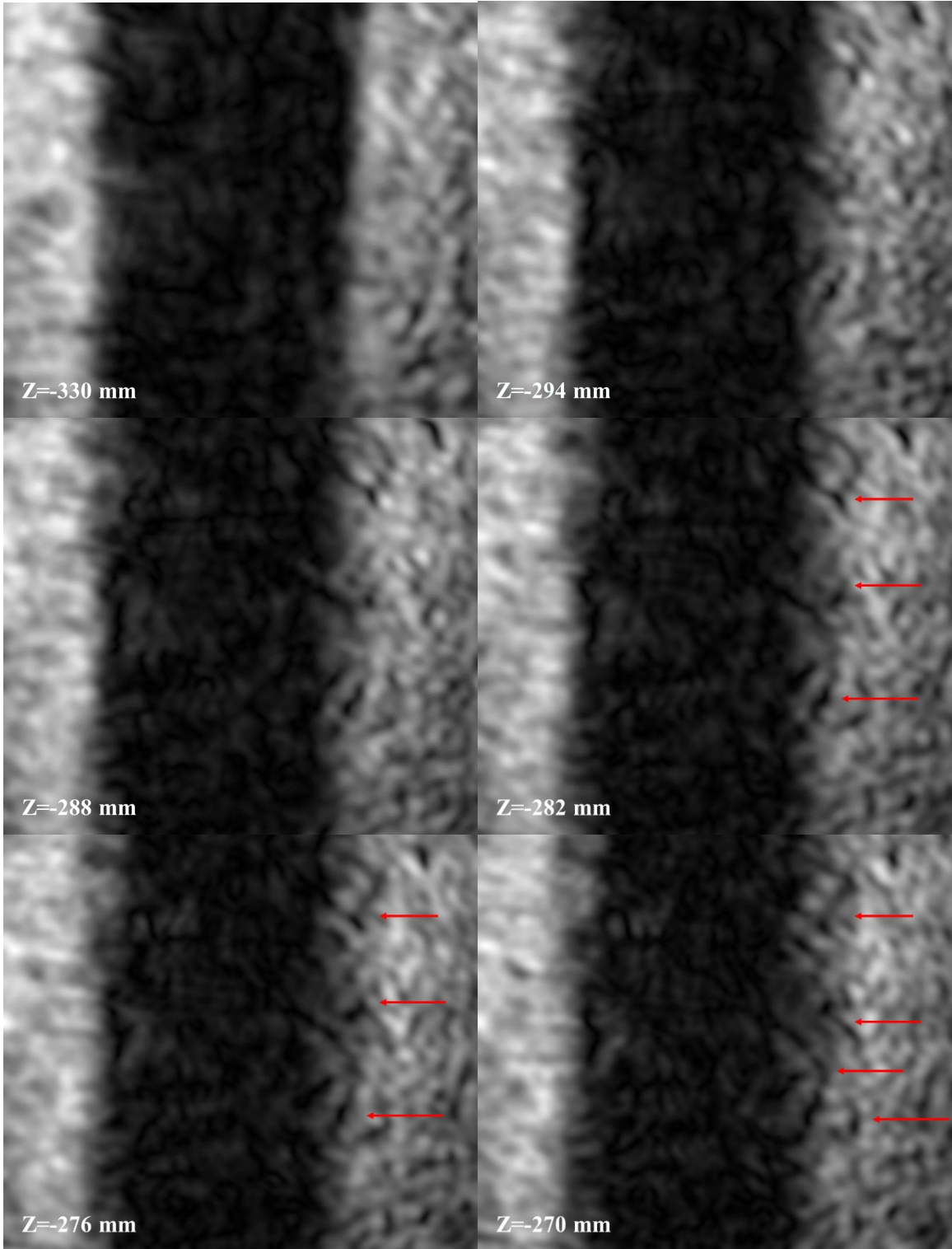


Figure 7.17 The region of interested shown in Figure 7.16 is reconstructed at different depths; voids and ligaments detaching from the spray core can be resolved. The in-depth resolution for a dense spray target has been estimated to be approximately 2 mm.

The depth of field offered by holography technique is showcased by the next figure, where droplets residing on the pressure vessel window's surface closer to the camera are resolved.

In the presented configuration, where the object wave is recorded after being modulated by being transmitted through the target field, the depth of field is not limited to the coherence length of the light source, and objects placed in planes centimeters away can be recorded in the same hologram. In this figure, the reconstruction plane is located on the pressure vessel window's inner surface. Dodecane droplets residing on the glass surface are resolved, 16.6 cm away from the spray nozzle, showing the extended depth of field embedded in a single hologram. The in-depth resolution depends on the target size and optical density, ranging from sub-mm for non-dense atomized sprays to approximately 2 mm for the dense spray imaged here. Further improvements in depth resolution would be highly desirable for the spray imaging community to identify features in 3D as comparison data for predictions from theory and simulations.

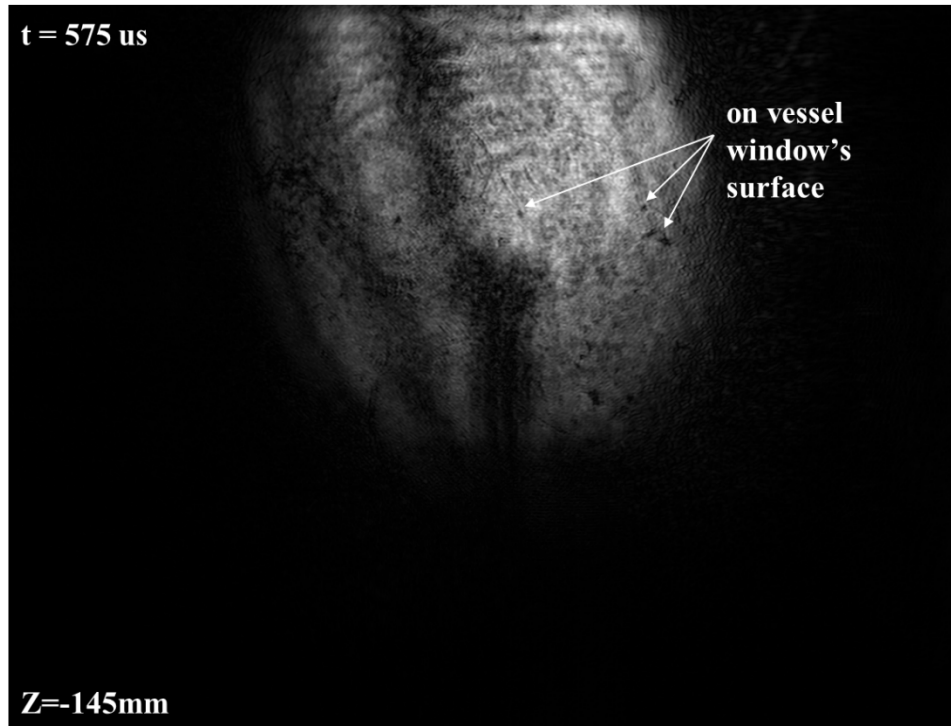


Figure 7.18 The pressure vessel's window that is closer to the camera is approximately 14 cm from the camera sensor. If we numerically reconstruct the previous hologram 145 mm from the sensor, these droplets appear. These are fuel droplets residing on the window's surface.

7.3 Section summary

USPODH was used for the first time to image the primary atomization region of the spray from a diesel injection. From these results, holography shows a solid shadow for the jet in the near nozzle region of a high-pressure dodecane spray, suggesting that it is likely that there is no atomization or that we are rejecting the signature from the shroud of primary atomization droplets. The solid, constant width jet observed is a liquid core that still

must go through primary breakup and atomization. Ligaments detaching from the spray core edges were observed, located in space and measured. The object-side resolution achieved is between 30 and 40 μm , resolution degrades as images are reconstructed further away from the sensor plane.

The technique's excellent multiple scattering noise rejection capability was proved by imaging the same dodecane spray in a vessel that was intentionally filled with dodecane mist left by previous injection events. The spray core was successfully imaged with no significant loss in resolution. The robustness of the technique was also demonstrated by imaging through thick fused quartz windows and pressure gradients. Coherence between the two pulses was not hindered by chromatic dispersion, and the hologram was correctly recorded.

The ultrafast laser pulse provides coherence filtering and freezes fast, transient sprays effectively. The holograms are not affected by vibrations that can cause blur in slower recording systems. The camera exposure time is irrelevant as the only illumination comes from the laser; the only requirements for the camera are that it has good dynamic range, low noise, and a pixel size small enough to correctly image the fringes of the interference

pattern. Numerical focus and optical sectioning were shown to conveniently resolve features that reside in different planes, freeing the user from having to focus on the target plane beforehand. Resolution of the technique will be improved by either moving closer to the target or by adopting a lensed arrangement. These improvements will be demonstrated in the last chapter of this dissertation. It is also essential to enhance the contrast in the gas to liquid interface to resolve structures that can be responsible for the generation of primary atomization droplets. The following chapters show how the proposed improvements have been implemented and this goal achieved.

Chapter 8

8 Challenges when imaging at high pressure and temperature

As a recap of the dissertation progress, USPODH's applicability to high-pressure, high-temperature environments was first investigated in a scaled-down setup that included a small pressurized heated cell containing a USAF resolution chart. These experiments happened chronologically before those presented in chapter 7, but are presented here because they add one degree of realism in moving towards imaging in engine-relevant conditions (chapter 9). The concern to be addressed is that the object and reference pulse might not interfere effectively at the camera sensor if the imaging pulse undergoes severe dispersion when traveling through the pressure vessel windows and the density and temperature gradients of the high-pressure gas.

Thick glass windows, temperature, and pressure gradients are known to create refraction index gradients along the object beam path which can have several detrimental effects on

the laser pulse properties on which USPODH relies in order to successfully create a hologram (short coherence length, pulse monochromacy, pulse polarization). Refraction index gradients can cause beam steering, which would impede the precise alignment necessary to pathlength match and interfere the reference and the object beam. The interaction between light and the electrons of a transparent medium causes a phenomenon called chromatic dispersion whose main effects that are relevant to this experiment are dispersive pulse broadening and chirping (time dependence of the instantaneous pulse frequency). As was discussed and calculated in chapter 5, a pulse has a finite spectral bandwidth, and chromatic dispersion can cause its frequency components to propagate at different velocities. Normal dispersion, for instance, leads to a lower group velocity of high-frequency components (positive chirp). This also affects pulse duration causing dispersive pulse broadening. If both these effects were severe enough they could impede interference between the reference and object pulse (if the object pulse was to become too temporally or spectrally stretched) or undermine the coherence filtering's efficacy by changing the object pulse coherence length. The experiments presented in this chapter quantify pulse broadening when imaging in conditions that are significant to fuel spray imaging. The quantification comes from comparing the measured duration of the elongated pulse to the ideal pulse duration that has been calculated in the Monte Carlo

simulations chapter. In addition, a USAF chart will be imaged in high pressure and temperature conditions to quantify USPODH’s ideal imaging potential in such an environment.

8.1 Experimental Setup Description

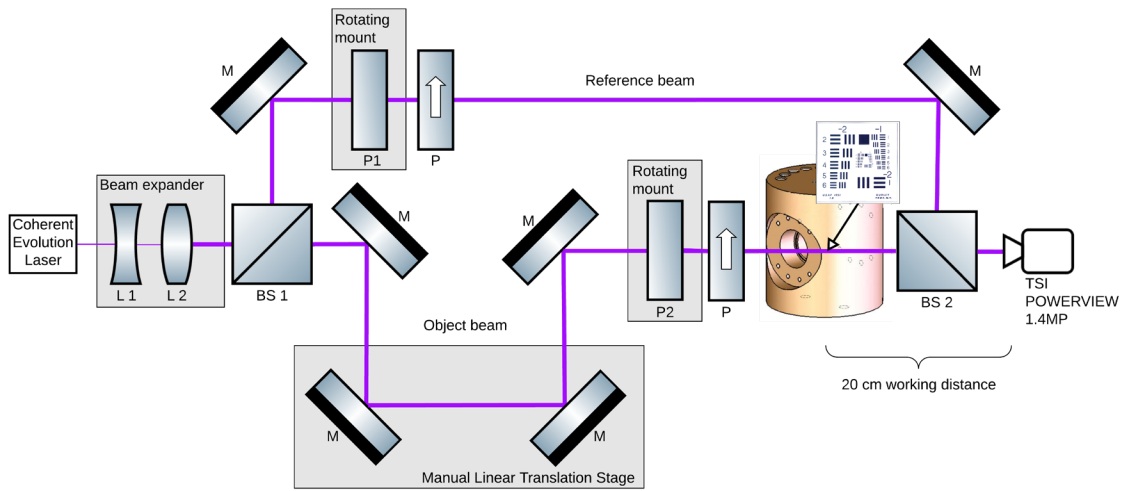


Figure 8.1 USPODH setup showing the pressure cell containing a USAF resolution chart.

A scaled-down USPODH setup has been built to image a USAF at the center of the pressurized cell (Figure 8.1). The measurement cell has 1” thick fused quartz windows and was designed to reach pressures up to 100 Bar. The pressure is monitored by an integrated pressure gauge. Heaters can be placed in bored holes throughout the body, and the temperature is monitored both by a thermocouple in the body (i.e., block) and a

thermocouple residing in the gas cavity near the center of the chamber (Figure 8.2). The current configuration uses silicone O-rings, which limits the operating temperature to about 477 K. Temperature is monitored and controlled via a Labview VI closed-loop PID controller.

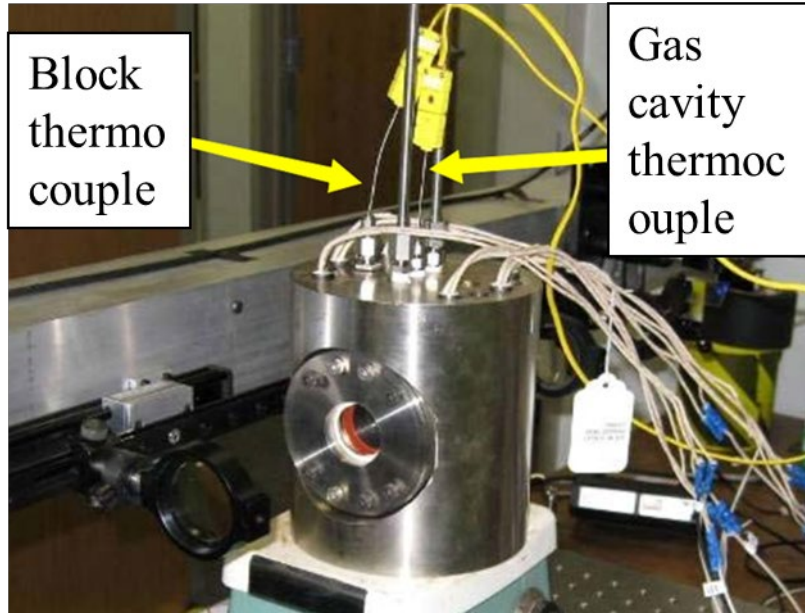


Figure 8.2 Small pressure cell with 1" diameter windows.

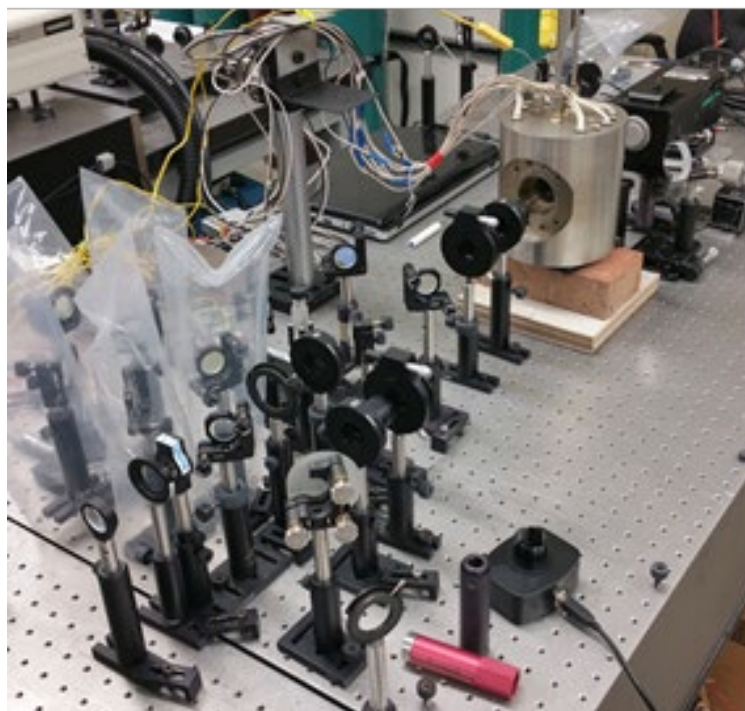


Figure 8.3 USPODH setup including a small volume temperature-controlled pressure vessel to investigate the effects of strong refraction index and density gradients along the imaging path.

8.2 Results

8.2.1 Pulse broadening quantification and effects

Pulse dispersion (the temporal and spectral broadening of the imaging pulse due to traveling through media of different densities and refractive indexes) was quantified by counting the number of fringes appearing in the hologram at different temperatures and pressures. Table 8.1 shows the range of delay stage adjustment for which fringes were visible on the camera sensor, together with the optimal delay adjustment (maximum contrast of the interference pattern) and the fringe count. These data are important to quantify pulse dispersion as temperature and pressure change and to allow prediction of the optimal delay stage adjustment that maximizes the interference pattern contrast for a given configuration (window thickness, vessel pressure, and temperature). Specifically, these data allowed the creation of a MATLAB tool that estimates the correct delay adjustment necessary to achieve pathlength matching for a given gas temperature, pressure, window thickness and gas refractive index (Figure 8.4 and Figure 8.5).

Table 8.1 Interference pattern visibility range and optical contrast setting measured at the object beam optical delay stage.

Windows	Pressure (bar)	Temperature (K)	Pattern appears (mm)	Peak contrast (mm)	Pattern disappears (mm)	Range (mm)	Fringe count
---------	-------------------	--------------------	----------------------------	--------------------------	-------------------------------	---------------	-----------------

No	1	295.15	15.713	15.672	15.625	0.088	130
No	1	443.15		15.673			
2-1'' thick	1	295.15	2.674	2.624	2.576	0.098	
2-1'' thick	1	295.15		2.618			
2-1'' thick	1	295.15	2.657	2.627	2.584	0.073	
2-1'' thick	1	295.15		2.628			
2-1'' thick	12.41	295.15	2.532	2.465	2.420	0.112	
2-1'' thick	5.52	295.15		2.555			
2-1'' thick	12.24	295.15		2.492			
2-1'' thick	17.6	295.15		2.460			
2-1'' thick	12.41	423.15		2.475			
2-1'' thick	12.41	443.15		2.474			
2-1'' thick	18.34	443.15	2.516	2.436	2.385	0.131	230
2-1'' thick	18.34	443.15	2.490	2.443	2.387	0.103	

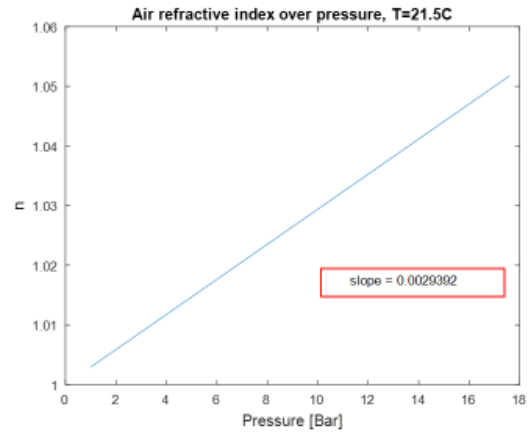
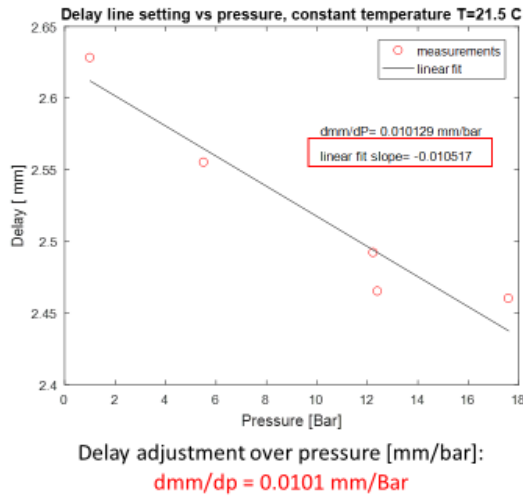


Figure 8.4 Optical delay stage adjustment required to maintain interference as pressure is increased at constant temperature ($T=21.5 \text{ }^\circ\text{C}$).

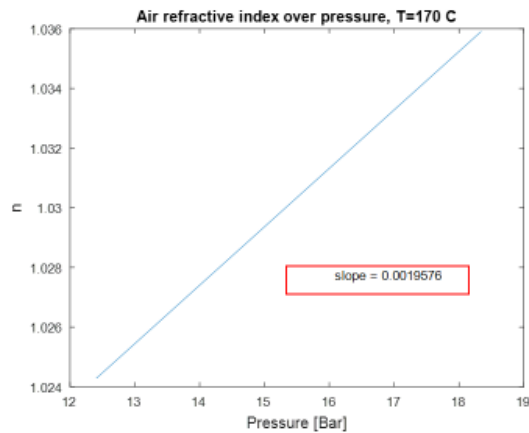
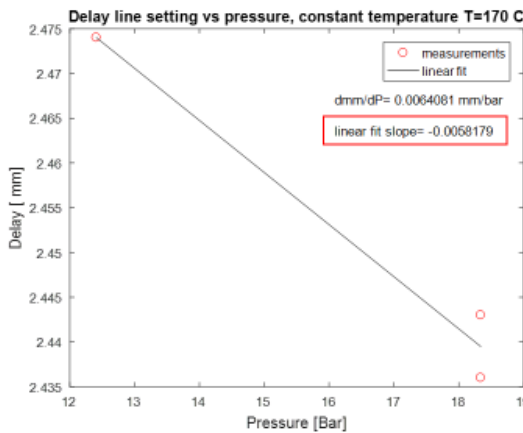


Figure 8.5 Optical delay stage adjustment required to maintain interference as pressure is increased at constant temperature ($T=170 \text{ }^\circ\text{C}$).

To quantify the imaging pulse dispersion at high temperature, high pressure, and when traversing denser media such as optical access windows, the number of fringes was counted while imaging at ambient pressure and temperature and at 18.34 bar - 443.15 K.

Approximately 100 more fringes were observed in these conditions, for a total of 230 (Figure 8.6). Knowing that:

$$\# \text{ fringes} * \text{ pulse wavelength} = \text{ coherence length}$$

$$230 * 0.4 \mu\text{m} = 92 \mu\text{m}$$

Which means that the broadened pulse length is:

$$\text{coherence length}/c = \text{pulse duration}$$

$$\frac{92 \mu\text{m}}{c} = 300 \text{ fs}$$

Hence, the pulse length is now 3 times the length of the original pulse, before accounting for any scattering event caused by the spray. The longer coherence length is expected to reduce coherence filtering performance, yet the measured broadened pulse length is still below the 500 fs that was shown in section 4.2 to be the maximum acceptable pulse length for discerning between ballistic and multiple scattering photons when imaging at OD 10.

A beneficial effect of having broadened coherence length and the higher fringe count is that the hologram size is increased, and as shown, both theoretically in section 5.6 and experimentally in Figure 8.7, the effect does increase the reconstructed image's field of view and improve its resolution. Figure 8.8 shows the effects of temperature gradients on several reconstructed images acquired sequentially at the same conditions. Localized defocusing of the finer features of the image can be observed (group 5). This defocusing can be compensated for by numerically reconstructing at a different depth where these features come back into focus. Nevertheless, this can be a concern when moving to larger pressure vessel or optically accessible engines where temperature gradients will be stronger and act over longer distances.

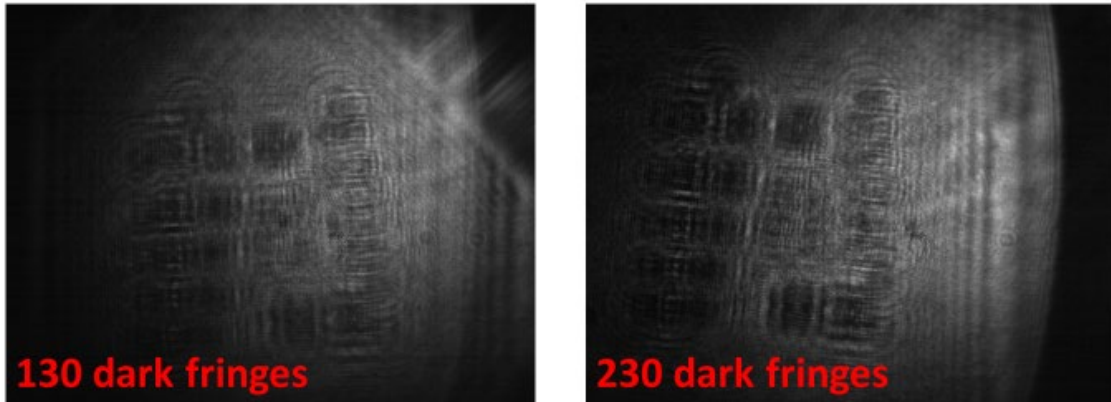


Figure 8.6 Interference fringe count at ambient temperature and pressure and at 18.34 bar - 443.15 K. Pulse broadening adds 100 more fringes at higher pressures.

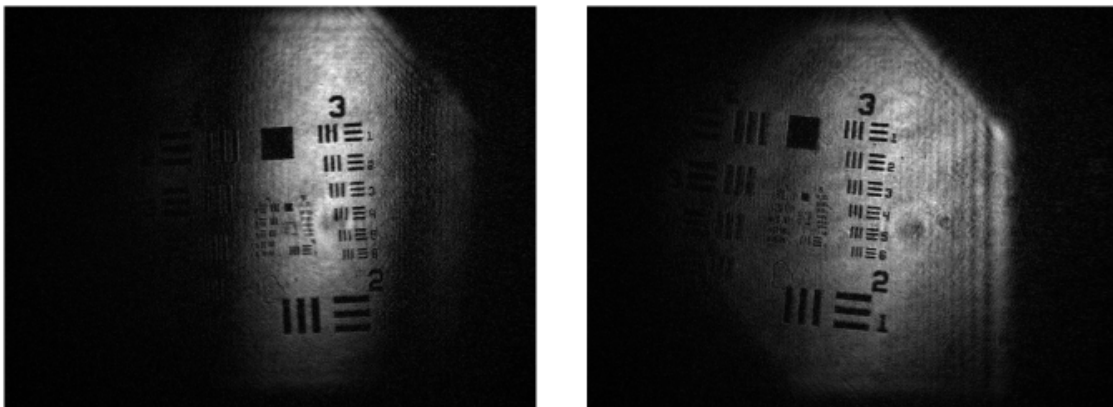


Figure 8.7 The pulse elongation caused by the windows and pressurized media is noticeable when looking at reconstructed images since the increased number of fringes in the hologram (see Figure 8.6) creates a larger field of view in the reconstructed image.

T= 170 C, ambient pressure, delay = 15.673 mm reconstruction depth -207.5mm (June 8th data)

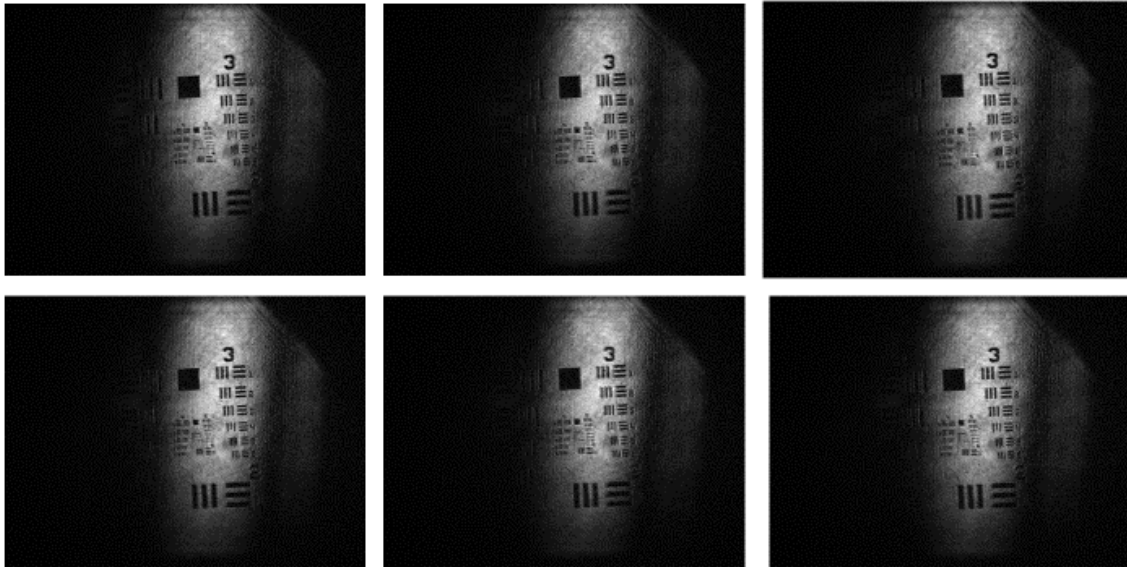


Figure 8.8 Reconstructions from different shots at 170 C, ambient pressure. Group 4 and 5 can be seen coming in and out of focus (density fluctuations of the media cause minor defocusing in the reconstructed image).

8.2.2 Reconstructed images of USAF chart at high temperature and pressure

Figure 8.9 shows the steps that can be taken to compensate for the defocusing effect caused by temperature gradients. A minor adjustment in numerical focus and delay (of the optical delay stage that pathlength matches object and reference beam) brings group 4 back to being resolved. The numerical refocusing and delay adjustments required by temperature gradients alone are minimal (1 μm delay adjustment and +.3 mm in-depth numerical refocusing when going from 21.5°C to 170 °C).

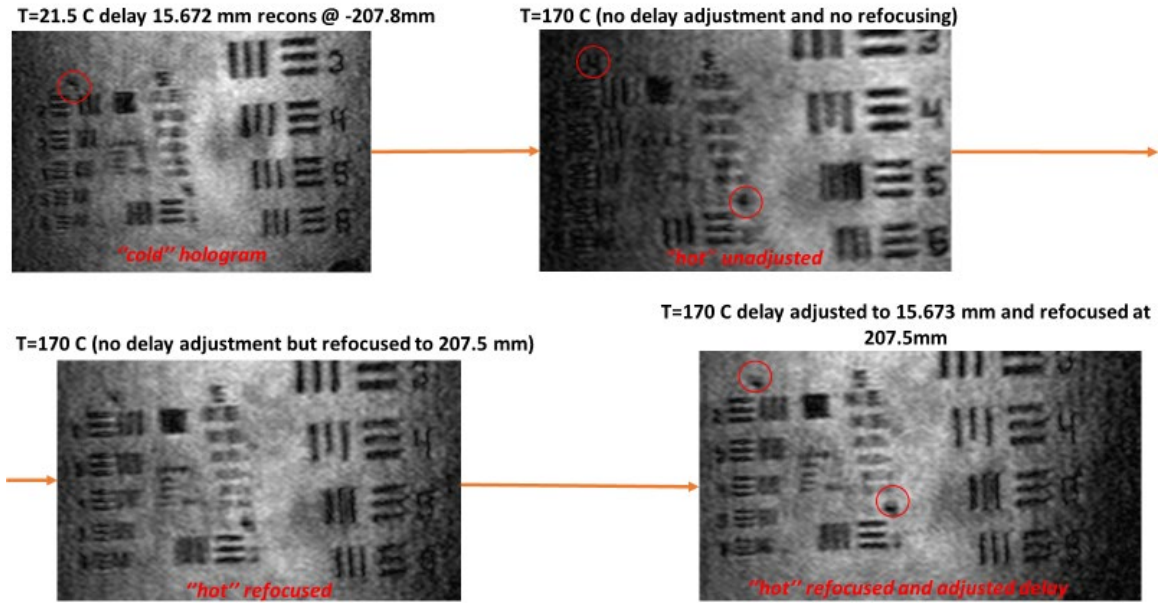


Figure 8.9 The figures above show numerical reconstructions from a hologram of a 1951 USAF resolution chart imaged at 170 °C. Temperature gradients cause slight defocusing in the reconstructed images, but this can be compensated by: 1. Minor adjustment of the optical delay stage 2. Numerical refocusing.

Figure 8.10 shows a reconstructed image of the USAF resolution chart, imaged inside the pressure cell at 18.34 Bar 443.15K. At these conditions, that are relevant for fuel spray imaging, element 3 of group 4 is resolved which corresponds to an object side resolution of approximately 25 μm at a working distance of approximately 20 cm. Imaging capability was not impaired by the presence of pressure and temperature gradients, or by the pair of 1" thick fused quartz windows.

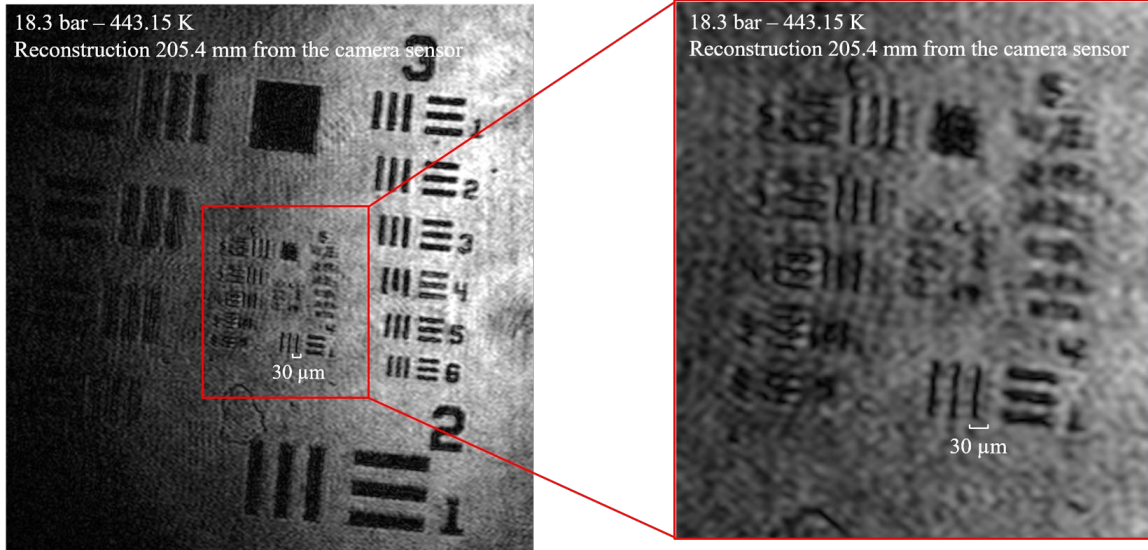


Figure 8.10 Reconstructed image of a 1951 USAF resolution chart in a pressure vessel at 18.3 bar and 443.15 K. Element 1 of group 4 is resolved.

8.3 CCD damage threshold

USPODH requires illuminating the camera sensor with an ultra-short laser pulse. When imaging a turbid environment, sufficient laser power is needed, and if there is a sudden loss of obscuration, the light pulse can damage the camera sensor. This damage was experienced as part of past experiments, so the sensor damage threshold was investigated to avoid damaging the camera. The damage can be avoided by improving standard operating procedures and better understand the mechanics of sensor damage. The past damage was due to the overlap of multiple imaging pulses when running the camera and laser system at 1 kHz [82]; this accumulates charges on the sensor surface and can cause electron discharge through the CCD. The accumulation can be avoided by strictly running

the system in a fully synchronized single-shot mode so that only a single 100 fs shot is captured by a single camera exposure. The energy concentration for a single 100 fs imaging pulse was calculated to be:

$$\text{Energy concentration} = \frac{\text{Pulse Energy (J)}}{\text{Beam Area (cm}^2\text{)}} = \frac{0.0015 \text{ J}}{0.64 \text{ cm}^2} = 0.0023 \text{ J/cm}^2$$

This value is well below the damage intensity for a typical CCD sensor [83], so as long as the laser is operated in single-shot mode laser damage can be avoided even for relatively high-intensity laser pulses.

8.4 Section summary

This chapter addressed what are widely considered to be the main obstacles to the successful application of a short coherence length, interferometric imaging technique in realistic laboratory setups, including thick optical access windows, high pressures, high temperatures, and strong temperature gradients. The broadened pulse length when imaging through 1'' fused quartz windows in engine relevant conditions was found to be 300 fs, with a coherence length of 92 μm . This pulse stretching is expected to reduce coherence filtering performance but is well below the 500 fs threshold that allows

discerning quasi-ballistic photons from multiple scattering ones. A resolution of 25 μm was achieved at a working distance of 20 cm at these conditions. These results show that pulse elongation will not be severe enough to hinder the technique's image reconstruction and multiple scattering noise rejection capability. Even if this becomes an issue at higher pressures causing coherence loss between reference and object beam a viable solution will be to re-route the reference beam inside the vessel so that it will experience the same dispersion as the object beam, or to implement pulse compression strategies to compensate for pulse broadening. The laser damage threshold of the CCD sensor was calculated and, as long as the system will be operated in single-shot mode, laser damage is not expected to happen. This is achieved by synchronizing the laser pulse to the camera and spray system in single-shot mode, as opposed to the 1 kHz free-running mode that was used in the early iterations of this experiment.

Chapter 9

9 Imaging of a realistic dodecane spray in engine-like conditions

In the past chapter, we have shown how it is possible to achieve multiple scattering noise rejection by means of “interference filtering” instead of time-gating when using ultra-fast lasers [11], [12]. This concept eliminates the need of having an optical Kerr-Gate (though it still requires an ultrafast laser source), and it offers the benefits of extended depth of field imaging, off-line focusing and allows the use of light phase information to measure refractive indexes or pinpoint surface location in space. We have demonstrated the efficacy of coherence filtering offered by ultra-short pulse off-axis digital holography (USPODH) in incrementally realistic conditions: first by imaging USAF resolution charts hidden behind mono and polydisperse scattering suspensions [11], [12], then by imaging plain jet water sprays placed at the center of a vessel filled with a high OD polydisperse water mist [13], [80] (chapter 6), then by imaging a commercial single orifice diesel fuel injector at ambient pressure and temperature [84] (chapter 7), and lastly we addressed the

potentially detrimental effects of chromatic dispersion when imaging at high pressure and temperature (chapter 8).

The goal of the work presented in this chapter, and the next increment in the realism of the system, is to show that USPODH can successfully image transient sprays in confined environments at pressures up to 17.4 Bar, both at ambient temperature and at high temperature, high evaporating rate conditions. The measurements evaluate the concern that temperature and pressure gradients would corrupt the imaging pulse to the extent of preventing it from interfering with the reference pulse and thereby negating the applicability of holographic imaging under these conditions. Successfully imaging the primary atomization region in such conditions is essential because it can potentially provide experimental data to enhance the understanding of primary breakup phenomena. Such data is valuable to the simulation community because it would provide currently non-existent tuning and validation material for DNS methods that include primary breakup [2], [5].

9.1 Experimental setup description

9.1.1 Spray and pressure vessel

The spray and pressure vessel system are the same as those presented in chapter 7 except that further precautions have been introduced to operate the experiment safely at pressure. The setup is now enclosed by ballistic Kevlar panels to protect the user area in the event of the vessel failing under pressure.

9.1.2 Optical Apparatus

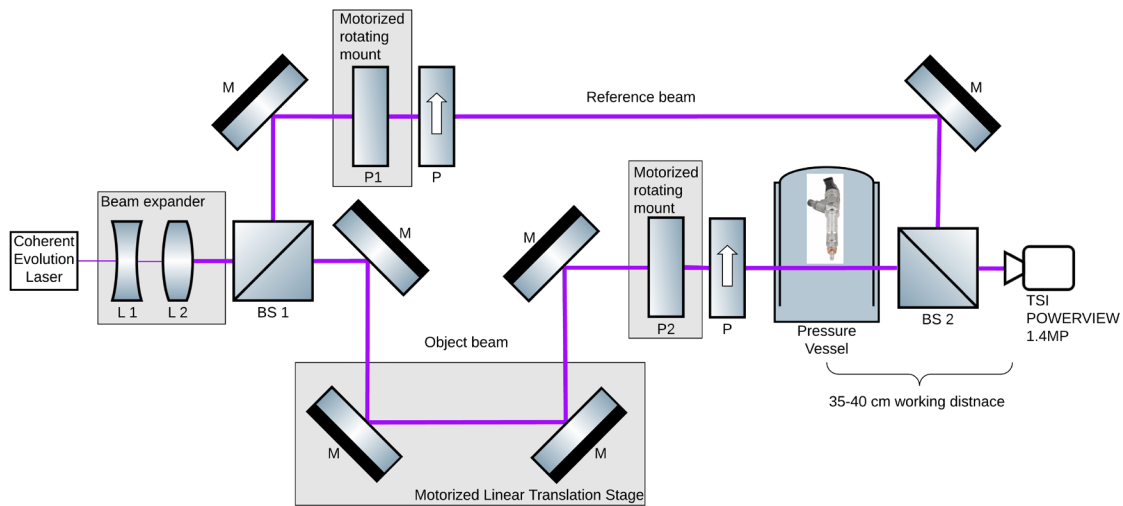


Figure 9.1 Optical apparatus

The optical setup is similar to the one presented in chapter 7. In order to protect the user from the pressurized environment, the polarizers on each beam path have been mounted

on motorized rotation stages, allowing the user to adjust the optics safely and remotely from a workstation protected by the ballistic panels.

9.2 Results

9.2.1 Ambient temperature and pressure

The mechanism describing the early stages of diesel fuel injection into a high temperature and high-pressure environment have been described in the introductory chapters, and this mechanism has been the focus of extensive research [1]–[5]. Briefly reviewing, the traditional understanding is that an intact stream of liquid fuel exists in the near-nozzle region; from this liquid core surface ligaments, bags and sheets form that eventually shed droplets via primary breakup. The size distribution of these droplets, bags, and ligaments have been predicted by models [4] and numerical simulations [2], [7] but there is limited experimental data for comparison with those models. High-speed shadowgraph images had difficulty accurately describing this gas-liquid interface because of possible ambiguity produced by multiple scattering noise from a layer of smaller droplets surrounding the jet core [1], [2]. This led to the development of ballistic imaging which theoretically had better potential for imaging ligaments and voids on the jet surface [1], [8]. Information can be inferred by observing the gas-fuel interface; for instance, ligaments may cease to exist

when vessel conditions exceed the fuel's critical point and would be replaced by a turbulent diffusive mixing layer [9]. The fair comparison between ballistic imaging and shadowgraphy (i.e., equivalent resolution, focusing, and spatial filtering) is rare, and so focused shadowgraph remains an essential tool.

The results presented here demonstrate that USPODH can successfully image targets in realistic diesel spray conditions, potentially delivering new data for furthering the study of primary atomization. The results are limited by the current pressure vessel capabilities and include holograms at pressures up to 17.4 Bar; conditions that would match an engine with a 17.2:1 compression ratio. This value is representative of a wide class of engines currently on the market; it is above the compression ratio for gasoline direct-injected engines (14:1) and within the range of diesel engines compression ratios (between 14:1 and 25:1).

The fuel used is n-dodecane; the average spray properties are reported in Table 9.1. They are close to the conditions for the widely-cited non-evaporating Spray A test case [2]. The test chamber is pressurized with nitrogen, and spray holograms have been acquired with vessel gas densities ranging between 1.15 and 20 kg/m³ in room temperature conditions.

Table 9.1. Average spray properties.

Fuel	n-dodecane (C ₁₂ H ₂₆)
Temperature (K)	295
Dynamic viscosity (Pa*s)	0.00134
Surface tension (mN/m)	25.35
Density (Kg/m ³)	750
Calculated fuel velocity at nozzle exit (m/s)	643
Re	57555
We	1.95*10 ⁶
Oh	0.024
Orifice diameter (μm)	160
P _{inj} (MPa)	150

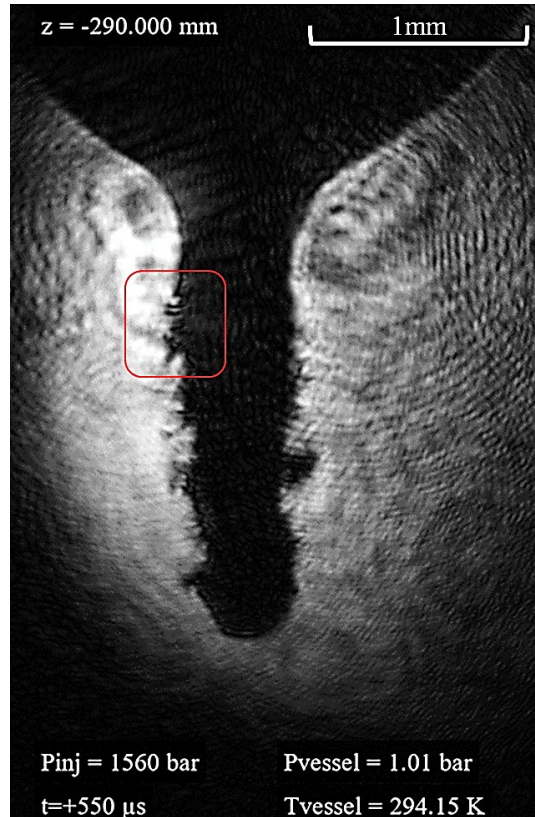


Figure 9.2 Intensity-based image reconstructed 290 mm from the camera sensor showing a dodecane spray injected at 1560 bar in a chamber at ambient pressure and temperature.

Figure 9.2 shows a reconstructed image of the early moments of injection in the primary breakup region. The image is reconstructed in a plane 290 mm from the camera sensor, and the image shows several ligaments detaching from the spray core edges, suggesting that the core is liquid because it displays liquid-like surface tension. The shadowgraph portions of the image (i.e., the regions of complete light obscuration) convey no information of the sides of the spray facing the laser and the camera, while good detail is retained at the spray edges. The spray penetration depth at the moment of image capture

is 2.1 mm, the object-side resolution is approximately 15-20 μm (estimated from the thinnest ligament that can be resolved in the ROI boxed in red in Figure 9.2 – note that this resolution is not equivalent to the formal resolution limit where two points can no longer be distinguished from each other but is instead the practical resolution definition referring to the size of an object that can be identified as a distinct feature). The features observed are consistent with those predicted by primary breakup theory in the turbulent jet region, where liquid turbulence creates surface perturbations, which in turn are stretched into ligaments because of the relative velocity difference at the gas-liquid interface. Capillary forces and turbulence cause the ligaments to break, generating a broad distribution of smaller droplets [2], [7]. This is confirmed by the reconstructed images shown in Figure 9.3, where no droplets can be seen detaching from the ligaments, confirming that if there are any droplets created by primary breakup they are of smaller size. Previous research has shown how turbid media made by polydisperse droplet distributions with a Sauter mean diameter (SMD) of 5-10 μm are substantially transparent to USPODH for OD values of 9-12 [13]. With a coherence length of 30 μm , this system is tuned to image the gas-liquid interface ligaments and larger droplets (20-30 μm) while rejecting noise from the smaller droplets surrounding the spray core that might obfuscate the interface surface in traditional shadowgraph images. The latest DNS

simulations for primary atomization in the near nozzle region predict droplet equivalent diameter below $6\ \mu\text{m}$ in similar injection conditions [2], [7].

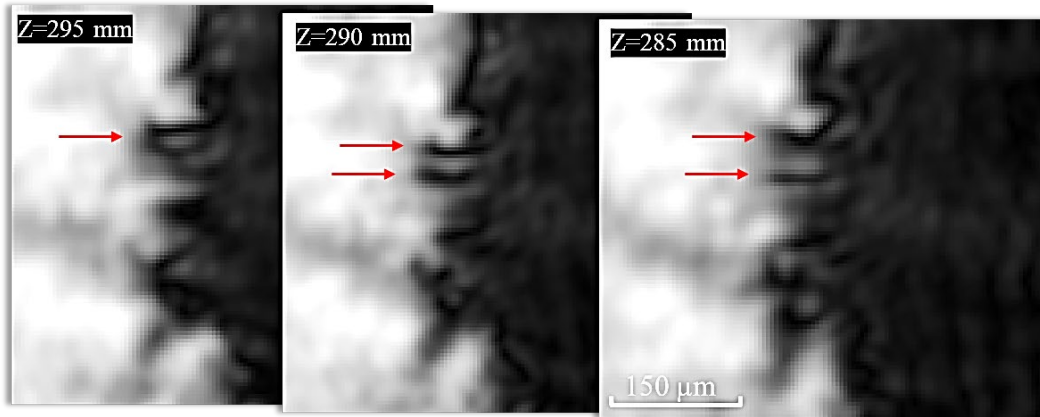


Figure 9.3 The ROI boxed in red in Figure 9.2 is reconstructed at 3 different distances from the camera sensor, 5 mm apart from each other. From measuring the spray core diameter we know what no spray is present in the 1st and 3rd image because they are located 10 spray diameters away from the nozzle, it is therefore important to develop algorithms to discern the focused spray image (middle one) from out of focus artifacts created by projecting the spray's shadow.

Figure 9.3 shows three numerical reconstructions of the ROI boxed in red in Figure 9.2. These reconstructions are 5 mm away from each other along the object beam axis. The middle one is in the injector nozzle plane. The images are an excellent example of the typical information included in a single-shot hologram, and of the challenge of correctly interpreting this information. Given that the nozzle size and the spray core diameter in the near nozzle region (which is $350\ \mu\text{m}$ downstream from the orifice exit measures approximately $500\ \mu\text{m}$ in diameter) we can assume that there are no spray remnants at

the physical plane where the first and last figure are reconstructed because they are 10 spray diameters away from the spray center plane. Nevertheless, there is an out-of-focus image of the spray core in these reconstructions. This shows the large depth of field in USPODH which can be an advantage for widely distributed objects of interest, but can be disadvantageous in that for useful quantitative results it will be essential to implement algorithms that locate the plane that is in focus and reject the ones that show an out of focus artifact of the object's shadow.

Figure 9.4 shows a reconstructed image shot under similar injection conditions but 8-10 μ s from the beginning of injection. The spray is now fully-developed, and its penetration depth is past the image's field of view. The magnified image in Figure 9.5 shows finger-like structures that are consistent with those shown in similar conditions by ballistic images [8], suggesting that USPODH is effectively rejecting the noise from small droplets surrounding the primary atomization region and successfully imaging the gas to liquid interface. The same ROI is reconstructed at 292 mm and 289 mm from the hologram plane in Figure 9.6. More about the interpretation of these images will follow in section 9.3.

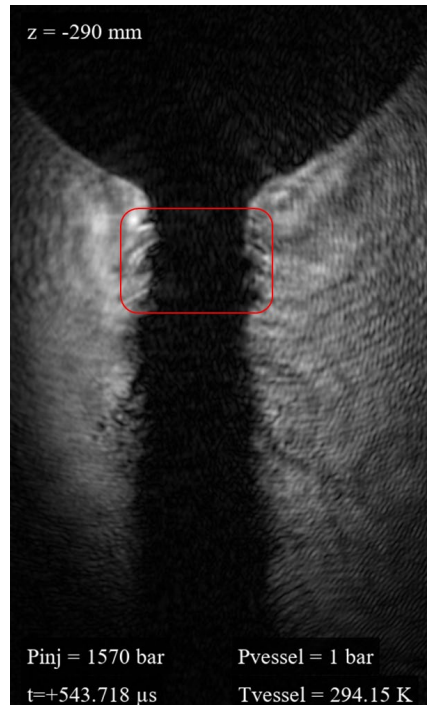


Figure 9.4 Intensity-based image reconstructed 290 mm from the camera sensor showing a dodecane spray injected at 1570 bar through a $160 \mu m$ nozzle in a chamber at ambient pressure and temperature.

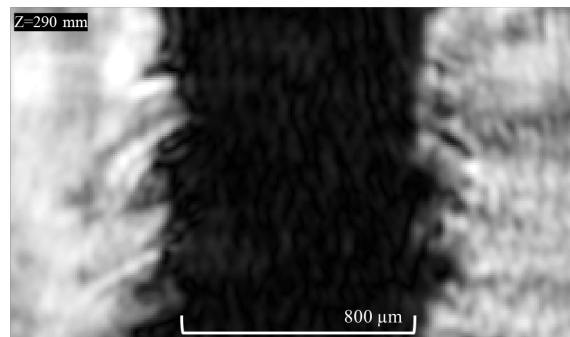


Figure 9.5 Magnification of the ROI highlighted in Figure 9.4 showing primary breakup structures at the gas to liquid interface of the spray core.

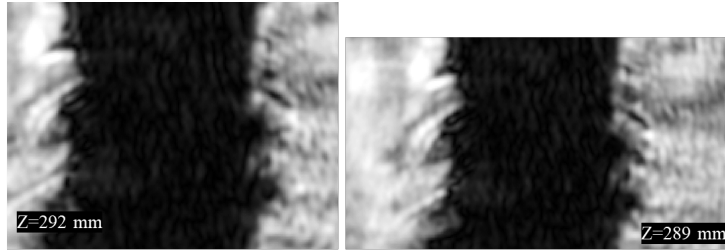


Figure 9.6 The same ROI is reconstructed 292 and 289 mm from the hologram plane.

The value of the three-dimensional reconstruction capability boasted by holographic imaging that was demonstrated in previous work [3] performed on more diluted, atomizing sprays is, for the most part, lost under spray conditions. The breakup region of a single jet, being a thick and optically dense object, does not allow any ballistic or quasi-ballistic photons through the liquid spray core. On the other hand, imaging detail is retained at the spray edges because enough light diffracts around and through the sides of the spray core. These results suggest that, for this class of applications, USPODH should be pursued less for its tridimensional imaging capability and more for its excellent gas-liquid interface imaging performance. In addition, it is evident from the results shown here that the liquid spray core is not a phase object (i.e., it does not merely adjust light wave phasing that passes through but entirely blocks the light), and the feasibility of imaging in a reflective configuration, instead of transmissive, should be explored in future USPODH implementations. This would, for example, also allow phase unwrapping to create

quantitative topological maps of the spray surface, at the expense of imaging using a much weaker backscattered signal.

9.2.2 High-pressure, ambient temperature

Figure 9.7 and Figure 9.8 show reconstructed images in the spray orifice plane at vessel pressures of 6.41 and 11.03 bar, corresponding to vessel gas densities of 7.36 and 12.67 kg/m³. USPODH can also provide commonplace qualitative spray data such as spray angle and penetration depth. The spray core length from the nozzle exit to the end of the field of view is approximately 3 mm; at 6.41 bar the spray cone angle is 18 degrees (Figure 9.7) while it is approximately 23 degrees at 11.03 bar (Figure 9.8). The observed increased spray dispersion is expected with higher vessel gas densities and corroborated by previous experimental data and models [85]. No lateral resolution degradation is observed at these pressures, with the smallest distinguishable feature being resolved measuring approximately 20 μm . Pathlength matching was as reliable and as stable as at ambient pressure confirming that the 100 fs imaging pulse does not undergo excessive beam dispersion when traversing multiple density gradients (air-glass-high pressure nitrogen-glass-air) and retains coherence with the reference pulse.

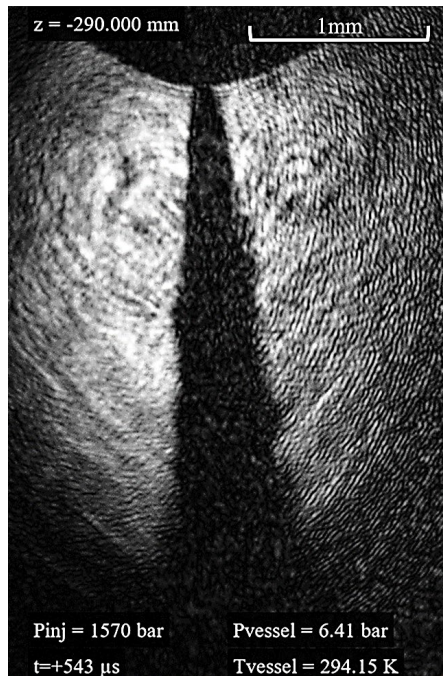


Figure 9.7 Intensity-based image reconstructed 290 mm from the camera sensor showing a dodecane spray injected at 1570 bar in a chamber filled with nitrogen at 6.41 bar and ambient temperature.

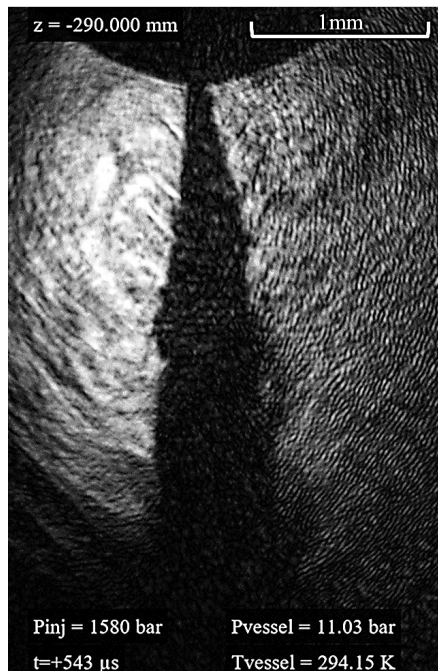


Figure 9.8 Intensity-based image reconstructed 290 mm from the camera sensor showing a dodecane spray injected at 1580 bar in a chamber filled with nitrogen at 11.03 bar

Figure 9.9 shows a reconstructed image of a dodecane spray injected into a chamber at 17.4 bar and ambient temperature together with a magnification of the gas to liquid interface. The interface appears fuzzier, with less defined structures than the ones observed at ambient temperature and pressure. Artifacts and noise are more noticeable in these high-pressure results. This is probably due to the deterioration of coherence gating performance due to stronger pulse dispersion at high pressure. In addition, the higher pressures produce higher density gradients that are themselves phase objects, and so the hologram picks up the features of these fluctuations. These gas field structures are formally considered “artifacts” from the spray image point of view, but they represent actual physical phenomena that can themselves be interesting to study. These results confirm that is possible to use an ultra-short coherence length interferometric technique on setups that present challenging, realistic, experimental conditions but it is crucial to reduce artifacts and noise while enhancing resolution. These goals and pathways to their accomplishment will be the focus of chapter 10.

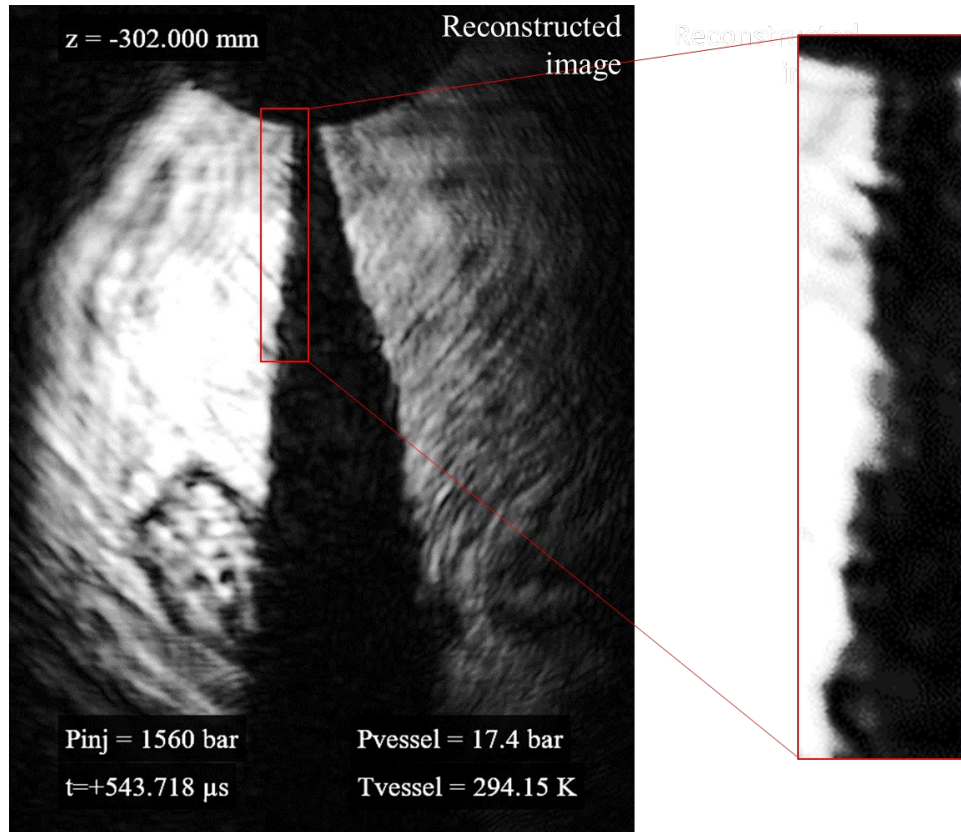


Figure 9.9 Dodecane spray injected at 1560 bar into a nitrogen-filled vessel, $P=17.4$ bar $T=294.15$ K. The gas to liquid interface is magnified on the right-hand side of the image.

9.2.3 Comparison to inline holography and lens less shadowgraph imaging

As mentioned earlier, without providing comparison imagery it is difficult to assess the value of different techniques designed to elucidate spray structure. Most comparisons intentionally or unintentionally compare the performance of one technique under conditions favorable to it with those of competing methods without revising the conditions

to favor the competitor. Figure 9.10 compares shadowgraph and holographic images from a dodecane spray injected into the vessel at 17.4 bar – 295 K. We acquired the shadowgraph image of the spray by blocking the reference beam (left), then we numerically reconstructed the same spray hologram as an inline hologram (center) and an off-axis hologram using a 400 px reconstruction box surrounding the cross-correlation term. The goal is to verify if adopting the off-axis configuration effectively delivers better image quality at the gas to liquid interface, based on its theoretically superior scattering noise rejection performance. The shadowgraph image shows strong bow shocks created by the liquid spray core, as the spray estimated velocity is 700-800 m/s, which well exceeds the speed of sound at this pressure and temperature of 352 m/s. The gas to liquid interface is impossible to distinguish as the spray appears defocused and with a broader silhouette than the one it shows in the reconstructed off-axis holograms, significantly distorted by the bow shocks. The reconstructed inline hologram (Figure 9.11) eliminates most of the bow shocks observed in the shadowgraph image, and it shows higher resolution and a larger field of view than the off-axis reconstruction. Nevertheless, the inclusion of the dc and conjugate cross-correlation terms in the reconstruction process conveys intense background noise, including circular artifacts that appear to be diffraction patterns and dark areas connected to the spray core corresponding to the bow shocks in

the gas surrounding the spray. These noise sources prevent us from resolving the gas to liquid interface with high contrast and resolution (Figure 9.11). The reconstructed off-axis hologram shown on the right side of Figure 9.10 and in Figure 9.12 shows a clear, high contrast reconstruction of the gas to liquid interface, free from the artifacts created by the bow shocks seen in the shadowgraph image and to some extent in the inline hologram reconstruction. This image is particularly meaningful in demonstrating the powerful combination of off-axis holography with ultra-short coherence filtering: the holographic reconstruction shows us the object beam collimated intensity in the plane where the shocks reside, whereas the shadowgraph image shows us the location where photons arrive on the CCD sensor after being deviated by the refraction index gradient. In other words, while with a traditional shadowgraph we can only see where photons are recorded on the camera sensor, a hologram can show us where those photons *were* in a specific depth plane, therefore rejecting the bow shocks dark streaks.

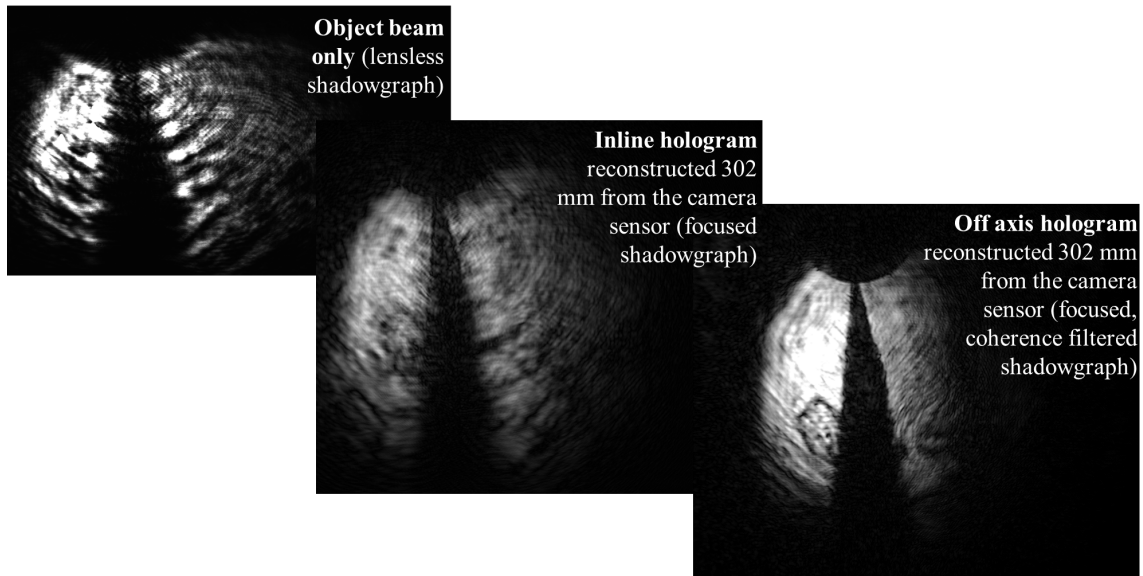


Figure 9.10 Comparison between lens less shadowgraph (left), reconstruction from an inline hologram (center) and off-axis hologram reconstruction of a dodecane spray injected at 1560 bar into a vessel at 17.4 bar – 295 K.

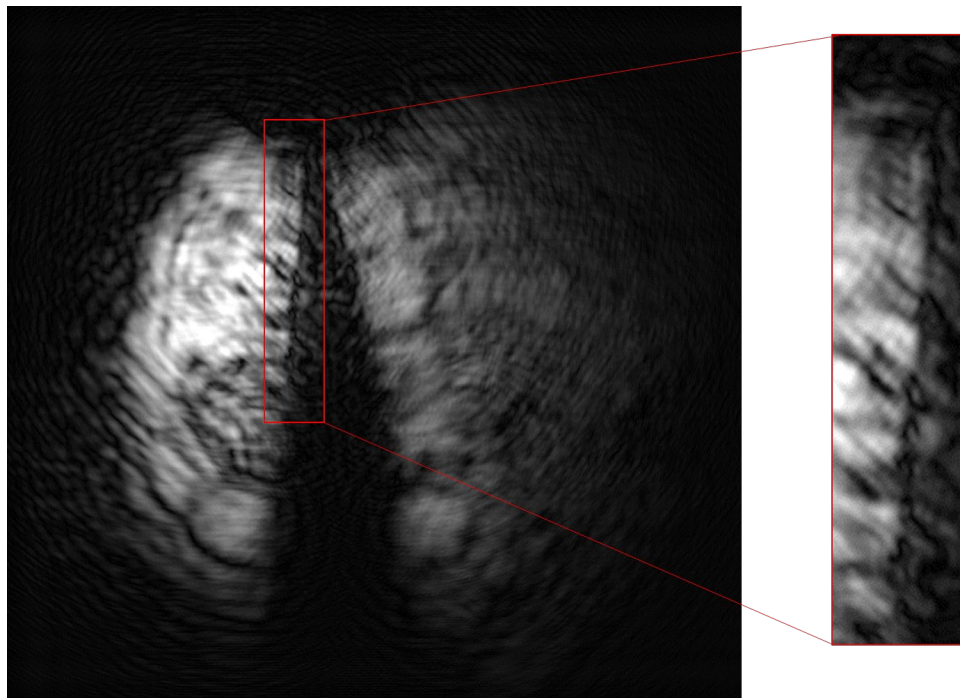


Figure 9.11 Reconstructed Inline Hologram, $Z=302\text{mm}$, 1000 px reconstruction area, $P_{\text{vessel}}= 17.4 \text{ Bar}$ $T_{\text{vessel}}= 295 \text{ K}$. The inline hologram does

not reject multiple scattering noise as effectively as the off-axis one, the spray appears wider, the gas to liquid interface has poor contrast and artifacts attached to the spray core are observed. The periodic distance between artifacts suggests that they are leftovers of the bow shocks observed in the shadowgraph image.

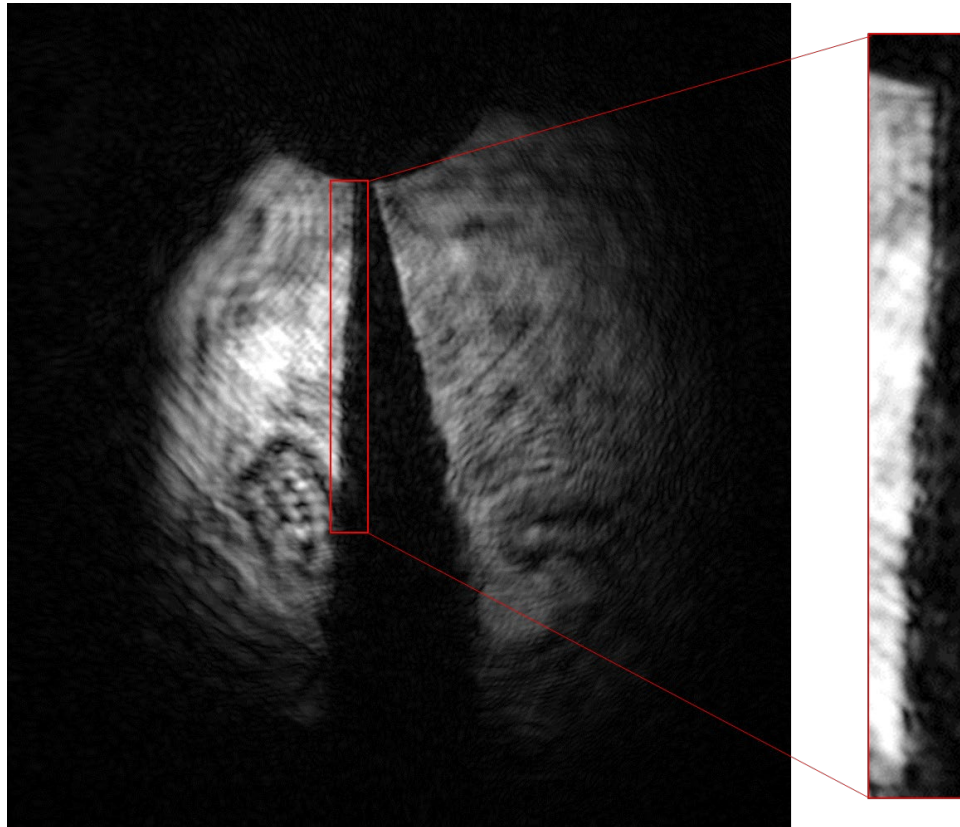


Figure 9.12 Reconstructed Off-axis Hologram, $Z=302\text{mm}$, 400 px reconstruction box, $P_{\text{vessel}} = 17.4 \text{ Bar}$ – $T_{\text{vessel}} = 295 \text{ K}$. The off-axis hologram reconstruction resolves the gas to liquid interface with good contrast and rejecting artifacts generated by bow shocks. Higher magnification and resolution would be desirable to identify turbulent fluid dynamic structures.

9.3 Issues

While the following items are not fundamentally associated with the optical methodology employed, it is worth identifying some of the important practical issues that were faced when moving USPODH towards measurements in realistic conditions of diesel sprays.

9.3.1 Window fouling

When the vessel internal temperature reaches and exceeds dodecane's boiling temperature at ambient pressure (216.2 °C), the evaporation rate is significantly increased, and we observed fuel condensation on the vessel window's internal surface. The liquid dodecane film refracts and diffracts the object beam causing the loss of coherence with the reference, as shown in Figure 9.13. Hence, imaging performance at engine relevant temperature has been demonstrated with a resolution chart instead of a real spray. Implementing solutions to prevent fuel condensation is necessary when imaging a fuel spray. A window heating system is currently under development to address this issue.

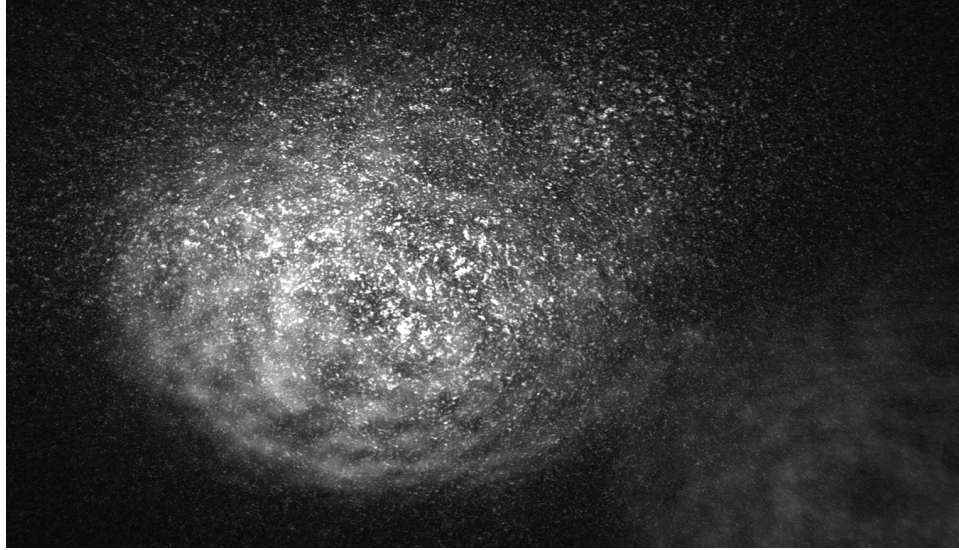


Figure 9.13 Dodecane condensation on the vessel window's surface impedes interference between the object and reference pulse.

9.3.2 Synchronization challenges

To be able to provide early injection images that can be compared to simulations it is important to have consistent timing performance of the spray-laser-camera system in order to image the same instant from the start of injection repeatedly. Microsecond resolution and precision would be desirable as primary atomization phenomena in realistic spray conditions are observed in the first tens of microsecond from the start of fuel injection into the chamber. Our setup showed excessive jitter, on the order of hundreds of microseconds, making it difficult to reliably and reproducibly capture images early in the injection. The cause for this significant jitter appears to be the pressure variation in the common rail, which then causes a variation in the fuel speed at the nozzle exit. Pressure

in the common rail is controlled by a booster pump which boosts the common rail fuel pressure to approximately 1700 bar and re-pressurizes it when the pressure drops below 1400 bar. It is the 300 bar window which produces the variance. Narrowing the pressure window is not feasible for this pump design as it would be firing continuously leading to excessive pump wear and failure.

To confirm the pressure fluctuation as the source of such jitter required exoneration of all the other components in the fuel injection process. The signal sequence synchronizing the laser-camera-spray system has been measured, and statistical analysis has been performed to find the source of excessive jitter (Figure 9.14-Figure 9.16). Figure 9.17 shows the trigger signals timeline: the signal from the “SDG Elite” laser synchronizer (red signal) triggers a pulse generator, which in turn triggers (blue signal) the camera and the DIDS unit which fires the fuel injector (green signal). The plot shows 10 or so acquisitions of this signal sequence. The crosses mark the half maximum of each rising edge, which was used to mark the time corresponding to the start of each trigger signal. From these timings, three latencies and the jitter value have been calculated: laser to pulse generator, pulse generator to fuel injector, and the overall latency between the laser and the fuel injector actuation. Jitter was calculated as the sum of the differences between all latency

measurements, divided by the number of measurements. The results are shown in Table

9.2.

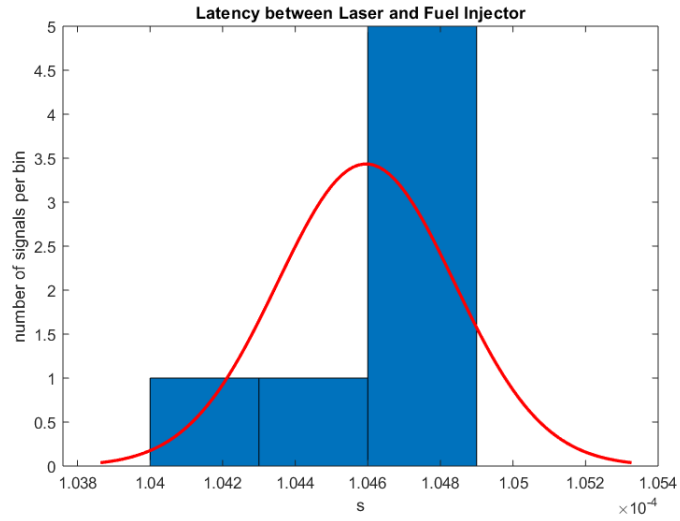


Figure 9.14 Latency between the SDG Elite laser synchronizer and the fuel injector actuation, 10 events.

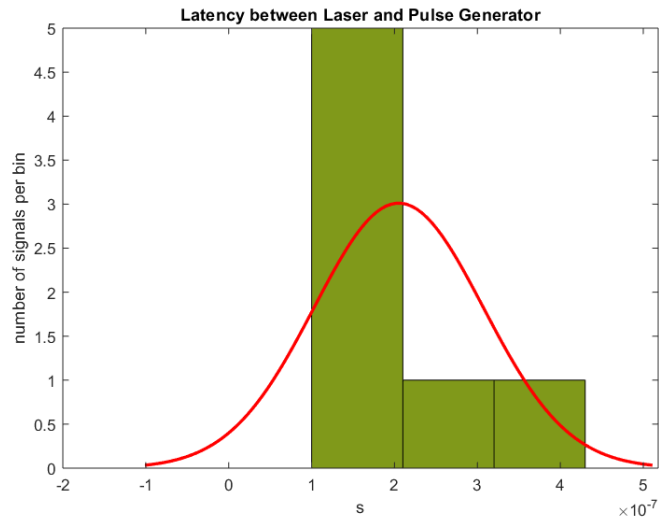


Figure 9.15 Latency between the SDG Elite laser synchronizer and the pulse generator, 10 events.

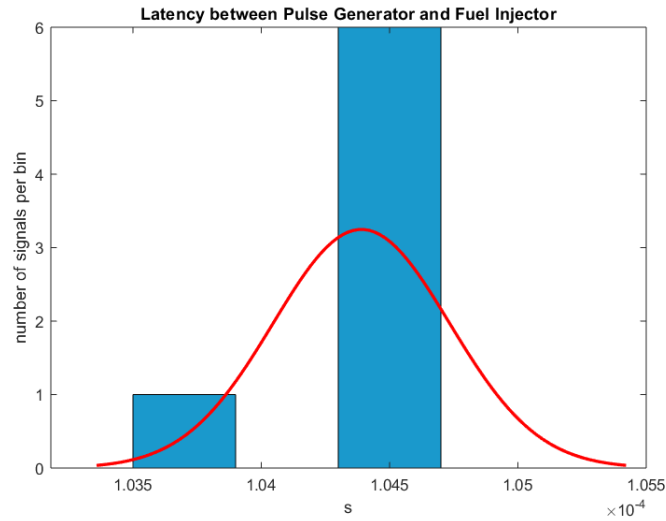


Figure 9.16 Latency between the pulse generator and the fuel injector actuation, 10 events.

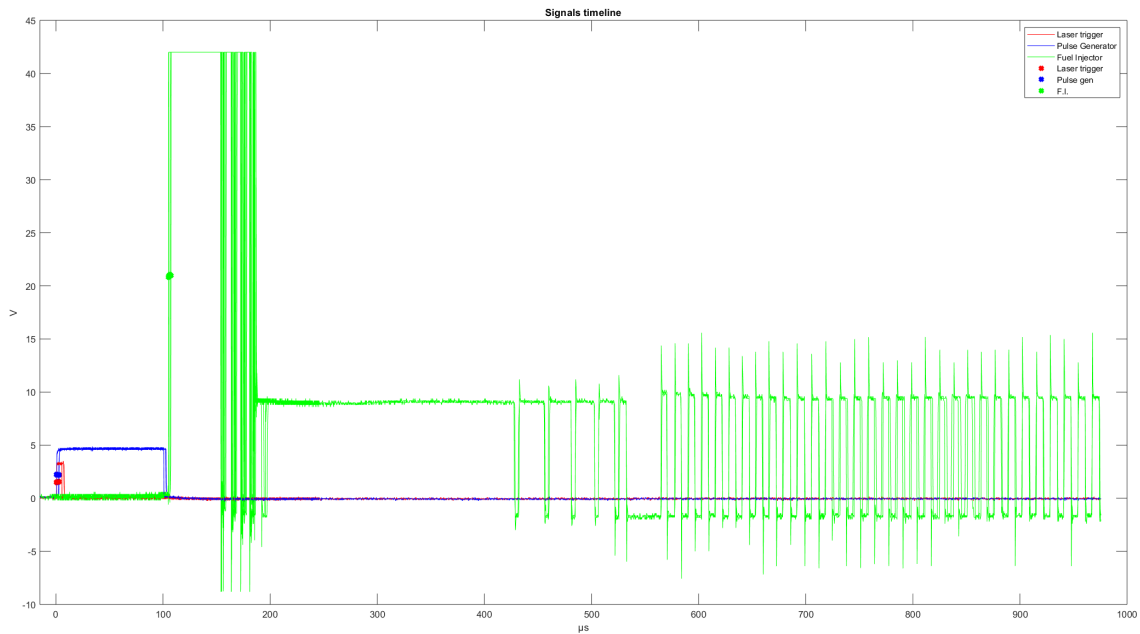


Figure 9.17 Trigger signals timeline: the pre-trigger signal (in red) from the SDG elite laser synchronizer triggers a pulse generator, which in turn triggers the camera and the DIDS module (in blue) controlling the spray. The DIDS energizes the fuel injector (in green), and a pre-determined fuel injection

sequence is initiated. The graph shows 10 different acquisitions of the described signal sequence.

Table 9.2 Latency, standard deviation, and jitter for 10 acquisitions of the signal sequence actuating the fuel injector.

	Laser synchronizer to pulse generator	Pulse generator to fuel injector	Laser to fuel injector (overall)
Latency (μs)	0.2050	104.39	104.595
Standard deviation (μs)	0.1020	0.3439	0.2439
Jitter (μs)	0.0812	0.2566	0.1790

The jitter value in the third row of the third column of Table 9.2 shows that the overall jitter from the initial laser pre-trigger to the signal energizing the fuel injector is only 0.18 microseconds. High-speed videos shot with the Phantom V4 camera show the spray exiting the nozzle anywhere between 400 to 750 microseconds after the initial laser pre-trigger signal. These results clearly exonerate LabVIEW and the DIDS module and the pulse generator from being the cause of the observed jitter and suggest that the jitter is caused by the pressure fluctuations in the common rail (between 1400 and 1700 bar). This should be addressed by adding a PCV valve, controlled by the DIDS unit, to the common rail. This would allow closed feedback control of the pressure in the common rail. Adding such a valve would cause the booster pump to fire continuously, so the use of an automotive-style, diesel common rail rotary high-pressure pump should be considered.

9.3.3 Artifacts and noise

Demonstrating the technique in realistic conditions highlighted the need to reduce artifacts. Towards this goal, improvements have been achieved both optically and computationally, but more needs to be done. From an optical standpoint, improving beam homogeneity by expanding the beam led to better contrast and signal to noise ratio in the surface to liquid interface region. The addition of motorized stages for the polarizers allowed to adjust object and reference pulse intensities to the optimal values for creating a highly contrasted interference pattern, and the use of a long travel stage for pathlength matching allowed to pathlength match while monitoring the cross-correlation term in the frequency domain. This latter strategy permitted nearly perfect pathlength matching. This also helped to tune the beam interference angle in order to achieve optimal separation between DC and cross-correlation term in the Fourier domain. The overall improvement is demonstrated by the following reconstructions (Figure 9.18) of the gas to liquid interface in the near nozzle region comparing early (above) and recent results (below).

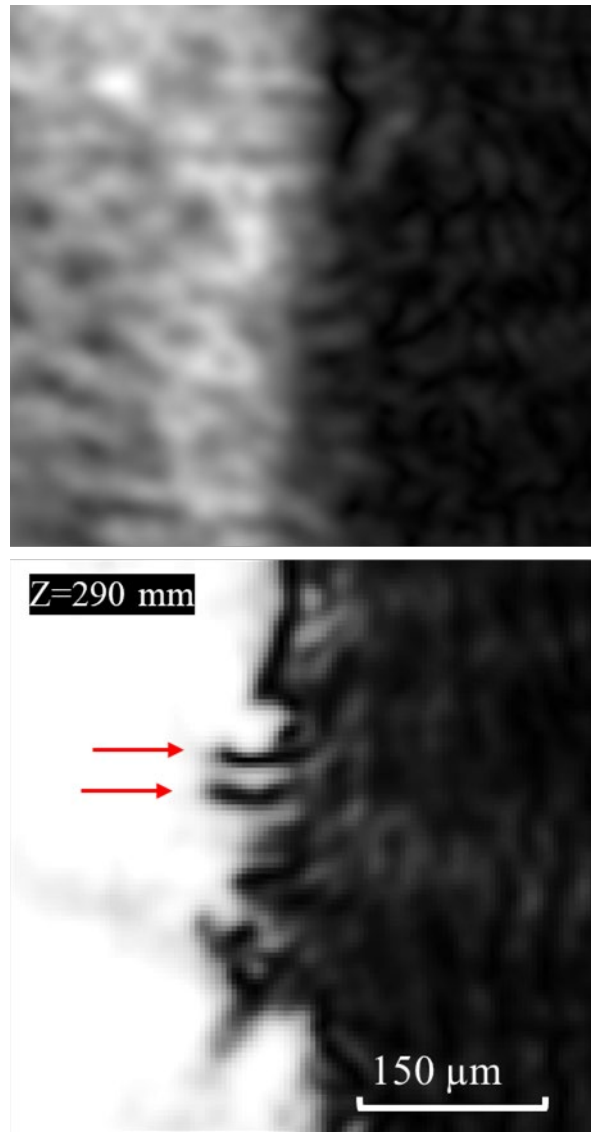


Figure 9.18 Gas to liquid interface of the liquid core generated by a dodecane spray injected at 1560 bar at ambient temperature and pressure. Both images show the left-half of the spray liquid core at the interface with the surrounding gas. This region is located approximately 200 μm downstream from the nozzle orifice. Early results (above) are compared to the one produced by the current setup.

Arc and ring-shaped features can be noticed, especially in the results at high-pressure and when imaging through thick windows with fuel residue or dust over them. These artifacts

are caused by the object beam diffracting off particles along its path and interfering with itself. That is, they are basically a Gabor, inline hologram. These have a different spatial frequency than the main interference pattern obtained by interfering object and reference beam at an angle, so the information they convey to the image is mostly contained in the DC term at the center of the frequency domain. When reconstructing an off-axis hologram we reconstruct only the cross-correlation term created by the coherent photons interfering at the camera sensor. When doing such a reconstruction, the area around the cross-correlation term is selected, and zero padding is applied to anything outside that box, thus rejecting most of the non-coherent information contained in the DC and conjugate cross-correlation term. Mainly, there is a trade-off between noise scattering rejection performance (smaller reconstruction box) and resolution (higher with a larger reconstruction box, that will include part of the DC term conveying noise). A substantial number of the inline holograms of dust speckles, fuel droplets or window imperfections are included in the reconstruction region in order to obtain sufficient resolution. These can be mitigated by trading noise rejection for resolution by reducing the size of the reconstruction region around the cross-correlation term in the Fourier domain (see Figure 9.19), but they are not as prominent in our current results because of the aforementioned optical setup improvements (Figure 9.18).

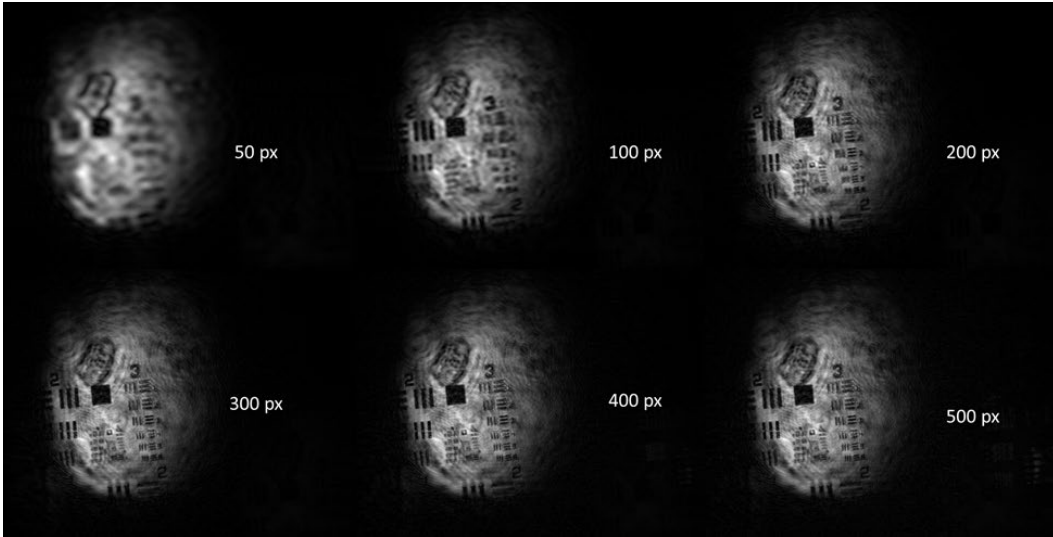


Figure 9.19 Reconstructed images of a USAF resolution chart placed inside the CSM pressure vessel. The noise is mostly caused by fuel residue on the window's surface, notice how there is a trade-off between noise and resolution as the reconstruction region size is increased from 50 to 500 px.

Figure 9.20 shows the results from applying a low pass filter to a spray hologram to eliminate the artifacts. The comparison shown here is to provide a context for absolute limits on the imaging performance in realistic environments. They are typical examples to illustrate trade-offs, and they demonstrate that additional image processing and reconstruction algorithm methodologies can continue to improve the outcome depending on the information targeted.

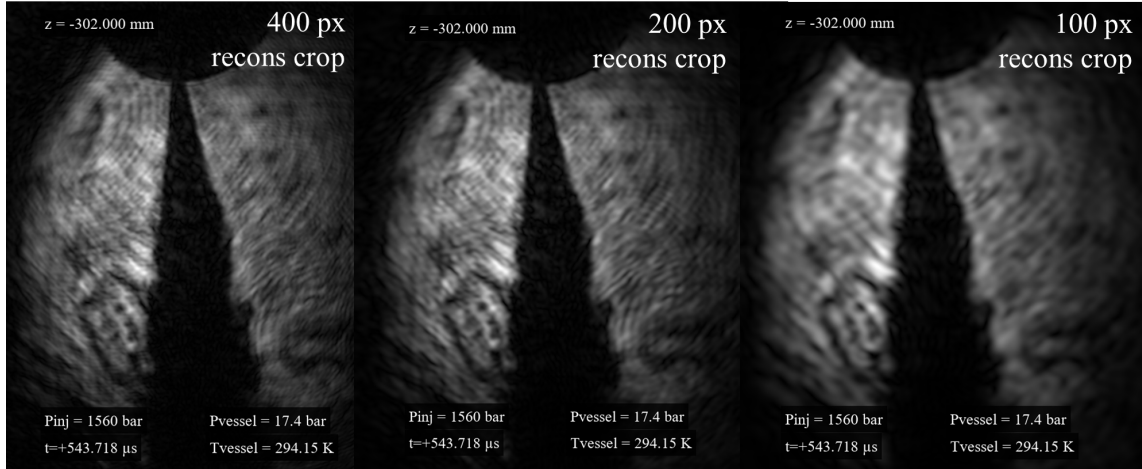


Figure 9.20 By restricting the area surrounding the cross-correlation term included in the reconstruction process (similar to applying a low pass filter) we can limit the number of artifacts observed in the reconstruction, at the expense of image resolution.

Lastly, another type of artifact is that coming from the shadow cast by a spray feature being numerically reconstructed in a plane past or before the feature. Figure 9.21 shows three reconstructions of the gas to liquid interface in the near nozzle region, 5 mm away from each other along the object beam axis. The middle one is in the injector nozzle plane. These images are an excellent example of the wealth of information included in a single-shot hologram and the challenge of correctly interpreting this information. The image is reconstructed 350 μm under the nozzle exit, where the spray has an approximate diameter of 500 μm . Hence, there should be no spray in the first and last reconstruction planes because they are 10 spray diameters away from the orifice plane. Yet, we observe an out of focus image of the spray core. This vast depth of field means that for USPODH

results to become a useful quantitative tool it will be essential to implement algorithms that locate the plane that is in focus and reject the ones that show an out of focus artifact of the object's shadow. In order to remove these artifacts, we can monitor a feature's edges as it gets reconstructed at different depths; the plane where the feature resides will show the sharpest edges, while the artifacts appear as cast shadows with blurred edges. Another approach under development is to pinpoint the spray surface boundaries at a prescribed reconstructed depth using a stereo disparity or edge detection algorithm [86], then a background noise hologram (shot in the same conditions but without firing the spray) is reconstructed at the same depth and subtracted from the spray's reconstructed hologram. Subtraction can be tuned to be more aggressive away from the spray region as identified by the stereo disparity or edge detection algorithm in order to avoid removing information of the gas to liquid interface that we are interested in imaging.

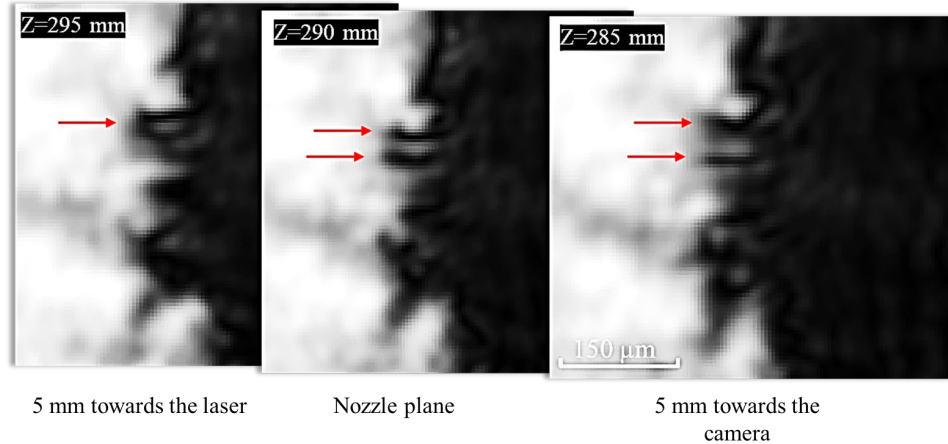


Figure 9.21 Intensity-based images reconstructed 295, 290 and 285 mm from the camera sensor showing a dodecane spray injected at 1560 bar in a chamber at ambient pressure and temperature. From measuring the spray core diameter we know what no spray is present in the 1st and 3rd image because they are located 10 spray diameters away from the nozzle, it is therefore important to develop algorithms to discern the focused spray image (middle one) from out of focus artifacts created by numerically propagating the spray's shadow in planes where no physical features exist.

9.4 Section summary

The chapter presented results to demonstrate the feasibility of using USPODH to image the gas to liquid interface in the primary atomization region of a high-pressure dodecane spray at engine relevant pressures at room temperature. The technique successfully imaged the gas-liquid interface of a dodecane spray jet, injected at 150 MPa into a vessel pressurized with nitrogen to pressures in excess of 17 bar. Surface turbulence and ligament structures consistent with primary breakup theory and simulations were observed with an

object-side resolution of approximately 20 μm . The results demonstrate that the 100-fs pulse does not undergo excessive chromatic dispersion and wavefront aberration when traversing the refraction index and pressure gradients typical of a realistic automotive spray environment.

Numerical, off-line focusing was demonstrated, which frees the user from having to focus on a fast, 3D target using high numerical aperture optics with shallow depth of field. Unfortunately, no ballistic or quasi-ballistic photons penetrate the liquid core of the spray, which reduces the tridimensional capability of the reconstructed images. Features in the near-nozzle region consistent with the fluid dynamic structures responsible for primary atomization have been resolved. A comparison between lens-less shadowgraph imaging, inline holography, and off-axis holography when imaging a high-pressure fuel spray demonstrated the beneficial effects of the technique presented in this dissertation. Lastly, the current system limitations have been presented, focusing on how artifact reduction will be fundamental to make USPODH a helpful, quantitative tool for spray imaging.

Chapter 10

10 Opportunities for improved performance

The previous chapter exposed some of the technique's current limitations and opportunities to improve USPODH's performance. These included primarily:

- identify and eliminate artifacts and noise
- implement strategies to address fuel condensation and allow imaging in high evaporation rate conditions
- optimize the optical setup and reconstruction process to increase resolution and allow imaging with magnification larger than one

This first two are being pursued in the ongoing work related to this technique. This chapter will show how the latter has been addressed by improving our reconstruction algorithm and optical setup.

10.1 Reconstruction algorithm improvements

Part of this dissertation work included improvements into Holotool, the MATLAB reconstruction tool developed originally by Colin Dankwart [12] that was used to reconstruct all holograms presented in this dissertation. These included the capability for batch processing, improvements in the zero-padding of images, and the reduction of undersampling aliasing.

10.1.1 Batch reconstructions

One of the challenges that have been mentioned throughout this document is the difficulty in correctly interpreting the reconstructed hologram and pinpointing the plane where features reside in space. As has been described, different strategies have been proposed in this dissertation and are currently being investigated, but the first step was to add the possibility to batch reconstruct a user-defined number of images from the same hologram. The user specifies the starting propagating depth d , the desired distance between two consecutive reconstructions in microns Δz , and the overall number of reconstructions N to be computed surrounding the defined central propagating depth. The software computes N reconstructions with d as the central propagation depth and saves them in a single, multi-page .tiff file. The propagation depth and other information

relevant to the experimental conditions are superimposed on each reconstruction. The user can then scroll through the hundreds of reconstructions while monitoring propagation depth to find the focus plane of features of interest.

10.1.2 Improved zero padding and reconstruction resolution

Our implementation of Ultra-Short Pulse Off-Axis Digital Holography (USPODH) numerically reconstructs an intensity-based image of the target at a user-defined distance from the hologram plane using the angular spectrum method, also known as the convolution method [62]. In off-axis holography, from digital holography theory, it is known that the reconstructed image resolution ($\Delta\varepsilon$, $\Delta\eta$) is proportional to the hologram size in pixels (N)

$$\Delta\varepsilon = \frac{\lambda d}{N\Delta x} \quad \Delta\eta = \frac{\lambda d}{N\Delta y}$$

Where λ is the wavelength of the reference beam used for reconstruction and d is the propagation distance measured from the hologram plane; Δx is horizontal pixel pitch on the camera sensor, and Δy is the vertical pixel pitch. Assuming that all the parameters are constrained, at a given propagation distance, the resolution will improve if N is larger, meaning that is beneficial to have a larger (in terms of pixel number) hologram. In off-axis holography, the size of the hologram to be reconstructed is limited by the need to

exclude the DC term and the Conjugate Cross-Correlation term from the reconstruction process.

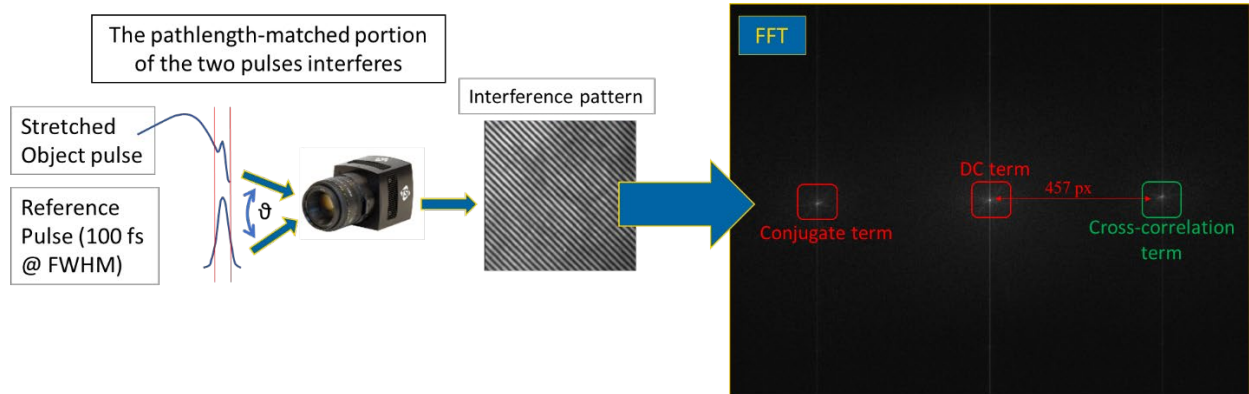


Figure 10.1 Diagram showing how the interference angle between object and reference beam is directly proportional to the interference pattern frequency, which in turn is proportional to the distance in the Fourier domain between the DC and Cross-correlation term.

The distance between the DC term and the cross-correlation term is proportional to the spatial frequency of the fringe pattern, which is a function of the source wavelength, the imaging pulse coherence length (30 μm) and the interference angle between object and reference beam. In inline holography the object and reference beam are parallel to each other (or are the same beam in Gabor holography), creating a single term in the Fourier domain that can be reconstructed into an image of the target. This leads to having maximum hologram size N and resolution, but also to including the DC-term and conjugate cross-correlation term in the reconstruction, which overlaps a pseudoscopic (inverted perspective) image of the target on the virtual image that we want to

reconstruct [62]. As we increase the interference angle between the object and reference wavefronts, therefore moving to an off-axis configuration, a fringe pattern is superimposed on the hologram. As we increase the interference angle the fringe pitch decreases, meaning that the spatial frequency of the pattern increases, thus increasing the distance between the cross-correlation and the DC term in the Fourier domain, as shown in Figure 10.1. This allows reconstruction of the cross-correlation term into an intensity-based image of the illuminated object without including the DC term into the reconstruction process. This includes all sources of incoherent noise, such as the out of focus shadow of the target conveyed by the object beam and, more importantly, the multiple scattering noise conveyed by all photons that traveled a distance longer than the imaging pulse coherence length (30 μm). The tradeoff is that by cropping the cross-correlation term, we are limiting the size of the hologram to the size of the crop surrounding the cross-correlation term. This can be mitigated by using zero-padding strategies, but nevertheless, information (resolution) is lost in exchange for noise reduction performance.

In our setup, reference and object beam are interfered to cause an optimal separation between Cross-Correlation and DC term in the Fourier domain of approximately 450 pixels. A zero-padding algorithm applies a 400-450 pixel wide square mask around the

cross-correlation term that maximizes resolution while rejecting most of the information from the DC-term, as shown in red Figure 10.2 and Figure 10.3. A larger reconstruction area allows increasing resolution (larger N) at the expense of including more noise conveyed by the DC-term at the center of the frequency domain (Figure 10.3).

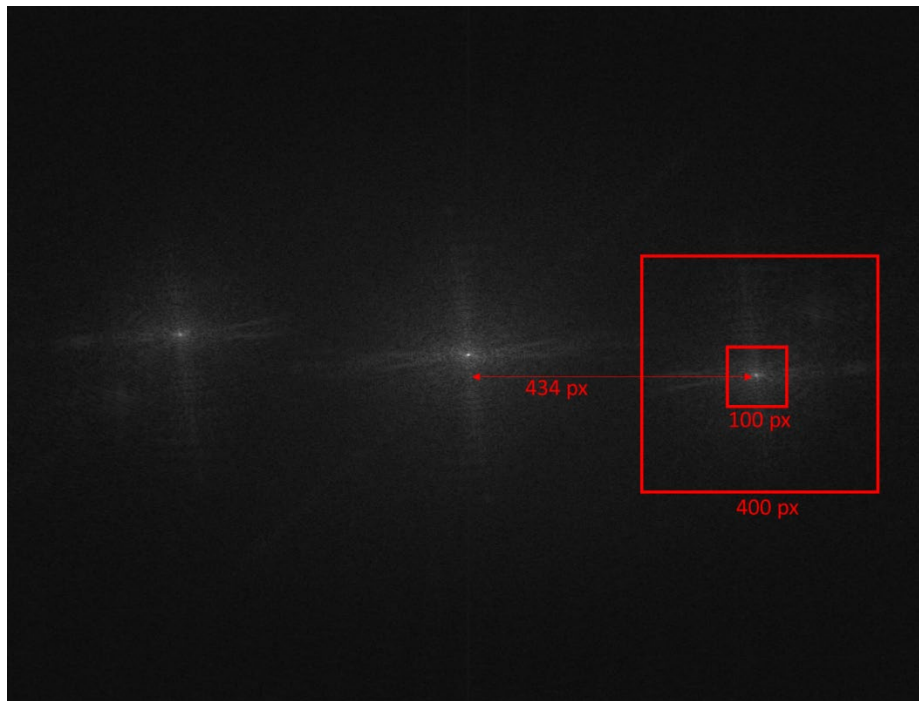


Figure 10.2 In off-axis holography, only a portion of the frequency domain space surrounding the cross-correlation term is numerically reconstructed into an intensity-based image of the target using an angular spectrum algorithm. This allows to tune in the amount of noise rejection at the expense of image resolution.

Expanding the size of the reconstruction area while still avoiding crosstalk with the DC-term would produce a resolution improvement without loss of scattering noise rejection performance. This was achieved by modifying the reconstruction algorithm by allowing

the user to select a rectangular reconstruction area centered on the cross-correlation term. The user can pick the width of the rectangle (thus controlling the amount of crosstalk with the DC-term) while the algorithm automatically adjusts the reconstruction area height in order to maximize N and therefore resolution.

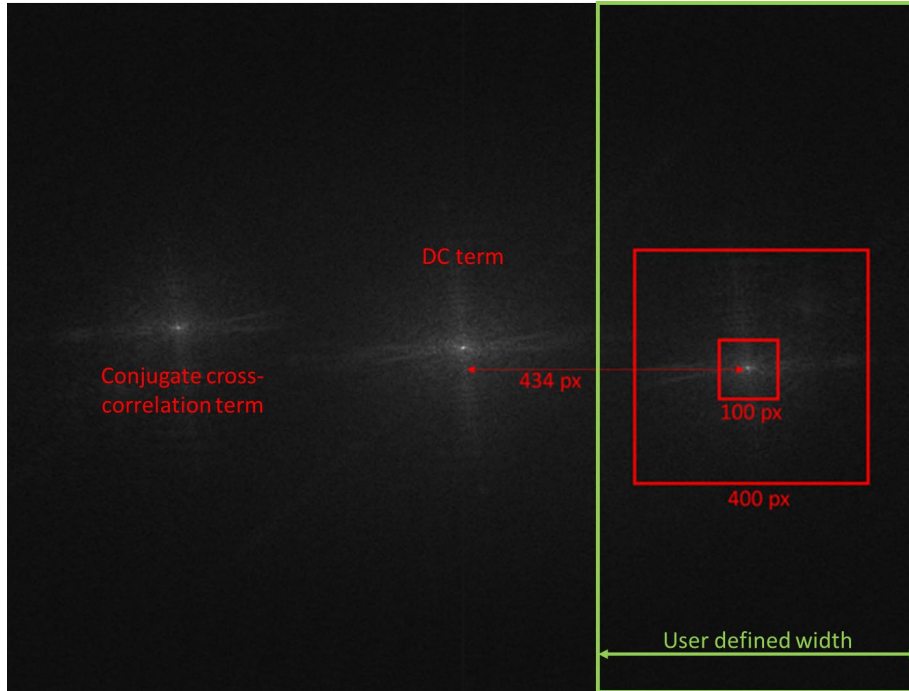


Figure 10.3 The green rectangle represents the new, larger reconstruction area that is selected, zero-padded, and then processed for reconstruction.

Here follows a selection of results showing the difference between the previous and the current algorithm. The results are grouped by the width of the reconstruction area. The previous square reconstruction area algorithm results are on the left; the results from the updated algorithm are on the right. The distance z reported in each image is the reconstruction depth measured from the hologram plane.

10.1.2.1 USAF resolution chart – 100 px wide reconstruction area

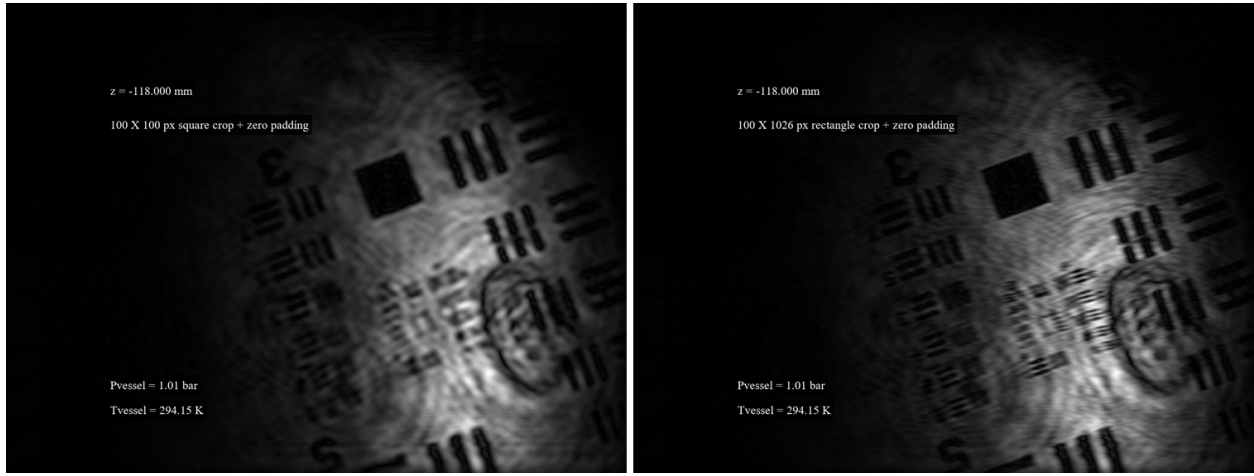


Figure 10.4 Left: USAF resolution chart image reconstructed 118 mm from the camera sensor using a 100px x 100px reconstruction area - Right: USAF resolution chart image reconstructed 118 mm from the camera sensor using a 100px x 1026px reconstruction area

10.1.2.2 USAF resolution chart – 400 px wide reconstruction area

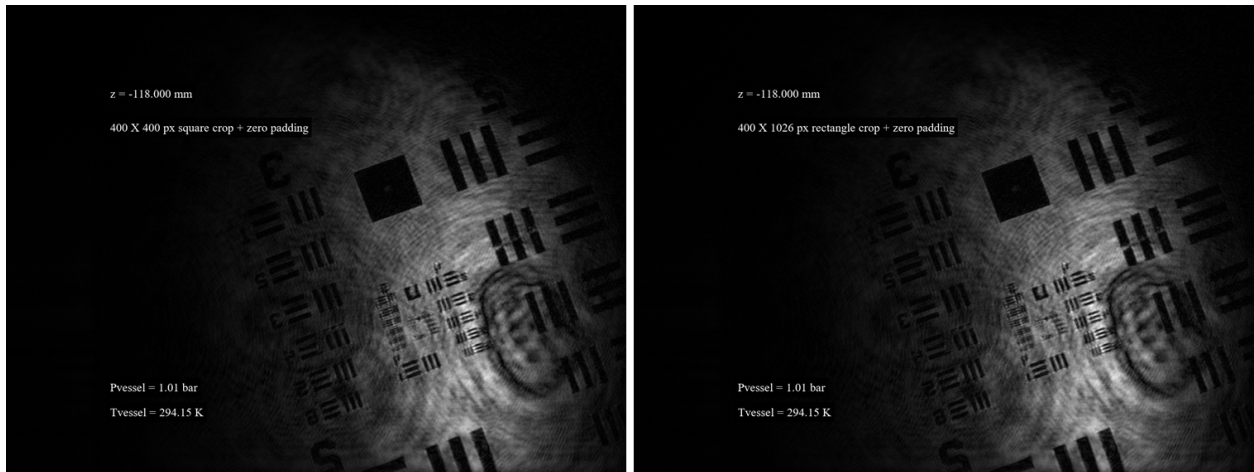


Figure 10.5 Left: USAF resolution chart image reconstructed 118 mm from the camera sensor using a 400px x 400px reconstruction area - Right: USAF

resolution chart image reconstructed 118 mm from the camera sensor using a 400px x 1026px reconstruction area

10.1.2.3 *Dodecane spray at early injection – 100 px wide reconstruction area*

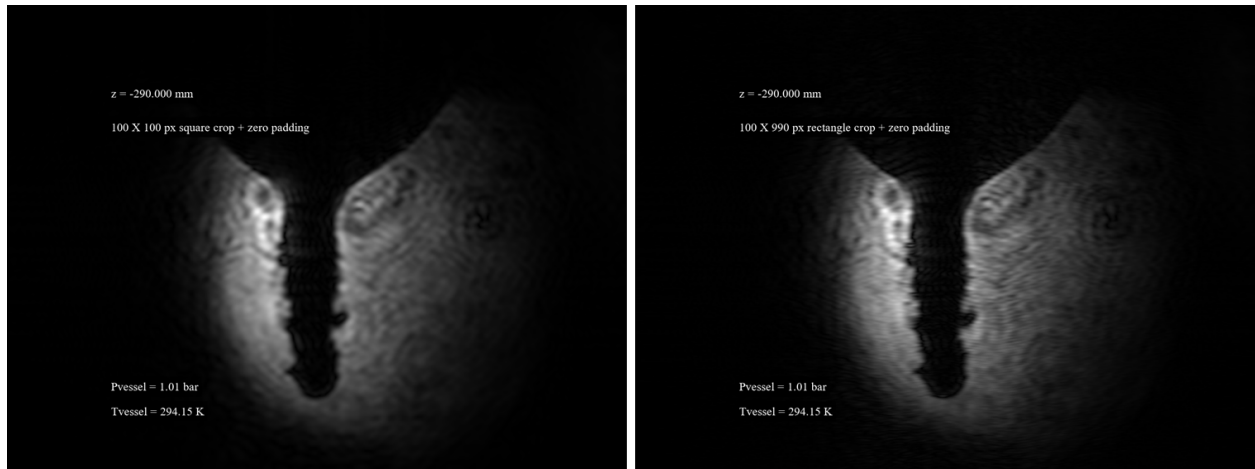


Figure 10.6 Left: Dodecane spray image reconstructed 290 mm from the camera sensor using a 100px x 100px reconstruction area - Right: Dodecane spray image reconstructed 118 mm from the camera sensor using a 100px x 990px reconstruction area

10.1.2.4 *Dodecane spray at early injection – 400 px wide reconstruction area*

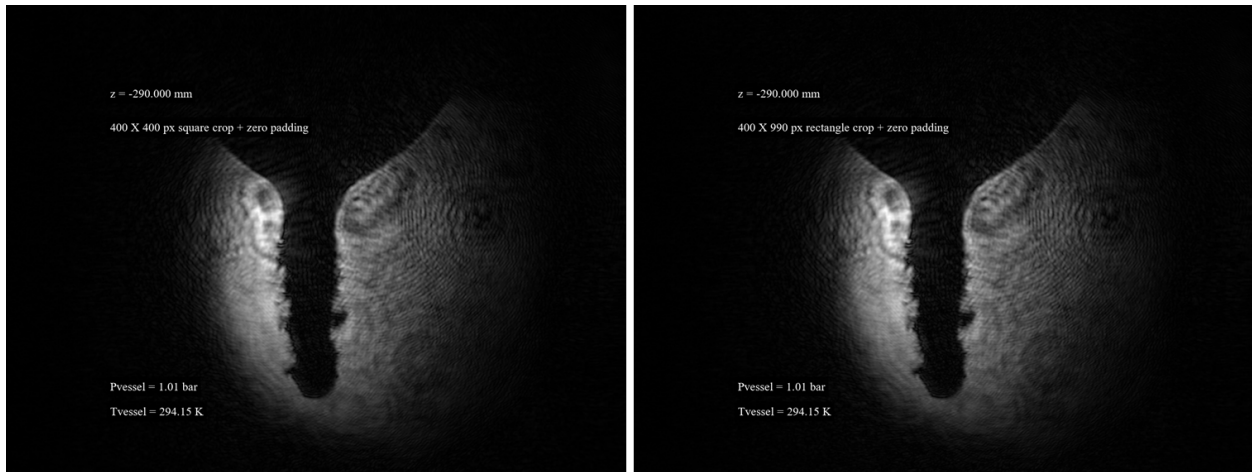


Figure 10.7 Left: Dodecane spray image reconstructed 290 mm from the camera sensor using a 400px x 400px reconstruction area - Right: Dodecane spray image reconstructed 118 mm from the camera sensor using a 400px x 990px reconstruction area

The resolution and sharpness achieved by the newer algorithm are always superior to the ones achieved by the previous one. This is especially true when the reconstruction area width is constrained to 100px. This is a reconstruction condition that is required in harsh scattering environments, where the amplitude of the DC-term is larger, and therefore the reconstruction area width must be smaller in order to avoid crosstalk and noise in the reconstructed image. Looking at Figure 10.4 the previous algorithm cannot resolve any element of group 4, while the newer reconstruction resolves element 1 of group 4, which corresponds to a 31.25 μm object-side resolution.

Resolution is greatly improved with a 400px wide reconstruction area. In Figure 10.5 the previous algorithm resolves element 1 of group 5 (15.6 μm resolution), while the newer

algorithm shows similar horizontal resolution but better vertical resolution by resolving element 2 (13.9 μm resolution). The spray images show improvement at the gas to liquid interface where ligament structures appear sharper and with higher contrast.

10.1.3 Addressing potential sources of aliasing from undersampling

In our setup, the reconstruction distance is dictated by the target of interest, as the large pressure vessel forces the camera sensor to be at approximately 30-40 cm from the target spray. Section 5.5 shows that the reconstructed image resolution when reconstructed using the angular spectrum method is inversely proportional to the reconstruction depth. This section describes a more complex tradeoff between image quality, reconstruction/recording distance and the numerical method used to compute the reconstruction.

The combination of kind of holographic imaging setup, recording distance, reconstruction distance, and reconstruction method can create aliasing and aberrations in the reconstructed image when the overall configuration is sub-optimal. Each of these categories imposes on the recording/reconstruction distance z . The parameters used for all the following calculations are based on average values representative of our off-axis layout

and camera while imaging a dodecane spray at 30-40 cm from the camera sensor with a spray core diameter of 1 mm:

M' = Central nonzero pixels of the image

M = total number of pixels of the CCD sensor = 1040

Δx = sampling period or pixel pitch = 6.45 μm

λ = recording/reconstruction wavelength = 400 nm

D = size of object = 1-100 mm

z = recording/propagation depth

All cases assume a $M \times M$ sensor size of 1040 px x 1040 px.

10.1.3.1 Pixel pitch and sampling frequency

The interference pattern is digitized by the CCD sensor, and usually, the practical resolution of its image is below the diffraction limit. We must be sure that we are correctly sampling the frequencies of the interference pattern in order to faithfully reconstruct its diffracted wavefront while avoiding aliasing. To understand this situation, consider having a Fresnel zone plate (FZP) by creating a hologram from a point source in an inline configuration. The local fringe frequency of the FZP is $x/\lambda_0 z_0$, where z_0 is the distance between the object point source and the plane where the hologram is recorded.

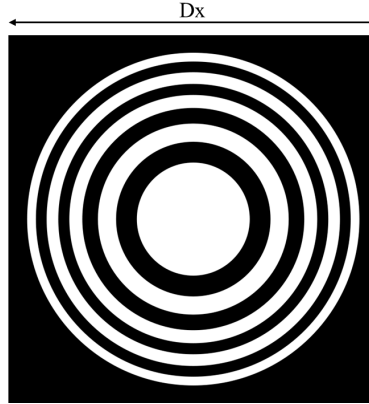


Figure 10.8 Fresnel zone plate (FZP) generated by the diffracting field from a point object source.

To record the finest fringes at the edges of the FZP, $D_x/2$ from the center, the required sampling frequency will be

$$f_s = \frac{1}{\Delta x_{CCD}} \geq \frac{2 * \frac{D_x}{2}}{\lambda_0 z_0}$$

Solving for the distance between the object and the hologram plane

$$z_0 \geq \frac{\Delta x_{CCD} D_x}{\lambda_0}$$

Which identifies a critical distance between the object and sensor plane, below which the finer structures of the FZP cannot be resolved, and aliasing occurs. For practical purpose we assume D_x to be equal to the sensor size in the worst-case scenario where the interference pattern covers the entire sensor, we find that

$$z_0 = \frac{\Delta x_{CCD} D_x}{\lambda_0} = \frac{6.45\mu m * 1024 * 6.45\mu m}{400 \text{ nm}} = 108\text{mm}$$

This critical distance is always respected by our setup.

10.1.3.2 Condition to record an off-axis digital hologram correctly

The critical distance for successful off-axis holography is [64]

$$z \geq \frac{4\Delta x(D + M\Delta x)}{\lambda}$$

Where D is the size of the object to be imaged, the following table shows this minimum critical distance for different values of D.

Table 10.1 Minimum recording distance (z) for an off-axis Fresnel hologram as a function of object size D

D	z
1 mm	0.426 mm
10 mm	4.26 mm
100 mm	42.6 mm

The calculated values of z represent the minimum distance between an object of size D and the CCD in order to have successful off-axis holography while avoiding aliasing.

These conditions are always respected by our current experimental setup. We can also calculate the critical offset angle for the reference beam that avoids cross-talk between the 0th and 1st orders of diffraction while avoiding under-sampling of the 1st order [64]

$$\vartheta_c = \sin^{-1}\left(\frac{3\lambda}{8\Delta x}\right) = 0.023 \text{ rad}$$

This is close to the value of 0.03 rad used in our setup.

10.1.3.3 Validity of the angular spectrum method

The angular spectrum method (ASM) can be used to numerically propagate the diffracted field generated from an aperture residing in an initial plane to a second diffraction plane. As shown in section 5.5, it can also be used for backward propagation, which means retrieving the object light in the initial plane from the hologram recorded in the diffraction plane. A condition for alias-free simulation applies to both forward and back-propagation; this condition is due to avoiding under-sampling of the incident field and the spatial frequency transfer function and their product which gives the diffracted field. Reference [64] provides the full derivation of the condition.

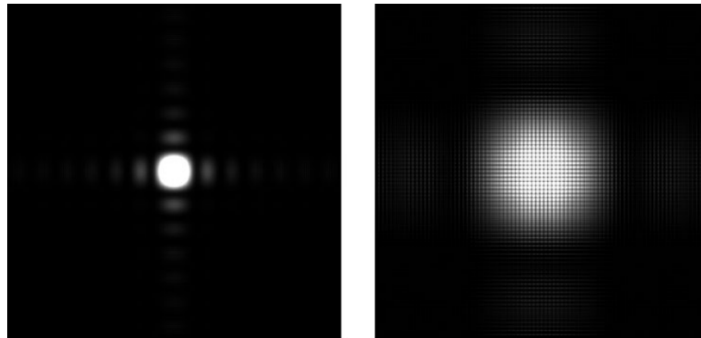


Figure 10.9 Simulated intensity pattern of the diffracted field from a rectangular aperture propagated using the ASM, left propagation distance $z=0.05$ m, right propagation distance $z=0.2$ m (showing aliasing error) [64]

A simulation with no aliasing error must satisfy

$$|z| \leq \frac{\sqrt{4\Delta x^2 - \lambda^2}}{2\lambda^2} (M - M')\Delta x$$

$M'=400$ px object size in pixel, which is the $M' \times M'$ pixels area containing nonzero values in the frequency domain, this region is then zero-padded and processed by ASM for reconstruction

$M=1040$ px number of pixels in the hologram plane

$\Delta x = 6.45 \mu\text{m}$ pixel pitch

$\lambda=400 \text{ nm}$ recording/reconstruction wavelength

As the object size in the frequency domain varies this critical propagation distance has been evaluated for a range of values

Table 10.2 ASM critical propagation distance (z) as a function of object size (M')

M' (px)	z (mm)
0	209
400	128.6
...	...
1040	0

These results show that for a typical object size of 400 pixels (typical size of the reconstruction box used surrounding the cross-correlation term to avoid cross-talk with the DC-term), aliasing error is introduced when numerically reconstructing the diffracted field more than 128 mm from the hologram plane. This distance goes to zero as the object size M' approaches the sensor size M . The pressure vessel holograms presented in previous chapters all infringe on this condition, as the physical distance between the camera sensor

and the object plane cannot be less than approximately 150mm, and most of the spray results have a reconstruction depth around 270mm. Numerical aliasing can be avoided with altering $(M-M')$ by increasing M , adding zero padding to the image before reconstruction. In order to use ASM while avoiding aliasing altogether at a long propagating distance, M would have to be around 5,500 pixels, which would require a substantial computational effort for reconstruction. Alternatively, numerical methods that perform better for longer propagation distances, like the Fresnel diffraction method (FDM), can be considered.

The condition for alias-free sampling when using the Fresnel diffraction method to calculate the diffracted field is

$$z \geq \frac{2M\Delta x^2}{\lambda}$$

This means that there is a minimum limit for the propagation distance to avoid aliasing error; again [64] provides the full derivation. Substituting in the values typical for our setup ($M=1040$, $\Delta x = 6.45\mu\text{m}$, $\lambda=400\text{nm}$), we obtain a minimum propagation distance of 286mm. These results suggest that we should either adopt the FDM to numerically reconstruct images at large propagation depths (>286 mm) or increase zero-padding and/or modify the optical setup in order to use ASM while avoiding aliasing error.

10.1.3.4 *Conclusions and corrective actions*

We found that, for a given sampling period Δx , for alias-free reconstruction of the diffracted field, the ASM is to be preferred for shorter propagation distances (Figure 10.10) and the FDM for longer ones. There is however a gap between the two methods where aliasing will be introduced (Figure 10.11). We have extended the maximum alias-free reconstruction distance of the ASM by increasing zero-padding (which increases M , see Figure 10.12), while the only way to reduce the FDM minimum reconstruction distance is to reduce the sampling period Δx , which is not feasible. The reconstruction code was modified to use the FDM for longer propagation distances, and to increase M by adding zero-padding whenever alias would have to be introduced by using the ASM. Figure 10.12 shows graphically how the current reconstruction algorithm applies the appropriate reconstruction method for a given propagation distance condition to avoid numerical aliasing at all times. Section 10.2 shows how a lensed USPODH setup was then created to minimize recording and propagating distance to enhance the quality and resolution of the reconstructed images even further.

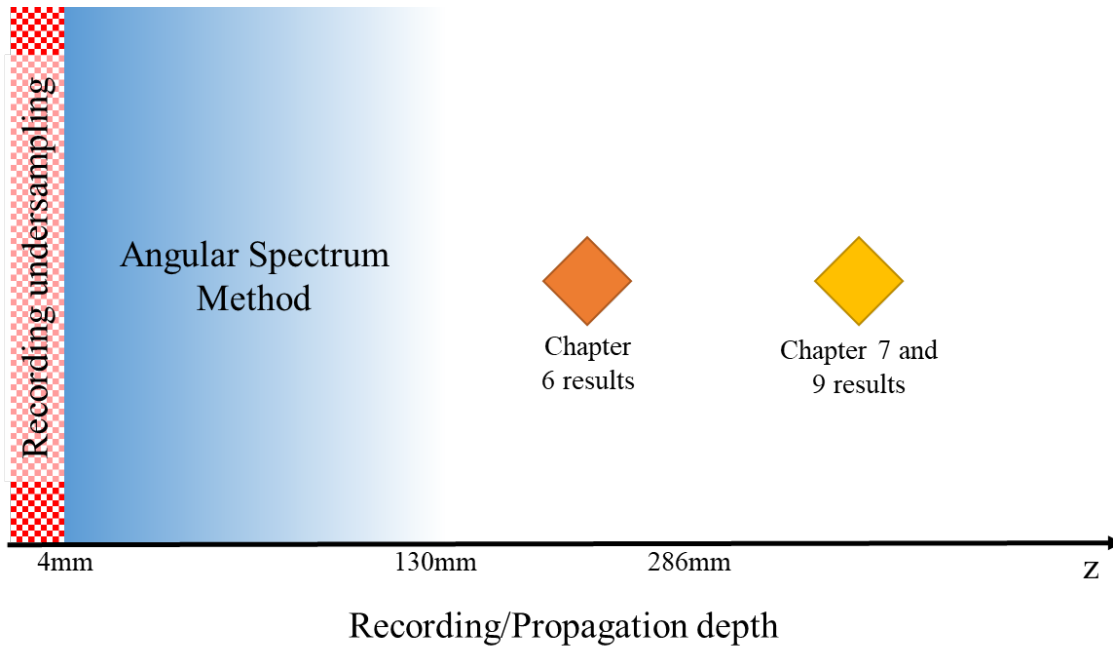


Figure 10.10 Diagram showing the ranges of recording and reconstruction distance that allow alias-free recording and reconstruction of an off-axis hologram. The colored rhombus shapes show where the results presented in this dissertation belong to given their hologram properties and reconstruction distance.

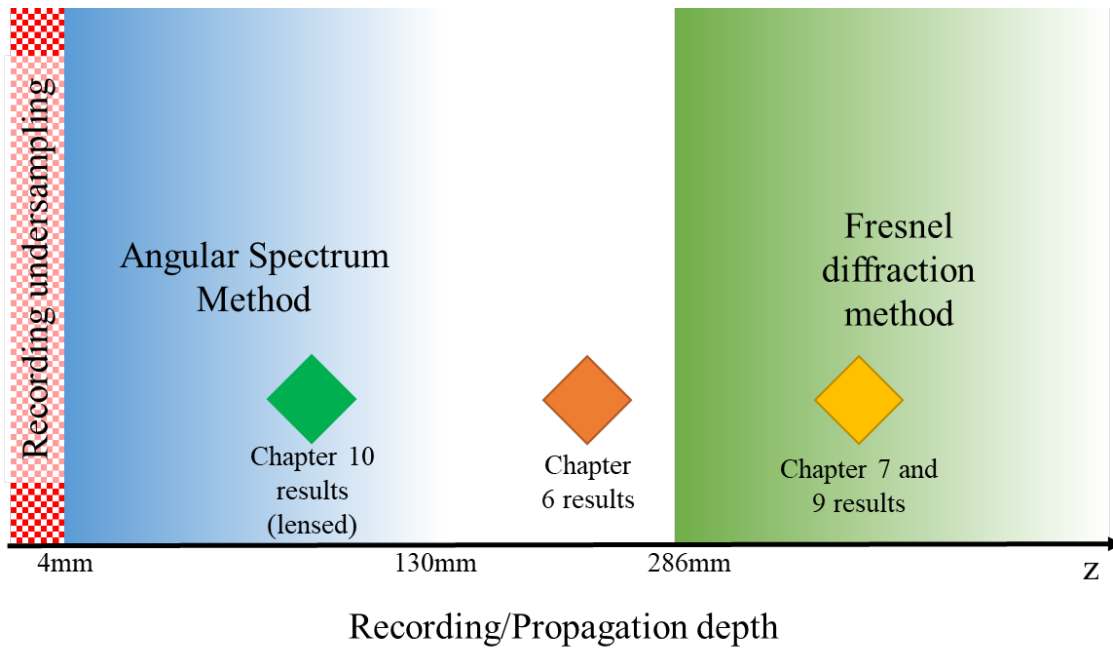


Figure 10.11 Diagram showing the ranges of recording and reconstruction distance that allow alias-free recording and reconstruction of an off-axis hologram. The implementation of the FDM for reconstruction allows alias-free reconstruction of holograms at a working distance larger than 286 mm.

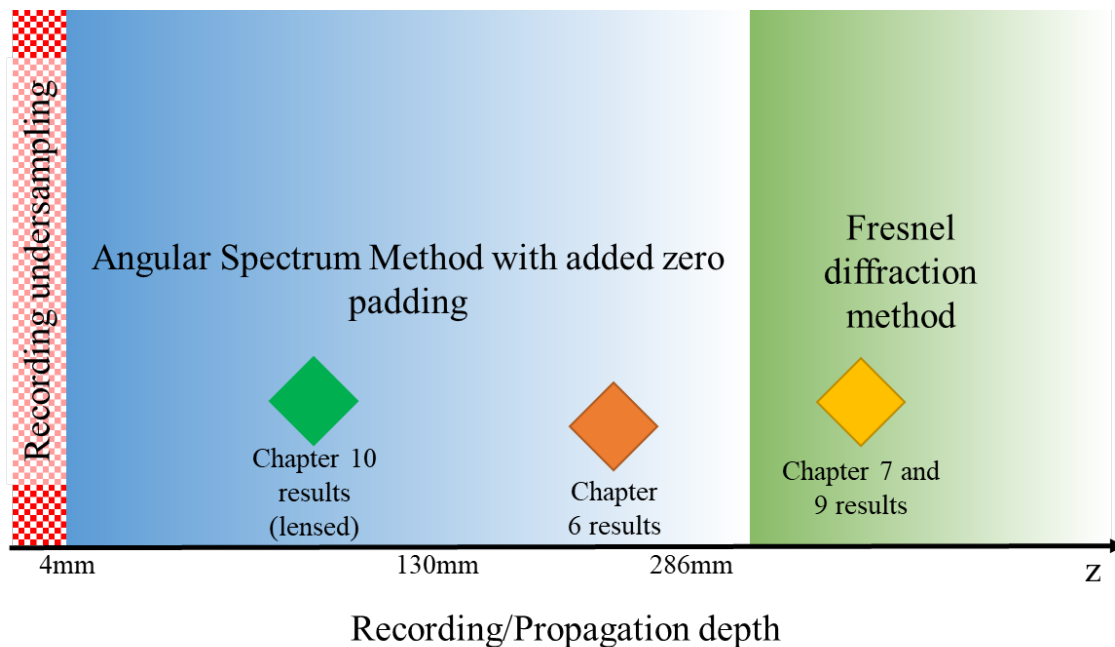


Figure 10.12 Diagram showing the ranges of recording and reconstruction distance that allow alias-free recording and reconstruction of an off-axis hologram. The addition of extra zero-padding allows extending the upper alias-free reconstruction limit of the ASM.

The next figures show a comparison between ASM and FDM reconstructions. Figure 10.13 is reconstructed 300 mm from the hologram. At this large propagation depth, the FDM reconstruction on the right shows better contrast and resolution than the ASM one. As expected, that is not true for the reconstructions in Figure 10.14, 118 mm from the hologram plane.

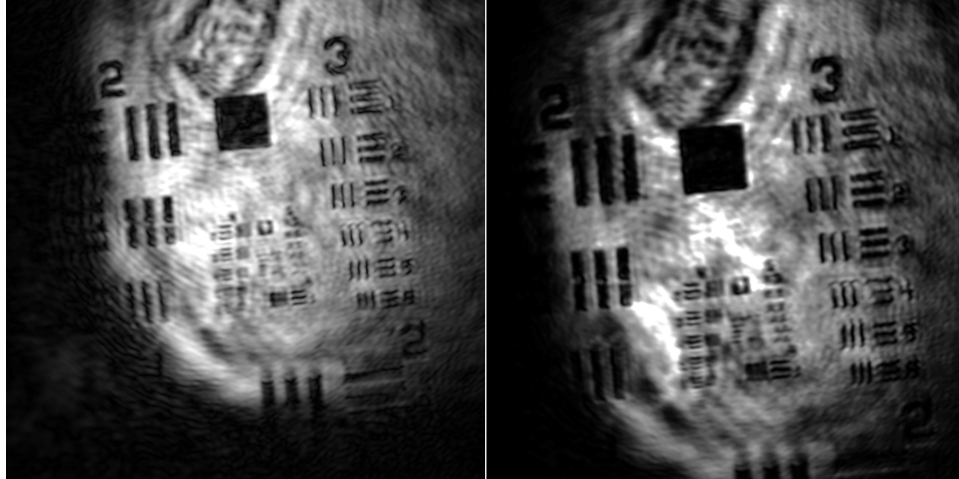


Figure 10.13 ASM (left) vs. FDM (right) reconstructed images of a resolution chart, 300 mm from the camera sensor, lensless off-axis holography.

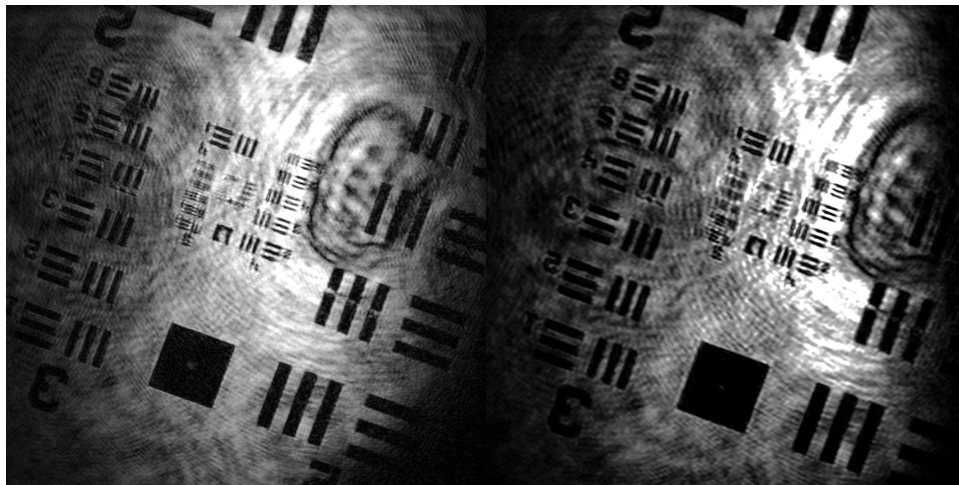


Figure 10.14 ASM (left) vs FDM (right) reconstructed images of a resolution chart, $z=118\text{mm}$, lensed off-axis holography, $f=118\text{ mm}$.

10.2 Optical improvements – lensed results

Increasing zero-padding to extend the alias-free propagation range of ASM is computationally costly, whereas reducing propagation length would both satisfy the alias-free reconstruction criteria expressed in section 10.1 and increase resolution. Due to physical constraints, it was impossible to move the camera sensor closer to the target, so an optical configuration that would reduce the propagation depth necessary to reconstruct an image of the target was introduced. Figure 10.15 shows a lensed USPODH setup where an achromatic doublet lens (L3) with a focal length $f=180$ mm has been placed between the beamsplitter BS2 and the camera sensor. The lens is placed as close as possible to BS2 at a distance from the object d_o of about 35 cm, the distance between the lens and the camera d_i can be adjusted to achieve the desired magnification and experiment with the focus. The results presented next will show how this setup successfully reduces the propagation distance between the hologram and object plane while increasing the reconstructed image resolution. The new recording and propagation distances, which is now governed by the distance between the front focal plane of the lens and the target, always fall within the range for alias-free reconstruction using the ASM.

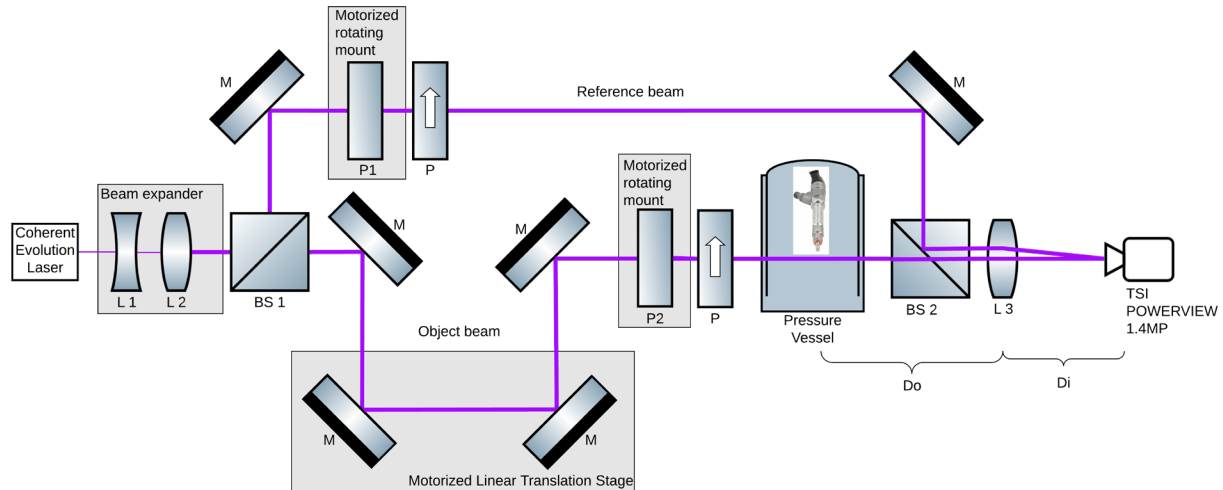


Figure 10.15 Lensed USPODH setup

10.2.1 USAF reconstructions – lensed configuration $f=180\text{mm}$

A USAF resolution chart was placed in the middle of the pressure vessel at the spray nozzle location in order to evaluate the resolution achieved by the lensed system. Figure 10.16 shows a reconstructed off-axis hologram reconstructed adopting a 400-pixel reconstruction mask surrounding the cross-correlation term and then zero-padding the image matrix to bring it to the original image resolution. The achromatic doublet lens with $f=180\text{ mm}$ is placed 35 cm from the chart. The camera is approximately 42 cm from the lens. The magnification factor M is approximately equal to 1.2 . In order to numerically focus the USAF chart, the hologram diffracted field has to be propagated only by $z=118\text{mm}$, a fraction of the actual physical distance of 35 cm between the target and the lens. According to holographic theory, this increases the resolution by virtually

moving the detector closer to the target and introduces no aliasing error when back-propagating the diffracted field via the ASM. Figure 10.17 shows a noticeable increase in resolution with respect to previous lensless results. Element 6 of group 4 is resolved which corresponds to an object side resolution of 17 μm .

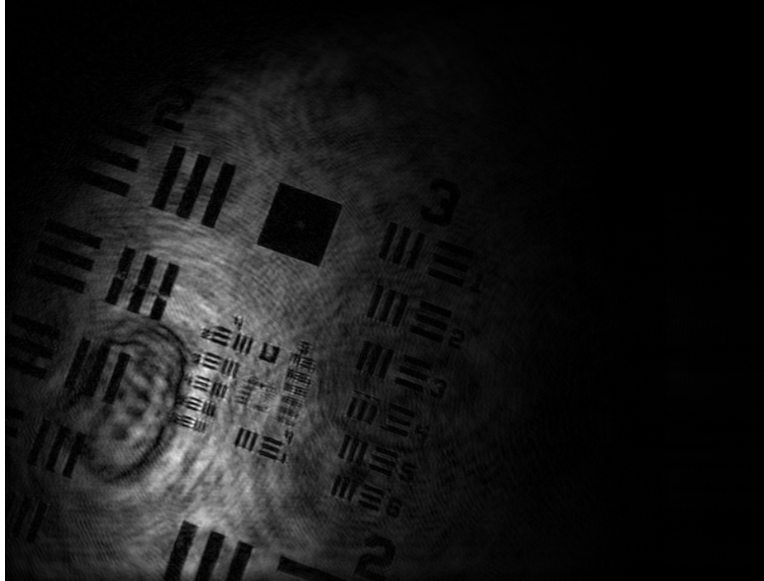


Figure 10.16 Reconstructed off-axis hologram of a USAF resolution chart placed at the center of the pressure vessel at the fuel injector location, $z=118\text{mm}$, 400 px reconstruction mask, $d_o=39\text{ cm}$ $d_i=42\text{ cm}$ $f=180\text{mm}$

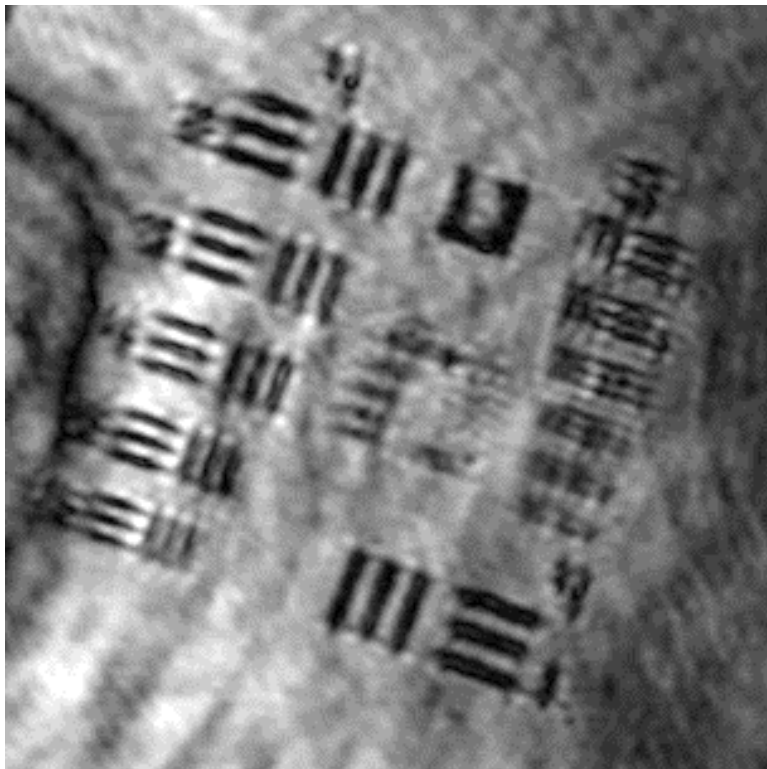


Figure 10.17 Magnification of group 4 and 5, element 6 of group 4 can be resolved which corresponds to an object side resolution 17 μm

We then moved the achromatic doublet lens closer to the target $d_o=35$ cm and adjusted $d_i=40$ cm so that the resolution chart would appear focused. We then shot and reconstructed an off-axis hologram (Figure 10.18). The propagation depth is now approaching zero, as the target is already in focus at the hologram plane. Despite the reduced propagation depth with respect to the previous case, we observe no noticeable resolution improvement, and on the contrary sharp artifacts covering group 4 and 5 are noticeable. This is attributable to the fact that when the lens is focused on the target plane it is as if we are recording the diffraction pattern in the near field of the diffracting aperture (the target), thus infringing on the minimum critical distance to record an off-axis Fresnel hologram without aliasing error that we investigated in the previous section (about 4 mm).

Finally, the camera was moved further away from the lens to achieve a magnification of $M=1.46$ for $d_i=51$ cm (Figure 10.20 and Figure 10.21). The higher magnification did not increase the image resolution, suggesting that we reached the resolution limit for the present configuration.



Figure 10.18 Reconstructed off-axis hologram of a USAF resolution chart placed at the center of the pressure vessel at the fuel injector location, $z=4\text{mm}$, $450 \times 998\text{px}$ reconstruction mask, $d_o=35\text{ cm}$ $d_i=40$ $M=1.14$ $f=180\text{mm}$

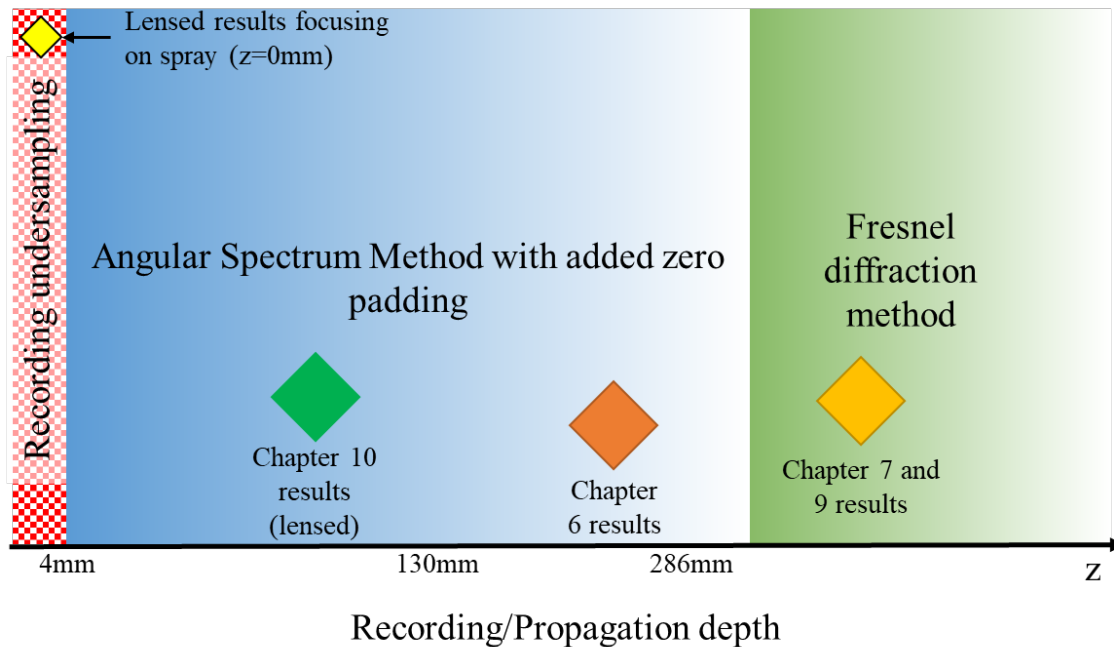


Figure 10.19

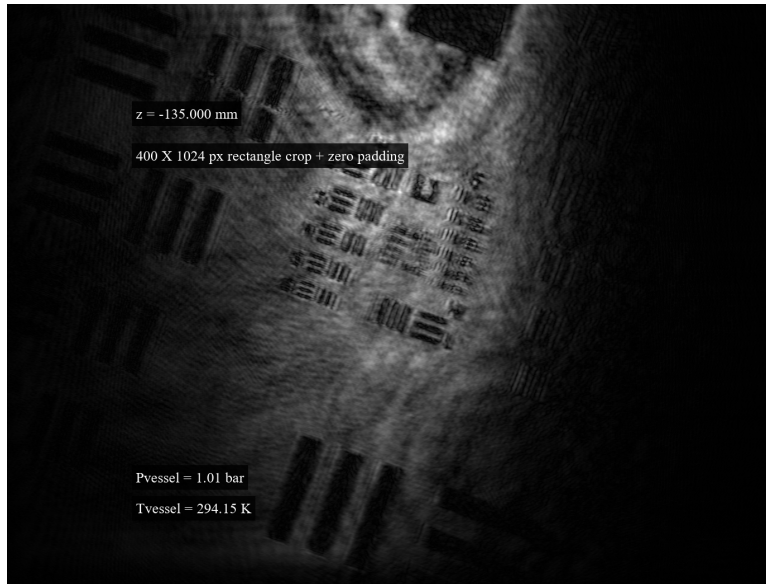


Figure 10.20 Reconstructed off-axis hologram of a USAF resolution chart placed at the center of the pressure vessel at the fuel injector location, $z=135\text{mm}$, $400\times 1024\text{px}$ reconstruction mask, $d_o=35\text{ cm}$ $d_i=51$ $M=1.46$ $f=180\text{mm}$

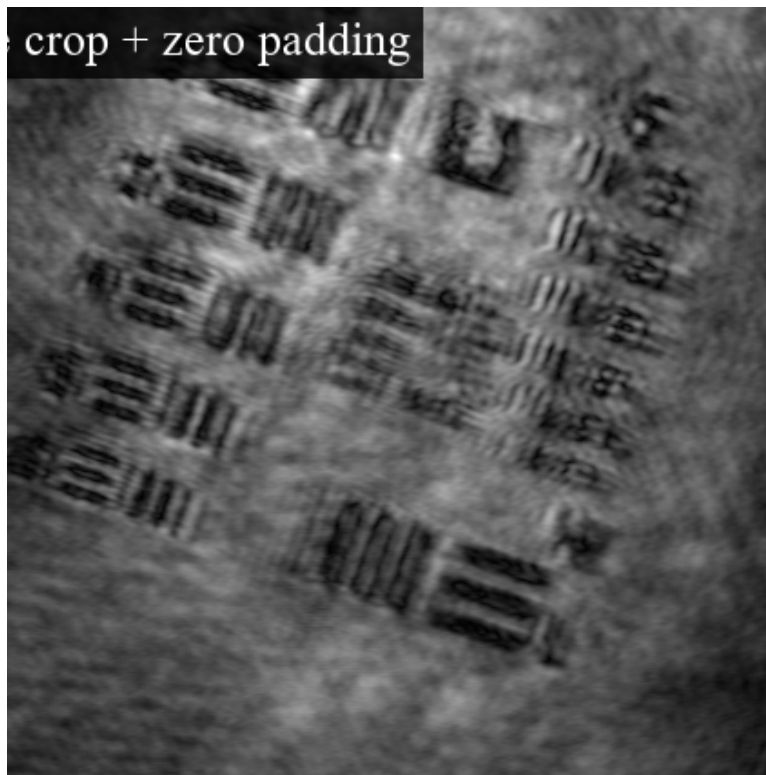


Figure 10.21 The higher magnification $M=1.46$ did not improve resolution we reached the resolution limit for the current combination of optics, target size, sensor size working distance, and numerical reconstruction method.

10.2.2 Spray reconstructions – lensed configuration $f=180\text{mm}$

Figure 10.22 shows a magnified view of the gas to liquid interface in the near-nozzle region. The injector nozzle diameter is $320\ \mu\text{m}$, less than 2 diameters from the nozzle we observe what appears as the side of a fluid lobe surrounding the liquid core that is shedding large sections of fluids in the surrounding gas (see the top of Figure 10.23). Ligaments that we could not resolve in previous iterations of the experiments are now clearly imaged as well as droplets detaching from such ligaments, the bottom of Figure 10.23 shows a ligament approximately $100\ \mu\text{m}$ long and $20\ \mu\text{m}$ thick surrounded by primary atomization droplets with diameters ranging from 40 to $20\ \mu\text{m}$. These may be the first images of primary atomization structures in the near nozzle region of a realistic dodecane spray, as they appear consistent with the structures predicted by primary atomization models [23]. Further confirmation that these are primary atomization fluid structures normally hidden by a shroud of highly scattering droplets is necessary and can be achieved by performing simultaneous shadowgraph imaging of the same region.

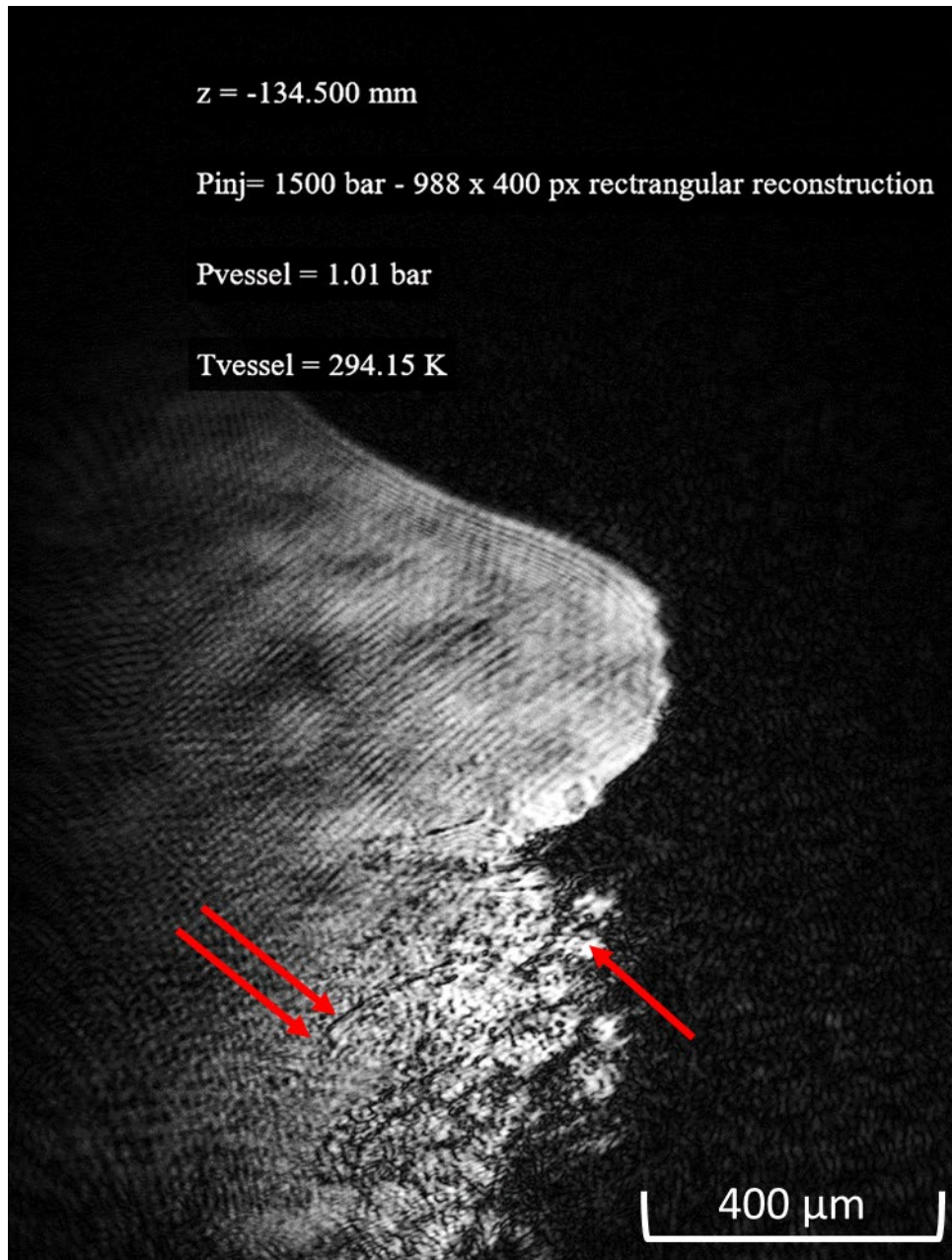


Figure 10.22 Reconstructed off-axis hologram - 988 x 400 rectangular mask - $z=-134.5$ - $d_o=35 \text{ cm}$ $d_i=51 \text{ cm}$ $M=1.46$ $f=180\text{mm}$. The regions indicated by the red arrows are expanded in the next figure.

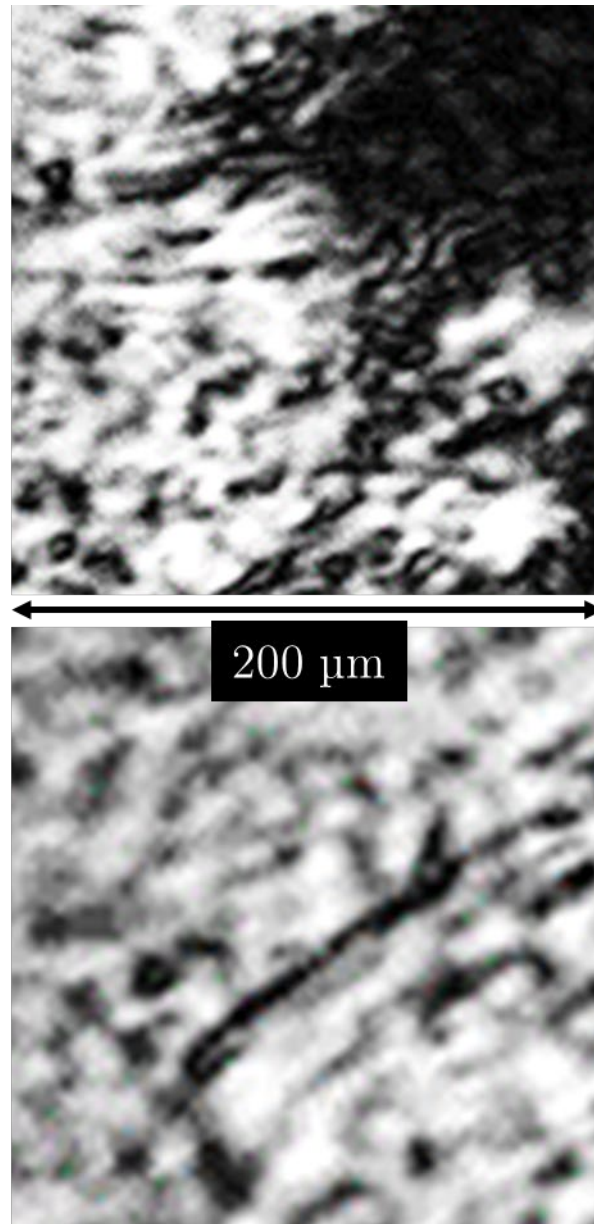


Figure 10.23 Primary atomization fluid structures in the near nozzle region.

10.2.3 Comparison between lensed shadowgraph inline holography and off-axis holography

The introduction of a lens to the setup finally allows for a direct comparison of lensed focused shadowgraph, inline holography, and off-axis holography when imaging a realistic spray. The lensed shadowgraph image (Figure 10.24) and the reconstructed inline hologram (Figure 10.25) have low pixel value as if the object beam was obstructed by a mist-like environment, yet information can be retrieved by raising brightness and contrast by 80-90% thanks to the excellent dynamic range of the camera. The off-axis hologram reconstruction is well illuminated and would be so even using a much less sensitive camera because of the reference beam amplification of the object pulse discussed in Chapter 5. The lensed shadowgraph image shows a large number of droplets surrounding the spray; these are present also in the inline hologram but not in the off-axis reconstruction. This suggests that this is a shroud of primary atomization droplets surrounding the core spray, and that the off-axis reconstruction is rejecting this source of multiple scattering noise, we are inclined to believe so also because the off-axis reconstruction consistently shows a spray with a smaller cone angle, again suggesting that the off-axis configuration is removing the obscuration of a layer of droplets surrounding the core. These, together with the images of ligaments at the gas to liquid interface, are encouraging results but to make

a conclusive statement on USPODH scattering rejection performance on realistic sprays it will be necessary to have a system that can simultaneously shoot lensed shadowgraph and off-axis holograms using the same light source, or address spray jitter by achieving a spray repeatability below 1 μ s.

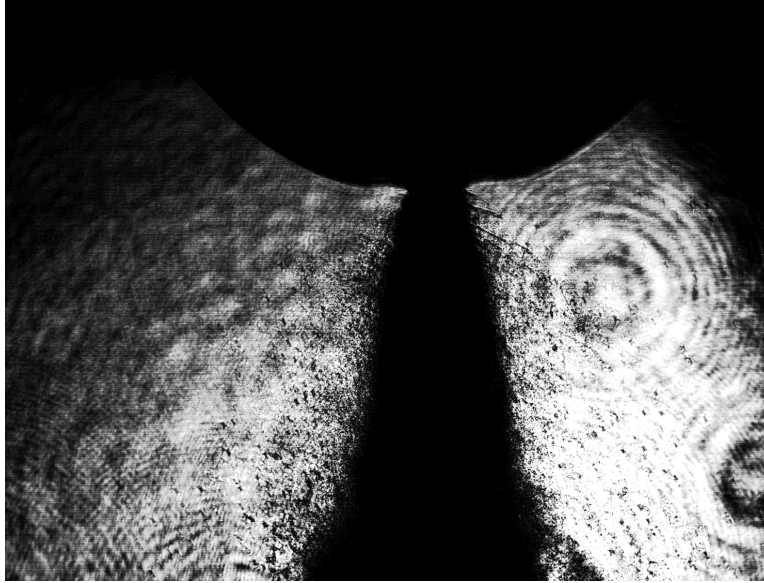


Figure 10.24 Focused shadowgraph (object beam only), brightness +80%, contrast +10%

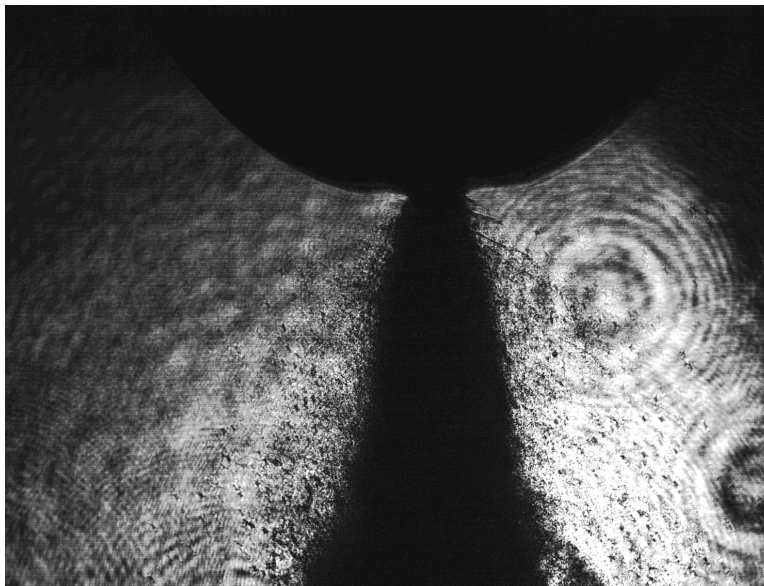


Figure 10.25 Reconstructed Inline hologram - 1000px reconstruction mask - $z=0\text{mm}$ - brightness +80%

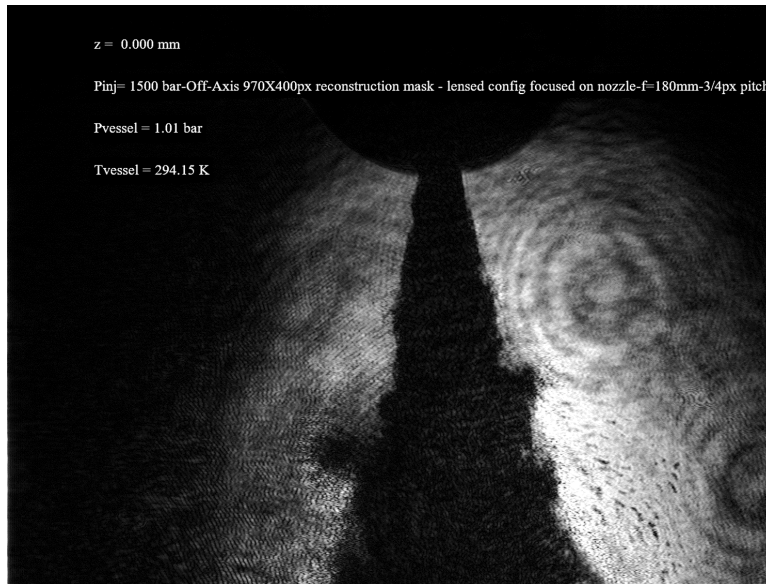


Figure 10.26 Reconstructed off-axis hologram, $z=0\text{mm}$, 970x400px reconstruction mask, +40% brightness, +5% contrast

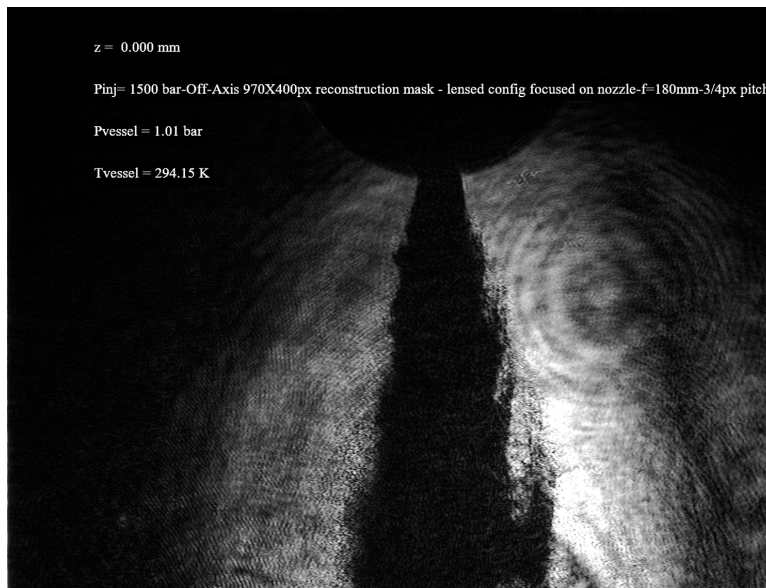


Figure 10.27 Reconstructed off-axis hologram, $z=0\text{mm}$, 970x400px reconstruction mask

10.3 Section summary

This section analyzed the potential inefficiencies that can lead to inaccurate hologram recording and reconstruction, and identified critical propagation and recording distances that guarantee correct sampling and numerical propagation of the diffracted field.

Solutions introduced always satisfy these optimal conditions:

- Improved the zero-padding algorithm to include more pixels for reconstruction, which increases resolution and raises the upper acceptable propagation depth for the ASM.
- Implemented the FDM for reconstructions free from aliasing at large propagation distances ($z > 28\text{cm}$).
- Introduced a lensed configuration that reduces the propagation distance necessary to focus on the object; the reduced propagation distance increases the reconstructed image resolution (measured object-side resolution $17\mu\text{m}$) and falls within the range for alias-free backpropagation of the diffracted field using the ASM.
- Presented preliminary spray results with the improved lensed setup and comparison with lensed shadowgraph imaging and inline holography, these results suggest that USPODH is successfully rejecting the shroud of primary atomization

droplets surrounding the spray core and imaging fluid structures at the gas to liquid interface which are consistent with the structures predicted by primary atomization models [23].

Chapter 11

11 Future recommendations

The optical sectioning performance achieved so far is promising but not yet sufficient to warrant the use of ultra-short pulse off-axis holography as a mainstream tool to resolve and locate precisely droplet distribution and ligaments in 3D. Tridimensional imaging is achieved, but it is sometimes complicated for the user to distinguish between focused particles residing in the current plane of reconstruction from slightly out-of-focus ones residing in other planes. A primary future goal will be to provide quantitative 3D location data for ligament and droplets by adopting the following strategies.

11.1 Beam Multiplexing

Adding multiple holograms on the same frame exposure multiplies the information available for reconstruction, with the condition that the holograms must be separated in the Fourier domain by different carrier spatial frequencies. Film holography classically used the possibility of recording different holograms on the same photo-plate for several

applications such as holographic interferometry, speckle interferometry, 3D location, and tracking of dynamic objects. Adding either multiple reference beams or multiple object beams will enable reconstructions along different optical axis thus providing stereoscopic information that will dramatically improve the technique's optical sectioning resolution and accuracy and open the possibility to holographic interferometry that can be used to quantify density gradients [87].

11.1.1 Multiple reference beams

Several digital holography setups used beam multiplexing to record multiple holograms on the same frame exposure for different purposes. Picart et al. [88] created spatial multiplexing by using two pairs of object and reference waves, making an incidence angle of $\pm 45^\circ$ respectively. The two pairs had different polarization states, the first pair with s ones and the second with p ones. This was to avoid noise due to supplementary interference fringes. Saucedo et al. [89] created the same multiplexing system with an incidence angle of $\pm 35^\circ$. The system had two different optical path lengths for each object-reference pair with both reference beams having an angle inclination of 1.5° with respect to the object beams (off-axis). Kühn et al. [90] performed two-wavelengths digital

holographic microscopy with a single hologram acquisition, using two reference waves with different wavelengths and propagation directions.

The schemes presented above all need numerous optical elements to achieve their respective setups. This introduces complexity and aberrations that is always important to minimize. Possible alternatives that simplify the setup complexity are presented next.

11.1.2 Single reference and multiple object beams

Boucherit et al. [91] successfully proposed an off-axis holography scheme that enables recording two holograms simultaneously on the same CCD sensor from two different optical axes using a single reference beam. Their setup uses a single reference beam and two orthogonal object beams, by correlation of the information from the two reconstructions of the images at successive depth locations they locate solid microparticles in a flow with their real 3D shape. One caveat presented by this approach is that the two object beams must have a slightly different optical path to avoid overlapping of the two reconstructed images. This could potentially be difficult (but not impossible) to apply to our setup where the short coherence length only allows for a pathlength mismatch smaller than the beam coherence length of 30 μm . Therefore, alternative approaches to achieve

the same outcome without the need for adding any extra reference of object beam are presented next.

11.2 Depth maps and 3D visualization

If beam multiplexing causes excessive complexity in the optical setup we propose using stereo disparity to create depth maps that will allow a clear distinction and quantification of the depth distance between objects residing in the current plane of reconstruction from others residing in other depth planes [86], [92]. Furthermore, we propose investigating 3D visualization strategies that will free the user from the current time consuming, multiple 2D reconstructions at different depth planes to create an extended depth of field image [93].

11.2.1 Stereo disparity method - recovering stereoscopic information from a single hologram

Holograms are reconstructed numerically by various wave propagation methods to recover the 3D object information, the Fresnel method, which is the propagation method adopted by our technique, enables calculation of the depth of microscopic objects from the phase information [94]. This phase information is wrapped for distances longer than the imaging

wavelength used to create the hologram, and phase unwrapping is practically impossible for macroscopic objects since the resolution of the recording is insufficient to record the wrapped fringes. The stereo disparity method is a technique for calculating depth maps from a single digital hologram, without having to recur to phase unwrapping. This technique was first described by Pitkäaho and Naughton [86]. Unlike incoherent photographic imaging, holograms lack a one-to-one correspondence between the pixels of the recorded interference pattern and a point of the object being imaged; this means that any partial crop of the hologram can be reconstructed into a complete image of the imaged object (at the cost of resolution loss). This allows splitting a digital hologram into two parts along one direction, numerically reconstruct each part separately at the same reconstruction depth and obtain two resultant images corresponding to a stereo image pair of the object. The hologram can be divided along different directions to obtain several stereo image pairs, and the stereo depth information can be merged with the 2D image of the object to visualize the object in 3D [92]. This allows to create, for instance, 2D reconstructions (see [86]) where all the features that are in front or behind the in-focus plane are color-coded to help the user access the 3D location embedded in digital holograms in an intuitive and genuinely quantitative fashion thus overcoming the limitations afflicting our current setup.

11.2.2 Stereoscopic viewing of digital holograms

An issue that afflicts digital holography is the lack of a proper method for the fruition of the 3D information embedded in each hologram: although nowadays digital propagation can be performed efficiently, only one depth plane is in focus in each reconstruction, and iterative reconstruction of every depth plane to create enhanced depth of field images is time consuming. This issue also affects our technique: an extensive amount of 2D reconstructions is required to map the object-field and identify interesting spray formations. Lehtimäki and Naughton [93] created a system where, using a 3D LCD monitor, reconstructions at different depths are presented to each eye allowing 3D perception of objects encoded in digital holograms with a significant computational cost reduction with respect to the creation of extended depth of field images. The implementation of this system on our setup would allow the creation and efficient fruition of a holographic spray database.

Chapter 12

12 Conclusions

A novel type of off-axis digital holography tuned for multiple scattering noise rejection was developed and applied to realistic fuel sprays. This technique uses “coherence filtering” from short coherence laser pulses to retain only ballistic and quasi ballistic photons, in lieu of hardware time-gating solutions. It also offers extended depth of field imaging from a single-shot, allowing the user to numerically refocus on features of interest, similarly to plenoptic imaging. A need for imaging data in the primary atomization region of high-pressure fuel sprays was identified, and the limitations of the current imaging technique identified the opportunity to complement the existing techniques with USPODH. Photon transport Monte Carlo simulations were used to quantitatively justify the use of short coherence filtering instead of time gating. In particular, the simulations showed that in order to image through high OD regions of atomizing sprays a gate switching time below 500 fs is necessary to filter out multiple scattering photons, and a time-gate with a switching time below 150 fs is ideal. This is

impossible to achieve with a single OKE CS₂ time-gate that has a switching time of approximately 1.1 ps, and can only be achieved with complex systems that use a combination of multiple OKE gates. Coherence filtering is well-suited as an alternative for this task because we have shown that it will also offer the shortest time gate possible for a given pulse length. We have also compared, numerically and experimentally, the effectiveness of aggressive spatial filtering versus picosecond time-gating and found that when performing time-gated ballistic imaging researchers might have benefitted from spatial filtering and erroneously attributed the scattering rejection performance to picosecond time-gating.

The ideal conditions for optimal holographic recording and reconstruction were derived from theory and implemented into the experimental setup. Imaging performance in a mockup dense spray with a controlled OD up to 12 was demonstrated to be superior to spatially filtered shadowgraph imaging. The OD value was measured experimentally, and the experimental measurements were validated using Monte Carlo photon transport simulations. Droplets as small as 25 μm in size were resolved in a multi-disperse OD 12 environment, at a working distance of approximately 140 mm. The comparison between USPODH and shadowgraph imaging was performed by matching the numerical aperture of the holographic system, applying spatial filtering and using the same fs light source in

order to give shadowgraph imaging the same scattering rejection performance of USPODH except for the effects and benefits of coherence filtering.

The experiment was then rebuilt around a pressure vessel with a diesel common rail fuel injection system, capable of emulating diesel engine-like injection and chamber conditions. Reconstructed images from a dodecane spray at ambient temperature and pressure resembled early ballistic imaging results, resolving objects as small as 30-40 μm at a working distance of approximately 270 mm. Early injection fluid structures that were observed by other researchers in similar conditions were also observed [78]. These first results were plagued by intense background noise and artifacts. 3D offline focusing was demonstrated by resolving features residing in different depth planes, up to 20 cm from one another.

The applicability of USPODH in realistic engine-like experimental conditions was demonstrated by imaging a USAF chart in a pressure vessel at pressures in excess of 18 bar and temperatures up to 450 K. Pulse broadening due to the presence of thick optical windows and high-pressure gas was quantified, as the stretched imaging pulse measured at approximately 300 fs FWHM, still below the 500 fs maximum pulse and gate length for

sufficient scattering rejection performance that was calculated using Monte Carlo simulations. Image blur caused by thermal gradients was observed, but it was shown that it could be compensated for by numerical refocusing on the feature of interest. To avoid laser damage to the camera sensor, the sensor damage threshold was calculated, and it was established that by operating the system in single-shot mode, sensor damage could be avoided altogether. To do so single-shot synchronization between the laser, cameras and spray system was implemented, also allowing to target specific early injection events.

USPODH was then applied to sprays injected in an environment at pressures equivalent to those found in engines with a compression ratio of 20:1. Ligaments that are thought to be responsible for generating primary atomization droplets were routinely imaged at the gas to liquid interface. All results show an interface displaying the effects of viscosity and surface tension, suggesting that near-critical conditions were not reached. This was not possible due to the limitations of the current chamber and will be addressed in future research. At ambient pressures up to 20 bar objects as small as 20 μm were resolved at a working distance of approximately 280 mm.

Given the long working distance imposed by the pressure vessel, we investigated image aliasing generated in the reconstruction process from using a reconstruction method outside of its range of validity. The Fresnel Diffraction Method was implemented for alias-free reconstructions at long working distances (>28 cm), and a new experimental layout that uses a relay lens to reduce the propagation distance necessary to focus on the target has been implemented. Lensed USPODH results of both spray and USAF resolution charts were presented, and objects as small as $14\ \mu\text{m}$ were resolved at a working distance of approximately 35 cm using a lens with $f=180$ mm. The improved resolution allowed to resolve a higher number of ligaments, surface waves, and primary atomization droplets at the gas to liquid interface in the proximity of the nozzle exit, whose appearance and size is consistent with the structures predicted by primary atomization models [23]. USPODH reconstructions were compared to focused lensed shadowgraph images and reconstructed inline holograms of the same spray. These images suggest that USPODH is successfully rejecting the signature from the shroud of primary atomization droplets surrounding the dense spray core. In the off-axis reconstructions, we see empty spaces in between what seem to be liquid roll-up structures or Kelvin-Helmholtz instabilities; these empty spaces appear obscured by droplets in both the shadowgraph images and inline reconstructions.

Lastly, we recommended methods to be investigated in the future to address the technique's current shortcomings. Beam multiplexing can significantly increase the amount of information available; similarly to ballistic imaging USPODH provides detail only of the spray edges, and combining multiple beams can allow creating a map of the fluid structures around the whole spray core. Beam multiplexing and stereo disparity methods can also be used to triangulate features in space and address the current uncertainty generated by observing the image of a feature in the plane where it resides as well as its out of focus shadow numerically propagated in other planes, where no such feature exists.

13 Bibliography

- [1] Z. Falgout, M. Rahm, D. Sedarsky, and M. Linne, “Gas/fuel jet interfaces under high pressures and temperatures,” *Fuel*, vol. 168, no. November, pp. 14–21, Mar. 2016.
- [2] J. Manin, “NUMERICAL INVESTIGATION OF THE PRIMARY BREAKUP REGION OF HIGH-PRESSURE SPRAYS,” *At. Sprays*, vol. 28, no. 12, pp. 1081–1100, 2018.
- [3] M. Linne, M. Paciaroni, T. Hall, and T. Parker, “Ballistic imaging of the near field in a diesel spray,” *Exp. Fluids*, vol. 40, no. 6, pp. 836–846, Jun. 2006.
- [4] D. Jarrahbashi, W. A. Sirignano, P. P. Popov, and F. Hussain, “Early spray development at high gas density: Hole, ligament and bridge formations,” *J. Fluid Mech.*, vol. 792, pp. 186–231, 2016.
- [5] M. Gorokhovski and M. Herrmann, “Modeling Primary Atomization,” *Annu. Rev. Fluid Mech.*, vol. 40, no. 1, pp. 343–366, Jan. 2008.
- [6] R. N. Dahms, J. Manin, L. M. Pickett, and J. C. Oefelein, “Understanding high-pressure gas-liquid interface phenomena in Diesel engines,” *Proc. Combust. Inst.*, vol. 34, no. 1, pp. 1667–1675, Jan. 2013.
- [7] A. Movaghar, M. Linne, M. Herrmann, A. R. Kerstein, and M. Oevermann, “Modeling and numerical study of primary breakup under diesel conditions,” *Int. J. Multiph. Flow*, vol. 98, pp. 110–119, Jan. 2018.
- [8] S. P. Duran, J. M. Porter, and T. E. Parker, “Ballistic Imaging of Sprays at Diesel Relevant Conditions,” *12th Int. Conf. Liq. At. Spray Syst.*, pp. 1–5, 2012.
- [9] R. N. Dahms and J. C. Oefelein, “On the transition between two-phase and single-phase interface dynamics in multicomponent fluids at supercritical pressures,” *Phys. Fluids*, vol. 25, no. 9, p. 092103, Sep. 2013.
- [10] Z. Falgout, M. Rahm, Z. Wang, and M. Linne, “Evidence for supercritical mixing layers in the ECN Spray A,” *Proc. Combust. Inst.*, vol. 35, no. 2, pp. 1579–1586, 2015.
- [11] A. Ziaee, “Ultra-short Pulse Off-axis Digital Holography and Kerr Effect Ballistic Imaging in Highly Scattering Environments such as Formation Region of Diesel Sprays,” University of California at Irvine, 2016.
- [12] A. Ziaee, C. Dankwart, M. Minniti, J. Trolinger, and D. Dunn-Rankin, “Ultra-short

- pulsed off-axis digital holography for imaging dynamic targets in highly scattering conditions,” *Appl. Opt.*, vol. 56, no. 13, p. 3736, May 2017.
- [13] M. Minniti, A. Ziaee, J. Trolinger, and D. Dunn-Rankin, “ULTRASHORT PULSE OFF-AXIS DIGITAL HOLOGRAPHY FOR IMAGING THE CORE STRUCTURE OF TRANSIENT SPRAYS,” *At. Sprays*, vol. 28, no. 6, pp. 565–578, 2018.
- [14] J. Oefelein, G. Lacaze, R. Dahms, A. Ruiz, and A. Misdariis, “Effects of Real-Fluid Thermodynamics on High-Pressure Fuel Injection Processes,” *SAE Int. J. Engines*, vol. 7, no. 3, pp. 2014-01–1429, Apr. 2014.
- [15] A. H. Lefebvre and V. G. McDonell, *Atomization and Sprays*, vol. 45, no. 5. Taylor & Francis Group, 6000 Broken Sound Parkway NW, Suite 300, Boca Raton, FL 33487-2742: CRC Press, 2017.
- [16] W. A. Sirignano, *Fluid Dynamics and Transport of Droplets and Sprays*. Cambridge: Cambridge University Press, 1999.
- [17] E. Berrocal, “MULTIPLE SCATTERING OF LIGHT IN OPTICAL DIAGNOSTICS OF DENSE SPRAYS AND OTHER COMPLEX TURBID MEDIA,” Cranfield University, 2006.
- [18] M. Linne, “Imaging in the optically dense regions of a spray: A review of developing techniques,” *Prog. Energy Combust. Sci.*, vol. 39, no. 5, pp. 403–440, Oct. 2013.
- [19] S. Duran, J. M. Porter, and T. E. Parker, “Ballistic Imaging and Scattering Measurements for Diesel Spray Combustion: Optical Development and Phenomenological Studies,” 1940.
- [20] W. Tan *et al.*, “High contrast ballistic imaging using femtosecond optical Kerr gate of tellurite glass.,” *Opt. Express*, vol. 21, no. 6, pp. 7740–7, 2013.
- [21] L. Wang, P. P. Ho, C. Liu, G. Zhang, and R. R. Alfano, “Ballistic 2-d imaging through scattering walls using an ultrafast optical Kerr gate,” *Science*, vol. 253, no. 5021, pp. 769–771, 1991.
- [22] H. Pitsch and O. Desjardins, “DETAILED NUMERICAL INVESTIGATION OF TURBULENT ATOMIZATION OF LIQUID JETS,” *At. Sprays*, vol. 20, no. 4, pp. 311–336, 2010.
- [23] D. Jarrahbashi, W. A. Sirignano, P. P. Popov, and F. Hussain, “Early spray development at high gas density: hole, ligament and bridge formations,” *J. Fluid Mech.*, vol. 792, pp. 186–231, Apr. 2016.
- [24] T. E. Parker, “A comparative study of room-temperature and combusting fuel sprays near the injector tip using infrared laser diagnostics,” *At. Sprays*, vol. 8, pp. 565–600, 1998.

- [25] W. D. Bachalo and M. J. Houser, "Phase/Doppler Spray Analyzer For Simultaneous Measurements Of Drop Size And Velocity Distributions," *Opt. Eng.*, vol. 23, no. 5, pp. 583–590, Oct. 1984.
- [26] S. V Sankar, B. J. Weber, D. Y. Kamemoto, and W. D. Bachalo, "Sizing fine particles with the phase Doppler interferometric technique," *Appl. Opt.*, vol. 30, no. 33, p. 4914, Nov. 1991.
- [27] G. A. Ruff, L. P. Bernal, and G. M. Faeth, "Structure of the near-injector region of non-evaporating pressure-atomized sprays," in *27th AIAA Aerospace Sciences Meeting*, 1989, vol. 1.
- [28] L. Arnone, F. Beretta, A. Tregrossi, A. D'Alessio, and F. Ossler, "Ensemble and time resolved light scattering measurements in isothermal and burning heavy oil sprays," *Symp. Combust.*, vol. 24, no. 1, pp. 1549–1555, Jan. 1992.
- [29] F. Beretta, A. Cavaliere, and A. D'Alessio, "Ensemble laser light scattering diagnostics for the study of fuel sprays in isothermal and burning conditions," *Symp. Combust.*, vol. 20, no. 1, pp. 1249–1258, Jan. 1985.
- [30] L. G. Dodge, D. J. Rhodes, and R. D. Reitz, "Drop-size measurement techniques for sprays: comparison of Malvern laser-diffraction and Aerometrics phase/Doppler," *Appl. Opt.*, vol. 26, no. 11, p. 2144, Jun. 1987.
- [31] P. G. Felton, A. A. Hamidi, and A. K. Aigal, "Measurement of drop size distribution in dense sprays by laser diffraction," *ICLASS-85; Proc. Third Int. Conf. Liq. At. Spray Syst.*, vol. 2, 1986.
- [32] Y. Yue, C. F. Powell, R. Poola, J. Wang, and J. K. Schaller, "QUANTITATIVE MEASUREMENTS OF DIESEL FUEL SPRAY CHARACTERISTICS IN THE NEAR-NOZZLE REGION USING X-RAY ABSORPTION," *At. Sprays*, vol. 11, no. 4, pp. 471–490, 2001.
- [33] Z. Liu *et al.*, "Ultra-Fast Phase-Contrast X-ray Imaging of Near-Nozzle Velocity Field of High-Speed Diesel Fuel Sprays," in *ILASS Americas, 22nd Annual Conference on Liquid Atomization and Spray Systems*, 2010, no. May.
- [34] W.-K. Lee, K. Fezzaa, and J. Wang, "Metrology of steel micronozzles using x-ray propagation-based phase-enhanced microimaging," *Appl. Phys. Lett.*, vol. 87, no. 8, p. 084105, Aug. 2005.
- [35] E. Berrocal, E. Kristensson, P. Hottenbach, M. Ald??n, and G. Gr??nefeld, "Quantitative imaging of a non-combusting diesel spray using structured laser illumination planar imaging," *Appl. Phys. B Lasers Opt.*, vol. 109, no. 4, pp. 683–694, 2012.
- [36] M. Storch *et al.*, "Two-phase SLIPI for instantaneous LIF and Mie imaging of

- transient fuel sprays,” *Opt. Lett.*, vol. 41, no. 23, p. 5422, Nov. 2016.
- [37] P. F. Flynn *et al.*, “Diesel Combustion: An Integrated View Combining Laser Diagnostics, Chemical Kinetics, And Empirical Validation,” 1999.
- [38] L. M. Wang, P. P. Ho, and R. R. Alfano, “Double-stage picosecond Kerr gate for ballistic time-gated optical imaging in turbid media,” *Appl. Opt.*, vol. 32, no. 4, p. 535, Feb. 1993.
- [39] a D. Sappey, “Optical imaging through turbid media with a degenerate four wave mixing correlation time gate.,” *Appl. Opt.*, vol. 33, no. 36, pp. 8346–54, Dec. 1994.
- [40] K. M. Yoo and R. R. Alfano, “Time-resolved coherent and incoherent components of forward light scattering in random media,” *Opt. Lett.*, vol. 15, no. 6, p. 320, Mar. 1990.
- [41] K. M. Yoo, Q. Xing, and R. R. Alfano, “Imaging objects hidden in highly scattering media using femtosecond second-harmonic-generation cross-correlation time gating,” *Opt. Lett.*, vol. 16, no. 13, p. 1019, Jul. 1991.
- [42] K. M. Yoo, F. Liu, and R. R. Alfano, “Imaging through a scattering wall using absorption,” *Opt. Lett.*, vol. 16, no. 14, p. 1068, Jul. 1991.
- [43] F. Liu, K. M. Yoo, and R. R. Alfano, “Ultrafast laser-pulse transmission and imaging through biological tissues,” *Appl. Opt.*, vol. 32, no. 4, p. 554, Feb. 1993.
- [44] M. Paciaroni and M. Linne, “Single-shot, two-dimensional ballistic imaging through scattering media,” *Appl. Opt.*, vol. 43, no. 26, p. 5100, Sep. 2004.
- [45] M. Paciaroni, M. Linne, T. Hall, J.-P. Delplanque, and T. Parker, “Single-Shot Two-Dimensional Ballistic Imaging of the Liquid Core in an Atomizing Spray,” *At. Sprays*, vol. 16, pp. 51–69, 2006.
- [46] M. a Linne, M. Paciaroni, J. R. Gord, and T. R. Meyer, “Ballistic imaging of the liquid core for a steady jet in crossflow,” *Appl. Opt.*, vol. 44, no. 31, p. 6627, Nov. 2005.
- [47] J. B. Schmidt, Z. D. Schaefer, T. R. Meyer, S. Roy, S. a Danczyk, and J. R. Gord, “Ultrafast time-gated ballistic-photon imaging and shadowgraphy in optically dense rocket sprays,” *Appl. Opt.*, vol. 48, no. 4, p. B137, Feb. 2009.
- [48] M. Linne, D. Sedarsky, T. Meyer, J. Gord, and C. Carter, “Ballistic imaging in the near-field of an effervescent spray,” *Exp. Fluids*, vol. 49, no. 4, pp. 911–923, Oct. 2010.
- [49] D. Sedarsky, J. Gord, C. Carter, T. Meyer, and M. Linne, “Fast-framing ballistic imaging of velocity in an aerated spray.,” *Opt. Lett.*, vol. 34, no. 18, pp. 2748–50, 2009.
- [50] D. L. Sedarsky, M. E. Paciaroni, M. a Linne, J. R. Gord, and T. R. Meyer,

- “Velocity imaging for the liquid-gas interface in the near field of an atomizing spray: proof of concept.,” *Opt. Lett.*, vol. 31, no. 7, pp. 906–8, Apr. 2006.
- [51] S. Idlahcen, C. Rozé, L. Méès, T. Girasole, and J. B. Blaisot, “Sub-picosecond ballistic imaging of a liquid jet,” *Exp. Fluids*, vol. 52, no. 2, pp. 289–298, 2012.
- [52] H. Purwar, S. Idlahcen, C. Rozé, D. Sedarsky, and J.-B. Blaisot, “Collinear, two-color optical Kerr effect shutter for ultrafast time-resolved imaging,” *Opt. Express*, vol. 22, no. 13, p. 15778, Jun. 2014.
- [53] J. Gao *et al.*, “Morphology of Diesel Sprays from Single-Orifice Micronozzles,” *ILASS Am. 22nd Annu. Conf. Liq. At. Spray Syst.*, no. May, 2010.
- [54] S. Moon *et al.*, “Ultrafast X-ray Phase-Contrast Imaging of High-Speed Fuel Sprays from a Two-Hole Diesel Nozzle,” *22nd Annu. Conf. Liq. At. Spray Syst. (ILASS Am. 2010)*, no. May, 2010.
- [55] Y. Wang *et al.*, “Ultrafast X-ray study of dense-liquid-jet flow dynamics using structure-tracking velocimetry,” *Nat. Phys.*, vol. 4, no. 4, pp. 305–309, Apr. 2008.
- [56] A. L. Kastengren, C. F. Powell, Y. Wang, K.-S. Im, and J. Wang, “X-Ray Radiography Measurements of Diesel Spray Structure At Engine-Like Ambient Density,” *At. Sprays*, vol. 19, no. 11, pp. 1031–1044, 2009.
- [57] S. Duran, J. Porter, and T. Parker, “Ballistic Imaging and Scattering Measurements for Diesel Spray,” Golden, CO.
- [58] E. Berrocal, D. L. Sedarsky, M. E. Paciaroni, I. V. Meglinski, and M. A. Linne, “Laser light scattering in turbid media Part I: Experimental and simulated results for the spatial intensity distribution,” *Opt. Express*, vol. 15, no. 17, p. 10649, Aug. 2007.
- [59] E. Berrocal, D. L. Sedarsky, M. E. Paciaroni, I. V. Meglinski, and M. A. Linne, “Laser light scattering in turbid media Part II: Spatial and temporal analysis of individual scattering orders via Monte Carlo simulation,” *Opt. Express*, vol. 17, no. 16, p. 13792, Jul. 2009.
- [60] E. Berrocal and J. Jönsson, “Development of future spray imaging techniques using General Purpose GPU accelerated Monte Carlo simulation Combustion Physics , Lund University , Sweden,” no. Mc, pp. 1–8, 2012.
- [61] A. Ziaee, “Time-gated picosecond digital holography on formation region of dense sprays,” Irvine, CA, 2013.
- [62] U. Schnars and W. Jueptner, *Digital Holography*. Springer, 2008.
- [63] J. W. Goodman, “Introduction to Fourier Optics McGraw-Hill Series in Electrical and Computer Engineering,” *Quantum Semiclassical Opt. J. Eur. Opt. Soc. Part B*, vol. 8, no. 5, p. 491, 1996.

- [64] T.-C. Poon and J.-P. Liu, *Introduction to Modern Digital Holography*, vol. 1. Cambridge: Cambridge University Press, 2013.
- [65] V. Kebbel, M. Adams, H.-J. Hartmann, and W. Jüptner, “Digital holography as a versatile optical diagnostic method for microgravity experiments,” *Meas. Sci. Technol.*, vol. 10, no. 10, pp. 893–899, Oct. 1999.
- [66] T. Kreis, *Handbook of holographic interferometry: optical and digital methods*. Wiley-VCH, 2005.
- [67] E. N. Leith and J. Upatnieks, “Reconstructed Wavefronts and Communication Theory*,” *J. Opt. Soc. Am.*, vol. 52, no. 10, p. 1123, Oct. 1962.
- [68] D. Dunn-Rankin *et al.*, “Time-gated holography to provide a glimpse into dense sprays,” *SPIE Newsroom*, Apr. 2013.
- [69] J. Trolinger, B. Buckner, I. Tomov, W. Van der Veer, D. Dunn-Rankin, and J. Garman, “Probing Dense Sprays with Gated, Picosecond, Digital Particle Field Holography,” *Int. J. Spray Combust. Dyn.*, vol. 3, no. 4, pp. 351–366, Dec. 2011.
- [70] D. Sedarsky *et al.*, “Quantitative image contrast enhancement in time-gated transillumination of scattering media –Laser light scattering in turbid media Part I: Experimental and simulated results for the spatial intensity distribution,” *Phys. Express*, vol. 190, no. 7, pp. 2011–31, 2011.
- [71] W. Tan, Z. Zhou, A. Lin, J. Si, J. Tong, and X. Hou, “Femtosecond nonlinear optical property of a TeO₂–ZnO–Na₂O glass and its application in time-resolved three-dimensional imaging,” *Opt. Commun.*, vol. 291, pp. 337–340, 2013.
- [72] a Heilig, M. Kaiser, and F. Dinkelacker, “Near Nozzle High-Speed Measurements of the Intact Core for Diesel Spray,” *ICLASS 2012, 12th Trienn. Int. Conf. Liq. At. Spray Syst.*, pp. 1–8, 2012.
- [73] J. Koo and J. K. Martin, “Droplet Sizes and Velocities in a Transient Diesel Fuel Spray,” in *SAE Technical Paper*, 1990.
- [74] J. Manin, “Numerical Investigation of the Primary Breakup Region of High-Pressure Sprays,” vol. 23, no. X, pp. 1–23, 2018.
- [75] J. Burke, C. F. Hess, and V. Kebbel, “Digital Holography for Instantaneous Spray Diagnostics on a Plane,” *Part. Part. Syst. Charact.*, vol. 20, no. 3, pp. 183–192, 2003.
- [76] Yan Yang and Bo-seon Kang, “Potential of digital holography in sprays measurement,” in *2008 7th World Congress on Intelligent Control and Automation*, 2008, pp. 1702–1707.
- [77] Y. J. Choo and B. S. Kang, “The characteristics of the particle position along an optical axis in particle holography,” *Meas. Sci. Technol.*, vol. 17, no. 4, pp. 761–

- 770, 2006.
- [78] C. Crua, M. R. Heikal, and M. R. Gold, “Microscopic imaging of the initial stage of diesel spray formation,” *Fuel*, vol. 157, pp. 140–150, Oct. 2015.
 - [79] H. M. Smith, *Principles of holography / Howard M. Smith*. Wiley-Interscience, 1975.
 - [80] M. Minniti, A. Ziaee, J. D. Trolinger, and D. Dunn-rankin, “Ultra-short Pulse Off-axis Digital Holography for Imaging the Core Structure of Transient Sprays,” in *ILASS Americas, 29th Annual Conference on Liquid Atomization and Spray Systems*, 2017, no. May.
 - [81] D. Dunn-Rankin, A. Ziaee, A. K. Dioumaev, M. Minniti, and J. D. Trolinger, “Spatially and temporally resolved diagnostics of dense sprays using gated, femtosecond, digital holography,” in *Applied Optical Metrology II*, 2017, vol. 10373, p. 25.
 - [82] B. Schwarz, G. Ritt, M. Körber, and B. Eberle, “Laser-induced damage threshold of camera sensors and micro-opto-electro-mechanical systems,” 2016, vol. 9987, no. 0, p. 99870D.
 - [83] L. Gallais and M. Commandré, “Laser-induced damage thresholds of bulk and coating optical materials at 1030 nm, 500 fs,” *Appl. Opt.*, vol. 53, no. 4, p. A186, 2014.
 - [84] M. Minniti, A. Ziaee, D. Curran, J. Porter, T. Parker, and D. Dunn-Rankin, “Ultra-short Pulse Off-axis Digital Holography Imaging under Realistic Diesel Spray Conditions,” in *ICLASS 2018, 14th international conference on liquid atomization & spray systems*, 2018.
 - [85] J. Naber and D. L. Siebers, “Effects of Gas Density and Vaporization on Penetration and Dispersion of Diesel Sprays,” in *SAE Technical Paper Series*, 1996, vol. 1, no. 412.
 - [86] T. Pitkäaho and T. J. Naughton, “Calculating depth maps from digital holograms using stereo disparity,” *Opt. Lett.*, vol. 36, no. 11, p. 2035, Jun. 2011.
 - [87] J.-M. Desse and F. Olchewsky, “Dual-reference digital holographic interferometry for analyzing high-density gradients in fluid mechanics,” *Opt. Lett.*, vol. 43, no. 8, p. 1635, Apr. 2018.
 - [88] P. Picart, E. Moisson, and D. Mounier, “Twin-sensitivity measurement by spatial multiplexing of digitally recorded holograms,” *Appl. Opt.*, vol. 42, no. 11, p. 1947, Apr. 2003.
 - [89] T. Saucedo A., F. M. Santoyo, M. De la Torre Ibarra, G. Pedrini, and W. Osten, “Simultaneous two-dimensional endoscopic pulsed digital holography for evaluation

- of dynamic displacements,” *Appl. Opt.*, vol. 45, no. 19, p. 4534, Jul. 2006.
- [90] J. Kühn *et al.*, “Real-time dual-wavelength digital holographic microscopy with a single hologram acquisition,” *Opt. Express*, vol. 15, no. 12, p. 7231, Jun. 2007.
- [91] S. Boucherit, L. Bouamama, R. Zegadi, and S. Simons, “Formulation of off-axis single reference beam and two angle views for digital holography,” *J. Opt.*, vol. 12, no. 3, pp. 0–5, 2010.
- [92] B. Özgürün, D. Ö. Tayyar, K. Ö. Ağış, and M. Özcan, “Three-dimensional image reconstruction of macroscopic objects from a single digital hologram using stereo disparity,” *Appl. Opt.*, vol. 56, no. 13, p. F84, May 2017.
- [93] T. M. Lehtimäki and T. J. Naughton, “Stereoscopic viewing of digital holograms of real-world objects,” *Proc. 3DTV-CON*, pp. 2–5, 2007.
- [94] C. A. Lindensmith *et al.*, “A Submersible, Off-Axis Holographic Microscope for Detection of Microbial Motility and Morphology in Aqueous and Icy Environments,” *PLoS One*, vol. 11, no. 1, p. e0147700, Jan. 2016.